Title: Equation of State and Damage in Polyethylene

Author(s): Coe, Joshua Damon; Brown, Eric; Cady, Carl Mcelhinney; Carlson, Carl A.; Clements, Bradford Edwin; Dattelbaum, Dana Mcgraw; Fezzaa, K.; Gustavsen, Richard L.; Hooks, Daniel Edwin; Iverson, Adam Joseph; Jensen, Brian J.; Jordan, Jennifer Lynn; Jones, David Robert; Junghans, Sylvia Ann; Lang, John Michael Jr.; LeBrun, Thomas John; Lewis, Matthew W.; Maerzke, Katie A.; Pierce, Timothy Henry; Ramos, Kyle James; Rigg, Paulo; et al.

Intended for: Report

Issued: 2019-10-21 (rev.1)

Equation of State and Damage in Polyethylene

Dynamic Materials Properties (Science Campaign 2)

Level 2 Milestone Report, FY 2017

Authors:
Eric N. Brown
Carl Cady
C. A. Carlson
Brad E. Clements
Joshua D. Coe*
Dana M. Dattelbaum*
K. Fezzaa
Rick Gustavsen
Dan Hooks
A. J. Iverson
Brian J. Jensen
Jennifer L. Jordan
David R. Jones
Ann Junghans
John M. Lang, Jr.
Thomas Lebrun
Matthew W. Lewis*
Katie A. Maerzke
T. H. Pierce
Kyle J. Ramos
Paulo Rigg
Benjamin F. Schilling
N. Sinclair
Jamie A. Stull
Erik Watkins
Cynthia F. Welch
Paul M. Welch

October 16, 2019

Contents

I Abbreviations

- APS *Advanced Photon Source*
- COD *crack opening displacement*
- DAC *diamond anvil cell*
- DCS *Dynamic Compression Sector*
- EOS *equation of state*
- FWHM *full width at half maximum*
- GAP *Glassy Amorphous Polymer*
- HDPE *high-density polyethylene*
- HEL *Hugoniot elastic limit*
- HPCAT *High Pressure Collaborative Access Team*
- IMPULSE *IMPact system for ULtrafast Synchrotron Experiments*
- LVDT *Linear Variable Differential Transformer*
- MW *molecular weight*
- PCI *Phase Contrast Imaging*
- PDV *photon Doppler velocimetry*
- PE *polyethylene*
- PMMA *Poly(methyl methacrylate)*
- PTFE *Polytetrafluoroethylene*
- PZT *lead-zirconate-titanate*
- RCP *Rapid Crack Propagation*
- SANS *small-angle neutron scattering*
- SAXS *small-angle X-ray scattering*
- SCG *Slow Crack Growth*
- SHPB *Split Hopkinson Pressure Bar*
- TA *technical area*
- TS *true strain*
- UHMWPE *ultrahigh molecular weight polyethylene*

II Executive Summary (*Dattelbaum, Lewis, Coe*)

The dynamic response of polymers differs significantly from those of metals, upon which many of the National Laboratories' deformation, damage, and failure models are based. Their moduli, yield strength, and damage characteristics are highly strain rate-, temperature-, and phase-dependent, requiring models that encompass a wide range of phenomena including some not in equilibrium. Recently, Los Alamos developed the Glassy Amorphous Polymer (GAP)[1] model [1] to address limitations in existing models of polymer deformation. GAP captures both volumetric (equation of state) and deviatoric (shear) response, including a non-equilibrium component to the former (a feature determined to be crucial in capturing the low-pressure, viscoelastic response to impact loading). GAP has already been applied to polymers such as PMMA, PTFE, epoxy, and Kel-F 800, but with an emphasis on impact response as opposed to damage or failure. The current effort was launched to address this gap in predictive capability. For reasons that will be made clear, semi-crystalline polyethylene (PE) was chosen to serve as a model system for parameterization and validation.

PE $(\text{-}C_2H_4\text{-})_n$ is one of the most widely used polymers in industrial and engineering contexts, chiefly due to the versatility of its mechanical response. This response can be tuned through network and chain structure, degree of crystallinity, and molecular weight. PE is found in several forms including low density (LDPE), high density (HDPE), and ultra-high molecular weight (UHMWPE). The focus here was on HDPE and UHMWPE, of pedigree described in the following section. Materials were well-characterized prior to study and are representative of semi-crystalline polymers of interest to DOE and DoD.

Semi-crystalline PE undergoes a glass transition at low temperature (-35°C) and melts across a range of moderate temperatures (∼80-180°C), depending on its structure. It is typically inert chemically, has low strength and high ductility, and the high strength and anisotropy of UHMWPE fiber, in particular, have driven its use in engineering, impact, and armor applications. Surprisingly little is known, however, about the influence of PE's crystalline structure and associated phase transitions (including melt) on its response to dynamic compression.

A broad suite of experiments was used to calibrate the GAP model for HDPE and UHMWPE. Section IV examines the effects of tensile strain on the structure and integrity of PE crystalline domains. These data were used to inform the preliminary damage model described in Section XII, whose roots lie in statistical physics and network theory. The viscoelastic and plastic components of GAP rely heavily on the stress-strain data of Section VI, which also include dynamic extrusion and Taylor anvil experiments used to validate the damage model. The thermal data of Section X provide crucial inputs to the equilibrium EOS in GAP, as well as the much broader range SESAME EOS whose construction is outlined in Section XI. Section VII details plate impact experiments characterizing the low-pressure shock locus and failure (spall) using *in situ* electromagnetic gauges. A previously reported "cusp" in the principal Hugoniot near 0.5 kbar was confirmed, and a multi-wave structure was observed over a limited input stress range above the cusp. This cusp is believed due to solid-solid phase transitions associated with the crystalline domains of the polymer.

Spall experiments relevant to engineering impact conditions showed that polyethylene fails by a ductile/damage accumulation mechanism. No evidence of brittle failure was observed by velocimetry, and the dynamic failure strength and mechanism were consistent with other semi-crystalline, ductile polymers such as PTFE, Kel-F, and Estane. A damage model based on statistical crack mechanics was folded into GAP and applied to polyethylene for the first time, and spall simulations based on this model showed it to adequately reproduce the measured velocity profiles associated with failure. This suggests that PE does not completely fail, but rather accumulates damage in dynamic tension under the conditions produced in the experiments. These results were corroborated by dynamic X-ray phase contrast imaging experiments at the Advanced Photon Source (Section VIII), which suggested a transition from ductile-to-brittle failure as tensile stress and strain rate were increased. Additional characterization included dynamic diamond anvil cell experiments (Section V) to pinpoint crystalline

---

[1] Many of the most commonly-appearing acronyms can be found in the previous section.

phase transitions and the high pressure melt line, as well as “deep release” from strongly overdriven shock states believed to be chemically decomposed. Modeling of these reacted states will form the subject of future work.

Under the auspices of this milestone, the Dynamic Materials Properties Campaign and Joint Munitions Program have advanced models for predicting the dynamic compressive and failure response of polymers in general, but with particular emphasis on one of broad interest to both the DOE and DoD. Tools and data detailed below are designed to inform material options for future stockpile applications, in addition to providing a baseline for current and future predictive capabilities.

Dana Dattelbaum, Campaign 2 Program Manager (*danadat@lanl.gov*)
Joshua Coe, Campaign 2 Project Leader (*jcoe@lanl.gov*)
Matt Lewis, JMP Project Leader (*mlewis@lanl.gov*)

III Materials (*Dattelbaum, C. Welch*)

Two different lots of HDPE and UHMWPE were studied. The first experiments were performed on extruded materials ("old") later found to have density variations. The only data reported here for the old material are found in Section VII.F (in particular, see Table 6).

We purchased large, rectangular, compression-molded sheets of HDPE (Densetec ®) [2] and UHMWPE (Polyslick ®) [3] from Polymer Industries in FY15. The sheets were of uniform density and percent crystallinity throughout, permitting valid comparison of experimental results obtained using samples taken from different locations. Table 1 provides details on the as-received sheets, used in all subsequent experiments. From integration of the melt endotherm by differential scanning calorimetry, the compression-molded HDPE was $78.5 \pm 2.0\%$ crystalline, had an initial density of 0.961 g/cc, and a MW of 300,000 g/mol. The UHMWPE was $52.2 \pm 1.1\%$ crystalline, had lower initial density of 0.930 g/cc, and higher molecular weight of ~6,000,000 g/mol; differences with HDPE are due to the long chain structure of UHMWPE. The average initial densities and % crystallinities of the materials are listed in Table 2.

Table 1: Details of the as-received polyethylene sheets.

	HDPE	UHMWPE
Manufacturer	Polymer Industries	Polymer Industries
Sheet dimensions (in)	2 x 48 x 96	2 x 48 x 96
Serial number	HDVN12051412061409	BADA3F112E11191309
Lot information	C:1; F:Lot PInOP_id:207378	C:1; F:Lot PInOP_id:184688
Molecular weight (g/mol)	300,000	6,000,000

Table 2: Description of HDPE and UHMWPE samples. % crystallinity was measured by integrating the melt exotherm to obtain the heat flow by differential scanning calorimetry. Densities were measured by immersion techniques.

Material	ρ_0(g/cc)	% crystallinity	Source
HDPE 12025 (old lot)	~0.960	67-76	—
HDPE 207 (new lot)	0.961	78.5±2.0	Polymer Industries Densetec
UHMWPE (old lot)	~0.933	44-54	—
UHMWPE (new lot)	0.930	52.2±1.1	Polymer Industries Polyslick

IV Morphology (*C. Welch, Stull, Junghans*)

IV.A Introduction

In semi-crystalline polymers such as PE, the crystalline domains serve as physical crosslinks distributed within an amorphous polymer matrix. The interactions between the crystalline and amorphous domains, as well as the interface between them, play a large role in determining the materials mechanical properties. A new long-term goal that has been identified during this project is to use our network model based on eigenvector centrality [166] to quantify the relationships between PE's semi-crystalline morphology and its mechanical properties. This same network model can also provide insight into the effects of extreme environments (mechanical, thermal, pressure, radiation, etc.) that alter the equilibrium nano-scale structure and subsequently affect performance, as detailed in Section XII. In order to apply the network model to polyethylene, we need to characterize various aspects of the semi-crystalline morphology, including the average number of chains that enter / exit a crystalline domain, the size distribution of the crystals, and the volume percentage of crystalline domains. Small-angle scattering and differential scanning calorimetry can provide these characteristics.

IV.B Small-angle X-ray scattering on as-received samples

Figure 1 shows representative two-dimensional scattering patterns obtained for the as-received HDPE (left) and UHMWPE (right) samples. These patterns display the scattering intensity recorded on the two-dimensional detector, Q_y vs. Q_x, where the scattering vector Q is inversely related to the length scale probed. The magnitude of Q is defined in terms of the X-ray wavelength λ and the scattering angle θ: $Q = (4\pi/\lambda)sin(\theta/2)$. The isotropic nature of the scattering patterns indicates that there is no orientation of the crystalline domains within these samples. Furthermore, scattering patterns taken from different points along the machined samples indicate no difference in scattering intensity across the samples, indicating uniformity.

IV.C Effects of tensile strain

To connect mechanical properties to the morphological interplay of crystalline and amorphous domains, we have been developing *in situ* small-angle scattering experiments with a tensile stage. As the sample is stretched, scattering patterns are recorded to monitor any nano-scale changes and/or damage to the semi-crystalline polymers. In FY15, we conducted preliminary small-angle neutron scattering (SANS) measurements with HDPE and UHMWPE samples at LANL's Lujan Neutron Scattering Center. However, the large hydrogen content in PE produced a significant amount of incoherent scattering that limited the usefulness of that data. To avoid this problem, we developed similar experiments in FY16 that utilize an X-ray beamline to yield small-angle X-ray scattering (SAXS) measurements in conjunction with a tensile stage sample environment. These experiments were conducted on the Bruker Nanostar instrument at LANLs Center for Integrated Nanotechnologies (CINT). Figure 2 shows the *in situ* tensile stage along with representative two-dimensional small-angle scattering patterns for the HDPE sample at true strains (TS, see Section VI.D.2 for a discussion) of 0 and 0.9. As tensile deformation is applied, the scattering pattern becomes anisotropic, reflecting the change in the crystalline domain morphology.

Two types of *in situ* SAXS experiments were conducted. In the first, a step strain loading profile was used to give information on the equilibrated morphology after each strain. After collecting data for the unstretched sample, it was elongated to the new strain value, equilibrated for 30 min, and then measured by SAXS. This cycle was repeated with increasing elongation distances until the maximum elongation was reached. The second type of experiment probed dynamic changes in morphology. Samples were strained to the same total extent as in the first type of experiment. However, rather than waiting 30 minutes for the morphology to equilibrate, we collected SAXS data during the continuous application of strain in 5-minute intervals. Stress-strain curves for both types of experiments are

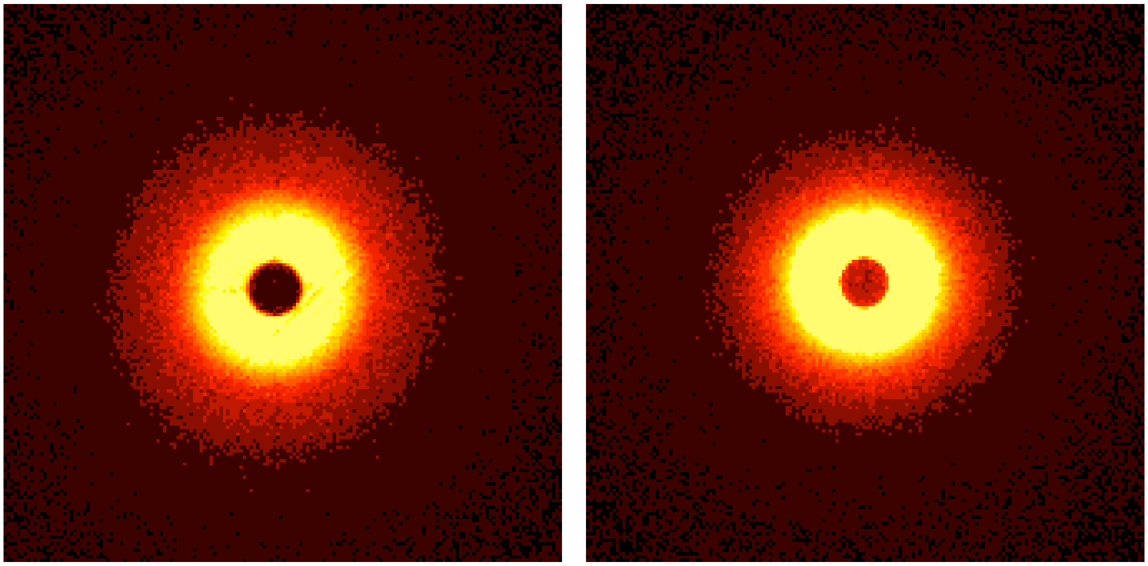

Figure 1: Two-dimensional small-angle X-ray scattering patterns of as-received (left) HDPE and (right) UHMWPE.

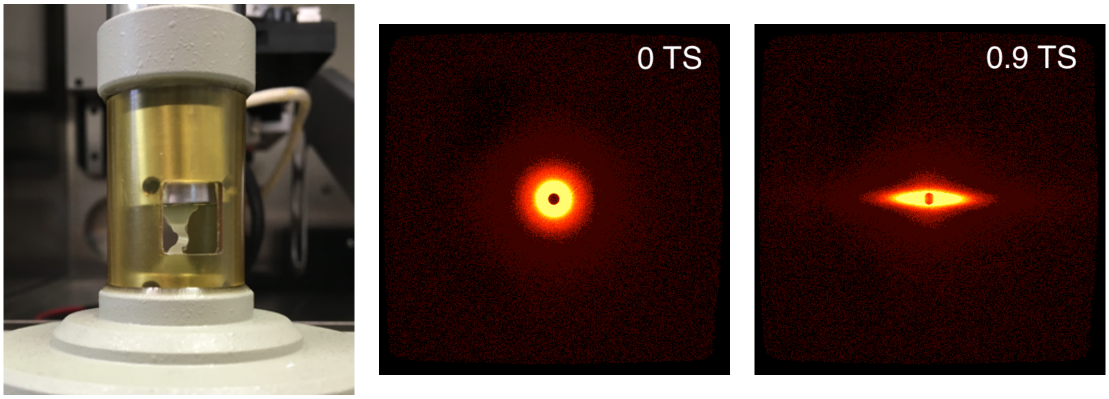

Figure 2: (left) *in situ* tensile stage adapted for use with the CINT Nanostar; (center) and (left) 2-D scattering patterns for HDPE, with tensile true strain values of 0 (center) and 0.9 (right).

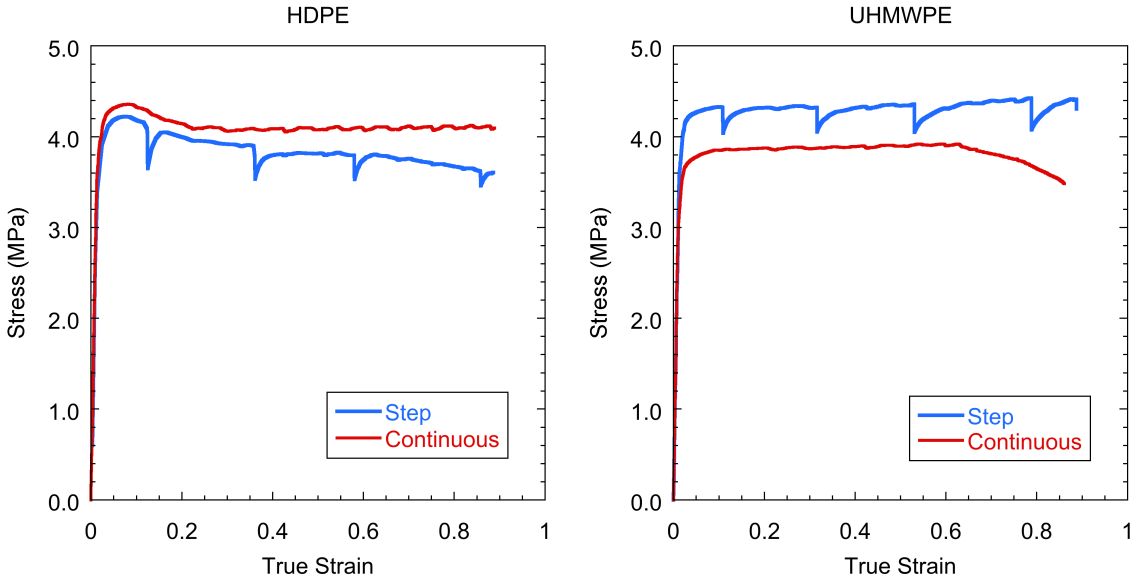

Figure 3: Stress-strain curves for (left) HDPE and (right) UHMWPE during *in situ* SAXS.

shown in Figure 3. For the step strain experiments, the dips in the stress-strain curves correspond to the step increases in strain. For HDPE, these TS values are 0.1, 0.4, 0.6, and 0.9, while UHMWPE was taken to TS values of 0.1, 0.3, 0.5, and 0.8.

SAXS data for all 4 sets of experiments are given in Figures 4 (step strain) and 5 (continuous strain). Significant changes in the scattering curves are noted as TS is increased for all cases, reflecting the change in morphology of the crystalline domains as the sample is stretched. Furthermore, the HDPE and UHMWPE samples behave quite differently from each other. For example, in Figure 4, the scattering curves for HDPE lose the features at $Q \approx 0.02$ Å^{-1} and $Q \approx 0.04$ Å^{-1} for TS values of 0.4 or greater. On the other hand, the peak for UHMWPE at $Q \approx 0.01$ Å^{-1} gradually decreases in intensity as TS increases. Figure 5 shows that the morphological changes that occur during the continuous strain experiments are quite similar to those observed during step strain experiments (Figure 4) for both polymers.

Within 24 hours of these *in situ* tensile strain experiments, pieces were taken from the end and middle of each dogbone sample to evaluate the changes in crystallinity between the unstretched (end) and stretched (middle) portions of the dogbone. Differential scanning calorimetry (DSC) experiments were performed on a TA Instruments Q2000 MDSC with hermetically sealed aluminum pans at a ramp rate of 10°C/min. Figure 6 shows results for all 8 samples, and Table 3 lists the peak melting temperature, heat of fusion (H_f), and weight fraction of crystalline domains (X_c) for each sample.

The most probable (mass-based) thickness of the crystalline lamellae (L) can be calculated from both the DSC and the SAXS data, and these results are also given in Table 3. The Gibbs-Thomson equation (Eq. (1)) is used to estimate L from the DSC data:

$$L = \frac{2\sigma}{H_f^0} \frac{T_m^0}{T_m^0 - T_m} \tag{1}$$

where σ is the energy required for the polymer chains to fold at the surface of the lamellae, and H_f^o and T_m^o are the heat of fusion and melting temperature, respectively, for a 100% crystalline polyethylene sample. While there is some debate about the appropriate values to use for σ and T_m^o [15,16], we used the well-established values of 90 mJ/m^2 for σ, 145.5°C for T_m^o, and 290 J/cm^3 for H_f^o [17–19]. Note that temperature must be in K when using Eq. (1).

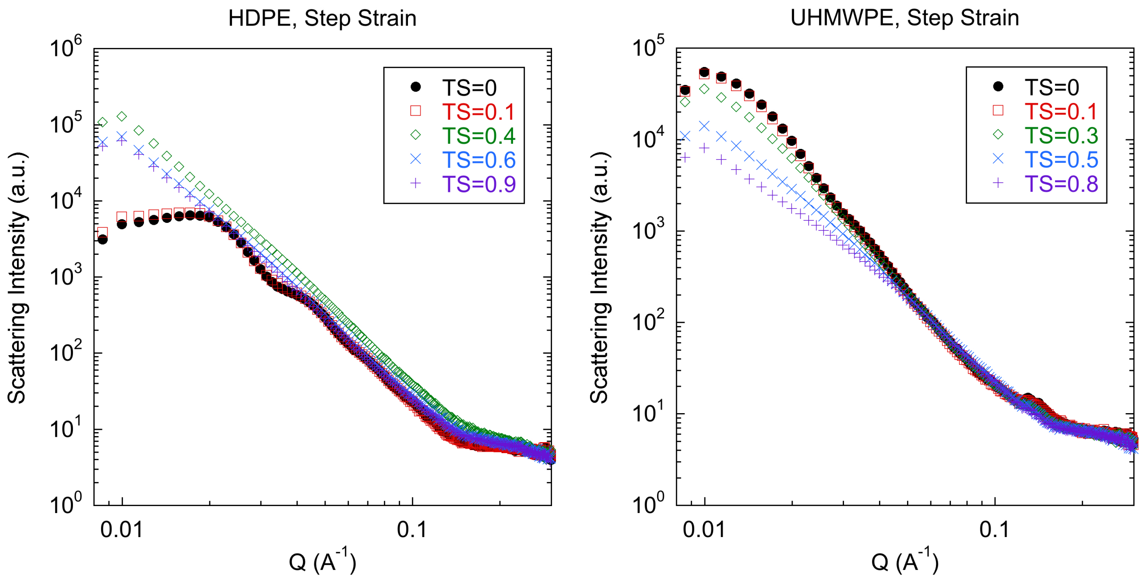

Figure 4: SAXS data for step strain experiments on (left) HDPE and (right) UHMWPE.

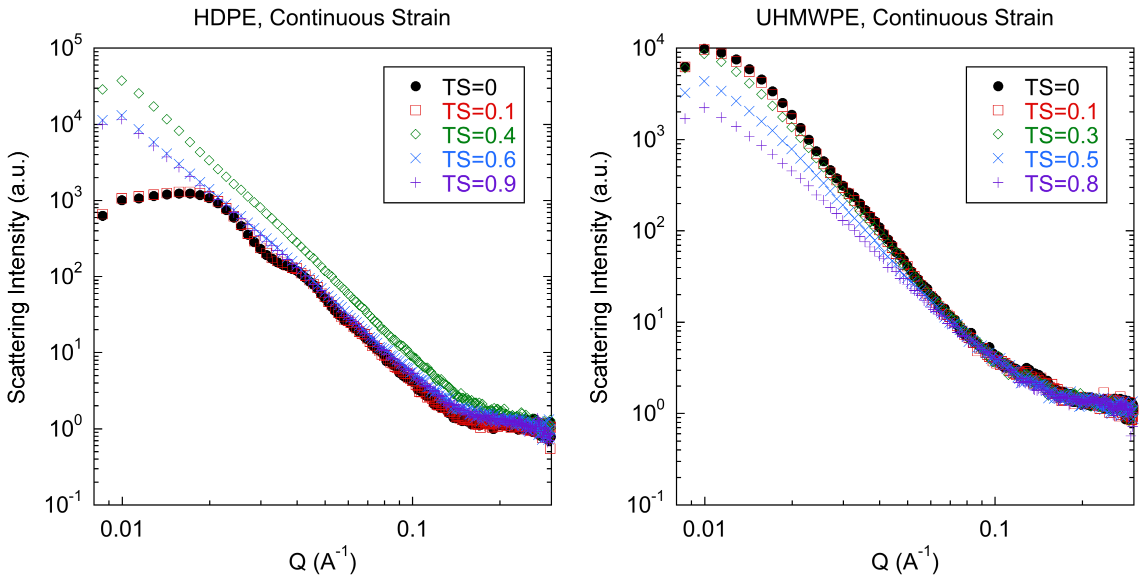

Figure 5: SAXS data for continuous strain experiments on (left) HDPE and (right) UHMWPE.

Table 3: DSC and SAXS results describing the crystalline domains of stretched and unstretched portions of polyethylene dogbones.

Sample	Strain Profile	True Strain	Peak T_m (°C)	H_f (J/g)	X_c	L_{DSC}(nm)	Peak Q(Å^{-1})	L_{SAXS}(nm)
HDPE	Step	0	135	231	0.80	24.8	0.0214	23.5
HDPE	Continuous	0	137	235	0.81	30.6	0.0199	25.6
HDPE	Step	0.9	133	209	0.72	20.8	0.00997	45.6
HDPE	Continuous	0.9	132	184	0.64	19.3	0.00997	40.1
UHMWPE	Step	0	135	155	0.54	24.8	0.0128	26.3
UHMWPE	Continuous	0	135	156	0.54	24.8	0.0128	26.5
UHMWPE	Step	0.8	134	135	0.47	22.6	0.00997	29.4
UHMWPE	Continuous	0.8	134	135	0.47	22.6	0.0128	22.9

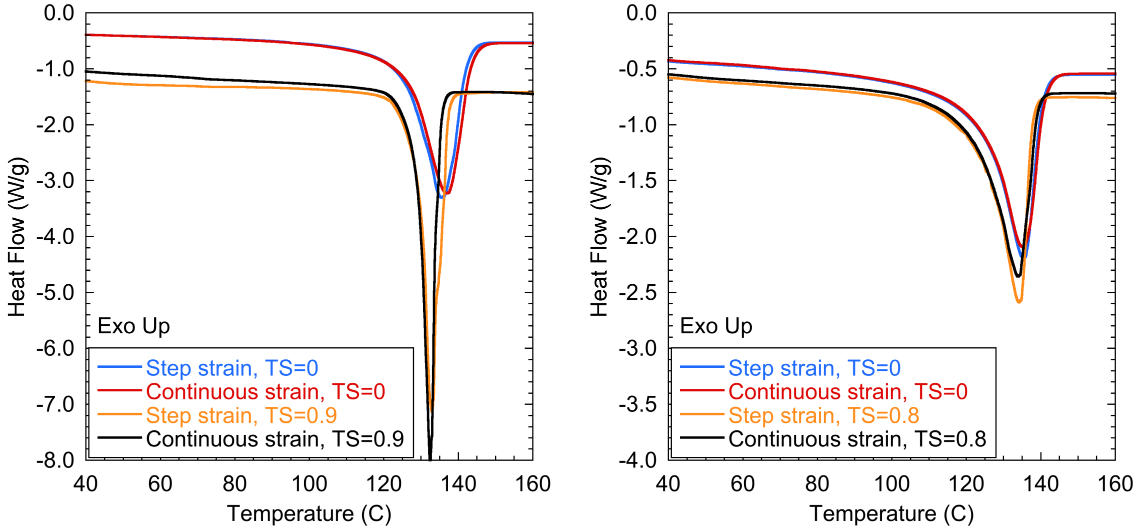

Figure 6: DSC measurement of melting transition for stretched and unstretched portions of dogbones of (left) HDPE and (right) UHMWPE.

Calculation of L from the SAXS data relies on Eq. (2):

$$L = \frac{2\pi X_c}{Q_{peak}}, \tag{2}$$

where Q_{peak} is the magnitude of the scattering vector at the first peak in the Lorentz-corrected intensity plot (IQ^2 vs. Q). As seen in Table 3, the two methods for calculating L agree fairly well, except for the two stretched ($TS = 0.9$) HDPE samples. For the UHMWPE samples, the DSC and SAXS results indicate that tensile deformation from $TS = 0$ to $TS = 0.8$ causes a reduction in X_c and probably a reduction in L. For HDPE, X_c decreases as TS increases to 0.9, and the L values calculated from the DSC data also decrease. Though the L values calculated from the SAXS data appear to increase substantially for the HDPE samples at $TS = 0.9$, these results are held suspect for two reasons. First, the Q_{peak} values for these two samples are very close to the minimum Q value measured in these experiments, so the peak could be an artifact due to the beam stop. However, if the peak is real, the disagreement between the SAXS and DSC results for L of these two samples suggests that the SAXS peak is caused by some other feature in the stretched sample. The most likely source of this peak is voids formed by cavitation, based on comparison to literature results of other small-angle scattering studies of PE [20,21]. By examining the SAXS curves for the continuously pulled sample at TS values between 0.1 and 0.4 (see Figure 7), we observe that cavitation likely begins at TS between 0.2 and 0.3, which is also where the sample begins to yield in the stress-strain data of Figure 3.

There is a vast array of studies examining the effects of tensile deformation on semi-crystalline polymers, and PE is often used as a model in these studies. Deformation of semi-crystalline polymers is quite complicated and involves an interplay of highly oriented chain segments in crystalline regions, randomly oriented chain segments in amorphous regions, and chain segments that fall in between, *i.e.*, in the interphase region. Various mechanisms have been proposed and observed experimentally, including melting followed by recrystallization [148,149], strain-induced crystallization [150], reversible fine chain slip within crystalline domains at low strains [18, 151], irreversible coarse chain slip and lamellar fragmentation at large deformations [18, 151], rubber-like deformation of the amorphous region [21]. and cavitation / void formation [20, 21, 150]. In most cases, multiple mechanisms are likely involved [152], depending on the lamellar thickness of the crystalline domains, % crystallinity, strain rate, deformation temperature, and the extent of strain.

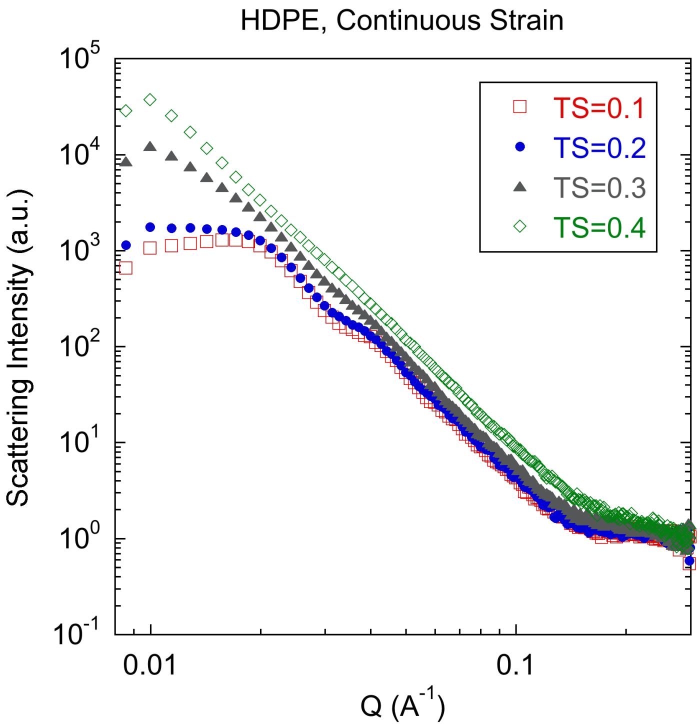

Figure 7: SAXS data for continuous strain experiments on HDPE for TS values of 0.1 to 0.4.

The initial analysis of the SAXS and DSC data presented above suggests that, for the two PE samples studied here, tensile strain causes melting and / or fragmentation of the crystalline domains. This mechanism appears to occur over the entire strain range tested, up to $TS = 0.8$ for UHMWPE and $TS = 0.9$ for HDPE. In addition, the SAXS data for the stretched HDPE sample is consistent with cavitation at TS values above 0.2.

The results presented above, especially the stress-strain curves of Figure 3 and the results presented in Table 3, represent part of the information needed to apply the network theory model [166] to semi-crystalline polyethylene. Further evaluation of the data should yield the remaining needed parameters, such as the average number of chains that enter / exit a crystalline domain and the size distribution of the crystals.

V Diamond Anvil Cell Experiments (*Watkins*)

A series of high pressure diamond anvil cell (DAC) synchrotron X-ray diffraction experiments were performed on HDPE at the HPCAT beamline of the Advanced Photon Source (APS). The work focused on dynamic pressure loading and resulted in software and analysis developments to generate diffraction maps and obtain sample pressure profiles under ramp loading. This approach allows phase transitions in samples under dynamic pressure loading to be clearly identified independent of the measured diffraction signals which may be applicable to study non-crystalline transformations.

High pressure measurements were performed at beamline 16ID-B using 30.5 keV X-rays transmitted through symmetric DAC cells and diffracted signals were detected using a 2-D Pilatus 1M-F detector. Samples consisted of solid HDPE containing crystalline domains. The crystalline domains were approximately 15 nm in size (FWHM), as determined from their diffraction peaks and the Scherrer equation. The HDPE samples were measured at room temperature under either static compression or dynamic loading of the sample from ambient pressure up to 50 GPa. Static compression measurements indicated a room temperature phase change at relatively low pressure (1-2 GPa) followed by disappearance of diffraction from the crystalline domains between 10-20 GPa. A series of seven pressure jump compressions were performed on the same material over a range of dynamic loading conditions. The DAC cells were loaded at rates of 1-100 psi/s, X-ray diffraction was collected every 100ms, and an internal Au pressure standard was used to determine the pressure within the sample as a function of time. Software was developed to automatically fit the Au diffraction and determine the sample pressure using the Au EOS in order to generate diffraction maps as a function of sample pressure vs. momentum transfer (Fig. 8, top). Despite the constant rate of pressure loading on the DAC, the rate of increase of the sample pressure exhibited discrete jumps which can be correlated to phase transitions within the sample. At lower loading rates (1-25 psi/s), changes in the sample pressure ramp rate corresponding to the 1-2 GPa phase transition were observed. However, changes corresponding to the disappearance of the crystalline domains were difficult to detect. At higher loading rates (50-100 psi/s), the low pressure phase transition occurred too rapidly to be detected with the 100 ms time resolution of the measurements. However, large changes in the sample pressure ramp rate corresponding to the disappearance of the crystalline domains were observed (Fig. 8, bottom). This allowed the onset and cessation of the transition to be determined more accurately than by observing the decreasing amplitude of the diffraction peaks. Furthermore, laser decomposition experiments were performed to test the capability to measure resulting carbon products and spatially resolved diffraction experiments were performed to test capabilities to ascertain sample heterogeneities.

In addition to synchrotron experimental work, efforts were made to set up a dedicated DAC lab located in TA-46, building 31, room 102A. Significant investments were made in diamond anvils, other DAC cell components, and a high quality stereomicroscope (Leica M205 C) to develop the high pressure experimental capabilities available in this lab space. These investments and efforts will facilitate future high-pressure studies on PE including preparation for synchrotron experiments and the ability to conduct LANL-based high-pressure measurements using optical microscopy and Raman spectroscopy.

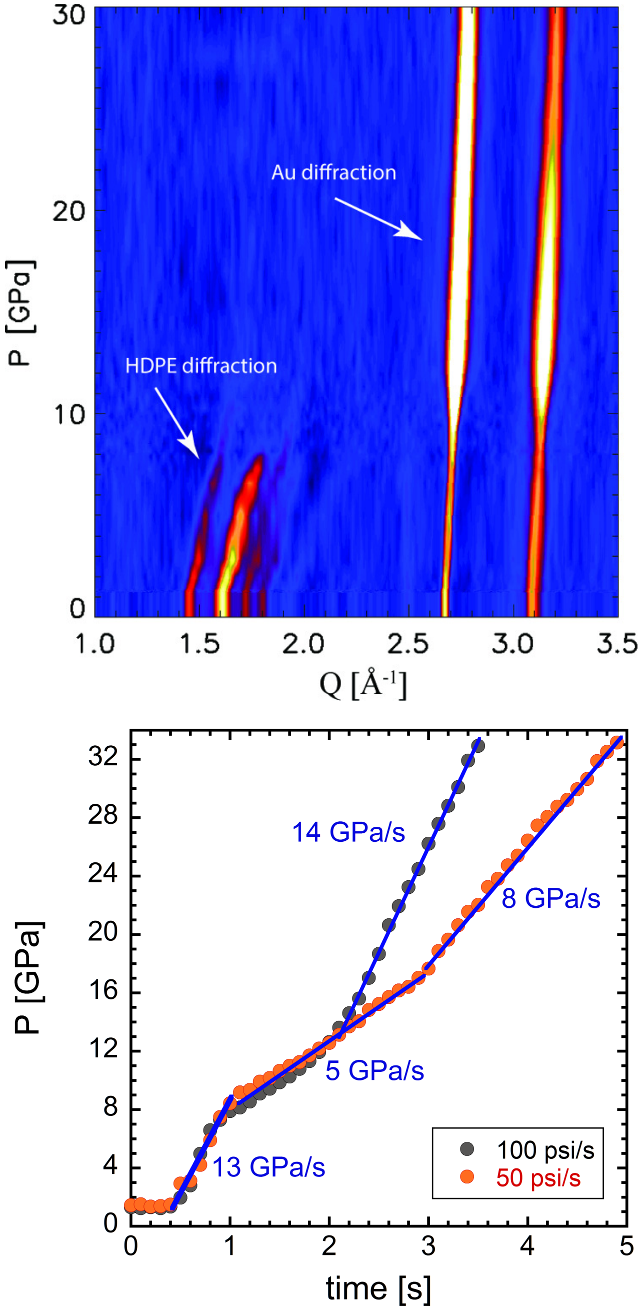

Figure 8: (top) Diffraction map of a 100 psi/s pressure jump experiment (bottom) Comparison of the pressure within HDPE samples under two different dynamic loading rates: 100 psi/s (black) and 50 psi/s (blue). The regions with reduced rates of increasing sample pressure (5 GPa/s) correspond to the disappearance of crystalline domains within the sample.

VI Mechanical Characterization (*Cady, Jones, Lebrun*)

VI.A Introduction

A series of mechanical tests were performed on HDPE and UHMWPE. In most cases, data generated for HDPE samples had the number 378 associated with the file. This represented the lot number for the starting plate of 207378. Similarly, the UHMWPE tests had filenames with the numbers 688 associated with them due to their derivation from lot 184688. The samples were cut from two sheets of material in different orientation in order to determine if processing effects influenced properties. The two sheets were nominally 2” thick by 2 feet wide by 6 feet long with sections of material distributed to the organizations doing characterization. Samples for this characterization were cut from a piece that was 2 feet wide by 18 inches long.

Several systems were used to characterize the compressive, tensile, and extrusion properties of both materials, including the MTS servo-hydraulic load frame, a split Hopkinson pressure bar, and the Taylor anvil system (for both Taylor impact and dynamic extrusion).

VI.B Dimensional measurements

All samples were measured before testing so that stress strain analysis could be conducted afterward. Sample measurements and test file names and conditions are documented in Tables 4 and 5 for the compression and tensile tests, respectively.

VI.C Mechanical Test Configuration

A wide range of strain rates, temperatures and test conditions were sampled for the characterization of the two types of polyethylene. Tests were conducted at temperatures from −75°C to 100°C and over strain rates from 0.0001/s to ∼2000/s. The primary test method was compression, but tensile, dynamic extrusion, and Taylor anvil experiments were also conducted in order to better inform model development.

The low-rate compression and tensile tests were conducted with an MTS model 880 test frame. In addition to the installed load cell and LVDT transducer, additional load measuring devices were used. Either a 100 lb. or 1000 lb. capacity load cell was used to ensure the most accurate measurement of the load. The control channel of these tests used the LVDT signal. For compression testing, an extensometer signal provided from COD (crack opening displacement) calibrated in the “closing” direction was used to measure the displacement without system compliance. This added a small additional load due to the spring constant of the device, but one that could be measured and subtracted from the experimental data when a high enough percentage of the overall load signal. Generally, the load increase was ∼0.75N per 0.5mm of displacement and was linear over its range of accuracy (0.5” displacement range). The analysis of the current results does not subtract away this known error because it was such a small fraction of the applied load. The samples were loaded up to approximately 50% true strain at a true strain rate and unloaded at the same rate. Analysis of the data was done using the smaller load cell and the extensometer data to achieve the most accurate results. The benefit to using this extensometer was that it eliminated system compliance and hysteresis in the displacement signal, thereby reducing the uncertainty of the load/displacement for the entire system. All tests were conducted with molydisulfide grease lubrication on optically flat tungsten carbide platens measuring 0.75 inches diameter. The samples were heated using resistance cartridges that were inside the loading fixture. Sample cooling was done by passing liquid nitrogen through channels that were cut into the loading fixture.

High-rate compression tests were conducted on a Split Hopkinson Pressure Bar (SHPB) over the same range of temperatures as were examined in the lower-rate tests. The SHPB system does not give a specific strain rate for a given test. The strain rate is approximated by adjusting the pressure that launches a striker bar at the incident and transmitted bars in the system. For our system, a near ideal strain rate of $\sim 2000/s$ is achieved by adjusting the pressure based on previous test results and the test temperature. A "valid" and acceptable test is one that has an average and nearly constant strain rate during plastic deformation of between $1800/s$ and $2400/s$ and also one where the reflected incident signal overlays the transmitted signal, but may have higher amplitude oscillations that get damped out in the transmitted signal by the deforming sample. Temperature adjustment was done by blowing heated or cooled nitrogen over the test sample and the bar system.

Tensile tests were conducted at varying temperatures with the hope that a ductile to brittle transition temperature could be found. These tests were conducted at a true strain rate of $0.001/s$ at temperatures from −40°C to −120°C. These tests were conducted in an environmental test chamber. In addition to the tension and compression tests, Taylor anvil and dynamic extrusion tests were also run on both materials. The Taylor anvil tests are most commonly used to verify material models that predict sample deformation at high strain rates. The Taylor tests were conducted at various impact velocities to acquire test results that also included sample failure. Similarly, dynamic extrusion was done to achieve different levels of extrusion from very limited deformation to fragmentation. These tests are important to look at damage initiation and failure processes.

For all tests conducted above or below ambient conditions the samples were held at the desired test temperature for a minimum of 5 minutes before testing in order to achieve thermal equilibrium.

VI.D Experimental Procedure

VI.D.1 Compression and Tension

The following steps were followed during the testing process to ensure the highest quality data was generated for this report. An MTS 880 servo-hydraulic load frame was used to load the test samples for low-rate tests. The system is calibrated annually to the A2LA standard by an outside contractor. The system is warmed up to minimize system compliance due to thermal changes in the system.

Sample dimensions were measured using a digital micrometer. Data acquisition for these tests was performed at a rate of 20 points/percent strain. Information captured in the data file included: time (s), LVDT displacement (mm), extensometer displacement (mm), load (N) from the 100 kN system load cell, and load (N) from a second load cell in the loading chain. Next, a test profile was generated either for tension or compression that calculated a loading rate based on sample dimensions. This test profile was used to test the sample at a true strain rate. The sample was brought to the desired test temperature and held for a minimum of five minutes to achieve equilibrium. Then the test was run and the data saved for later evaluation and additional tests were run per the test plan.

Similarly, for high strain rate tests the sample was measured, the sample information was entered into the data acquisition software and the system was prepared to receive the signals from the strain gages attached to the bars of the SHPB system. Again, the sample was brought to the desired test temperature and held for a minimum of five minutes to achieve equilibrium. The system was pressurized and fired and the data captured for analysis. Manipulation of the test data will be described in the next section of this report. Lubrication was used for all tests to prevent friction effects from influencing the mechanical response of the materials. The lubricant used for the compression tests was MoS_2 grease. Optically flat tungsten carbide platens were used as loading surfaces for low rate testing. The bar interface in the SHPB testing are machined and ground for flatness. Tension, Taylor anvil, and dynamic extrusion tests were done without lubrication.

Generally, test samples are loaded at a loading rate calculated to match the desired true strain rate based on initial sample length or gage length, compression or tension respectively.

VI.D.2 Data Analysis

Analysis proceeded as follows:

1. The extensometer data in the as-collected data file were shifted such that their slope during the initial loading passed through the origin of the load-displacement plane.

2. Using the shifted data, stress and strain values were calculated according to the following equations. Engineering strain using the "corrected" displacement data was

$$\epsilon^{eng} = \frac{l_f - l_0}{l_0} = \frac{\delta}{l_0}, \tag{3}$$

   and true strain was

$$\epsilon^{true} = \ln\left(\frac{l_f}{l_0}\right) = \ln\left(\frac{\delta + l_0}{l_0}\right). \tag{4}$$

   Assuming conservation of volume, engineering stress was

$$\sigma^{eng} = \frac{load}{area} = \frac{load}{\pi d^2/4} = \frac{load}{l \times w}, \tag{5}$$

   whereas true stress was

$$\sigma^{true} = \sigma^{eng} \times (1 + \epsilon^{eng}). \tag{6}$$

   Note that all values are negative in compression.

3. True Stress versus True Strain was plotted in a way to best illustrate the influence of temperature and strain rate.

VI.D.3 Taylor Anvil Test

The Taylor impact test is designed to probe material response at strain rates on the order of 105/s. This rate is achieved through sudden deceleration via impact of a rapidly moving specimen (velocity 100-800 m/s) against a massive anvil. During these Taylor cylinder impact experiments, also known as Taylor anvil experiments, extreme plastic deformation occurs near the impact face. This is driven by the momentum of the trailing part of the projected specimen, much of which may not plastically deform at all (Figure 9). Taylor impact experiments performed at LANL on HDPE, UHMWPE and cross linked polyethylene have been previously reported. [11]

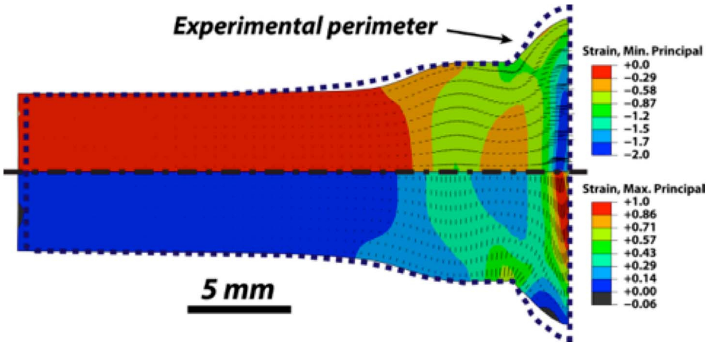

Figure 9: FEA and Taylor rod impact experimental results (outlined) for HDPE at 234 m/s; the moment of maximum compression approximately 80 μs after impact and just prior to rebound is shown (see [11]). Principal strain vectors are overlaid to show direction of flow. The maximum compressive logarithmic strain is approximately -2.0, while the maximum tensile strain approaches 1.0.

VI.E Mechanical Test Results

VI.E.1 Effect of Strain Rate - Compression

Both materials were tested in compression from −75°C to 100°C over strain rates from 0.0001/s to ∼2000/s. As shown in Figure 10, strain rate sensitivity decreased as the strain rate increased, or (phrased differently) the change in flow stress and yield strength lessened with strain rate. This plot also shows that HDPE had approximately twice the yield strength of UHMWPE, but the work hardening rate of UHMWPE was higher than that of HDPE (as evidenced by the flatter flow stress).

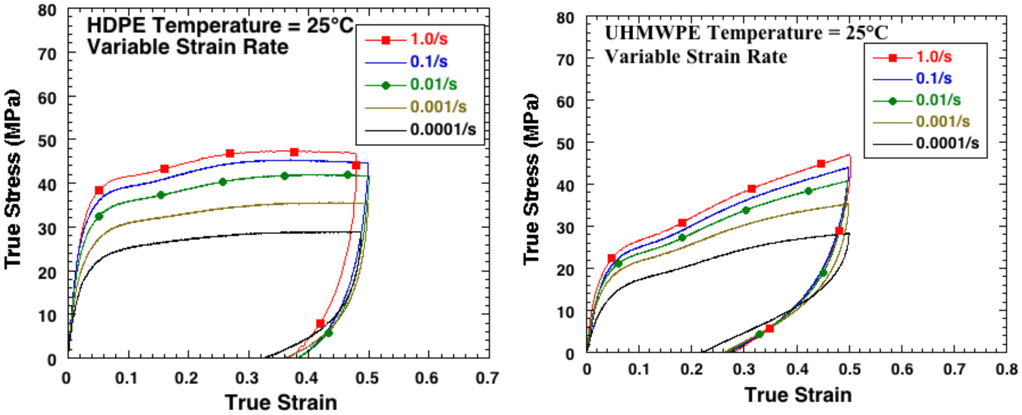

Figure 10: Plots of low strain rate data for HDPE (left) and UHMWPE (right).

VI.E.2 Effect of Temperature - Compression

The temperature response of the two materials are compared side-by-side in Figures 11 to 15). The yield strength of the HDPE was higher than that of UHMWPE at comparable temperatures, but the relative difference was not as consistent as that seen in the strain rate response. The flow stress response was also consistent with the work hardening rate being higher in the UHWMPE as compared with the HDPE. The general trends over the strain rates tested show no unusual dependence on either strain rate or temperature and there were no unusual features in material response anywhere across the data set.

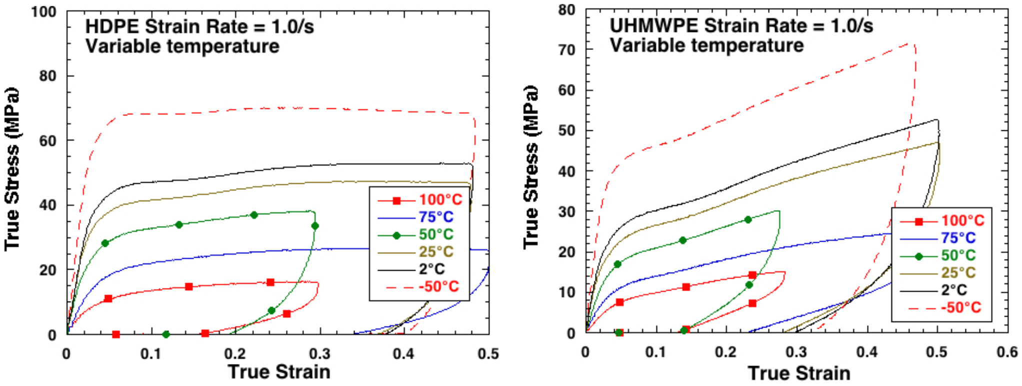

Figure 11: Effect of temperature at a true strain rate of 1.0/s HDPE (left) and UHMWPE (right).

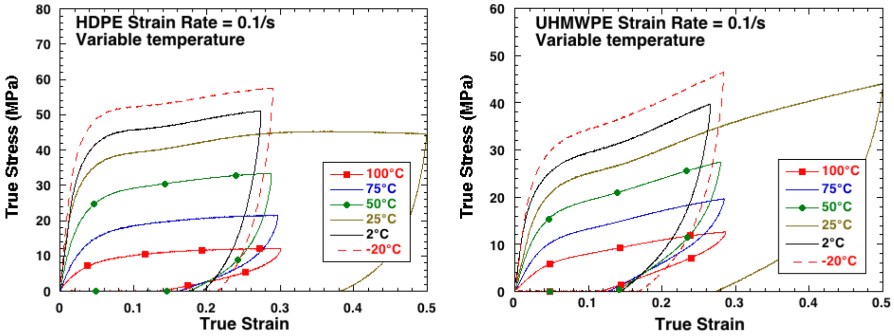

Figure 12: Effect of temperature at a true strain rate of 0.1/s HDPE (left) and UHMWPE (right).

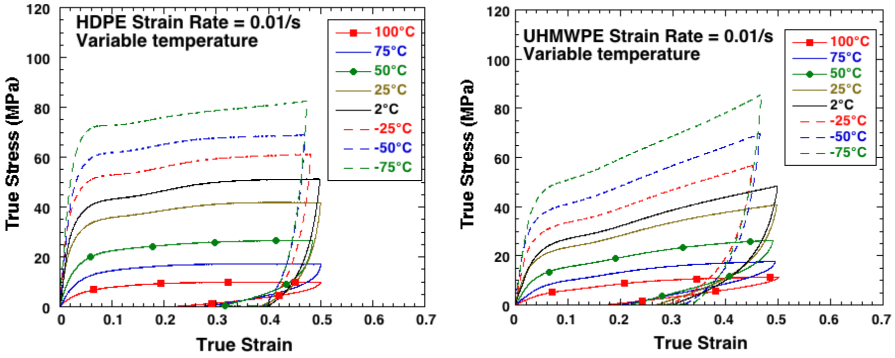

Figure 13: Effect of temperature at a true strain rate of 0.01/s HDPE (left) and UHMWPE (right).

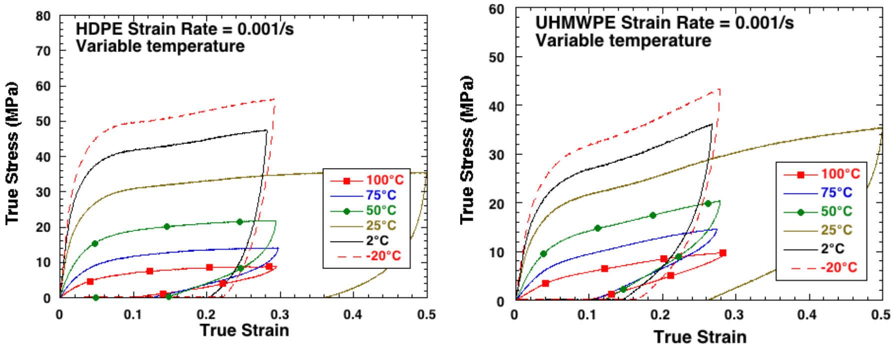

Figure 14: Effect of temperature at a true strain rate of 0.001/s HDPE (left) and UHMWPE (right).

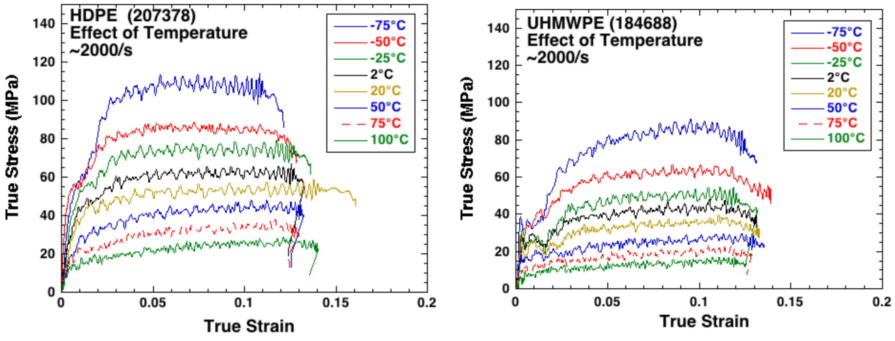

Figure 15: Split Hopkinson bar data for HDPE (left) and UHMWPE (right).

VI.E.3 Effect of Temperature - Tension

Tensile tests were conducted at −120°C to −40°C, at a strain rate of 0.001/s, in order to try and force the material into a brittle failure mode. The temperature range was chosen based on DMA results (see Section X.C) showing phase transitions near −40°C and −120°C. In all tests the strain to failure exceeded 40% strain and there was no indication of material embrittlement. There was only one remarkable difference in the material response: HDPE showed a load drop, followed by a gradual increase flow stress, that was not observed in UHMWPE (Fig. 16). Also, there was indication that the strain to failure of the UHMWPE was greater than that of HDPE over the range of temperatures tested.

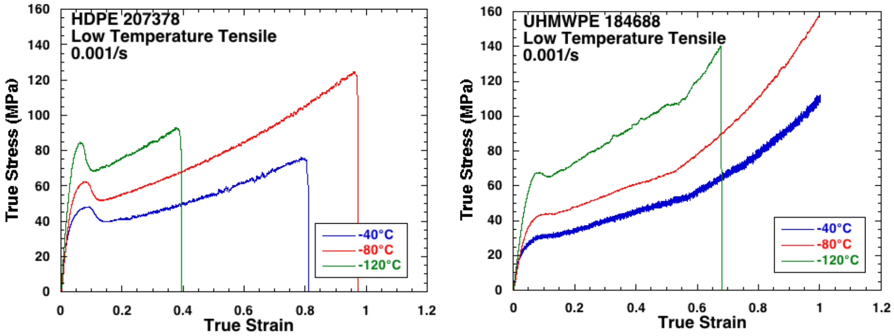

Figure 16: Tensile stress-strain response as a function of temperature at 0.001/s strain rate for HDPE (left) and UHMWPE (right).

VI.E.4 Taylor Anvil Testing

Four Taylor impact shots were fired using HDPE and five with UHMWPE. The range of velocities tested on the HDPE was from 265 m/s to 289 m/s and none of the samples failed. Figure 17 shows the deformation during impact (left) and upon rebound (right). Figure 18 provides the corresponding images taken during the testing of the UHMWPE. The range of strain rates investigated for the UHMWPE was 240-326 m/s, with only the highest velocity sample failing at the impact face. It is clear by comparing corresponding images that the deformation in these two materials was quite different: deformation of UHMWPE was uniform, whereas that in HDPE was more localized. This was consistent with the flatter work hardening seen in the HDPE compression tests and a higher work hardening rate seen in the UHMWPE compression tests. In general, the HDPE samples showed much greater plastic strain as compared to the UHMWPE. Also, the UHMWPE samples tended to recover quite a bit more of their initial shape than did the HDPE.

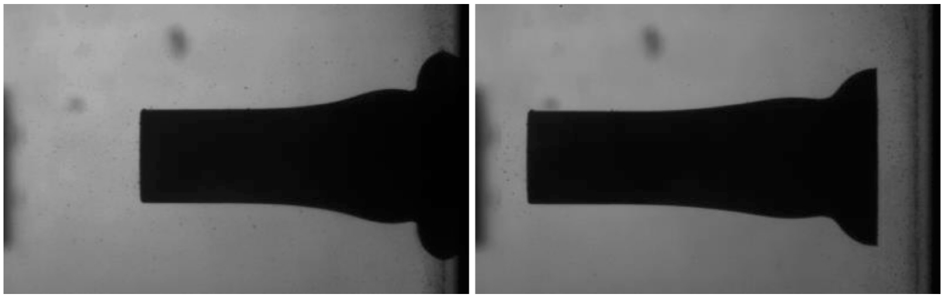

Figure 17: Taylor anvil impact test of HDPE at 265 m/s at impact (left) and after rebound (right).

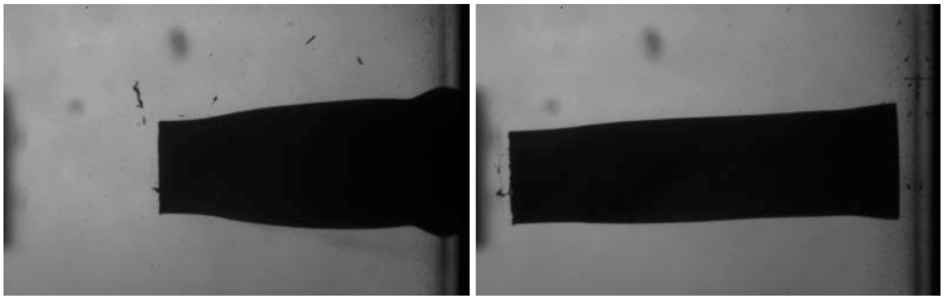

Figure 18: Taylor anvil impact test of UHMWPE at 262 m/s at impact (2c) and after rebound (2d).

VI.F Conclusions

The response of the two materials to variation in both temperature and strain rate were very similar. HDPE had a higher yield strength and lower work hardening rate than UHMWPE. It also showed a lower strain to failure when tested in tension and a load drop after yield that was not observed in the UHMWPE. All other side-by-side comparisons showed little overall difference between the two.

There was no evidence of either damage initiation or reduced strain-to-failure that would have shown void initiation and growth leading to failure for the tension or compression tests.

Taylor anvil tests showed that UHMWPE behaved more rigidly than did HDPE, both during loading and after the sample had rebounded. This corresponded well with the stress-strain response seen in compression testing, where the HDPE displayed flatter work hardening at all temperatures and strain rates than did the UHMWPE.

VI.G Appendix

Table 4: Compression test file names and details.

Sample	Length (mm)	Diameter (mm)	Load rate (s^{-1})	T (°C)
378HD1981e-21_198K_0.01s_S	6.322	6.349	0.01	-75
378HD2231e01_223K_1s_S	6.322	6.351	1.0	-50
378HD2231e-21_223K_0.01s_S	6.307	6.357	0.01	-50
378HDPE2531e-1t_253K_0.1s_S	6.333	6.360	0.1	-20
378HD2481e-21_248K_0.01s_S	6.320	6.349	0.01	-25
378HDPE2531e-3t_253K_0.001s_S	6.330	6.356	0.001	-20
378HD2751e01_275K_1s_S	6.317	6.340	1.0	2
378HDPE2751e-1t_275K_0.1s_S	6.377	6.374	0.1	2
378HD2751e-21_275K_0.01s_S	6.319	6.336	0.01	2
378HDPE2751e-3t_275K_0.001s_S	6.328	6.355	0.001	2
378HD2971e01_297K_1.0s_S	6.316	6.360	1.0	25
378HD2971e01_297K_1s_S	6.329	6.341	1.0	25
378HD2971e-11_297K_0.1s_S	6.316	6.360	0.1	25
378HD2971e-21_297K_0.01s_S	6.321	6.347	0.01	25
378HD2971e-31_297K_0.001s_S	6.326	6.356	0.001	25
378HD2971e-41_297K_0.0001s_S	6.323	6.344	0.0001	25
378HDPE3231e0t_323K_1.0s_S	6.331	6.361	1.0	50
378HDPE3231e-1t_323K_0.1s_S	6.324	6.367	0.1	50
378HD3231e-21_323K_0.01s_S	6.331	6.334	0.01	50
378HDPE3231e-3t_323K_0.001s_S	6.340	6.353	0.001	50

378HDPE3231e-4t_323K_0.0001s_S	6.331	6.347	0.0001	50
378HD3481e01_348K_1s_S	6.330	6.354	1	75
378HDPE3481e-1t_348K_0.1s_S	6.328	6.369	0.1	75
378HD3481e-21_348K_0.01s_S	6.326	6.354	0.01	75
378HDPE3481e-3t_348K_0.001s_S	6.314	6.362	0.001	75
378HDPElen3731e0t_373K_1.0s_S	6.347	6.340	1	100
378HDPE3731e-1t_373K_0.1s_S	6.326	6.359	0.1	100
378HD3731e-21_373K_0.01s_S	6.329	6.345	0.01	100
378HDPE3731e-3t_373K_0.001s_S	6.328	6.358	0.001	100
378HDPE__T_293K_2200s	6.310	6.340	2200	20
378HDPE_T_293K_2200s	6.334	6.350	2200	20
378HDPE_T_293K_2500s	6.310	6.350	2500	20
378HDPEt1_T_275K_2100s	6.342	6.336	2100	2
378HDPEt2_T_275K_2100s	6.325	6.352	2100	2
378HDPEt3_T_248K_2100s	6.317	6.324	2100	-25
378HDPEt4_T_248K_2150s	6.324	6.352	2150	-25
378HDPEt5_T_223K_2150s	6.326	6.366	2150	-50
378HDPEt6_T_223K_2000s	6.323	6.332	2000	-50
378HDPEt7_T_198K_2050s	6.334	6.347	2050	-75
378HDPEt8_T_198K_1950s	6.323	6.342	1950	-75
378HDPEt9_T_323K_2200s	6.326	6.343	2200	50
378HDPEt10_T_323K_2100s	6.315	6.349	2100	50
378HDPEt11_T_348K_2050s	6.353	6.327	2050	75
378HDPEt12_T_348K_2100s	6.328	6.329	2100	75
378HDPEt13_T_373K_2100s	6.309	6.346	2100	100
378HDPEt14_T_373K_2200s	6.309	6.345	2200	100
688UHMW1981e-21_198K_0.01s_S	6.326	6.354	0.01	-75
688UHMW2231e01_223K_1s_S	6.307	6.357	1.0	-50
688UHMW2231e-21_223K_0.01s_S	6.308	6.340	0.01	-50
688UHWM2531e-1t_253K_0.1s_S	6.320	6.366	0.1	-20
688UHMW2481e-21_248K_0.01s_S	6.303	6.360	0.01	-25
688UHWM2531e-3t_253K_0.001s_S	6.332	6.348	0.001	-20
688UHMW2751e01_275K_1s_S	6.318	6.365	1.0	2
688UHMW2751e-1t_275K_0.1s_S	6.339	6.365	0.1	2
688UHMW2751e-21_275K_0.01s_S	6.328	6.375	0.01	2
688UHMW2751e-3t_275K_0.001s_S	6.318	6.372	0.001	2
688UHMW2971e01_297K_1s_S	6.329	6.346	1.0	25
688UHMW2971e-11_297K_0.1s_S	6.314	6.344	0.1	25
688UHMW2971e-21_297K_0.01s_S	6.316	6.348	0.01	25
688UHMW2971e-31_297K_0.001s_S	6.300	6.341	0.001	25
688UHMW2971e-41_297K_0.0001s_S	6.305	6.342	0.0001	25
688UHMWlen3231e0t_323K_1.0s_S	6.331	6.338	1.0	50
688UHMW3231e-1t_323K_0.1s_S	6.324	6.369	0.1	50
688UHMW3231e-21_323K_0.01s_S	6.321	6.347	0.01	50
688UHMW3231e-3t_323K_0.001s_S	6.330	6.352	0.001	50
688UHMW3231e-4t_323K_0.0001s_S	6.330	6.365	0.0001	50
688UHMWlen3481e0t_348K_1.0s_S	6.323	6.349	1	75
688UHMW3481e01_348K_1s_S	6.314	6.327	1	75
688UHMW3481e-1t_348K_0.1s_S	6.330	6.354	0.1	75
688UHMW3481e-21_348K_0.01s_S	6.323	6.340	0.01	75
688UHMW3481e-3t_348K_0.001s_S	6.340	6.375	0.001	75

688UHMWlen3731e0t_373K_1.0s_S	6.314	6.380	1	100
688UHMW3731e-1t_373K_0.1s_S	6.341	6.340	0.1	100
688UHMW3731e-21_373K_0.01s_S	6.324	6.355	0.01	100
688UHMW3731e-3t_373K_0.001s_S	6.327	6.364	0.001	100
688UHMWthick_T_293K_2100s	6.333	6.343	2100	100
688UHMWwidth_T_293K_2100s	6.324	6.347	2100	100
688UHMW_T_293K_2250s	6.324	6.347	2250	20
688UHMWt1_T_275K_2000s	6.385	6.343	2000	20
688UHMWt2_T_275K_2100s	6.333	6.341	2100	20
688UHMWt3_T_248K_2000s	6.330	6.324	2000	2
688UHMWt4_T_248K_2050s	6.338	6.360	2050	2
688UHMWt5_T_223K_2050s	6.326	6.352	2050	-25
688UHMWt6_T_223K_2200s	6.329	6.327	2200	-25
688UHMWt7_T_198K_2000s	6.323	6.332	2000	-50
688UHMWt8_T_198K_2050s	6.312	6.335	2050	-50
688UHMWt9_T_323K_2100s	6.348	6.333	2100	-75
688UHMWt10_T_323K_2000s	6.337	6.350	2000	-75
688UHMWt11_T_348K_2050s	6.305	6.329	2050	50
688UHMWt12_T_348K_2000s	6.353	6.327	2000	50
688UHMWt13_T_373K_2000s	6.309	6.346	2000	75
688UHMWt14_T_373K_1950s	6.330	6.315	1950	75

Table 5: Tensile Test file names and details.

Sample	L (mm)	D (mm)	loading rate (s^{-1})	T (°C)
378HDPE1531e-32_153K_0.001s_NC	14.638	2.320	0.001	-120
378HDPE1931e-32_193K_0.001s_NC	14.398	2.283	0.001	-80
378HDPE2331e-32_233K_0.001s_S	14.563	2.325	0.001	-40
688UHMW1531e-32_153K_0.001s_NC	15.0835	2.331	0.001	-120
688UHMW1931e-32_193K_0.001s_NC	14.587	2.306	0.001	-80
688UHMW2331e-3_233K_0.001s_NC	14.628	2.288	0.001	-40

VII Low Pressure Shock & Failure (***Dattelbaum, Schilling, Clements, Jordan, C. Welch, Stull***)

VII.A Summary

HDPE and UHMWPE were investigated for the influence of crystallinity (>60%) on their shock response and dynamic tensile failure (spall). We applied *in situ* electromagnetic gauging techniques to measure the evolution of particle velocity wave profiles with wave propagation distance to elucidate the nature of previously-reported Hugoniot discontinuities at low pressure. The first evidence of a three-wave structure in highly crystalline polyethylene was measured above a shock stress of 0.5 GPa. Above this region of discontinuity, the transition was overdriven and a single shock wave was observed to stresses exceeding 10 GPa. Details about the nature of the transition, including wave velocities and changes in density, will be presented. Further, a series of dynamic tensile experiments were performed on polyethylene to assess the dynamic tensile (spall) strength as a function of shock stress. Experiments were performed over a range of input stresses, and with two different types of impactors to vary the dynamic tensile condition, and the results for polyethylene were compared with earlier results for polymers such as polytetrafluoroethylene and polychlorotrifluoroethylene. The dynamic failure experiments were modeled using a failure criterion in the glassy amorphous polymer (GAP) model, which captures the volumetric and deviatoric responses of polymers at low shock stresses.

VII.B Introduction

Polymers can be categorized in a variety of ways thermoplastic (polymer that can be reprocessed by heating) vs. thermoset (cross-linked polymer that cannot be reprocessed), glassy (below glass transition temperature) vs. rubbery (above glass transition temperature), and semi-crystalline vs. amorphous. PE is a semi-crystalline thermoplastic, the various forms of which have been studied as a function of strain rate and temperature [11,54,167,168]. HDPE has linear chains that increase crystal packing, with density range of 0.941-0.965 g/cc and crystallinity of 60-80% [169]. The amorphous part of HDPE contains tangled chains held together with weak inter-chain forces, namely van der Waals or hydrogen bonding [170]. While the crystalline portion is made up of micron-sized spherulites containing chains stacked into lamellae $\mathcal{O}(10)$ nm in thickness [170]. HDPE is highly anisotropic due to the strong bonds along the length of the chain and the weak bonds between chains [170].

VII.C Previous Work

VII.D Shock

Several earlier reports have provided shock Hugoniot data for polyethylene over a broad range of conditions to very high shock stresses. The LASL Shock Compendium [45] reports principal Hugoniot data obtained by explosively-driven flyer plate experiments for low (0.916 g/cc) and high density (0.954 g/cc, linear Marlex) polyethylene. Dowell [31] later reported an EOS for HDPE using the Marsh data, and a Rankine-Hugoniot fit to the data in the $U_S - u_p$ plane of $U_S = 2.8233 + 1.6810u_p - 0.0339u_p^2$. Both Dowell and (later) Carter and Marsh [49] noted a discontinuity or transition near $u_p = 3.3$ km/s, believed due to shock-driven decomposition of PE to carbon and fluid products. This notion received additional support from cylinder experiments by Morris, *et al.* designed to reach states above the transition using a Mach stem in PE [30] and PTFE [29]. Recovery of HDPE, for example, showed decomposition to carbon (soot) and gaseous products. Nellis, *et al.* [32] extended the measured principal Hugoniot of HDPE at high shock stresses using gas gun-driven plate impact techniques, noting differences in the linear Rankine-Hugoniot behavior compared to Marsh. The data for HDPE are plotted in Figure 19.

Additional studies have examined shock-induced electrical conduction and polarization of polymer, many in the P, T regime of shock-driven dissociation. Weak shock-induced electrical polarization has

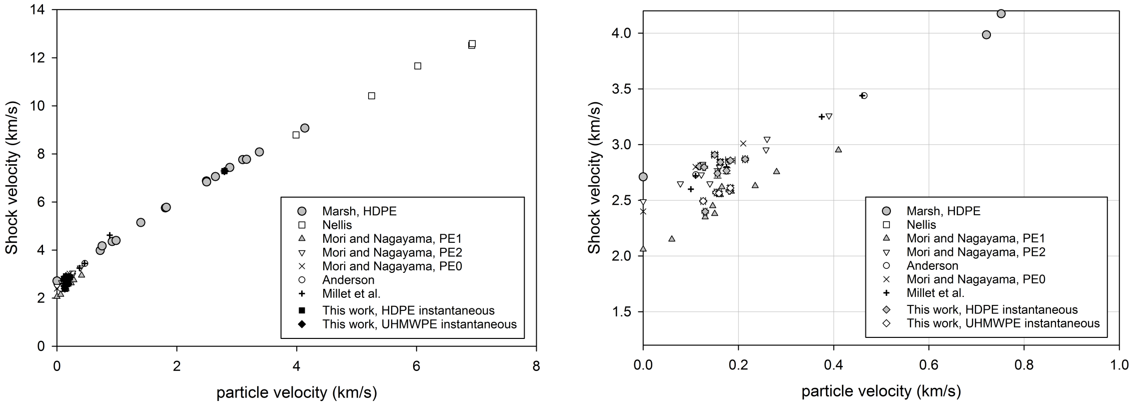

Figure 19: (left) Overlay of Hugoniot data for polyethylene in the shock velocity-particle velocity plane. (right) Focus on low pressure data illustrating a potential cusp in the data near 0.5 GPa.

been observed in polyethylene at compressions greater than 30% by Hauver [23], and Novitskii, *et al.* [24] Graham [25] proposed a correlation between shock-induced electrical activity and monomer repeat structure, suggesting shockwave mechano-chemistry preferentially occurred in more complex (e.g. ring-containing) monomer structures. More recently, Champion [26] measured the electrical resistivity of low-(65% crystalline) and high-density (93% crystallinity) polyethylene, and observed a linear decrease in electrical resistivity with increasing shock stress between 20-30 GPa *by greater than 11 orders of magnitude*. Interestingly the onset of electrical activity in PE correlates well with the on-set and expected 'mixed phase' region of shock-driven dissociation and densification. Additional measurements of the release isentropes are described in Section IX.

Surprisingly, little is known about the influence of PE's crystalline structure and associated phase transitions (including melt) on its dynamic compression response. Some earlier reports have focused on the low-pressure shock regime relevant to low velocity impacts. Mori, *et al.* [27] developed and applied a total internal reflection method to measure shock wave breakout in polymers near 1 GPa, well in the non-linear portion of the Hugoniot in the $U_S - u_p$ plane, where a rounded wavefront is expected due to viscoelastic effects. Using this technique, Mori, *et al.* [172–174] noticed unusual and discontinuous low pressure behavior in the Hugoniots of crystalline forms of polyethylene near 150 m/s. These data, along with other literature Hugoniot data for PE, are plotted in the right panel of Figure 19. At low shock input pressures above the "cusp", the shock wave was also observed to slow by over 10% with propagation distance, in contrast to the breakout behavior observed in PMMA at a similar shock condition. Mori, *et al.* [172–174] attributed the decrease in the wave velocity to a dynamic relaxation process. This is consistent with earlier analysis of shocked polymethylmethacrylate by Barker and Hollenbach [44], Schuler and Nunziato, and others in which a rounded two-wave structure was observed due to viscoelasticity and relaxation from instantaneous to equilibrium states at low shock stresses. It is also possible that a decrease in the first wave velocity could be due to a phase transition, particularly in highly (> 50%) crystalline polymers such as polytetrafluoroethylene and polyethylene. Thus, an objective of this work is to measure the wave profiles in two types of PE similar to those studied by Mori [172–174], and determine if a multi-wave structure is formed near a shock stress of ∼0.5 GPa.

VII.D.1 Dynamic Tensile Failure

There have few investigations of spall in polymers. Spall in polymers depends strongly on the polymer structure and the temperature/strain rate under which the tests were conducted. Polymers are highly temperature and strain rate dependent and can change from ductile to brittle materials with decreased temperature or increased strain rate [176]. Glassy polymer, i.e. polymers that are below their glass transition temperature at room temperature (or the test temperature), fail in tension by a brittle failure mechanism. For example, Takahashi [177] investigated spall in polymethyl methacrylate (PMMA), an amorphous, glassy thermoplastic polymer at room temperature, and observed disk shaped cracks that join to form a spall surface, similar to the brittle failure in ceramics. Curran, Shockey, and Seaman [178] observed the propagation of cracks starting at flaws present in as-received polycarbonate (PC), where the larger defects were activated at lower stresses. However, rubbery polymers, like natural rubber, are used above their glass transition temperatures, and spall failure is more ductile than the glassy polymers [179]. This behavior may change depending on the strain rate dependence of the glass transition temperature in the polymer. There have only been limited studies on spall in HDPE [180, 181] and other semi-crystalline polymers [182].

VII.E Plate Impact Experiments

Gas-gun driven plate impact experiments were performed on two different large bore light gas guns at Los Alamos National Laboratory. The majority of the experiments were performed on a 78 mm-launch tube diameter single stage gas gun with a wrap-around breech configuration, and velocity range from ∼75-900 m/s. Additional experiments were performed using a two-stage light gas gun with a 50 mm-launch tube bore described previously.

Two types of plate impact experiments were performed. In the first type, embedded electromagnetic gauging techniques were employed to obtain particle velocity wave profiles in the PE samples. Right cylinder samples were machined into a 30° wedge geometry, Figure 20a, from PE blocks. An electromagnetic gauge package, Figure 20b, was inserted into the material at 30°, which spaces the gauge elements at varying depths from the impact surface. A single gauge element, referred to as a stirrup gauge, Figure 20c, was then affixed onto the front of the target to obtain the shock input condition. The gauges operate on the principle of Faradays law with the measured voltage proportional to the gauge length, electromagnetic field (1.2 kG), and particle (mass) velocity in the material as described previously. PE targets containing the embedded gauges were then aligned to the exit interface of the launch tube and magnetic field. Z-cut sapphire or Kel-F 800 polymer impactors were used in the experiments depending on which gun was used and the projectile velocity. Particle velocity wave profiles were obtained at up to 10 Lagrangian positions in both HDPE and UHMWPE samples.

The second type of experiment performed was of a symmetric impact configuration designed to put the PE into dynamic tension or "spall". Figure 21a shows the configuration of the experiment. HDPE disks, ∼2 mm thick, were prepared as planar impactors, and mounted in the front of a Lexan sabot, backed by either a glass microballoon polymer foam ($\rho_0 = 0.54$ g/cc) or a polyurea aerogel ($\rho_0 = 0.25$ g/cc). The HDPE was then impacted into an HDPE disk nominally 4 mm thick using the single stage light gas gun. Eight positions of photonic Doppler velocimetry (PDV) [43] were fielded on the target: 4 at the impact face for projectile velocity and impact time and 4 at the rear free surface for free surface particle velocity wave profile measurements. An example PDV spectrogram from one of the free surface probes in shot 1s-1585 is shown in Figure 21b.

VII.F Results & Discussion

VII.F.1 Low-Pressure Shock Response

A large series of plate impact experiments were performed on HDPE and UHMWPE, and the data are summarized in Table 6. The majority of the experiments were focused at input stresses near the data reported by Mori, *et al.* [172–174] to investigate the dynamic response in the regime of the reported cusp. This $P - V - T$ regime is also relevant to impact scenarios and overlaps with the dynamic spall experiments described below. An additional experiment was performed using the LANL 50 mm bore-launch tube two state light gas gun aimed at reaching conditions in which HDPE may melt based on our measurements (not reported here) of the high pressure melt line of HDPE. The volume

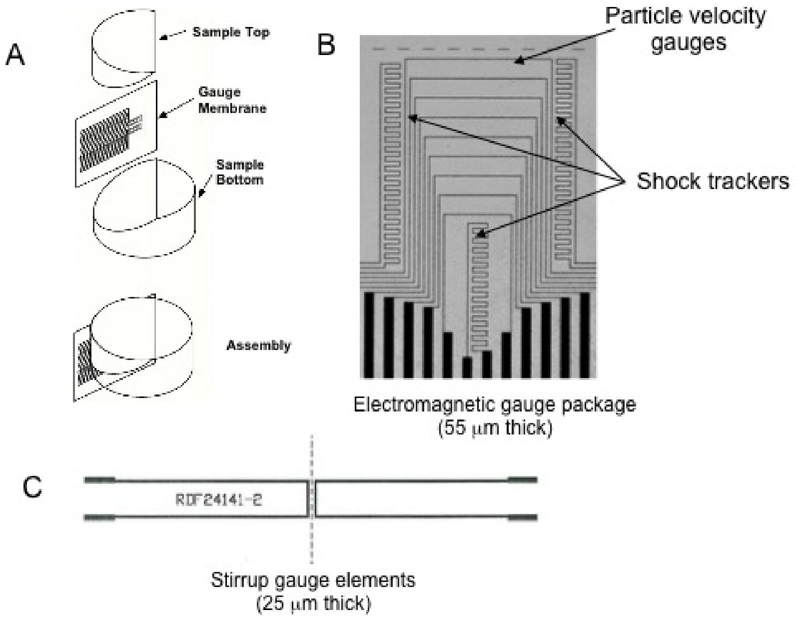

Figure 20: (a) Exploded view of wedge target with embedded gauge inserted at a 30° angle, (b) Optical photograph of the embedded gauge package showing 9 particle velocity trackers and 3 ladder-like shock tracker elements, (c) A single gauge element, or "stirrup" gauge is affixed to the front surface of the target to obtain the shock input condition to the polyethylene.

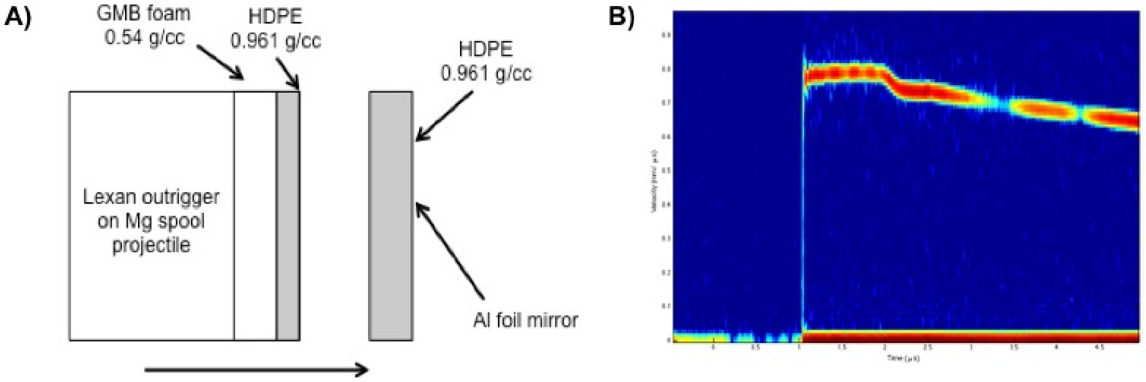

Figure 21: (a) Experimental schematic for symmetric impact spallation experiments. An HDPE impactor approximately 2 mm thick, and backed by either a glass microballon-based foam or a polyurea aerogel, was impacted into an HDPE target approximately 4 mm thick. B) Multiple (8) PDV measurements were made at the impact interface (of projectile velocity and impact) and at the rear free surface of the particle velocity wave profiles. The figure is an example PDV spectrogram from shot 1s-1585 of the wave profile measured at the rear surface of the HDPE target.

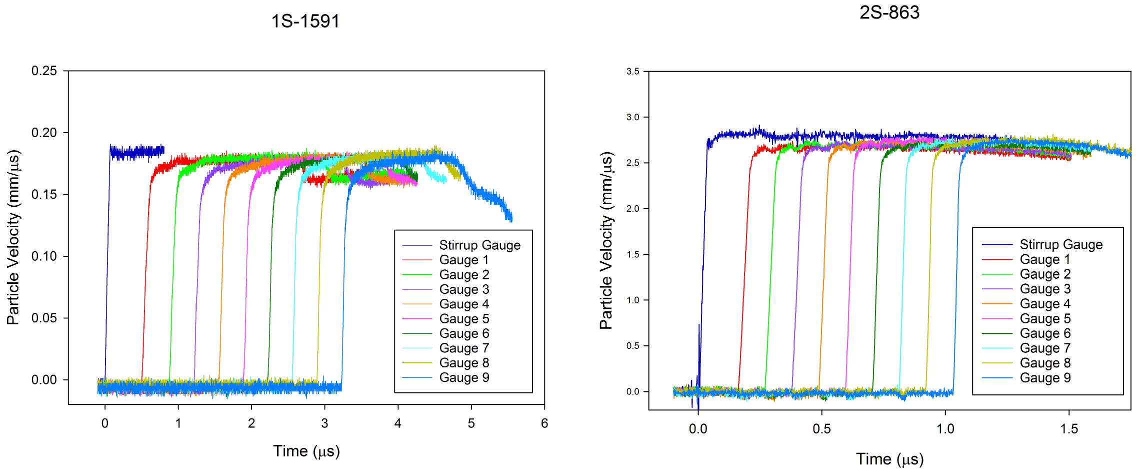

Figure 22: (left) Particle velocity wave profiles from shot 1s-1591, HDPE impacted by z-cut sapphire at 0.193 km/s. The particle velocity from the stirrup gauge on the front of the target is reported in Table 6 as the instantaneous particle velocity. The wave profile evolves in distance and time into a two-wave or "rounded" profile indicative of instantaneous and equilibrium states. The arrival of the rarefaction head from the rear of the impactor is also clearly seen in the profiles. The impedance mismatch between the gauge and HDPE results in a lower measured particle velocity for the embedded gauges (by ∼3-4%). (right) Particle velocity wave profiles from shot 2s-863, an experiment with a Kel-F 81 impactor impacting HDPE at 3.338 km/s. Here, the viscoelastic behavior is overdriven and the wave profiles are of a single wave character.

change associated with melting from static experiments is on the order of 20% and should be readily discernible in the particle velocity profiles. However, we did not observe any evidence of melting in the particle velocity wave profiles.

Figure 22 shows the particle velocity wave profiles from shots 1s-1551 (left) and 2s-863 (right). In 1s-1591, HDPE was impacted by a z-cut sapphire impactor at $u_0 = 0.193$ km/s. The initial shockwave imparted to the HDPE is recorded by the stirrup gauge at the impact interface of the target (purple trace at $t = 0$). The wave shows a prompt risetime and reasonably flat top, consistent with a sustained shock input to the material. Over time and distance, the wave then evolves into a two-wave or "rounded" profile indicative of shock compression to an instantaneous state, followed by evolution and relaxation to an equilibrium state, similar to earlier observations for polymers such as PMMA, PTFE, and Kel-F 800. At later time, best observed in gauge 9 in the left panel of Figure 22, the arrival of the rarefaction wave from the rear of the z-sapphire impactor is observed by a decrease in the particle velocity. The majority of plate impact experiments on HDPE and UHMWPE focused near the discontinuity observed by Mori, *et al.* [172–174] near $P = 0.4$ GPa (see Figure 19). Table 6 summarizes the instantaneous states measured in the experiments. These were obtained using the particle velocity from the stirrup gauge, and the first wave velocity from the embedded gauge responses (including the shock trackers, not shown). Also reported in the table are the equilibrium particle velocities recorded in the experiments. Note that these are low by $\sim 3-4\%$ due to the impedance mismatch between the embedded gauge package (FEP-Teflon) and the lower density PE targets.

At higher pressures, the viscoelastic effect is overdriven, and the wave profiles do not show rounding in the front due to the viscoelastic relaxation process. In shot 2s-863, with a shock input condition of $P = 19.55$ GPa, the viscoelastic effect is overdriven, and the resulting Hugoniot locus is consistent with shock data reported by Marsh and Nellis for $\rho_0 = 0.952$ g/cc HDPE, Figure 19. No evidence of shock-driven melting by temporal evolution in the particle velocity was observed in the experiment.

Table 6: Summary of Hugoniot states measured in gas gun-driven embedded gauge experiments on HDPE and UHMWPE. The initial densities of the samples were: HDPE 207 ρ_0 = 0.961 g/cc, HDPE 12025 ρ_0 = 0.961 g/cc, UHMWPE ρ_0 = 0.930 g/cc. In all of the single stage experiments (denoted 1s-), z-cut sapphire was used as the impactors. In the two stage experiments (2s-), Kel-F 81 impactors were used. The instantaneous states were determined from the initial particle velocity from the stirrup gauge, and the first wave shock velocity. The equilibrium particle velocities are also reported, and are ~3-4% low due to the impedance mismatch between the embedded gauge and lower impedance PE sample. From the evolution of the wave fronts (increase in particle velocity) from instantaneous to equilibrium states, an estimate of the relaxation time, τ, is reported for some of the experiments.

Shot	Material	u_0(km/s)	$u_{p,int}$(km/s)	$U_{S,int}$(km/s)	P_{inst}(GPa)	$u_{p,E}$(km/s)	τ(ns)	Comments
1s-1549	HDPE 12025	0.189	0.162	2.843	0.443	0.161		Multi-wave
1s-1550	HDPE 12025	0.162	0.156	2.742	0.411	0.150		Multi-wave
1s-1551	HDPE 12025	0.240	0.214	2.869	0.590	0.203	340	
1s-1552	HDPE 12025	0.135	0.118	2.804	0.318	0.114	540	
1s-1591	HDPE 207	0.193	0.183	2.858	0.503	0.176	420	
1s-1592	HDPE 207	0.161	0.150	2.909	0.419	0.134		
1s-1578	UHMWPE old	0.189	0.181	2.586	0.435	0.177	240	Multi-wave
1s-1579	UHMWPE old	0.163	0.153	2.570	0.366	0.155		
1s-1580	UHMWPE old	0.132	0.126	2.493	0.292	0.126	810	
1s-1595	UHMWPE new	0.190	0.183	2.611	0.444	0.180	280	
1s-1598	UHMWPE new	0.165	0.159	2.563	0.379	0.158		
1s-1599	HDPE 207	0.182	0.175	2.766	0.465	0.160	370	Multi-wave
1s-1600	HDPE 207	0.134	0.130	2.398	0.300	0.123		
1s-1601	HDPE 207	0.128	0.128	2.797	0.344	0.123		
2s-863	HDPE 207	3.338	2.793	7.285	19.55	Overdriven		

The melt transition is known to shift to higher temperatures with pressure, and our own measurements of the high pressure melt line at static conditions using high pressure diamond anvil cells indicate this experiment should be well into the melt or decomposition region of the phase diagram.

The data in Table 6 are overlaid with literature data in the two panels of Figure 19. The density and % crystallinity of the samples reported previously in the literature are summarized in Table 7. From inspection of the data in the Figures, a few features are worth noting. Similar to other polymers as well as liquids, linear Rankine-Hugoniot behavior does not extrapolate to the bulk sound velocity at $u_p = 0$. There is curvature in the Hugonot data in the $U_S - u_p$ plane due to preferential compaction of free volume at low shock input conditions. Inspection of the data at low pressures from this work, and from the literature clearly shows a differentiation of the shock response of HDPE and UHMWPE. The long chain structure of the UHMWPE inhibits crystallization compared to HDPE, resulting in a lower initial density, $\rho_0 = 0.930$ g/cc, and more compressible shock response. In the $U_S - u_p$ plane, the shock adiabat for UHMWPE is lower by almost $U_S = 0.5$ mm/μs at the same particle velocity, consistent with lower % crystallinity (density) and greater free volume.

Table 7: Literature reports of the shockwave compression response of polyethylene. Densities are as reported, and % crystallinity and type of polyethylene is listed if given by the authors. The Hugoniot data from literature reports are plotted in Figure 19.

Author	ρ_0(g/cc)	%crystallinity	Type
Carter & Marsh [49]	0.954	90	linear
Carter & Marsh [49]	0.916	55	branched
Mori & Nagayama [172–174]	0.957	70.6-73.9	PE0(HDPE)
Mori & Nagayama [172–174]	0.921	35.4-48.6	PE1
Mori & Nagayama [172–174]	0.960	65.9-71.4	PE2
Millet, *et al.* [189]	0.95	Unknown	Unspecified
Anderson	0.955	Unknown	HDPE
Nellis [32]	0.954		HDPE

Near $u_p = 0.16$ mm/μs, there is increased scatter in the Hugoniot data from this study and Mori, *et al.* [172–174] and an apparent “cusp” or discontinuity in both HDPE and UHMWPE. Just above this transition, in some of the experiments, a three-wave structure was observed, with a low amplitude (u_p ~0.3-0.55 mm/μs) quasi-elastic wave, and the same rounded two-wave structure observed in all of the experiments. Hugoniot discontinuities result in shock wave splitting and multi-wave structures due to shock wave instability, as detailed elsewhere. Wave splitting for a densification transition is characterized by $U_{S,2} \leq U_{S,1}$ (the slope of the 2nd wave Rayleigh line is less than or equal to that of the 1st wave). Here, we did not perform analysis of this low amplitude first wave, but its appearance is noted in Table 6. The first wave could be associated with a shock-driven phase transformation of the crystalline domains near $u_p = 0.18$ mm/μs, or $P \sim 0.4$ GPa, similar to that postulated for semi-crystalline PTFE. In static high pressure experiments, crystalline PE has been found to exhibit a rich polymorphism. Crystalline polyethylene at room temperature is usually found to exhibit an orthorhombic P_{nam} structure. Above 0.3 GPa and 200 °C, a second all-*trans* configuration of the orthorhombic phase has been observed. Above $\sim$ 4 GPa, Fontana, *et al.* [41,42] observed the stability of a previously undiscovered phase assigned to monoclinic $P2_{1/m}$, which transforms as a distortion of the β-angle of the orthorhombic phase. Above 14 GPa, a higher pressure phase was found to be of the $A2/m$ space group. The orthorhombic to monoclinic transformation has been found to be shear-driven as a result of sample manipulation confirmed by the presence of the monoclinic phase near ambient conditions by X-ray diffraction in diamond anvil cells, and could be readily accessed in the shock compression experiments and consistent with a small volume change. The P, V regime in which multiple waves are present has been referred to as the “mixed phase” region reflective of the fact that physicochemical transformation is slow relative to the risetime of the initial shock (typically 1 ns). The evolution of the multi-wave structure suggests that the transformation is sluggish, as the

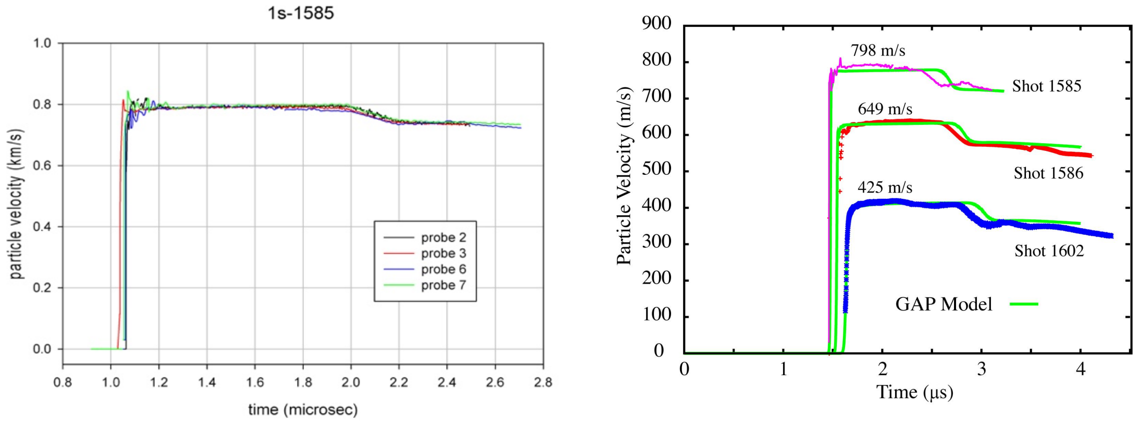

Figure 23: (left) Overlay of four particle velocity wave profiles measured at the rear free surface in shot 1s-1585. (right) GAP-ABAQUS simulations of impacted HDPE overlaid with the experimental free surface particle velocity wave profiles.

multi-wave structure becomes evident over long run distances on the order of 5 mm near 0.4 GPa.

VII.F.2 Dynamic Spall Strength

Four symmetric impact spallation experiments were performed on HDPE at impact velocities ranging from $u_0 = 428 - 800$ m/s. The impact velocities (u_0), free surface and in-material particle velocities (u_{fs}, u_p), shock velocities (U_S), shock stress (P), and pullback in particle velocity from the free surface profiles (Δu) are given in Table 8. In all of the experiments a supported, planar shockwave was established in the HDPE targets. Two of the experiments were matched in impact velocity, differing only by the foam material behind the impactor. Shot 1s-1602 used a polyurea aerogel of a lower initial density to provide a deeper (lower pressure) initial release compared with 1s-1590. The input condition was determined by the measured shock velocity and $u_p = \frac{1}{2}u_0$. The input stresses ranged from $0.6 - 1.3$ GPa; all above the stress of the discontinuity observed by Mori, *et al.* [172–174] in Hugoniot measurements, and above the calculated stress for complete material failure for the experiments described by Golubev. Inspection of the free surface wave profiles shows a flat-topped shockwave, followed by a shallow pullback signature in the particle velocity associated with spall. The lack of a distinct recovery in the particle velocity and subsequent ringing appears to be a hallmark of ductile polymers, as similar profiles have been observed previously for PTFE, Kel-F 81, and Estane. We interpret this signature as a ductile yielding of the polymer, and lack of integrity of a spall “scab”. Weak evidence of wave “ringing” or reverberation in the spalled PE was observed in a couple of the experiments, most notably in shot 1s-1602 (Figure 23, right panel), and supports a conclusion of tensile failure.

The pullback in the free surface wave profile was remarkably consistent in all 4 experiments. Example PDV free surface particle velocity profiles from shot 1s-1585 are shown in Figure 23 (left panel), and illustrate the consistency of the profile measurements across an ∼ 12-18 mm probe diameter on the rear surface of the target. The dynamic tensile or spall strength was estimated using the pullback signature in the free surface particle velocity (Δu), shock velocity (U_S), and initial density according to equation (7):

$$\sigma = \frac{1}{2}\rho_0 U_S \Delta u_{fs}. \tag{7}$$

Profiles from shots 1s-1585, 1s-1586, and 1s-1602 are shown in the panel of Figure 23, overlaid with model predictions from the GAP model (see [1] and Section XIII for details). Assuming an initial (mode I) flaw size of 0.8 μm and an initial number density of cracks per unit volume of $10^{-16}/\text{m}^3$, and by adjusting the fracture toughness in the model to $10^{7.3}$ Pa×m$^{1/2}$, we find that GAP can capture the observed pull back in the velocity profiles. Note that the arrival times of the shock experiments were adjusted to agree with the model. To carry out these simulations, GAP was implemented in the commercial code ABAQUS [10]. Overall, the model comparisons agree well with the magnitude of the pull back of the material. The errors in capturing wave arrival times are likely due to improvements needed within the EOS (particularly sound velocities at pressure), and properties of the foam materials used in the experiments.

VII.G Conclusions

Hugoniot and spall experiments were conducted on HDPE. The Hugoniot experiments agreed will with previous experiments on polyethylene with similar density and crystallinity. Additional analysis of the particle velocity profiles is needed to fully determine the presence of a low pressure transition in the polymer. Spall experiments showed a relatively constant spall stress independent of impact velocity.

Table 8: Summary of spall experiments where the initial density of the material was 0.961±0.001 g/cc, u_{pr} is the impact velocity, u_p is the particle velocity determined from the impact velocity, Δu_{fs} is the difference between the peak free surface velocity and the pull-back signal, U_S is the shock velocity, P is the equilibrium pressure in the material, and σ is the spall strength.

Shot #	Foam Material	u_{pr}(km/s)	u_p(km/s)	Δu_{fs}(km/s)	U_S(km/s)	P(GPa)	σ(GPa)
1s-1585	glass microballoon	0.800±0.003	0.399±0.001	0.048±0.005	3.37±0.01	1.29±0.001	0.05±0.01
1s-1586	glass microballoon	0.649±0.003	0.325±0.002	0.063±0.003			0.07±0.01
1s-1590	glass microballoon	0.428±0.012	0.213±0.006	0.061±0.009	3.04±0.01	0.62±0.003	0.07±0.01
1s-1602	polyurea	0.425±0.001	0.213±0.001	0.057±0.007	2.88±0.01	0.59±0.003	0.06±0.01

VIII *In Situ* Phase Contrast Imaging & Spall (***Ramos, Jensen, Pierce, Montgomery, Liu, Iverson, Carlson, Dattelbaum, Brown, Fezzaa, Sinclair, Rigg***)

VIII.A Summary

In experiments for creating dynamic tension by impact and release, velocimetry is used to detect dynamically created interfaces associated with material damage by observing wave interactions with free surfaces. Interpretation of these wave interactions is often difficult and not unique. Therefore, phase contrast imaging (PCI) of gas gun driven impacts has been performed at the Advanced Photon Source. PCI was used to study the behavior of HDPE and compare and contrast it to the behavior of PMMA, a characteristically brittle polymer. Ductile polymers do not exhibit pronounced spall traces with ringing in the scab. Reduction of loading upon release with no load recovery in velocimetry has been attributed to ductile damage by nucleation and coalescence of voids and modeled as such. This study will test this prevailing attribution in literature with *in situ* observation of damage using PCI.

VIII.B Introduction

With the recent advances in X-ray PCI, materials response in solids can be observed *in situ* with unprecedented spatial, temporal, and density resolution during shock loading. PCI is particularly useful for observing physical and density interfaces. It relies on the spatial variation in the phase of coherent or semi-coherent X-rays and their interference, rather than on their absorption [183]. It is more sensitive to interfaces through interference effects and can be used with intense polychromatic synchrotron beams that make it possible to image high-rate deformation on picosecond time scales [184, 185]. For example, interfaces associated with damage and those associated with pressure discontinuities at shock and release waves can be imaged. This capability has recently been developed and used successfully to investigate damage in glasses, polymers, and metals during uniaxial shock and release experiments that create dynamic tensile stress states [186]. This experimental configuration is frequently called a spall experiment as it refers to flakes of material that may be broken off a larger solid body of material if the shock and release, and thus tensile stress state, are of sufficient amplitude. Fielding PCI on spall experiments is a significant advance because *in situ* observations of spatial and temporal evolving damage accumulation processes can be correlated with features in velocimetry and microstructures observed in recovered specimens to lessen ambiguity in interpretation and support material models development and validation. Examples of sources of ambiguity include affects of localized, heterogeneous damage on features in velocimetry and specimen deceleration/unloading on microstructures recovered for postmortem characterization.

HDPE is a ductile polymer compared to PMMA and exhibits distinctly different behavior. When subjected to dynamic tensile stress, PMMA exhibits release and pullback features that are the typical hallmarks of spall response in interface velocimetry for a wide range of materials. The particle velocity difference between the peak impact and pullback is proportional to the spall strength [56]. Shock and release waves reflect between impedance difference at the tensile stress plane and the rear surface of the target producing the characteristic ringing that proceeds after the pullback. In contrast, ductile polymers such as HDPE do not exhibit pullback or ringing. Johnson and Dick modeled this behavior for Estane 5703 in a pioneering study in 1999 [187]. They employed several common assumptions to match the velocimetry as summarized in Figure 24. Material separation, constant longitudinal stress, threshold spall strength with residual strength all failed to reproduce the velocimetry; whereas, modeling assuming void-growth and viscoelastic constitutive behavior was most successful. Subsequent to this study, void nucleation and coalescence became the prevailing interpretation for spall in ductile polymers in literature [11, 167, 188–193].

There has been relatively little recovery of HDPE from spall experiments for microstructure characterization. Golubev, *et al.* used an explosively thrown flyer to investigate spall failure of PMMA,

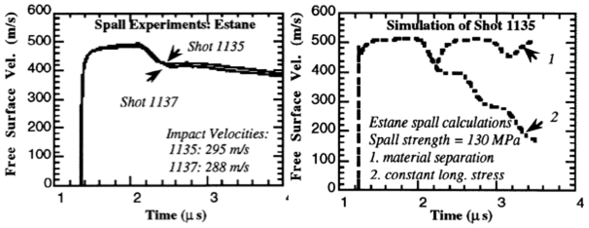

Spall in Estane (i.e. ductile polymer)

Modeling with two common assumptions that failed

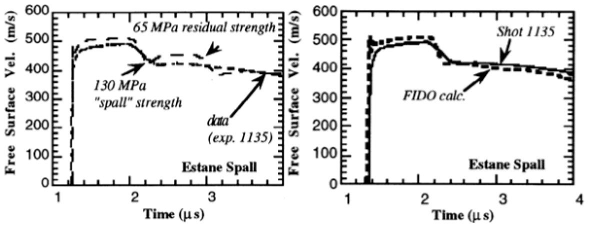

Modeling assuming threshold spall strength and a residual strength

Modeling assuming void-growth model and viscoelastic constitutive behavior

Figure 24: Summary of pioneering study of dynamic damage of ductile polymers under dynamic tensile stress states performed by Johnson and Dick [187]. This study set the prevailing interpretation of damage in ductile polymers in spall experiments.

Teflon and polyethylene (0.92 g/cc) as a function of temperature [180]. Damage in recovered samples was reported as a function of impact and initial temperature in terms of no visible failure, partial spall failure, and complete spall failure. Unfortunately, no micrographs of the samples or spall surface were published for polyethylene [180, 181]. Spall failure initiated at 0.25, 0.16, and 0.14 GPa respectively at room temperature and had an increasing trend as melt temperature were approached for PMMA and Teflon; whereas, the resistance to spall failure decreased for polyethylene.

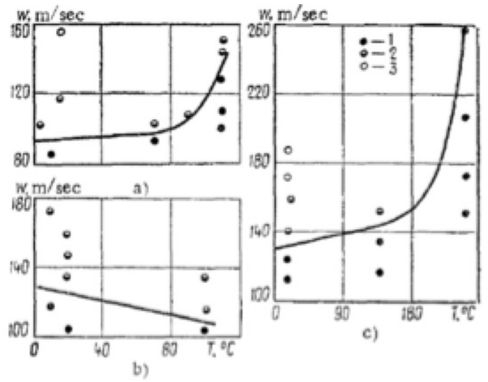

Figure 25: Golubev, *et al.* results of tests with PMMA (a), polyethylene (b), and Teflon (c) specimens: 1) no visible failure; 2) partial spalling failure; 3) complete spalling failure [181].

Ductile-to-brittle transitions have been observed (Figure 26) and documented for water and gas line pipe failures and extensively studied. Ductile-to-brittle transitions are reported to occur in several regimes: slow crack growth (SCG) and rapid crack propagation (RCP) [194–198]. SCG occurs in plane strain, rather than plane stress, as temperature is increased [194]. This involves fatigue of material in the process zone that can fail (i.e. failure of fibrils in the craze zone) leading to an increased rate of crack tip advance [195, 199]. This process can be environmentally assisted and detailed stress, time, and temperature models have been developed [200]. While this process is not likely to occur on the time-scales of spall experiments, it could clearly provide localized nucleation sites for damage initiation in components for weapons applications. Literature reports RCP occurs at lower temperatures and at high loads but has not been documented nearly as broadly in literature [198]. This contradicts the trend reported by Golubev, *et al.* but tests were at much lower strain rates and involved loading of notched samples [180, 181]. The phenomena of SCG and RCP impact facture tend to have similar failure appearance but RCP impact fracture surfaces in PE display a flaky, scaly appearance whereas SCG reveals a fibrous texture as illustrate in Figure 27, indicating they possess fundamentally different failure mechanisms [194, 198].

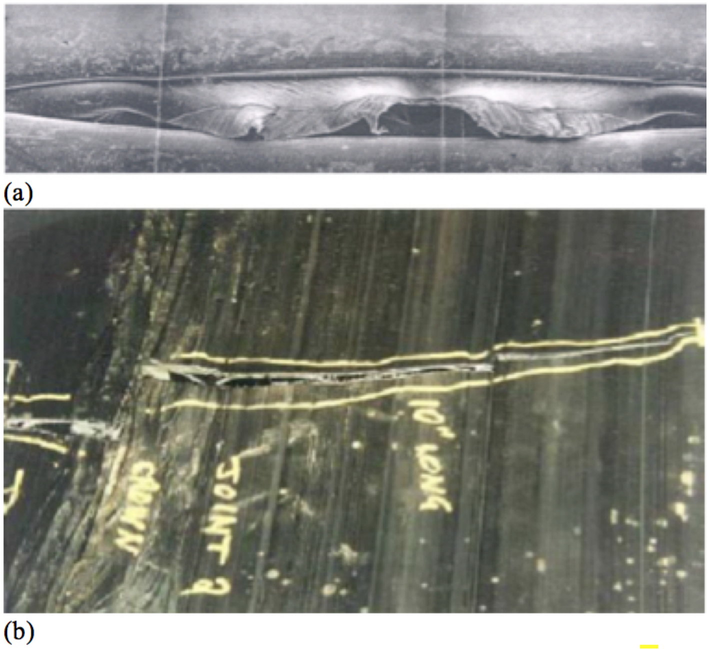

Figure 26: (left)Ductile and (right) brittle failure of HDPE pipe [198].

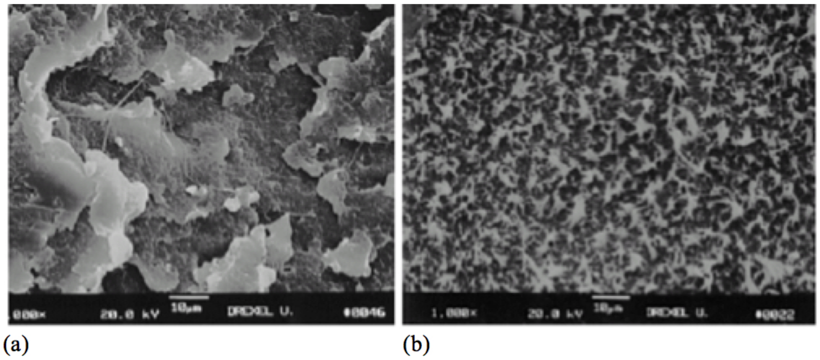

Figure 27: (left) RCP and (right) SCG fracture surface [198].

Battelle's plastic pipe research program, under the sponsorship of the Gas Research Institute, performed an extensive investigation of short term methods for predicting resistance to SCG and

RCP in PE gas distribution systems [198]. As of 1983, 80% of new and replacement gas distributions systems were of PE. They sought understanding of the time dependent behavior of PE under load levels similar to those experienced in gas distribution service so they could predict the likelihood of achieving a service design life of 50 years or more even though PE had only been in service for 20 years to that point. This required developing the necessary understanding of PE material behavior under a wide range of loads, to develop short term tests to measure properties relevant to long term strength and to develop theoretical predictive methodologies that could correlate short term test results with long term strength behavior. Full scale tests and modified Robertson tests on many PE materials and pipe diameters demonstrated that the simple LEFM model of RCP could be used to obtain excellent correlation between dynamic fracture toughness, measured by a simple Charpy test, and the capability of a pipe of any diameter to arrest a dynamically running crack driven by a known initial internal pressure.

Clearly the intent of the Battelle's studies have similarities with potential weapons applications and the RCP results can supplement understanding of PE failure at higher strain rates that is under development here. For example, the full-scale RCP tests consisted of pressurizing a 6-12 inch diameter by approximately 40 feet long pipe with a 10-to-15 inch long notch 80% through a butt weld as illustrated in Figure 28. The notch was wrapped with three layers of fiberglass tape to prevent the notched section from deforming during pressurization and an explosive cutter was used to sever the tape and initiate the crack propagation. Fracture diagrams were draw to show the path of the crack and a typical arrest and propagation fracture is shown in Figure 29. From this data, it is clear that PE can fail catastrophically under dynamic loading in the presence of a flaw/stress concentrator. However, it is uncertain if PE will fail dynamically if damage has to be first nucleated.

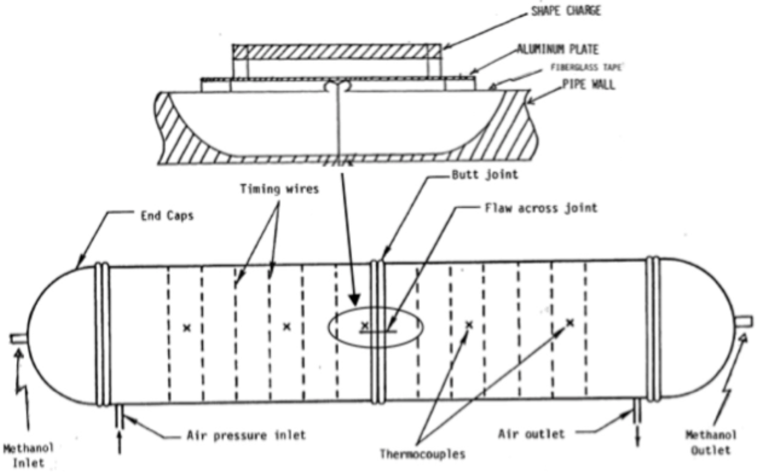

Figure 28: Schematic of Battelle's Rapid Crack Propagation experimental setup with explosive cutter for initiating the crack [198].

Here we apply PCI to study the behavior of high density polyethylene (HDPE) under dynamic tension created by impact and release and compare and contrast it to the behavior of Poly(methyl methacrylate) (PMMA), a characteristically brittle polymer. The intent is to:

1. demonstrate new *in situ* PCI for studying dynamic damage processes in polymers ranging from brittle-to-ductile and correlate with velocimetry to improve interpretation
2. assess void nucleation and coalescence as the dynamic damage mechanism for ductile polymers
3. assess the recovery results of Golubev, *et al.* [180,181]

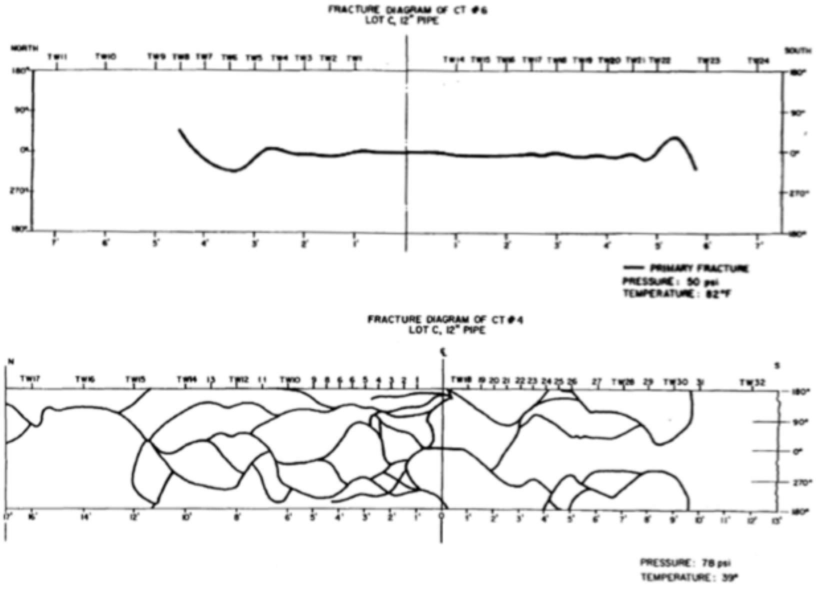

Figure 29: Fracture diagram show arrested (top) and propagated (bottom) fracture results from Battelle's full-scale RCP test [198]. Note the extensive crack branching in the case of propagated fracture.

4. assess the possibility of ductile-to-brittle transitions and the propensity of catastrophic failure of HDPE without a pre-existing flaw under dynamic tensile stresses.

This will first be done using a uniaxial impact and release configuration to determine threshold for damage and spall strength. This data can then provide the basis for future experiments involving engineered defects to nucleate damage and non-uniaxial release configurations to examine stochasticity and shear dependence of crack dynamics [186, 201].

VIII.C Experimental

PCI experiments were conducted at the APS Sector 32 and 35 beamline using the standard mode that provides 80 ps duration (FWHM) X-ray pulses every 153.3 ns [202]. U33, U18, and U27 undulators were used as indicated in Table 9. Detailed specifications of the beamlines and guns designs are described elsewhere [203, 204]. Figure 30 illustrates the PCI experimental configuration. This arrangement has been described in detail elsewhere [204, 205]. Briefly described, a series of slow and fast shutters are used to bracket the impact event typically within 15-30 ms of X-ray exposure. The beam is transmitted through X-ray transparent windows and interacts with the sample during impact. The X-rays are converted into visible light by the LSO scintillator and directed towards the Princeton Instruments PI-MAX ICCD optical cameras by a turning mirror. PI-MAX II and IV cameras were used in this work to obtain four and eight frames in a single experiment, respectively. A 7.5X microscope objective was used to attain the desired magnification and the light split and relayed to multiple ICCD cameras. For experiments using the PI MAX IV cameras, light was collected from both sides of the LSO scintillator using a pellicle mirror through which the X-ray traversed. Figure 31 illustrates the impact experiments fired on half inch bore guns. They consisted of either symmetric or asymmetric impacts and release as summarized in Table 9. The signal from a lead-zirconate-titanate (PZT) impact pin triggered a delay pulse generator (Stanford Research Systems DG535) that in turn triggered the ICCDs, and photon Doppler velocimetry (PDV) to record data at desired times after impact. PDV was either recorded on the aluminum coating on the rear surface or interfaces throughout

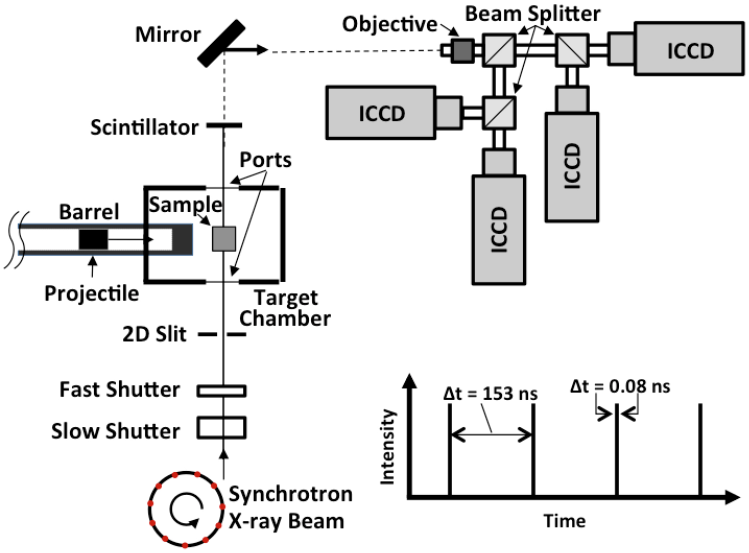

Figure 30: Arrangement for gas-gun driven experiments using PCI at APS Sector 32 and 35.

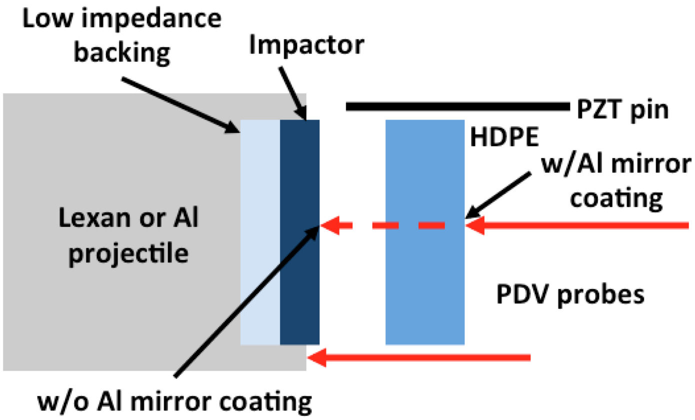

Figure 31: Schematic of experimental target.

the impact assembly when the laser was transmitted through the sample. The guns were intentionally rotated 0.25-0.8 degrees out of perpendicularity to the X-ray beam path to increase the width of the shock and release wave fronts. PCI has a line width function and if features are of the same width or smaller the positive and negative portion of the phase contrast effect will not be resolved rendering the feature unobserved.

VIII.D Results

Impact configurations and resulting velocimetry measures extracted from PDV profiles are listed in Table 10. PDV was analyzed with short-time Fourier transforms using a Hann window with 1024, 4096, and 896 window, Fourier transform, and overlap points, respectively. The pixels in resulting velocity spectra were 5.1 ns and 4.8 m/s. The uncertainty in extracted values is 1 pixel. PDV profiles were extracted from the velocity spectra by maximum intensity value within a user selected envelope and plotted over the spectra for comparison. Corresponding pressures and velocities (Table 10) were

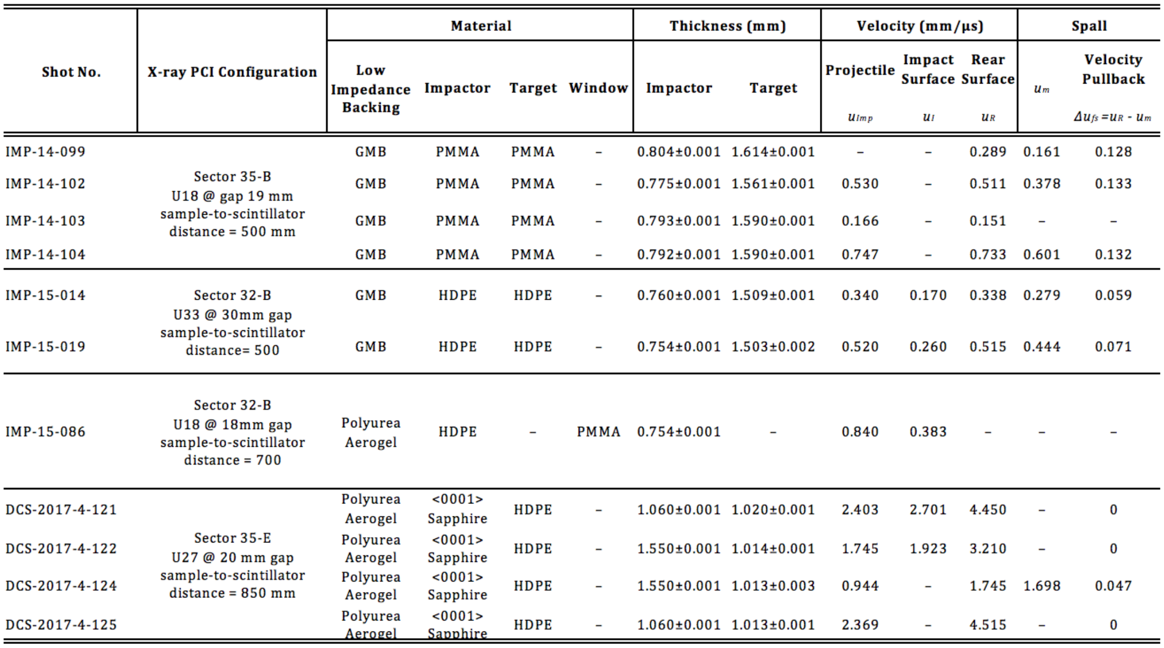

Shot No.	X-ray PCI Configuration	Material				Thickness (mm)		Velocity (mm/μs)			Spall	
		Low Impedance Backing	Impactor	Target	Window	Impactor	Target	Projectile u_{Imp}	Impact Surface u_I	Rear Surface u_R	u_m	Velocity Pullback $\Delta u_{fs} = u_R - u_m$
IMP-14-099	Sector 35-B U18 @ gap 19 mm sample-to-scintillator distance = 500 mm	GMB	PMMA	PMMA	–	0.804±0.001	1.614±0.001	–	–	0.289	0.161	0.128
IMP-14-102		GMB	PMMA	PMMA	–	0.775±0.001	1.561±0.001	0.530	–	0.511	0.378	0.133
IMP-14-103		GMB	PMMA	PMMA	–	0.793±0.001	1.590±0.001	0.166	–	0.151	–	–
IMP-14-104		GMB	PMMA	PMMA	–	0.792±0.001	1.590±0.001	0.747	–	0.733	0.601	0.132
IMP-15-014	Sector 32-B U33 @ 30mm gap sample-to-scintillator distance= 500	GMB	HDPE	HDPE	–	0.760±0.001	1.509±0.001	0.340	0.170	0.338	0.279	0.059
IMP-15-019		GMB	HDPE	HDPE	–	0.754±0.001	1.503±0.002	0.520	0.260	0.515	0.444	0.071
IMP-15-086	Sector 32-B U18 @ 18mm gap sample-to-scintillator distance = 700	Polyurea Aerogel	HDPE	–	PMMA	0.754±0.001	–	0.840	0.383	–	–	–
DCS-2017-4-121	Sector 35-E U27 @ 20 mm gap sample-to-scintillator distance = 850 mm	Polyurea Aerogel	<0001> Sapphire	HDPE	–	1.060±0.001	1.020±0.001	2.403	2.701	4.450	–	0
DCS-2017-4-122		Polyurea Aerogel	<0001> Sapphire	HDPE	–	1.550±0.001	1.014±0.001	1.745	1.923	3.210	–	0
DCS-2017-4-124		Polyurea Aerogel	<0001> Sapphire	HDPE	–	1.550±0.001	1.013±0.003	0.944	–	1.745	1.698	0.047
DCS-2017-4-125		Polyurea Aerogel	<0001> Sapphire	HDPE	–	1.060±0.001	1.013±0.001	2.369	–	4.515	–	0

Table 9: Shot configuration and velocimetry results. PDV was analyzed with short-time Fourier transforms using a Hann window with 1024, 4096, and 896 window, Fourier transform, and overlap points, respectively. The pixels in resulting velocity spectra were 5.1 ns and 4.8 m/s. The uncertainty in extracted values is ±1 pixel.

calculated by impedance matching using the Hugoniots listed in Table 11. The Grüneisen parameter is not known accurately from experiment for HDPE so a value of 1.5 was assumed and used to estimate sound speeds to plan PCI timing and interpret results. The timing for PCI was planned to catch the opposing release waves in the first frame before tensile stress states were to be created; however, there is a plus or minus one pulse uncertainty in achieving desired timing due to the period of the synchrotron (i.e. 153 ns for standard mode) since the radio frequency signal from the synchrotron enables the triggering of the delay generator for the PCI ICCD cameras [Jensen IMPULSE pub]. The PCI image timing with respect to impact can be determined afterwards from recorded PZT pin, radio frequency, and the ICCD trigger output signals recorded for each experiment [204, 205].

For PMMA, experiments were performed at 0.268, 0.483, 0.943, and 1.402 GPa using symmetric impact. Localized features are observed in PCI at and above 0.483 GPa but not at 0.268 GPa. Texture in the contrast is observed on the plane of tensile stress in early PCI frames and evolves in contrast and spatial extent as a function of time. The texture in contrast develops into clearly identifiable features associated with damage. The damage becomes less localized spatially as impact stresses are increased. The PDV is consistent with this interpretation and contains the typical spall pulse signature. The 9 mm width of the targets limits the duration of periodic ringing observed because the experiments are no longer uniaxial. This complicates the interpretation of the PDV for the 0.268 GPa, DCS-14-103 shot. Intermittent loss of signal prohibits following the trajectory toward zero velocity before rebound. We attribute the rebound to late time effects not associated with the uniaxial portion of the experiment. Otherwise, the velocity would have trailed off to zero, which is typically the case when a material is put in tension below the threshold for spall initiation [56, 206].

For HDPE, experiments were performed from 0.468 to 13.208 GPa using both symmetric and asymmetric impact. No changes in contrast or intensity were observed in PCI for symmetric impacts up to 1.47 GPa and PDV showed features analogous to those observed by Johnson and Dick in their

Table 10: Conditions at impact interface calculated by impedance matching. Shots with asymmetric material impacts have two entries.

Shot No.	Measured Projectile Velocity	Pressure	Particle Velocity	Shock Velocity	Density	ΔDensity	Lagrangian bulk sound speed	Lagrangian longitudinal sound speed	Eulerian bulk sound speed	Eulerian longitudinal sound speed
	(mm/µs)	(GPa)	(mm/µs)	(mm/µs)	(g/cc)	Δrho/rho$_0$	(mm/µs)	(mm/µs)	(mm/µs)	(mm/µs)
IMP-14-099	–	0.483	0.145	2.817	1.250	0.054	3.037	3.857	2.881	3.659
IMP-14-102	0.530	0.943	0.265	3.000	1.301	0.097	3.405	4.325	3.105	3.943
IMP-14-103	0.166	0.268	0.083	2.724	1.223	0.031	2.850	3.619	2.763	3.509
IMP-14-104	0.747	1.402	0.374	3.164	1.345	0.134	3.740	4.750	3.299	4.190
IMP-15-014	0.340	0.468	0.170	2.867	1.021	0.063	3.191	4.053	3.002	3.812
IMP-15-019	0.520	0.758	0.260	3.036	1.050	0.094	3.537	4.492	3.234	4.107
IMP-15-086	0.840	1.470	0.389	3.394	1.107	0.153	4.187	5.317	3.630	4.610
		1.470	0.389	3.188	1.351	–	3.788	4.811	3.326	4.224
DCS-2017-4-121	2.403	13.208	2.114	11.479	4.088	–	13.216	16.785	12.884	16.363
		13.208	2.114	6.507	1.422	0.481	11.907	15.122	8.038	10.209
DCS-2017-4-122	1.745	8.221	1.564	11.371	4.050	–	12.717	16.150	12.514	15.893
		8.221	1.564	5.476	1.344	0.400	9.171	11.647	6.552	8.322
DCS-2017-4-124	0.944	3.471	0.867	11.267	4.013	–	12.062	15.318	11.979	15.213
		3.471	0.867	4.171	1.212	0.262	6.008	7.631	4.760	6.045
DCS-2017-4-125	2.369	12.928	2.086	11.473	4.086	–	13.191	16.753	12.866	16.340
		12.928	2.086	6.454	1.419	0.478	11.763	14.939	7.961	10.110

Table 11: Materials and reference Hugoniots used in impedance matching calculations in Table 10. Densities were measured for materials used in this study, but Hugoniots were taken from the literature.

Material	Density (g/cc)	C (mm/μs)	S	R
PMMA [215]	1.186	2.598	1.516	1.5
HDPE [172]	0.960	2.549	1.872	1.5
$< 0001 >$ Sapphire [215]	3.985	11.190	1.000	1.5
Glass microballoons	0.500	-	-	-
Polyurea aerogel	0.205	-	-	-

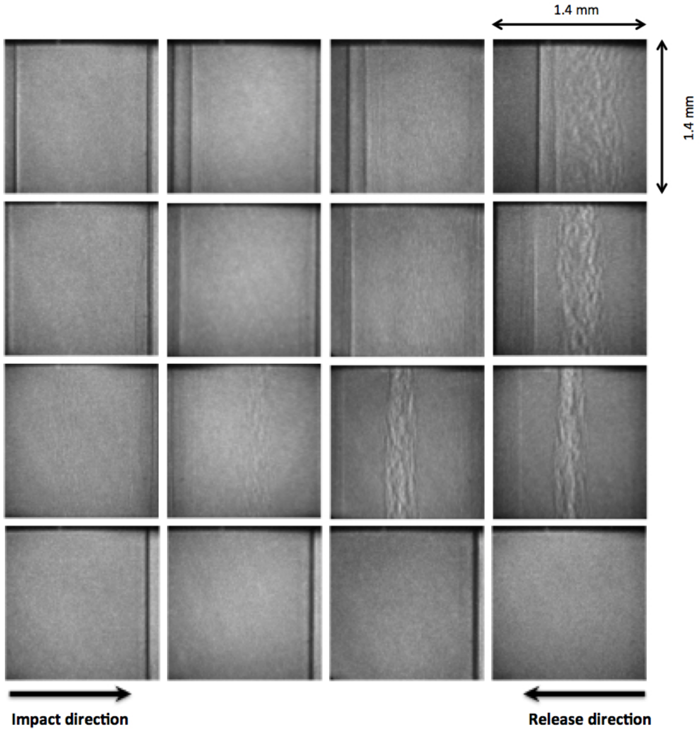

Figure 32: PCI for PMMA experiments: IMP-2014-104, -102, -099, -103 from top to bottom rows.

study of Estane 5703 [187]. Symmetric impact experiments were repeated with a lower density backing for the flyer. Polyurea aerogel was used in place of the glass microballons (GMB) with no change in results. Free space backing was attempted but the HDPE at ∼0.75 mm thickness would not remain flat within acceptable tolerance. Asymmetric impact experiments with $< 0001 >$ sapphire backed with polyurea aerogel were then performed. In this configuration, spatial changes in intensity or contrast texture were observed in PCI at 3.471 GPa and became localized at 8.221 GPa.

Several notable features were observed at 8.221 GPa impacts (i.e. 1.745 mm/s projectile velocity) and above on the Dynamic Compression Sector (DCS) single stage gas gun in the E-Hutch: a narrow feature that transited the field of view (FOV) and ejecta from the HDPE rear surface. The narrow feature was observed repeatedly to transit the PCI field of view without disturbing the sample, optical beam interrupt diagnostic for measuring projectile velocity, or the PDV. There were unexplained discrepancies from planned PCI image timing with respect to impact for shots DCS-2017-4-121 and 122. Impact was expected in frame two to three but did not arrive until frame six to seven and five to six, respectively. Possible explanations for the narrow feature are air shock or accelerant gases blowing by the projectile. Both of these possibilities could have potentially triggered the PZT pin and would be consistent with the PCI image timing since the feature arrived in the third frame for both shots. However, the recorded PZT signal appeared to be consistent with normal projectile impact and the target chamber vacuum was below 100 militorr, as usual, prior to firing the shots. In shot DCS-2017-4-125 the narrow feature was again observed but the shock had reached the rear surface in frame three before the appearance of the feature. In all of the shots at or above 8.221 GPa ejecta was observed from the rear HDPE surface upon shock arrival; whereas, no ejecta was observed for shots at and below 3.471 GPa.

PDV was fielded in two configurations for the HDPE experiments: laser reflected off an aluminum coating on the rear surface of the HDPE or laser transmitted through the HDPE and reflected off of every interface encountered. The original purpose of this was to avoid spalling the physical vapor

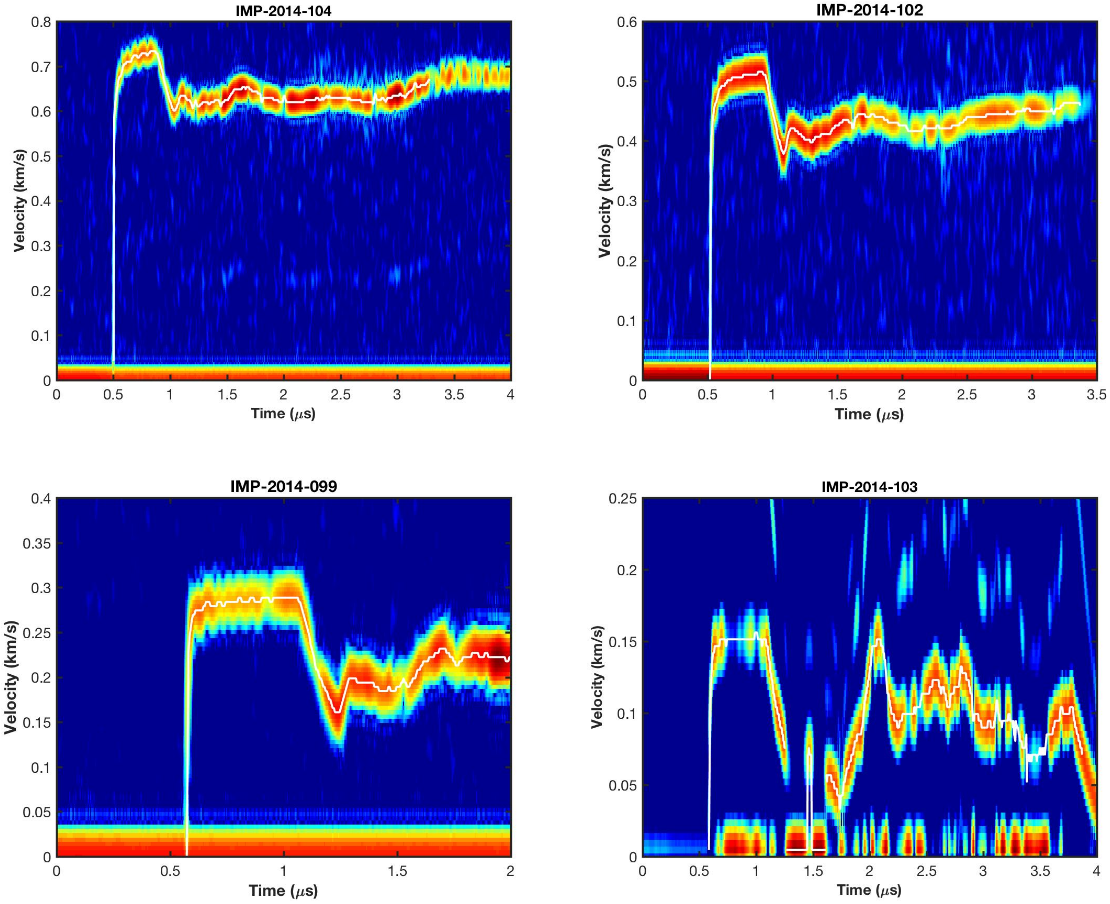

Figure 33: PDV for PMMA experiments.

deposited aluminum coating off the HDPE upon release since adhesion of aluminum to HDPE is relatively poor. HDPE surfaces polished with 1μm Al_2O_3 embedded lapping film produced sufficient return for recording PDV. For shots IMP-15-014 and -019 and DCS-2017-4-121 and -122 PDV was recorded with the 1550 nm laser transmitted through the HDPE; whereas, in IMP-15-086 and DCS-2017-4-124 and -125 the PDV was recorded from an aluminum coating. When transmitted through the HDPE, velocities of the projectile, impact interface, rear surface, and spall interface (if present) are recorded. This is most clear in the velocity spectrum for DCS-2017-4-122. For the DCS-2017 series of experiments, the thickness of the HDPE targets was reduced because of the high sound speed of single crystal sapphire. This delayed the effects of release waves in the PDV. The second rise to the free surface velocity is associated with the spall surface, which is also observed in the PCI for shots at and above 8.221 GPa impacts. When fielded off of the aluminum coating on the rear surface no signature of tension or spall is seen for shots at and above 8.221 GPa impacts; whereas, signatures of tension were observed for the lower velocity impacts.

Several features in the PCI from shot DCS-2017-4-124 are notable. For this shot and -125, the HDPE sample was positioned initially on the edge of the PCI FOV so that the rear surface was observable. Once impacted the shock arrival at this surface was evident and the sample transited into the FOV as damage nucleated and evolved. The shock arrived at the rear surface between frame one and two. Spatial variations in transmitted intensity are evident in frame three and evolve between

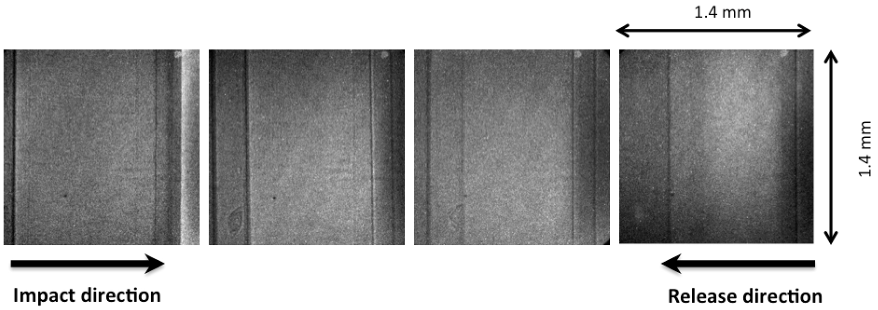

Figure 34: PCI for HDPE experiment IMP-2015-019.

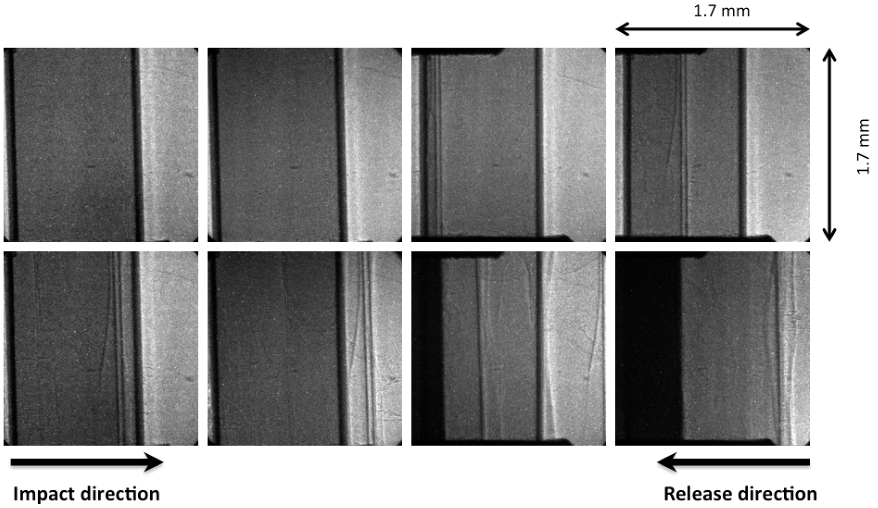

Figure 35: PCI for HDPE experiment DCS-2017-4-121.

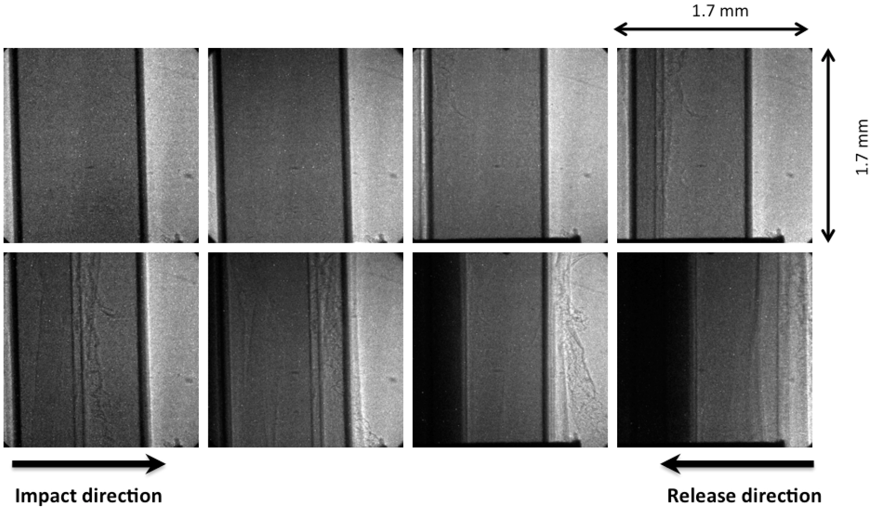

Figure 36: PCI for HDPE experiment DCS-2017-4-122.

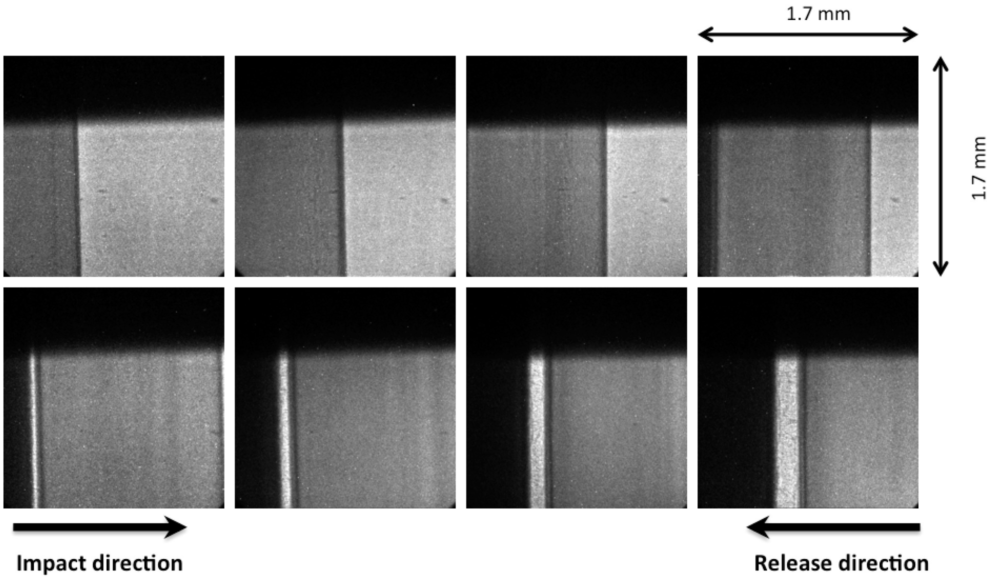

Figure 37: PCI for HDPE experiment DCS-2017-4-123.

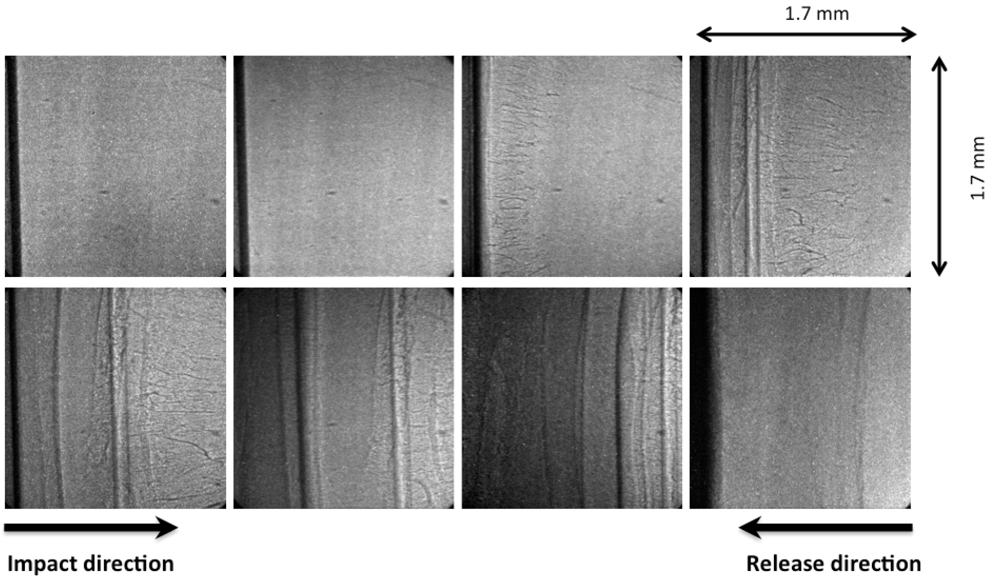

Figure 38: PCI for HDPE experiment DCS-2017-4-124.

the four subsequent frames before exiting the FOV. In frame five, the sapphire is no longer in contact with the HDPE impact surface and the rear HDPE surface is just in the FOV at the top of the image. The HDPE sample that was originally 1.013 mm before impact was $\sim$1.3 mm upon release in the zero pressure state. This was achieved within the PCI time frame of this experiment because of the vastly different impedances of sapphire and HDPE.

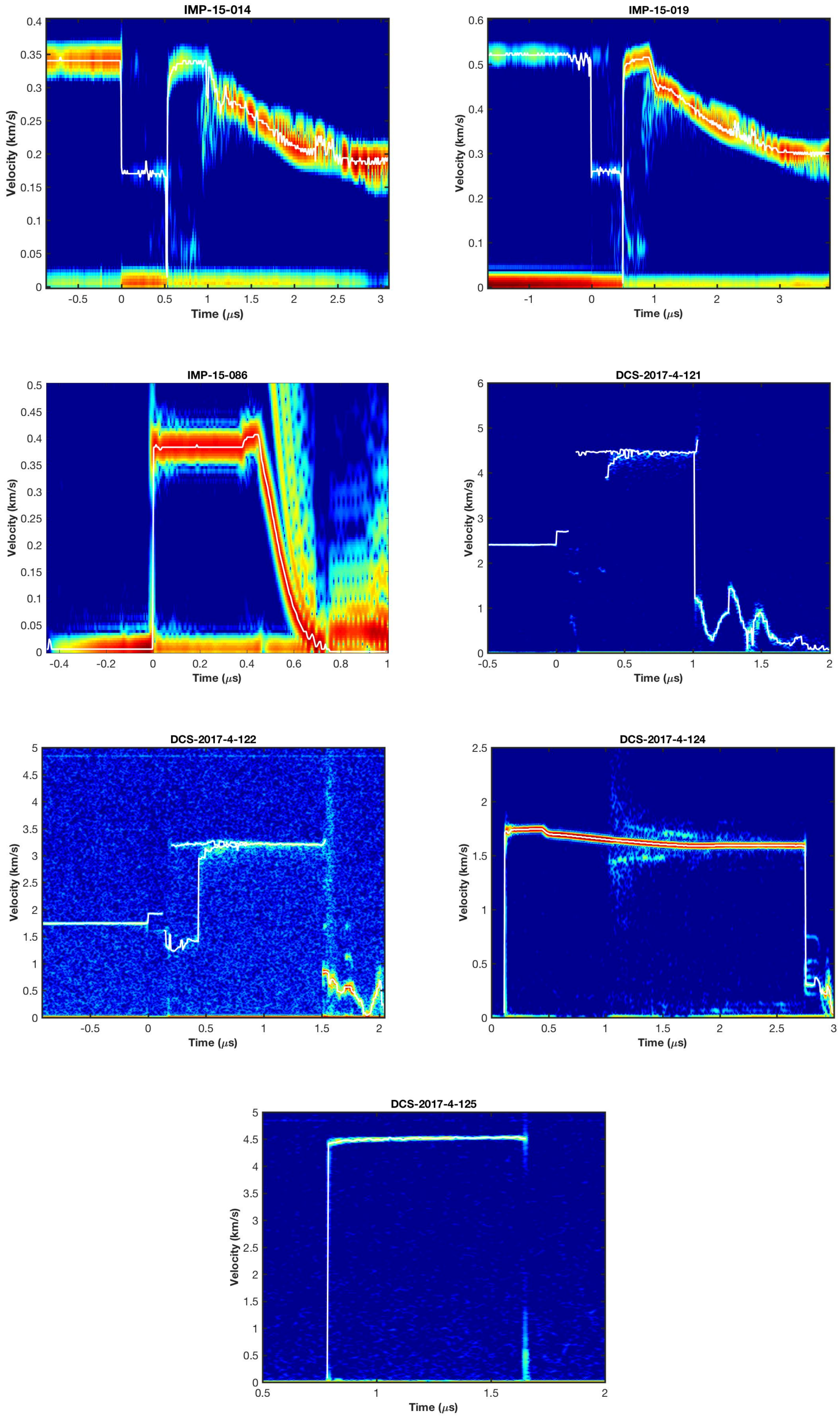

Figure 39: PDV for HDPE experiments IMP-2015-014, -019, -086, and DCS-2017-4-121, -122, -124, -125.

VIII.E Discussion

There are some tradeoffs while performing shock and release spall experiments with PCI that are often in direct opposition to what would be otherwise designed for shock physics experiments diagnosed traditionally with velocimetry. Compromises in experiment design have to be made judiciously. The samples must have a small diameter (e.g. 0.5" projectiles with 9-10 mm sample size for the IMPULSE and DCS gas guns) to permit sufficient transmission of the X-rays. This sets an upper bound on the sample thickness and temporal duration of the tensile pulse during which damage is nucleated, evolves, and is recorded. For this reason, the experiments were planned to create tensile stress states in the center of the thickest targets possible to allow damage to nucleate and evolve over the longest duration of tensile stress. This compromised velocimetry and its interpretation in two ways. First, there was relatively early arrival of release waves at the point of measurement. This can be seen in the IMP-15 HDPE shot series that used thicker targets wherein constant particle velocity is not maintained much after the unloading associated with the tensile stress state. This was somewhat unavoidable for symmetric impact and release experiments with HDPE because the duration of release was relatively long (i.e. du/dt is gradual on release) and necessitated thicker samples see the front surface impact PDV for IMP-15-086. The asymmetric impact experiments mitigated this by using elastically loaded sapphire as the impactor and thinning the HDPE targets this compromise was intended to localize the spatial extent of tensile stress within the HDPE sample. Second, established researchers of spall phenomena prefer to design experiments so that the tensile stress state is created at a plane near the rear surface [56]. This is done to minimize the effects of wave dispersion and plasticity on the spall signature in velocimetry as waves transit and ring between the rear surface and the low impedance/damage region on the spall plane. While this preserves the spall signature, improves interpretation of the velocimetry, and enables estimation of spall strengths with analytic equations, it results in measurement of the upper threshold of spall strengths for time dependent damage processes since the temporal duration of tensile stress states is limited by the proximity to the target free surface. In this study, asymmetric impact experiments were performed using elastically loaded sapphire as the impactor. This imposed a steeper release nearer to the tensile stress plane from one side and was deemed especially important for HDPE because its response as a ductile polymer is very time dependent. Ultimately, three-dimensional simulations are necessary to quantitate and then evaluate the effects of limited spatial and temporal extent of tensile stress states and release waves.

The spatial and temporal evolution of damage on the tensile stress plane was successfully imaged, the threshold for spall damage was determined, and a pressure dependence of damage was observed with PCI for PMMA. At 0.268 GPa symmetric impact, PMMA exhibited no change in intensity or texture in the contrast indicative of damage. The PDV velocity profile was consistent with this interpretation but could have been clearer if thinner samples had been used to delay the onset of release waves at the pont of measurement. As pressure was increased above 0.483 GPa, texture in the contrast developed at early time and evolved into clearly defined features associated with damage. The features became less localized as impact stress was increased but the velocimetry remained remarkably consistent and unaffected (Figure 40). Samples with larger aspect ratios may allow investigation of the effects of the delocalization of damage on the period and evolution of ringing that was not clearly exhibited here.

Damage localization on the tensile stress plane is clearly observed in PCI for PMMA; whereas, it is not as evident or localized for HDPE. The lack of features observed by PCI was initially attributed to several experiment design aspects unrelated to the dynamic tensile response of HDPE. This involved the density of the low impedance backing and the spatial extent of the release waves and the subsequent region subjected to tension. The density of the impactor backing was reduced as much as practically feasible with no effect for the symmetric impacts. Asymmetric impact produced features in PCI indicative of damage at 3.471 GPa but a symmetric impact at comparable stress amplitude has not yet been performed so it is uncertain if the observation is attributable solely to impact stress or the spatial and temporal extent of the tensile stress state in addition. Shot IMP-15-086 was fired as a front surface impact onto PMMA and confirmed Moris Hugoniot and timing at this stress level and

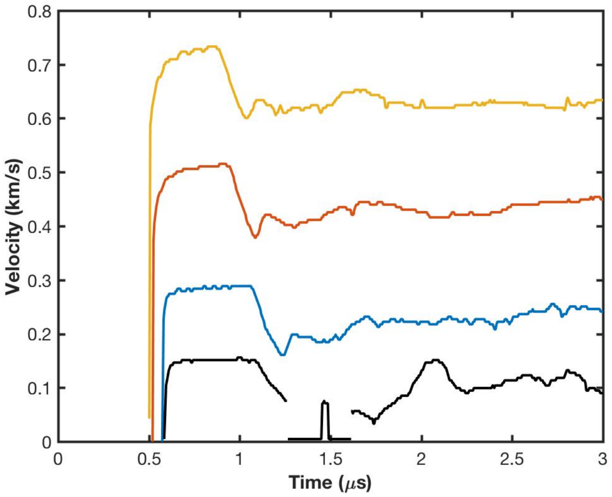

Figure 40: Velocity profiles extracted from PDV spectra for PMMA experiments.

quantitated the relatively gradual rate of release for HDPE [172]. Interaction of two such releases in symmetric impact experiments would undoubtedly spread the tensile stress spatially throughout the sample and cause it to develop gradually in time over an extended portion of the sample thickness. Further experiments and simulations are needed to evaluate these aspects. Front surface impacts such as IMP-15-086 should be repeated for other impact conditions and used to validate the equation of state for the HDPE in future simulations.

The threshold for complete spall in HDPE occurs somewhere between 3.471 and 8.221 GPa as observed *in situ* with X-ray PCI. Changes in X-ray intensity transmitted through the HDPE are not observed until 3.471 GPa and do not become localized until 8.221 GPa. Figure 41 compares image profiles for shots at 3.471 and 0.468 GPa asymmetric and symmetric impacts, respectively. In shot DCS-2017-4-124 the HDPE was uniaxially compressed to a reduced volume of 73.8%, or 0.748 mm thickness, based on impedance matching and was imaged in the pressure equals zero state at ∼1.3 mm thick. The overall length changed by 0.552 mm and was not uniform as regions of increased transmission, or localized density reduction, is observed. The image profiles in Figure 41 illustrate the evolution of the features in frames three through six. In contrast to PMMA, clearly defined and localized features associated with damage are not observed. At impacts of 8.221 GPa and above, defined interfaces associated with spall planes are observed.

Transmitting the laser through the HDPE provides much more information than reflecting off aluminum coated free surfaces. Velocities at each interface from impact to the rear surface can be recorded. In shots where spall interfaces were observed in PCI, a second rise to the free surface is exhibited in PDV. In Table 12, measured impact interface velocities and shock velocities from measured transit times are compared with those calculated from Mori's Hugoniot [172]. The agreement listed in Table 12 is very good for the low velocity impact shots and much worse for those at high velocity. For DCS-2017-4-121 and -122, signal is lost intermittently between impact and breakout at the free surface and could lead to inaccurate shock velocities; however, the percent difference for the impact interface velocities are also very large. It is likely that extrapolating Moris Hugoniot to these conditions is inaccurate and Hugoniot measurements need to be made.

All the profiles transmitted through HDPE are plotted for comparison in Figure 42 (left). The PDV profiles measured from the rear surface of HDPE below 8.221 GPa impacts are consistent with those published in literature for ductile polymers. A reduction of loading after release with no load recovery is observed. For shots at and above 8.221 GPa, this feature is missing and there is a second

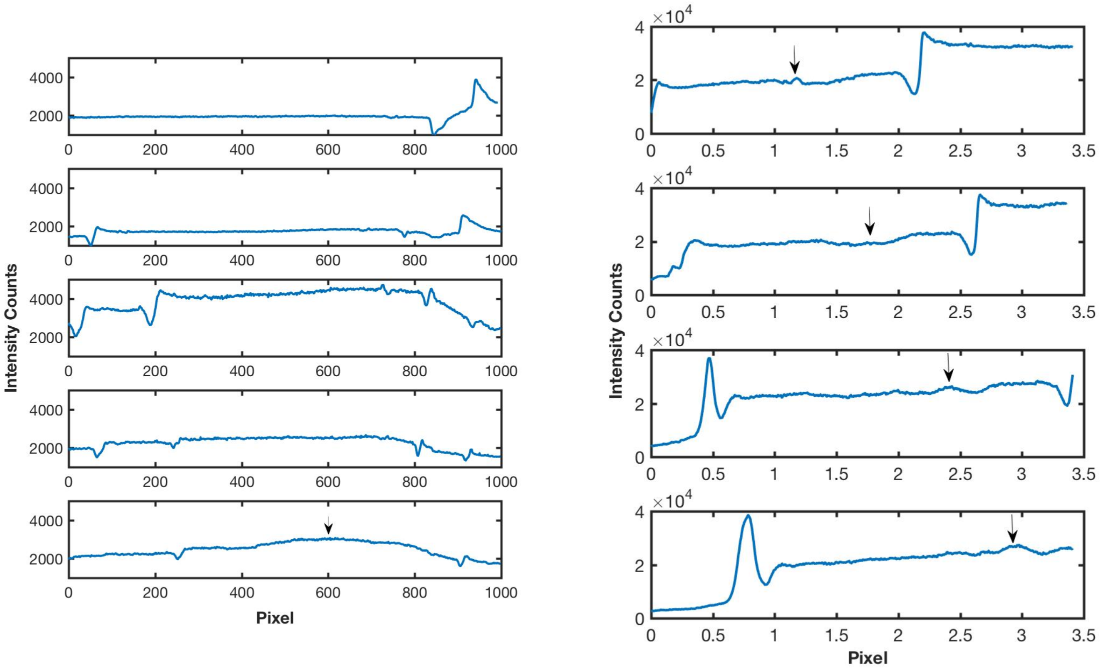

Figure 41: Comparison of image profiles extracted from PCI for IMP-15-019 and DCS-2017-4-124.

Shot No.	Thickness (mm)	Projectile Velocity (mm/μs)	Impact Interface Velocity (mm/μs)			Transit time (μs)	Time release to tension (μs)	Shock Velocity (mm/μs)		
	Target		Measured	Calculated	% Difference			Measured	Calculated	% Difference
IMP-15-014	1.509±0.001	0.341	0.170	0.170	0	0.536	0.446	2.815	2.867	3.18
IMP-15-019	1.503±0.002	0.520	0.260	0.260	0	0.500	0.476	3.006	3.036	1.71
DCS-2017-4-121	1.020±0.001	2.403	2.701	2.114	24.37	0.141	0.266	7.234	6.507	19.39
DCS-2017-4-122	1.014±0.001	1.745	1.923	1.564	20.62	0.203	0.312	4.995	5.476	18.12

Table 12: Hugoniot estimation from velocimetry for shots without aluminum coating on rear surface. Calculated velocities are from impedance matching, as in Table 10.

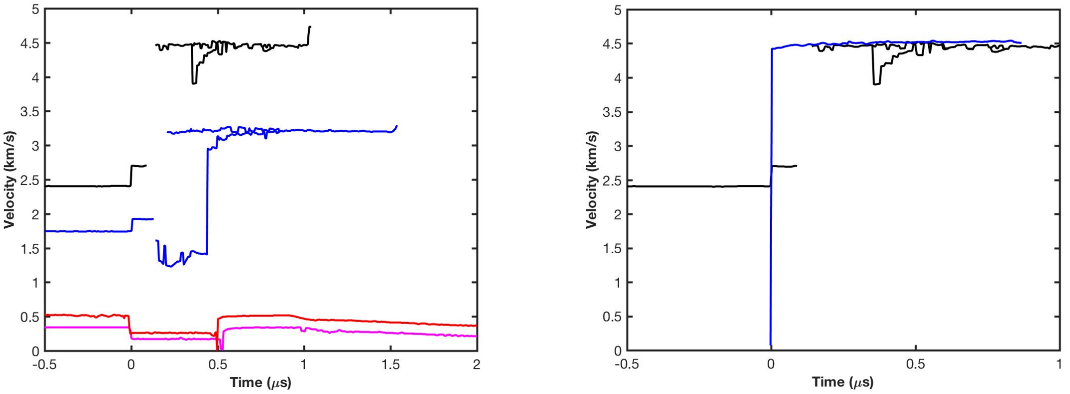

Figure 42: Velocity profiles extracted from PDV spectra for HDPE experiments IMP-2015-014, 019 and DCS-2017-4-121, 122 wherein no aluminum coating was used on the rear surface (left). Comparison of velocity profiles for DCS-2017-4-121 and -125 wherein a coating was used and not used respectively (right).

rise to the free surface. Shot DCS-2017-4-121 and -125 were fired at similar impacts but PDV was fielded through the HDPE and off of an aluminum coating on the rear surface, respectively. Figure 42 (right) illustrates that the profiles are consistent and prove that the missing feature is not an artifact of how the PDV was fielded. So the observation of spall interfaces in PDV, the appearance of the second rise to the free surface velocity, and the disappearance of the reduction of loading after release with no load recovery occur coincidently and are consistent with complete spall of the HDPE.

The disappearance of the reduction of loading after release with no load recovery in the profiles as a function of pressure is interesting. Kanel, *et al.* observed something similar in their studies of X-cut quartz [206]. Quartz is a class of brittle solids for which the Hugoniot collapses to the isentrope when loaded over the HEL because of a total loss of shear strength [207–209]. Figure 43 illustrates the loss of features indicative of tension or spall once the X-cut quartz is loaded above the Hugoniot elastic limit (HEL) because tension cannot be supported. It appears that HDPE undergoes an analogous loss of shear strength when impacted to 8.221 GPa or above in the experiments presented here. HDPE is not brittle so there has to be an alternative mechanism for the inability to support tension. Based on the observation of ejecta by PCI for these impacts, thermal softening is a likely explanation. The amount of heating from plastic work can be expected to be quite high for the large compaction and extension of the ductile polymer. This was seen directly with PCI at lower impact conditions in shot DCS-2017-124. For shot DCS-2017-4-125 it is even greater but the relationship between the rate of plastic work and temperature rise is not known for HDPE. In metals an empirical factor of 0.9 has been determined by calorimetry [210]. Determination of the relationship between the rate of plastic work and temperature rise would enable quantitative evaluation of the proposed mechanism of thermal softening for the total loss of shear strength in HDPE.

Gobulev, *et al.* reported partial spall failure at 0.25 and 0.14 GPa for PMMA and polyethylene, respectively. In contrast, damage was shown to initiate somewhere between 0.268 to 0.483 and 3.47 to 8.221 GPa. The discrepancy is quite large for HDPE. Material, loading configuration, and success of deceleration and recovery are possible explanations for the difference. Gobulevs results show that the threshold for initiating damage is reduced as temperature is increased for polyethylene [180, 181]. Battelle's results shows that fracture propagation, rather than arrest, is more likely at low temperature [198]. This implies that damage nucleated dynamically at higher temperatures may not propagate; whereas, at low temperature the threshold for damage nucleation will be higher but is more likely to propagate and be catastrophic once nucleated. Taken together these results potentially have important implications for weapons applications. Several experimental configurations have been

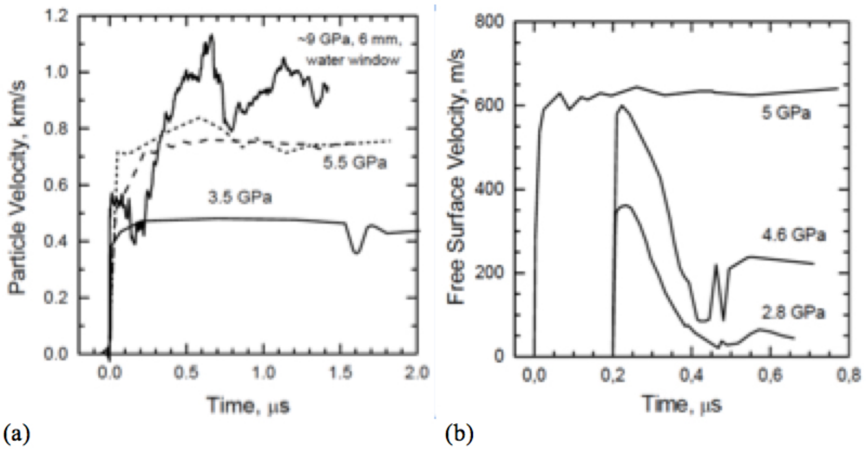

Figure 43: Spall response of X-cut quartz loaded above and below the HEL [206]. (a) Free surface velocity profiles for 4-mm-thick x-cut quartz samples. The shot at the highest stress, ∼9 GPa, was done with a 6-mm-thick sample and a water window. (b) Free surface velocity profiles for x-cut quartz at different peak stresses generated by 0.2- or 0.4-mm-thick aluminum impactor plates.

developed to investigate crack propagation of a pre-cracked sample under shock and release as well as the effects of strain state on shear dependence and stochasticity of cracking with PCI [186]. These experiments can be employed to further quantitate implications for weapons applications.

PCI is useful for observing the nucleation and evolution of damage in spall experiments but quantitative measures of the material state need to be extracted. Density may be extracted from the data directly. However, current algorithms for density retrieval were developed for strong or weak phase objects [211]. Solid samples do not fall into this category and iterative algorithms for both phase and amplitude are needed. These algorithms are under development at LANL but are not yet ready for use. When they are, the PCI of spall presented here will be prime candidates. Kitchens, *et al.* demonstrated that the texture in the contrast of PCI images could be analyzed to determine particle/void size distributions [212]. In their derivation for use in biological applications, they assumed random packing [213]. This cannot be assumed for damage on spall planes. Barber has rederived the statistics without this assumption and it may be possible to apply the analysis to the spall data in the near future to extract void size distributions associated with spall damage [214]. Algorithms for iterative retrieval of both phase and amplitude are again the limiting factor.

VIII.F Conclusions

A comparative study of the behavior of Poly(methyl methacrylate) and high density polyethylene under dynamic tension created by impact and release was performed using PCI. Damage localization on the tensile stress plane was clearly evident for PMMA and was consistent with spall signatures in PDV. Damage became less localized as impact pressure was increased, illustrating a change in the mechanism or process. Damage was not as evident or localized for HDPE. Subtle changes in transmitted intensity were observed at low impact pressures, and localization was not observed until complete spall. Transmitting the PDV laser through the HDPE enabled recording velocities at impact, rear, and spall interfaces. Observation of ejecta and spall interfaces in PCI and the appearance of the second rise to the free surface velocity and the disappearance of the reduction of loading after release with no load recovery in PDV all occurred coincidently. This was interpreted as signs of complete loss of strength and thermal softening was proposed as a likely mechanism. This data provides further insight and an alternative to the prevailing interpretation involving void nucleation and coalescence as the mechanism for spall in ductile polymers.

IX High Pressure Deep-Release Experiments (***Hooks, Lang, Coe, Dattelbaum***)

IX.A Summary

The high pressure dynamic response of polymers is important to a wide variety of applications. The details of compressibility and reactivity can have a large effect on overall behaviors of dynamic systems even when polymers are used in small amounts. Polyethylene is of broad interest for a variety of applications, as an ingredient and as a pure material. It is also of significant interest as a model system to understand the correlating effects of polymer dynamics in a material with a relatively simple chemical composition that can have highly varied properties through the alteration of molecular weight and associated crystallinity of the material. Although a variety of Hugoniot and dynamic information is available for polyethylene, it is a challenge to obtain information on the product equation of state at pressures high enough to achieve decomposition. Following recent successes in producing deep release states in compressed epoxy material, a series of plate impact experiments was performed in the same configuration on high density and ultra-high molecular weight polyethylene at high pressures. The experiments and the results, intended to calibrate a product equation of state and compare the behaviors of these two varieties of polyethylene, are described.

IX.B Introduction

The high rate mechanical and shock response of PE has been studied at some length, with interest in its Hugoniot and failure response across a large range of pressures [29–32, 35, 45, 49]. In particular, evaluation of volume collapse at low pressure has driven a large body of work, and the variability of the molecular weight, crystallinity, and density of the material has been shown to contribute to measureable differences in this regime. This low-pressure behavior and dynamic failure response is the subject of a forthcoming review [36].

PE can also undergo chemical reaction at sufficient pressure, contributing energy to energetic material formulations, although the time scale of reaction may or may not be useful, depending upon the desired characteristics of the energetic material. Once chemical reaction occurs, the product equation of state is of primary interest. Previous papers have noted a minor inflection in the Hugoniot for PE at a particle velocity up of about 3.3 km/s [29–32, 49]. Recovery experiments suggested this inflection was related to chemical reaction.

Fredenburg *et al.* described an evaluation of possible techniques to interrogate the equation of state of products at high pressure by measuring the release profile from a high-pressure shock [37]. Transmission and front surface impact experiments were considered, and ultimately the front surface impact geometry was recommended. In this shot design, the traditional front surface impact technique is performed, wherein the sample was contained in the flyer and impacted into a well-characterized window [38]. The flyer is just a few mm thick, and is backed by a low-density material so that the shock is released after a short duration. First experiments with this design were carried out to investigate the release profile in Epon 828 [39].

In this work, release profiles were measured in PE samples shocked to pressures between about 33 and 43 GPa using the short-shock front surface impact technique. Samples of high density PE (HDPE) and ultra-high molecular weight PE (UHMWPE) were investigated to compare the response of these two types of PE.

IX.C Experimental

Three experiments on each of the HDPE and UHMWPE materials were performed on a high performance two stage powder gun, with hydrogen gas as the launching medium. The bore diameter of the launch tube was 25.4 mm. Impact experiments were performed in a front surface impact configuration, with 12.8 mm thick LiF as the target material. HDPE and UHMWPE impactors were machined to a 3 mm thickness, leaving a 4 mm pocket to be filled with glass microballoon syntactic foam (GMB). This layered impactor was bonded into a Lexan projectile and machined to final diameter to match the launch tube bore.

The LiF target was coated with an 8 kÅAl film in the central portion, providing a reflector for four Photon Doppler Velocimetry (PDV) probes [43] at a radius of 4.762 mm and one Velocity Interferometry System for Any Reflector (VISAR) probe [44] on the target center to measure interface velocities at the impactor/target interface. Four additional PDV probes were placed outside of the aluminum reflecting film, providing four independent measurements of the projectile velocity v_p and a measure of impact tilt. A schematic diagram of the target and projectile configuration and the placement of PDV and VISAR probes is shown in Figure 44.

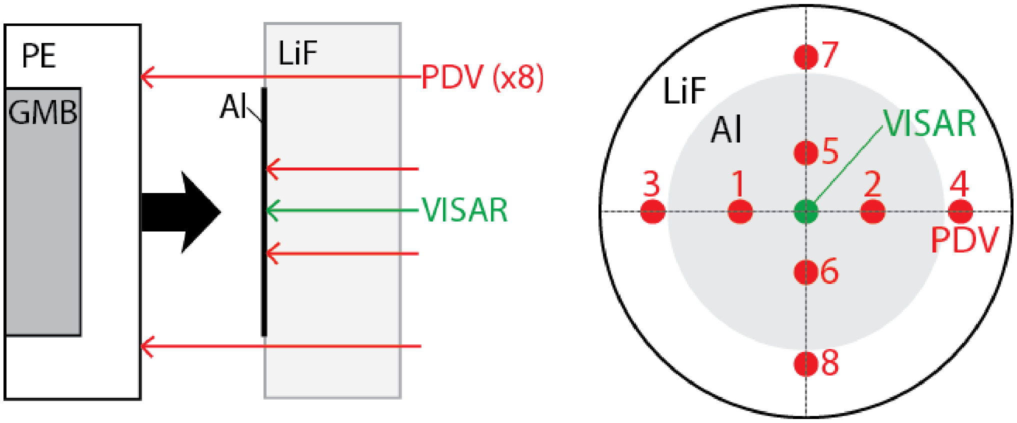

Figure 44: (left) Schematic of the shot setup. PE (either UHMWPE or HDPE) backed by glass microballoon (GMB) syntactic foam impacted a LiF window. The impact surface of the LiF window was vapor-plated with a 15.2 mm diameter Al mirror. Not to scale. (right) Schematic of probe positions. The projectile velocity was measured by the four outer PDV probes, numbered 3,4,7,8 on a 4.762 mm radius. Four additional probes and one VISAR probe on the Al-mirrored section of the window measured particle velocity at the impactor-window interface, numbered 1,2,5,6 on a 10.922 mm radius. Not to scale.

The LiF material was obtained from REFLEX Analytical Corporation, and is High Purity Single Crystal Visible Ultra-Violet Lithium Fluoride, with the (100) plane along window thickness ±2 degrees. HDPE and UHMWPE materials were compression molded plates from Polymer Industries Densetec, and are the same stock as a series of experiments to be reported elsewhere for consistency [36]. The crystallinity and initial density ρ_0 was measured to be 78.5% and 0.9587 g/cc for the HDPE and 52.2% and 0.9262 g/cc for the UHMWPE. GMB Ecco-float EL-34 material was purchased from Trelleborg. Assembly was performed with AngstromBond 9110LV. Sample dimensions were recorded to ensure glue bonds and sample flatness to <2 μm. Impactor tilt was typically a few mrad, and at most ∼12 mrad.

Wave profiles were extracted from the PDV spectrograms by applying a centroid routine to a bracketed portion of the images. The LiF window correction of Rigg *et al.* ($u_p = 0.7887 u_A^{0.9927}$) was applied to the profiles [40]. Profiles were synchronized with impact at the center of the target at $t = 0$.

The impact particle velocity u_p^i in the target materials was determined by subtracting the window particle velocity u_p^w from the projectile velocity v_p. Impact stress P and density ρ in HDPE and UHMWPE were calculated from the window particle velocity u_p^w and the LiF Hugoniot ($U_s^w = 5.148 + 1.353 u_p^w$) [40].

IX.D Results & Discussion

Three experiments were completed for HDPE and UHMWPE, ranging from 33 to 43 GPa. The three experiments on UHMWPE were at slightly lower pressures, as the highest velocity shot on HDPE showed signs of instability in the petal valve at the transition from the pump tube to the launch tube. VISAR records were not usable for any of the shots due to loss of light upon impact. PDV data return was good, with usable profiles on most of the probes. A typical spectrogram is shown in Figure 45 (left) from shot 69ts-17-05 on HDPE, with the extracted velocity traces from all of the central probes corrected for the LiF window and shifted to impact at $t = 0$ at the center of the target as shown in Figure 45 (right).

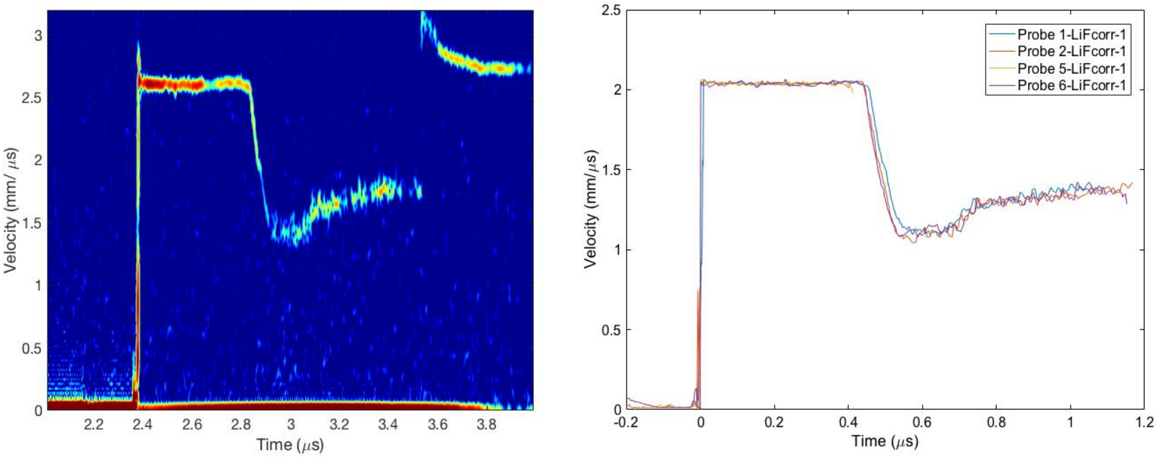

Figure 45: Representative wave profile data. (left) Spectrogram from PDV probe 1 from shot 69ts-17-05 on HDPE at 42.52 GPa. (right) Velocity profiles extracted from spectrograms from all four PDV probes for shot 69ts-17-05 on HDPE, synchronized to impact at t=0 at the center of the target and corrected using the LiF window correction of Rigg, *et al.* ($u_p = 0.7887 u_A^{0.9927}$) [38].

Table 13 lists the experimental details and results for all six experiments on HDPE and UHMWPE. The impact stress P, shock velocity U_s, and particle velocity u_p were calculated from the measured impact and interface velocity as described in the experimental section above. Impact stresses in this range of 33-43 GPa are well above the suspected transition to access the reacted state of PE, and are within the range of peak detonation pressures of several explosive formulations.

Table 13: Summary of data from deep release experiments.

Shot	Material	v_p(mm/μs)	P(GPa)	ρ(g/cc)	U_s(mm/μs)	u_p(mm/μs)
69ts-17-03	HDPE	5.638±0.025	33.07±0.08	1.752±0.020	8.731±0.065	3.951±0.040
69ts-17-06	HDPE	6.175±0.024	38.28±0.59	1.780±0.042	9.311±0.197	4.290±0.032
69ts-17-05	HDPE	6.609±0.031	42.52±0.54	1.814±0.040	9.705±0.178	4.570±0.070
69ts-17-04	UHMWPE	5.544±0.047	31.75±0.83	1.676±0.067	8.773±0.322	3.909±0.057
69ts-17-07	UHMWPE	5.905±0.027	34.44±0.93	1.741±0.071	8.931±0.325	4.165±0.091
69ts-17-08	UHMWPE	6.339±0.033	38.46±0.61	1.771±0.042	9.337±0.197	4.447±0.040

Plotting the results in stress vs. particle velocity and shock velocity vs. particle velocity planes, shown in Figure 46, highlights the differences in compressibility between HDPE and UHMWPE. The larger molecular weight of the UHMWPE leads to lower crystallinity and thus lower density; this lower density translates into higher free volume, and thus higher compressibility and increased shock heating. There was consistently more error in the determination of peak particle velocity for the

UHMWPE, which translates into more error in the calculated quantities as well, but the observed trend is greater than the error. Comparing the calculated compressed densities to the initial densities, the UHMWPE exhibits a compressibility ratio $\sim 1 - 2\%$ higher than that of HDPE in this pressure range.

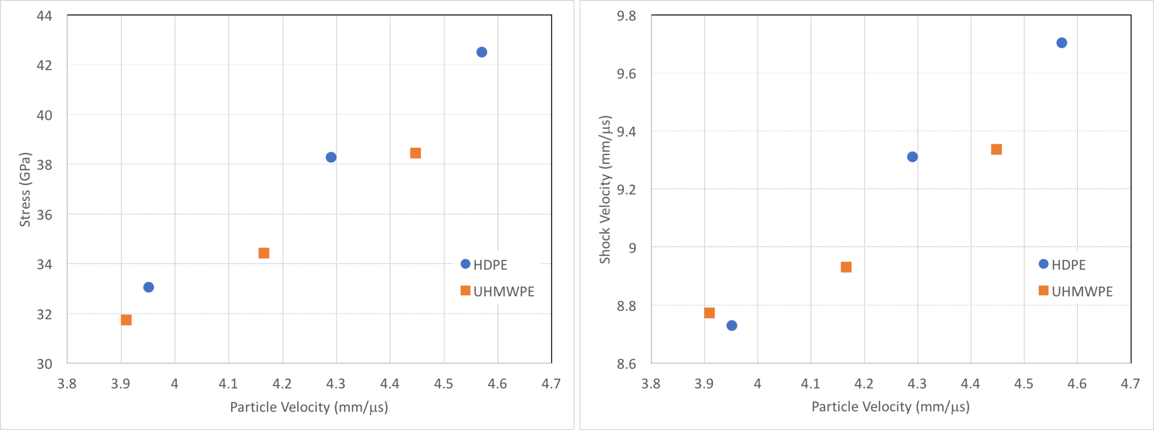

Figure 46: Hugoniot data: (left) Stress vs. particle velocity. (right) Shock velocity vs. particle velocity. The apparent crossover of points for UHMWPE and HDPE at the lowest pressure, more obvious in the shock vs particle velocity plane, is due to increased error in the UHMWPE shock velocity, up to 0.325 GPa.

Differences in the release profiles for the two materials are not obvious by inspection (not shown). There is, possibly, an apparent transition from a slightly curved release to a more linear release in both materials with increasing pressure (also not shown), but this difference has not been quantified. Careful analysis of the release profiles from these experiments remains to be done to reveal any differences in the product equation of state.

IX.E Conclusions

High-pressure deep release shock experiments on HDPE and UHMWPE exhibit difference in compressibility of these two materials in a range of pressures relevant to ballistic applications and explosives formulations. The compressibility differences are consistent with the differing crystallinity and density of the materials, with UHMWPE showing compressibility ratios about 1-2% higher than HDPE. In future work, the release profiles from the peak states will be used to develop product equations of state.

X Thermal Properties (*C. Welch*)

X.A Introduction

Semi-crystalline polymers, such as polyethylene, typically undergo multiple transitions as a function of temperature. The glass transition (T_g) reflects the temperature at which chain segments in the amorphous domains change from being glassy (or immobile) to rubbery (or mobile). The melting transition (T_m) brings analogous changes to the crystalline domains, as chain segments in those domains lose their crystalline structure and become extremely mobile. These changes can significantly affect mechanical properties, as well as properties related to equation-of-state (see Section XI). To better understand these thermal transitions and their effects in polyethylene, thermal analysis experiments were conducted to measure the glass and melting transitions, heat capacity (C_p), and coefficient of thermal expansion (CTE). In addition, torsional dynamic mechanical analysis (DMA) experiments were performed to probe low-strain mechanical response as a function of temperature.

X.B Thermal analysis

X.B.1 Differential Scanning Calorimetry: Thermal Transitions

Standard and modulated DSC experiments were performed on a TA Instruments Q2000 MDSC with hermetically sealed aluminum pans. Temperature calibration was performed with an indium standard. Non-modulated DSC experiments with a liquid nitrogen cooling system (in conjunction with a helium purge gas) were conducted with a ramp rate of 20°C/min to probe for the glass transition temperature (T_g) in the range of -150°C to 0°C. Literature values of T_g for all grades of PE vary widely from approximately 0°C to -140°C. However, the values at the low end of that range are likely due to a γ-relaxation related to exchanges between gauche and trans configurations. In addition to this transition, two types of glass transitions have been postulated in the literature: T_g(U) $\approx$ -33°C, associated with amorphous loops and ties between crystalline domains, and $T_g(L) \approx$-73°C, associated with amorphous chain ends and other material rejected by crystallites [61]. Figure 47 shows that both of the PE grades examined here exhibit the γ-relaxation in the range of -125°C to -130°C and T_g(U) in the range of -34°C to -35°C.

Additional standard DSC experiments with a refrigerated cooling system and a nitrogen purge gas were conducted to measure the melting transition and %crystallinity of the as-received materials. Each sample was heated from 30°C to 200°C at a ramp rate of 10°C/min. Figure 48 shows representative results for both HDPE and UHMWPE, and Table 14 gives the peak melting temperature, heat of fusion, and % crystallinity, averaged over 5 replicates for each grade. The % crystallinity was calculated by first integrating the melting peak over the range of 60°C to 180°C to obtain the heat of fusion (in J/g), and then dividing by the heat of fusion for a 100% crystalline polyethylene sample, 289 J/g.

X.B.2 Modulated Differential Scanning Calorimetry: Heat Capacity

Heat capacity is the amount of heat required to raise the temperature of a material by a given amount (e.g., 1°C). For polymers, this value is directly related to molecular mobility; it reflects the capacity of the polymer to absorb heat through molecular motions such as bond vibrations, rotations, and

Table 14: DSC results for the melting transition in as-received polyethylene sheets.

	HDPE	UHMWPE
Peak melting temperature (°C)	137.5±0.9	136.3±1.1
Heat of fusion (J/g)	226.8±5.7	149.8±5.5
Crystallinity (%)	78.5±2.0	51.8±1.9

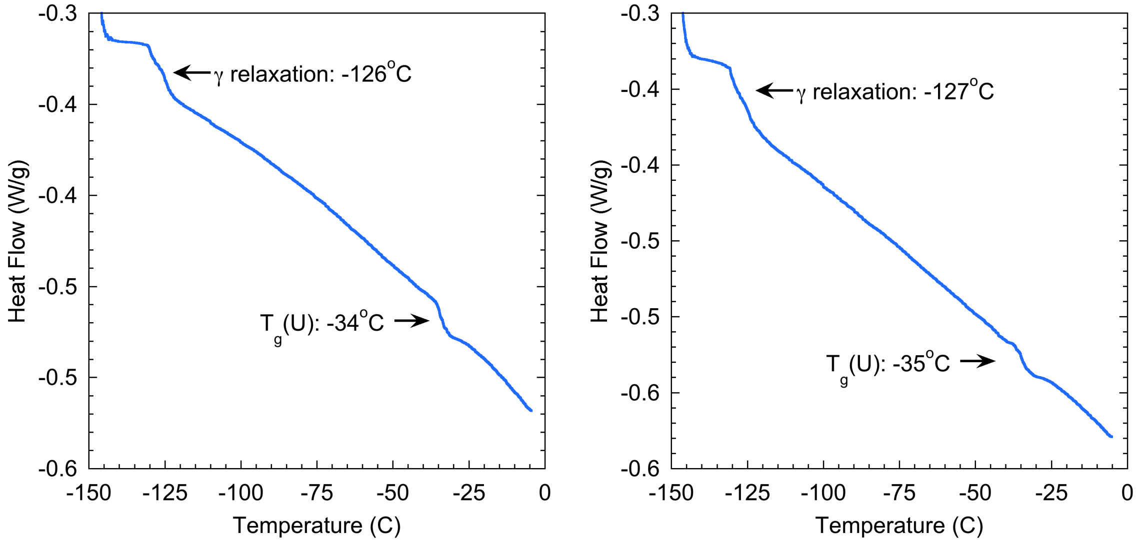

Figure 47: DSC measurement of γ-relaxation and T_g(U) for (left) HDPE and (right) UHMWPE.

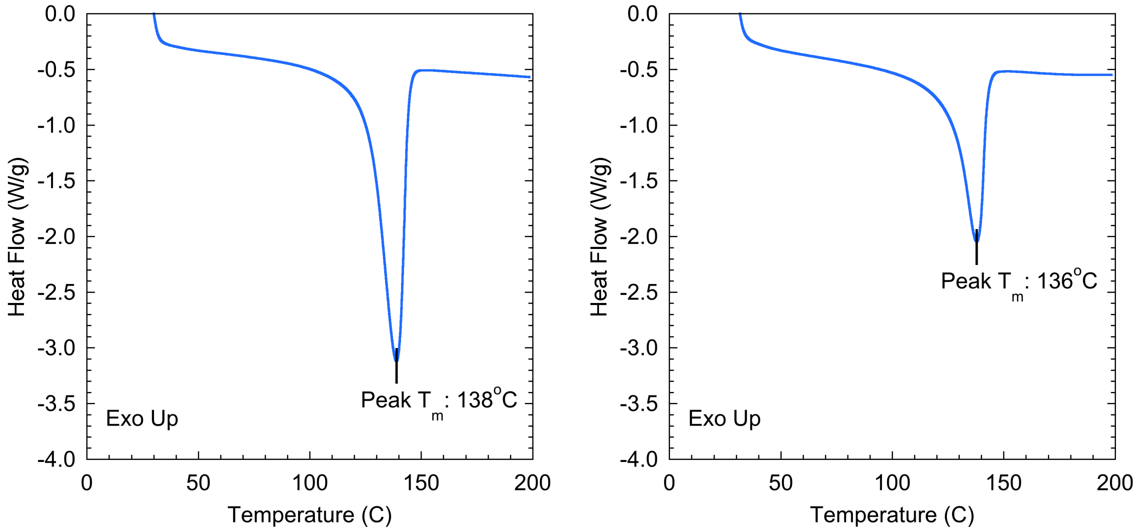

Figure 48: DSC measurement of melting transition for (a) HDPE and (b) UHMWPE.

translations. Heat capacity values can be determined through differential scanning calorimetry (DSC) experiments. Conventional DSC is not a direct measurement of the heat capacity but can be estimated with Equation (8):

$$C_p = K\frac{HF_s - HF_{mt}}{m_s R} \tag{8}$$

where K is a calibration constant; HF_s and HF_{mt} are the differential heat flows for the sample and reference (empty) pan, respectively; m_s is the mass of the sample; and R is the heating rate. Equation (8) is an approximation, as it ignores the difference in heating rate between the sample and the reference pans. This difference is caused by the slowly changing heat capacity of the sample, and it limits the theoretical accuracy of the measurement to ±3%. In practice, however, accuracies of only ±10% are commonly achieved because of the difficulty associated with maintaining a highly stable baseline throughout the three experiments per sample (baseline, sapphire standard, and sample) that are required with this approach.

On the other hand, Modulated Differential Scanning Calorimetry (MDSC) can obtain heat capacity values with one experiment, and the accuracy can be improved to ±2% [62]. MDSC differs from conventional DSC in that MDSC uses two simultaneous heating rates: the conventional linear ramp and a modulated sinusoidal ramp. The data obtained from the linear ramp provide information similar to standard DSC, while the modulated heating rate permits the simultaneous measurement of the sample's heat capacity. Thus, MDSC is a direct measurement of heat capacity and is described by Equation (9):

$$C_p = K\frac{HF_{HR2} - HF_{HR1}}{(HR_2 - HR_1)m_s}, \tag{9}$$

where K is the calibration constant, HF_{HR1} is the differential heat flow of the sample at HR_1, HF_{HR2} is the differential heat flow of the sample at HR_2, HR_1 is Heating Rate 1, HR_2 is Heating Rate 2, and m_s is mass of the sample. MDSC experiments were performed to measure heat capacity (C_p) in the range of -60°C to 100°C. Obtaining accurate heat capacity values requires the optimization of experimental conditions, including sample size, heating rate, modulation heating rate, and period of modulation. An ASTM [62] and two TA Technical Papers [63, 64] were followed to ensure that the procedure was optimized to obtain accurate measurements. For each measurement, a portion of the sample (typically 5 to 10 mg in mass) was encapsulated in a high-sensitivity aluminum Tzero®pan. Three specimens of each PE grade were tested to obtain the standard deviation (as given by the error bars in Figure 49).

For each PE specimen, experiments were performed from -80°C to 105°C, with a ramp rate of 3°C/min and a modulation of ±0.95°C every 120 s. Before each MDSC sample run, a sapphire standard was run using the same experimental conditions. The sapphire data were compared to literature values [65] to create multi-point calibration curves for reversible heat capacity, with calibration values (K) calculated at every temperature data point collected. The sample data curves were then corrected using these calibration curves.

Figure 49 compares the reversible C_p results for HDPE and UHMWPE to literature C_p values for PE taken from the Advanced Thermal Analysis System (AThAS) database [34, 67]. The database values are given for both purely crystalline and purely amorphous PE; these values are determined from calculations of vibrational modes for the purely crystalline material and an empirical fit to literature data for the purely amorphous material. Since both the HDPE and UHMWPE samples are semi-crystalline polymers, the experimental data for each fall between the two database sets, with HDPE being closer to the purely crystalline. Neither the HDPE nor the UHMWPE show a large jump in Cp at the T_g(U), unlike the database results for purely amorphous PE. This is likely due to the high degrees of crystallinity for these samples. Also, the measured Cp values begin to rise at a faster rate at ∼ 50°C, which is not reflected in the AThAS data. This increase is likely due to the onset of the melting transition. As seen in the standard DSC data of Figure 48, the melting transition is broad, extending from 60°C to 180°C. In the MDSC experiments, the slower ramp rates combined

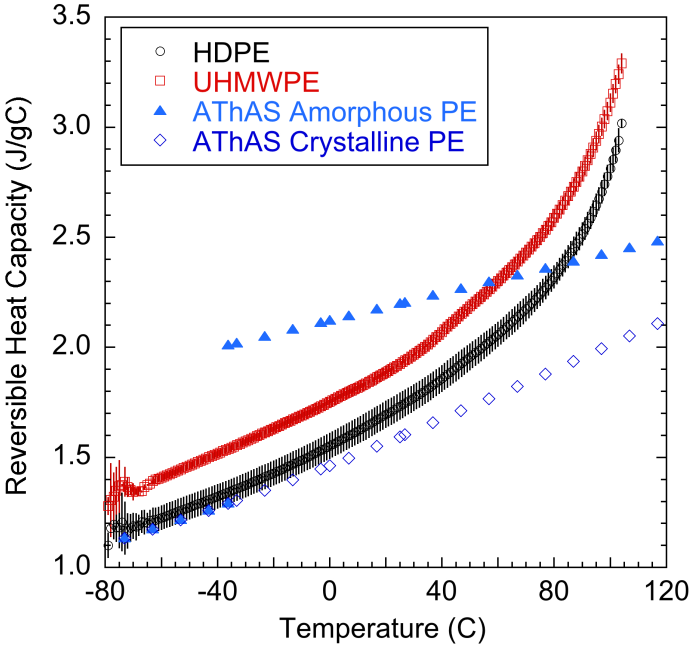

Figure 49: MDSC measurements of reversible C_p for HDPE and UHMWPE, compared to values for purely amorphous and purely crystalline PE.

with the temperature modulation allow the crystalline domains to begin melting at slightly lower temperatures.

X.B.3 Thermomechanical Analysis: Coefficient of Thermal Expansion

TMA was performed on a TA Instruments Q400 EM to measure the linear coefficient of thermal expansion (CTE) over the range of -55°C to 65°C, using a ramp rate of 2°C/min and a preload force of 0.1 N. High-purity nitrogen flowed through the sample area at a rate of 50.0 mL/min. The instrument was calibrated using aluminum and indium standards. PE sample cubes were machined to have dimensions of 5 mm x 5 mm x 5 mm. Three specimens of each PE grade were tested to obtain the standard deviation. To test for anisotropy in the CTE, the cube sides were labeled 1 to 6, with 1 opposite of 3, 2 opposite of 4, and 5 opposite of 6. For each cube, TMA experiments were conducted in the three different orientations such that the linear CTE was determined along each spatial direction. Figure 50 shows a representative set of results for one of the HDPE cubes along one direction; results are given as a plot of dL/L_0 vs. temperature, where L_0 is the initial sample length and dL is the instantaneous change in length as a function of temperature. The linear CTE, α, is determined from the slope of the line, and this slope changes slightly as temperature increases. Thus, the temperature range was divided into three regions for the CTE calculations: -55°C to -30°C, -30°C to 15°C, and 15°C to 65°C. Table 2 summarizes the results for both HDPE and UHMWPE. For any given temperature range, the CTE for UHMWPE is larger than that for HDPE. For both PE grades, the CTE increases with temperature. Finally, both grades show a small amount of anisotropy in that one “side (i.e., Side 2 for HDPE and Side 1 for UHMWPE) has a slightly larger CTE than the other two sides; this anisotropy is more pronounced at higher temperatures.

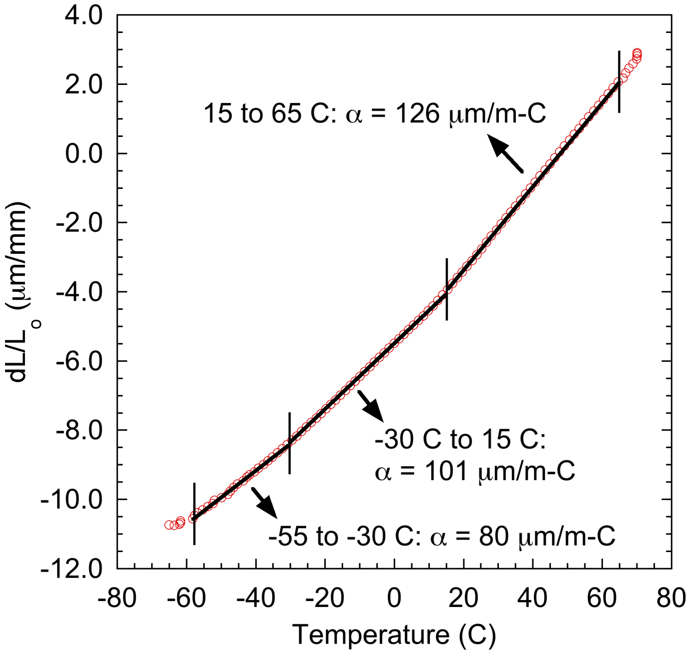

Figure 50: TMA measurement of linear CTE for one HDPE sample.

Table 15: CTE results for HDPE and UHMWPE.

Sample	-55°C to -30°C	-30°C to 15°C	15°C to 65°C
HDPE Side 1	85±5	100±3	124±3
HDPE Side 2	91±2	114±3	150±3
HDPE Side 5	80±1	99±1	120±4
UHMWPE Side 1	114±4	136±2	177±4
UHMWPE Side 2	100±5	118±3	158±3
UHMWPE Side 5	108±5	125±1	157±1

X.C Torsional dynamic mechanical analysis

Torsional DMA provides information on the temperature-dependent viscoelastic properties that can be fed into a viscoelastic constitutive model. Three HDPE and three UHMWPE samples were machined to give rectangular bars with dimensions of 40 mm×10 mm×2 mm. Torsional DMA experiments were conducted on a TA Instruments ARES rheometer over a temperature range of -50°C to 100°C with a 0.1% oscillatory strain (i.e., strain-control mode). Frequency sweeps (0.1 to 100 rad/s) were collected using the following temperature sequence:

1. Equilibrate at -50°C for 30 min, then perform frequency sweep.
2. Increment temperature by +5°C, equilibrate for 15 min, and perform frequency sweep.
3. Repeat step 2 until reaching -30°C.
4. Increment temperature by +10°C, equilibrate for 30 min, and perform frequency sweep.
5. Repeat step 4 until reaching 20°C.
6. Increment temperature by +5°C, equilibrate for 15 min, and perform frequency sweep.
7. Repeat step 6 until reaching 30°C.
8. Increment temperature by +10°C, equilibrate for 30 min, and perform frequency sweep.
9. Repeat step 8 until reaching 100°C.

Thus, frequency sweeps were collected at 19 temperatures (-50°C, -45°C, -40°C, -35°C, -30°C, -20°C, -10°C, 0°C, 10°C, 20°C, 25°C, 30°C, 40°C, 50°C, 60°C, 70°C, 80°C, 90°C, and 100°C), with isothermal equilibration periods of 15 or 30 min, depending on whether the prior temperature was lower by 5°C or 10°C, respectively. For a given temperature, frequency sweep data sets were averaged over the 3 samples measured for each PE grade.

Figure 51 gives the frequency sweep results for HDPE, while UHMWPE data are shown in Figure 52. At the low end of the temperature range probed, polyethylene is below its T_g, and the viscoelastic properties of both HDPE and UHMWPE are mostly independent of temperature. As temperature increases from -30°C to 100°C, frequency-dependent behavior can be seen in all of the data sets. For all temperatures tested, the complex viscosity (η*, top left of Figures 51 and 52) shows a power-law, shear-thinning trend with increasing frequency; as temperature increases, both the magnitude of the viscosity and the power law exponent decrease. For HDPE at -50°C, the exponent is -0.99; at 25°C, the exponent decreases to -0.94, and at 100°C it is -0.84. For UHMWPE at -50°C, the exponent is -0.99; at 25°C, the exponent decreases to -0.96, and at 100°C it is -0.87. The complex shear modulus (G*, top right in Figures 51 and 52) increases slightly with frequency at all temperatures above -30°C, with the frequency dependence becoming more pronounced as temperature increases. The phase angle (bottom panel of Figures 51 and 52) describes the amount of energy lost to the viscous nature of the polymer, compared to the energy input by the oscillatory shear. Phase angles close to zero reflect a polymer that is behaving elastically; as the phase angle increases, more viscous losses occur. Below the T_g, both HDPE and UHMWPE exhibit phase angles close to zero across the entire frequency range. However, as temperature increases, the phase angle increases. Generally, as the oscillation frequency is increased, less loss occurs, as the polymer molecules have less time to relax.

Figures 53 (HDPE) and 53 (UHMWPE) illustrate the temperature dependencies more clearly by plotting η*, G*, and phase angle as a function of temperature at frequencies of 0.1, 1, 10, and 100 rad/s. Above -30°C, η* and G* decrease with temperature, while the phase angle approaches a maximum as temperature increases. In one case (UHMWPE at 0.1 rad/s), the maximum occurs within the temperature range examined, at 70°C.

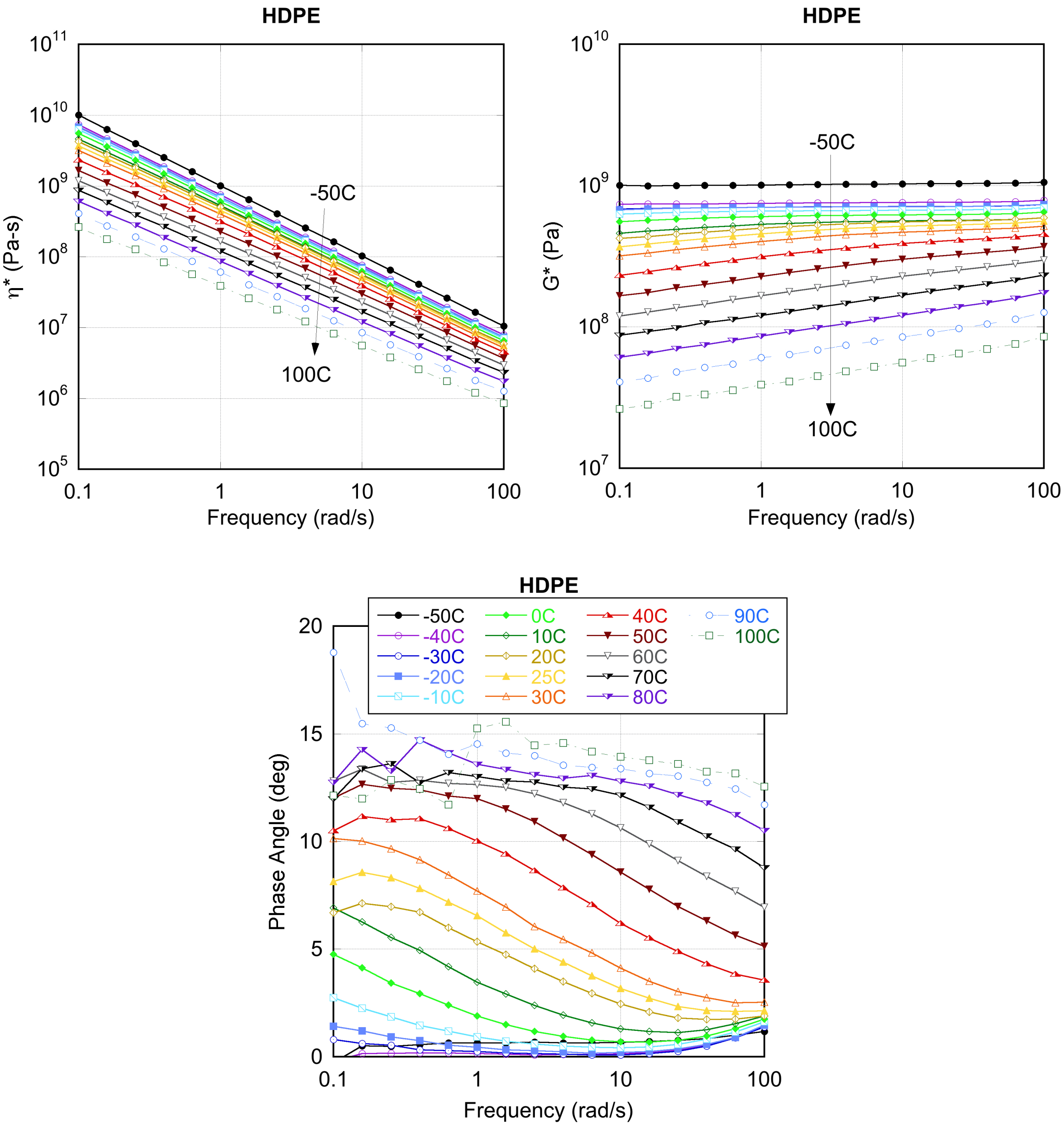

Figure 51: Torsional DMA data (frequency sweeps) for HDPE: (top, left) complex viscosity (η^*), (top, right) complex modulus (G^*), and (bottom) phase angle.

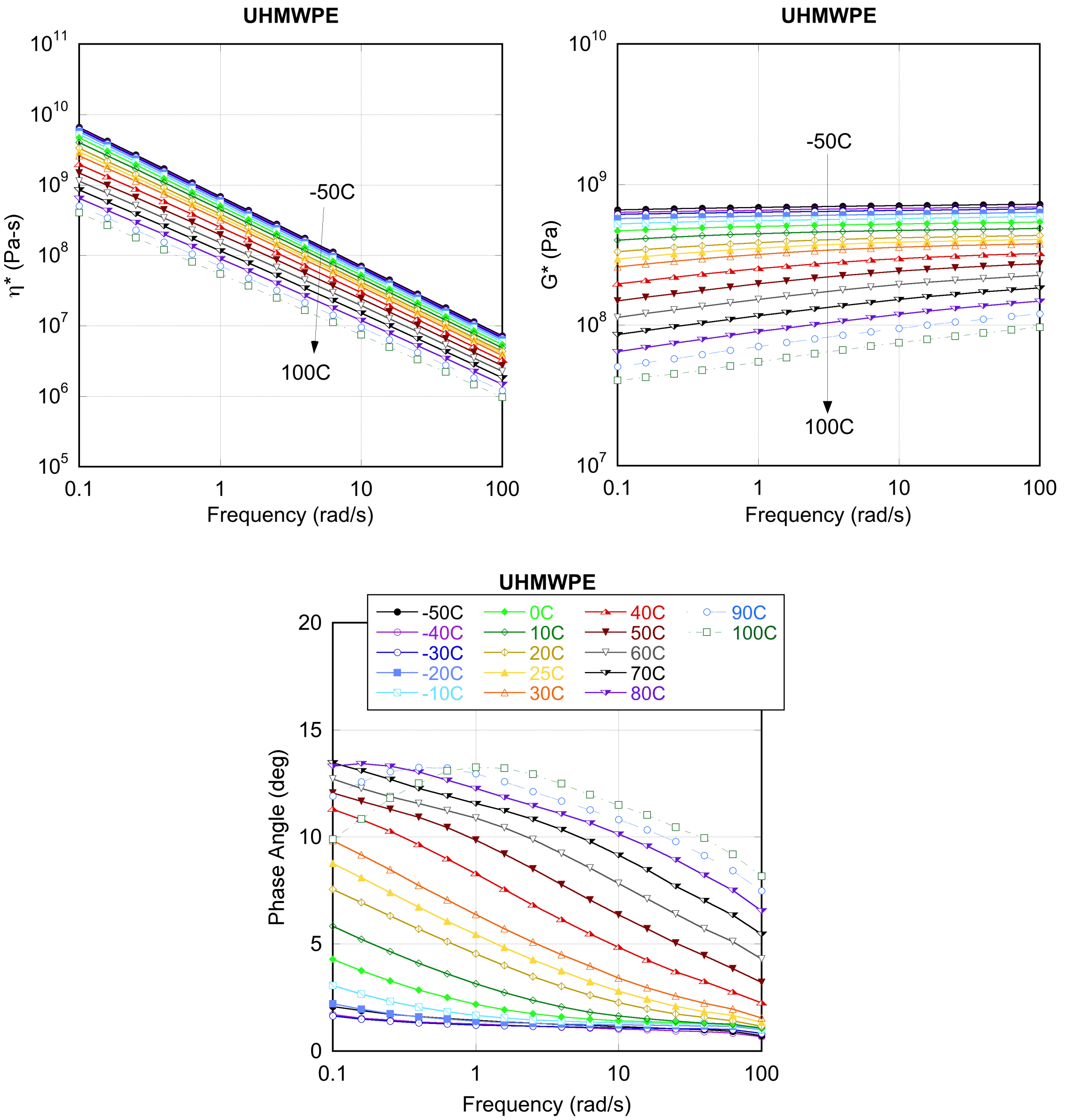

Figure 52: Torsional DMA data (frequency sweeps) for UHMWPE: (top, left) complex viscosity (η^*), (top, right) complex modulus (G^*), and (bottom) phase angle.

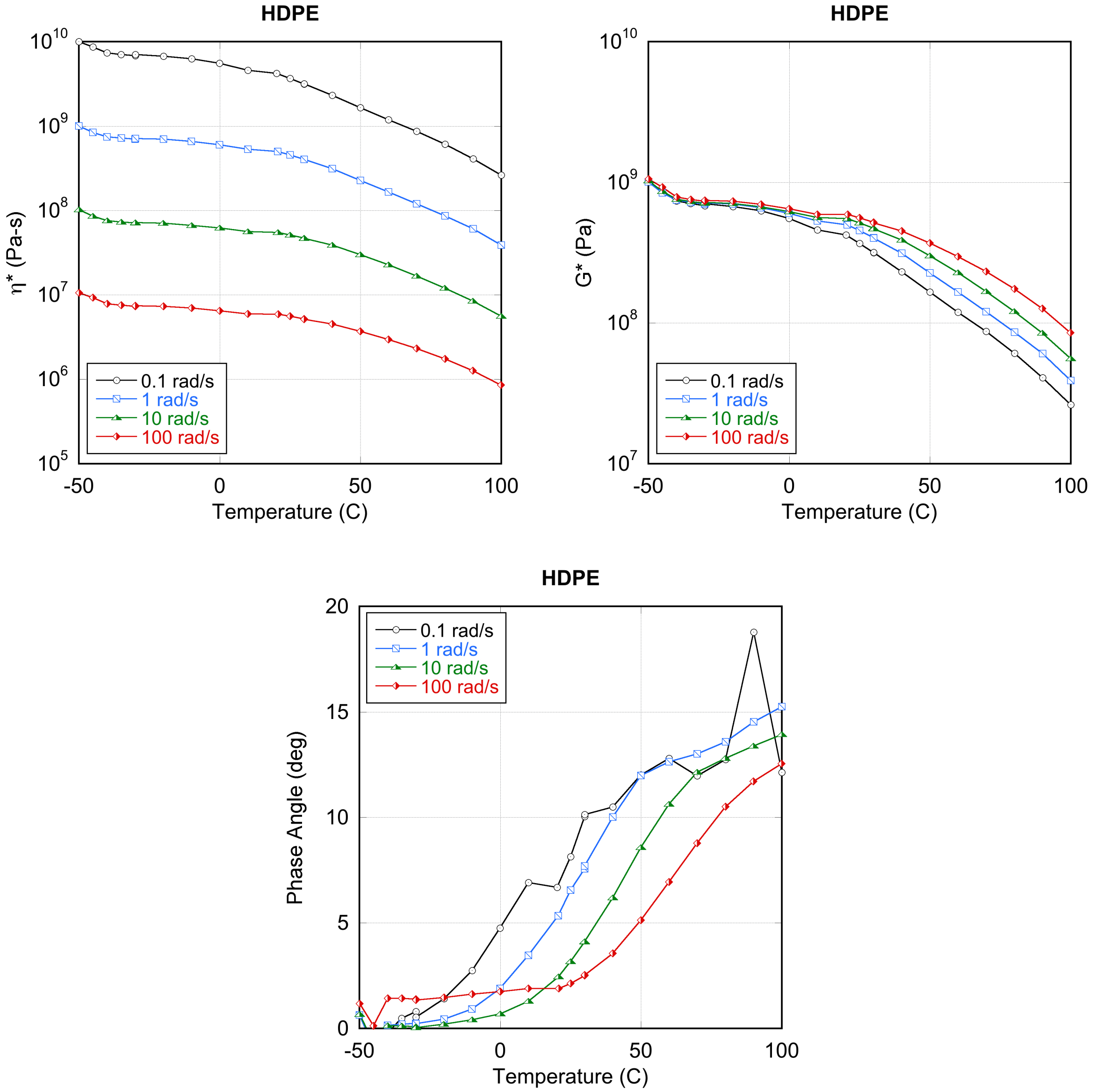

Figure 53: Torsional DMA data as a function of temperature for HDPE: (top, left) complex viscosity ($\eta*$), (top, right) complex modulus ($G*$), and (bottom) phase angle.

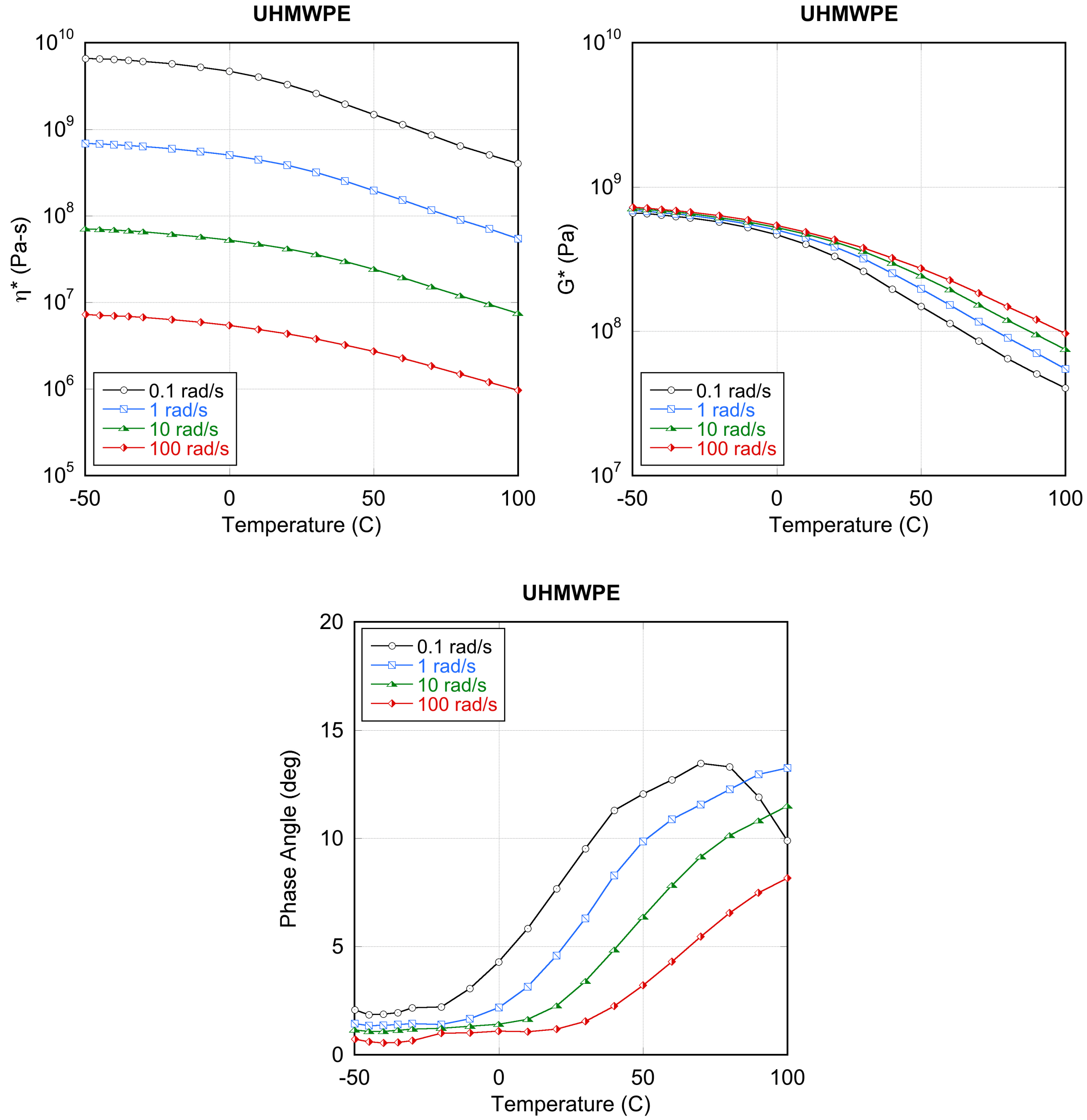

Figure 54: Torsional DMA data as a function of temperature for UHMWPE: (top, left) complex viscosity ($\eta*$), (top, right) complex modulus ($G*$), and (bottom) phase angle.

Since polyethylene is a semi-crystalline polymer, multiple relaxation processes are expected at temperatures between T_g and T_m; thus, the time-temperature superposition principle does not apply [68]. Additionally, polyethylene does not always display thermorheological simplicity at temperatures above T_m; rather, various forms of thermorheological complexity have been observed, depending on the molecular weight and degree of branching [69, 70].

XI SESAME Equations of State (*Maerzke & Coe*)

XI.A Introduction

Effective modeling of polymers using existing EOS frameworks is challenging. Due to the molecular structure of the material, soft matter has some unique properties, including curvature at low u_p in the $U_\mathrm{S}-u_\mathrm{p}$ Hugoniot and shock-induced chemical decomposition accompanied by a volume change [30,49, 72]. Moreover, using a simple Debye-like model leads to unsatisfactory agreement with experimental thermal data. One common class of polymers in poly(ethylene) (PE), which exists in several forms depending on the molecular weight, degree of branching, and extent of cross-linking. Here we will examine HDPE and UHMWPE. Even within a specific type of PE, the material properties can vary significantly. Some key properties for data sources we have used can be found in Table 16. Recently, new gas gun shock compression experiments have been performed to better understand the behavior at low particle velocity (see Section VII) as well as at higher pressures (see Section IX). In addition, thermal properties such as the coefficient of thermal expansion and constant pressure heat capacity have been measured (see Section X). With this new data, we have created new SESAME equations of state for unreacted HDPE and UHMWPE. A legacy EOS (7180) from 1982 [31] exists for HDPE, but not for UHMWPE (though there is one for low-density PE). In the future we will use thermochemical modeling to create equations of state for the decomposition products.

Table 16: Reference densities, percent crystallinity, sound speeds, glass transition temperatures (T_g) and melting temperatures (T_melt) for HDPE and UHMWPE. $^{(a)}$This is the temperature at which the material “softens” [75].

material	ρ_0 [g/cm^3]	% crystallinity	c_0 [km/s]	T_g [K]	T_melt [K]
HDPE	0.962	80	–	239	–
UHMWPE	0.929	55	–	238	–
HDPE [53, 54]	0.9698	80.9	2.264	276	407
UHMWPE [53, 54]	0.9268	38.6	1.927	–	406
Marlex 50 [45, 59, 75]	0.954	93	2.17	–	400 – 403$^{(a)}$
Marlex 6065 [45]	0.954	–	–	–	–

XI.B Equation of State Model

A chemically inert equation of state (EOS) was constructed using the SESAME model, in which the the Helmholtz free energy F is expressed as a three-part decomposition,

$$F(\rho, T) = F_\mathrm{cold}(\rho) + F_\mathrm{ionic}(\rho, T) + F_\mathrm{elec}(\rho, T) \tag{10}$$

as a function of density ρ and temperature T. The first term represents the cold curve, or the free energy of the electronic ground state with the ions in their equilibrium configuration (which does not include zero point energy). The second term describes the ionic motion in the ground electronic state, and the third term the electronic excitations. Electronic excitations, which are generally negligible, were calculated using the Thomas-Fermi-Dirac model [52].

The cold curve was fit to recent gas gun shock data measured at LANL (Sections VII and IX), as well as older data from Nellis et al. [32] and Marsh [45]. The reported data in Marsh is for Marlex 50 and Marlex EMN 6065. Marlex is the trade name for a specific type of HDPE originally developed by the Phillips Petroleum Company (which is now Chevron Phillips Chemical Company). Some information on the properties of Marlex 50 is available [59, 75], but the only specific reference

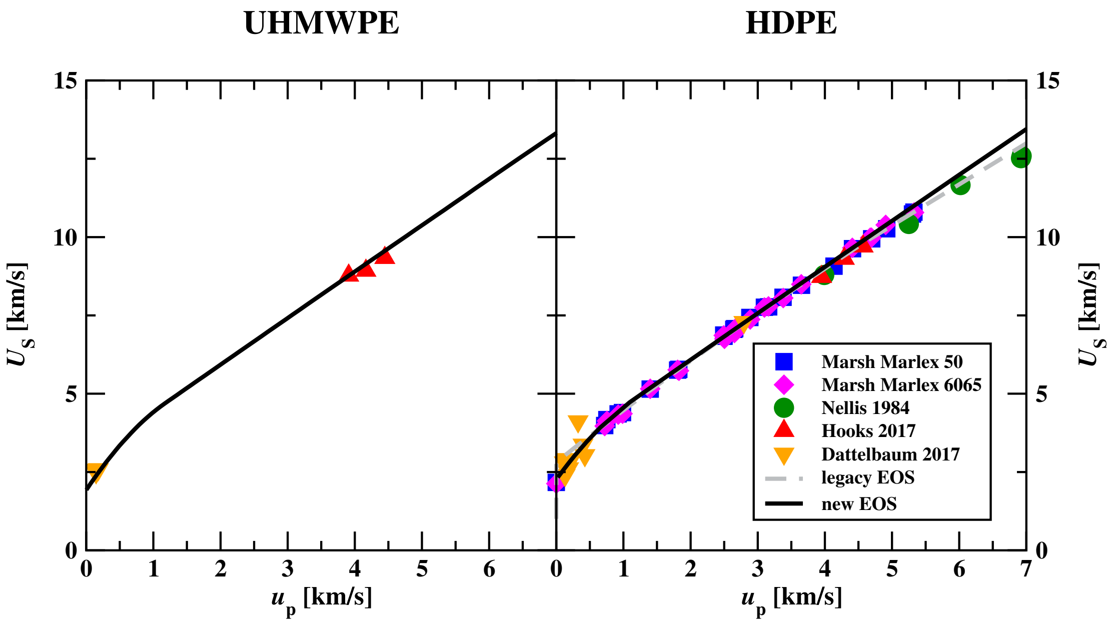
UHMWPE

HDPE

Figure 55: $U_\mathrm{S} - u_\mathrm{p}$ Hugoniot plots for UHMWPE (left) and HDPE (right). Marsh Marlex 50 (blue squares) [45], Marsh Marlex EMN 6065 (magenta diamonds) [45], Nellis et al. (green circles) [32], new LANL shock data from Sections IX (red triangles up) and VII (orange down triangles) of this report, the legacy HDPE EOS (dashed gray line), and our new EOS (black solid line). Note that we have very little data for UHMWPE.

to Marlex EMN 6065 is in Marsh. Marlex 50 is quite similar to the modern HDPE that has been recently studied at LANL, though the density is slightly lower and the crystallinity is higher. The shock data for both varieties of Marlex are verey similar, though there are small differences. Nellis et al. do not specify the source of their PE, but based on the average ρ_0 it is likely Marlex 50. The extremely limited amount of shock data for UHMWPE limits the degree of accuracy we can expect from the resulting EOS, though the material is similar enough to HDPE that we can use the HDPE EOS to inform the development of the UHMWPE EOS.

Polymers typically exhibit curvature at low u_p in the $U_\mathrm{S} - u_\mathrm{p}$ plane [49] due to the macromolecular nature of the material. When compressing a polymer, the gaps in the material caused by inefficient packing of polymer chains are eliminated before the material itself is compressed. These weaker intramolecular van der Waals interactions take less force to compress than the stronger intermolecular bonds found along the polymer backbone, which accounts for the softening in the Hugoniot. To capture the curvature at low u_p, we used a quadratic equation to fit data below $u_\mathrm{p} \approx 1.2$ km/s,

$$U_\mathrm{S} = c_0 + s_1 u_\mathrm{p} + s_2 u_\mathrm{p}^2 \tag{11}$$

where c_0 is the bulk sound speed. We have used the sound speeds measured by Rae and Brown [53] for HDPE and UHMWPE. Above $u_\mathrm{p} \approx 1.2$ km/s, we used a linear fit to the data. The linear portion of the curve was fit to HDPE shock data, then for UHMWPE we used the same slope and adjusted the intercept to better match the low u_p portion of the UHMWPE Hugoniot (where we do have some data). The two sections of the cold curve were joined such that the curve and its derivative are continuous.

By using the two-part fit, we reduce the sound speed for HDPE from 3.10 (the result of a purely linear fit) to 2.264 km/s, which changes the bulk modulus ($B_S = c_0^2 \rho_0$) from 9.28 to 4.93 GPa. Note

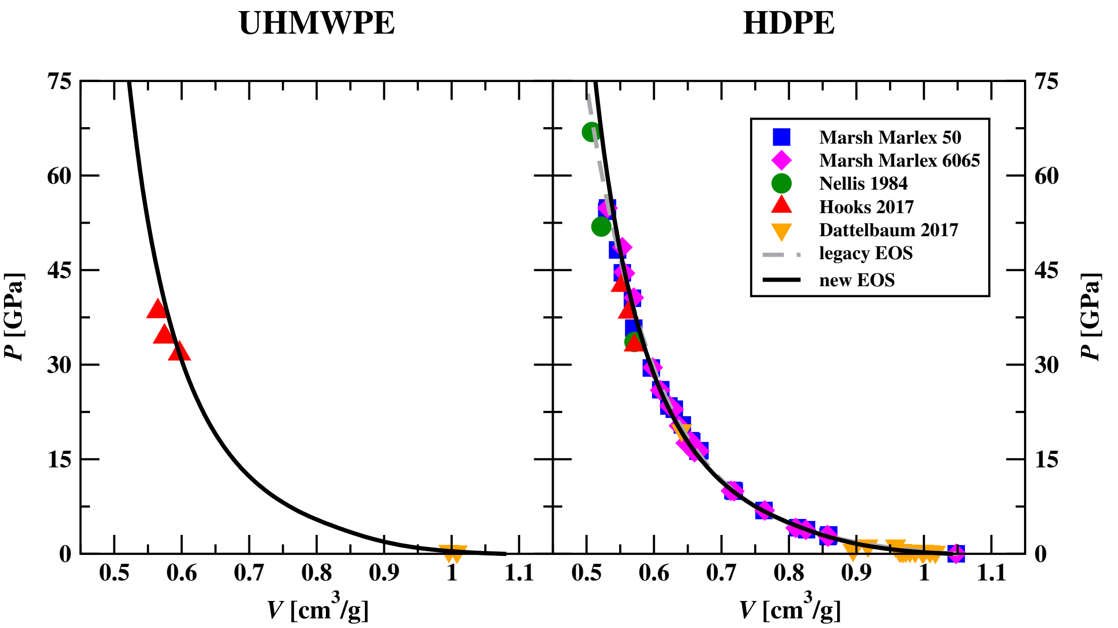

Figure 56: $P - V$ Hugoniot plots for UHMWPE (left) and HDPE (right). Marsh Marlex 50 (blue squares) [45], Marsh Marlex EMN 6065 (magenta diamonds) [45], Nellis et al. (green circles) [32], new LANL shock data from Section IX (red triangles up) and Section VII, the legacy HDPE EOS (dashed gray line), and our new EOS (black solid line). Note that we have very little data for UHMWPE.

that the legacy EOS for HDPE does not include curvature at low u_p and has a noticeably higher sound speed of 2.82 km/s, which implies B_S is 7.59 GPa. This is at odds with the value of $B_S = 4.48$ mentioned in the original Tech Report [31], so there is an inconsistency somewhere in the legacy EOS. For UHMWPE, c_0 is 1.927 km/s. The change in bulk modulus affects the value of Γ ($\Gamma = \alpha B_s/C_P\rho$), which in turn affects the entire EOS. Since we have measured values of α and C_P, we can explicity calculate values for Γ at the reference state. For HDPE we obtain $\Gamma_0 = 1.152$, which would be 2.17 without curvature at low u_p, while for UHMWPE we find $\Gamma_0 = 0.962$.

With our new EOS, we obtain excellent agreement to the HDPE shock data (see Figures 55 and 56). Above $\approx 3-3.5$ km/s, or $25-30$ GPa, we expect that PE reacts and chemically decomposes [30,49,72]. This will cause a small volume collapse and lowering of the shock velocity. Hence, we do not expect our inert EOS to match the data from Nellis et al. [32] or some of the new higher pressure shock data (Section IX). This data will be used in the future to constrain a separate EOS for the decomposition products. In constrast, the legacy EOS attempts to match all of the data. This results in a noticeable difference between the legacy EOS and our new EOS at higher pressures/higher particle velocities. By attempting to capture all of the data with a single EOS, the legacy EOS misses important physics and chemistry that occurs at high shock compressions. For UHMWPE, we do not have much shock data, and most of what we do have is likely reacted. Given the limited data, our new EOS is very reasonable.

Due to the molecular nature of PE, thermal ionic contributions were calculated using the Tarasov model [66], rather than a more typical Debye-like model. Instead of a single vibrational frequency corresponding to a single characteristic temperature, the Tarasov model divides the vibrational spectra into different regions, corresponding to different types of molecular motion, each of which has its own characteristic temperature (or range of temperatures). In addition, different regions are approximated using either a 1-dimensional or 3-dimensional Debye function, as appropriate. In the absence of any

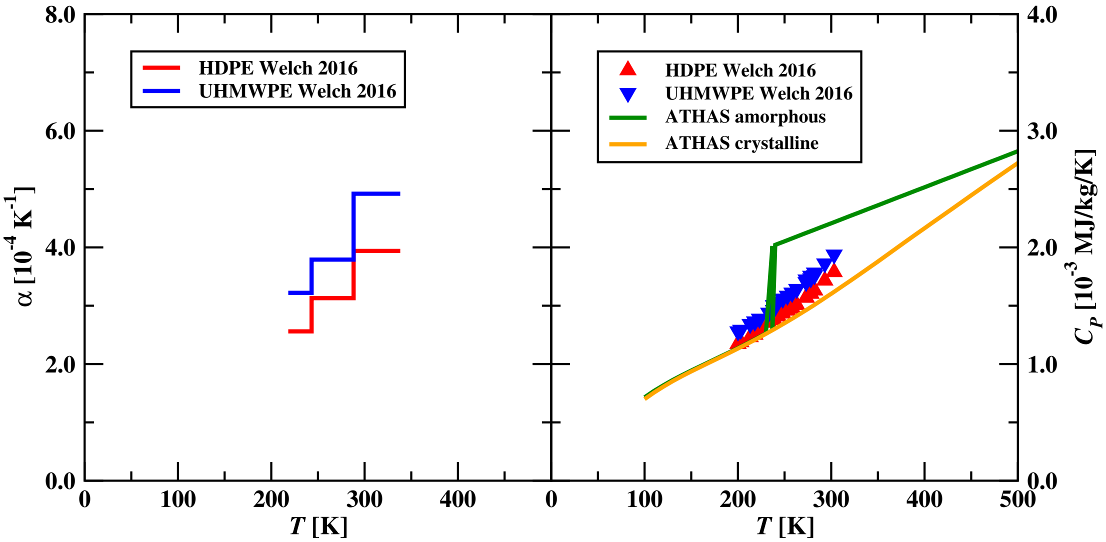

Figure 57: The coefficient of thermal expansion (α, left) and constant pressure heat capacity (C_P, right) reported in Section X for UHMWPE (blue) and HDPE (red). For comparison, heat capacities from the ATHAS database for fully amorphous and crystalline PE are also shown (green, orange).

vibrational spectra for the specific materials we are interested in, the Tarasov parameters are fit to reproduce C_P data reported in Section X. The Wunderlich [66] values of the characteristic temperatures for PE (based on the vibrational spectra) are used as a guide. Due to the likely differences in crystallinity and density (it is unclear which material Wunderlich used), we have felt free to adjust these values to fit the new C_P data measured for the specific varieties of PE we are modeling. Differences in initial density and crystallinity will have an effect on the thermal data, which can be seen in Figure 57. The differences between HDPE and UHMWPE are not large, but UHMWPE consistently has a higher heat capacity and coefficient of thermal expansion than HDPE.

For HDPE, low frequency vibrational modes corresponding to polymer backbone motion, also called skeletal modes, are represented by 3D and 1D Debye functions with a characteristic temperatures of 150 K and 500 K, respectively. For UHMWPE these values have been adjusted slightly, to 100 and 400 K. Higher frequency vibrations corresponding to more localized motions of isolated groups of atoms (e.g., monomers) are modeled with a band of 1D Debye functions with characteristic temperatures of $1100-2300$ K for HDPE and $1000-2100$ K for UHMWPE. Very high frequency C-H stretches are modeled using an Einstein function with a characteristic temperature of 4100 K for both HDPE and UHMWPE. As can be seen in Figure 58, our new equations of state yield an excellent match to the available data. Our new HDPE EOS is a clear improvement over the legacy EOS.

The coefficient of thermal expansion was measured as a linear value for the three different directions in a solid cube. To obtain the average volume coefficient we have averaged the linear values in the different directions and multiplied by three. Though this ignores the small amount of anisotropy present in the materials, it is a reasonable approximation. Our EOS models cannot take into account anisotropy. Note that the measured CTE is constant over certain temperature ranges. A SESAME EOS is not able to reproduce this behavior, but we do manage to reproduce the data quite well in an average way. Our new EOSs pass through each constant region, and reproduce the ambient value.

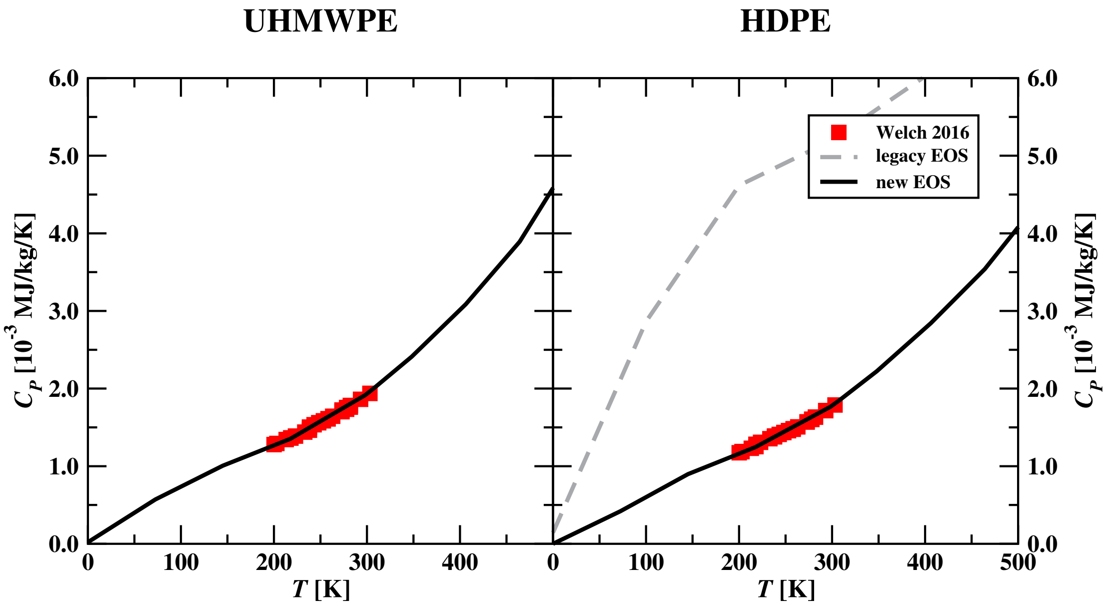

Figure 58: Constant pressure heat capacity (C_P) for UHMWPE (left) and HDPE (right) Experimental data from Section X, new EOS (black solid line), and the HDPE legacy EOS (gray dashed line).

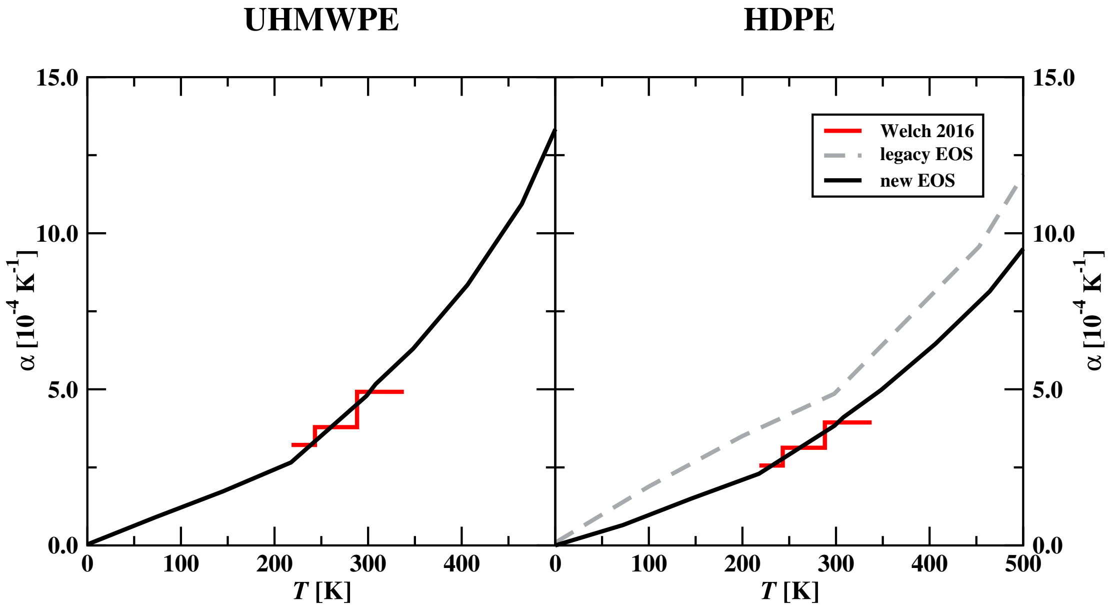

Figure 59: The coefficient of thermal expansion (α) for UHMWPE (left) and HDPE (right). Experimental data from Section X (red squares), new EOS (black solid line), and the HDPE legacy EOS (gray dashed line).

XI.C Conclusions

Our new equations of state for HDPE and UHMWPE yield excellent agreement with the available shock and thermal data for unreacted material. In the case of HDPE, our new EOS is a clear improvement over the legacy EOS. For UHMWPE, we have provided a new modeling capability in that no legacy EOS exists. In the future, we will extend our modeling capability by developing separate equations of state for the decomposition products of each material. By creating separate a EOS for unreacted and reacted material we take into account more of the physics and chemistry that occurs when the polymer is subjected to strong shock compression. Moreover, improved physics models for thermal properties, such as Tarasov, that take into account the molecular nature of the material result in improved agreement with experimental data.

XII Theoretical Models for Damage in Semi-Crystalline Polymers (*P. Welch*)

XII.A Overview

Defining damage as a permanent change in the material's morphology upon some mechanical insult, variations in the percent crystallinity and attendant orientation of domains constitute the primary form of damage one may expect in polyethylene (PE). Though many computational studies have been undertaken of crystallization in this material over the past few decades, several challenges still stand that limit our knowledge of this process. A significant barrier manifests in the difficulty in assessing which domains in the simulation model actually correspond to crystalline regions. This arises from the multi-phase nature of semi-crystalline polymers, comprised of crystalline domains, amorphous domains, and transition zones. Thus, our first step toward studying morphological changes in PE via simulation draws upon recent advances in statistical or machine learning to aid in our analysis. Section XII.B.1 below details our application of these methods and our efforts to test them by extracting new insight into the relationship between the dynamics in the amorphous domain and those at the growth front. Those results were reported in the *Journal of Chemical Physics* in 2017.

With this new tool suite, we then proceed to examine the changes in morphology upon isotropic compression in a molecular dynamics model of PE in Section XII.B.2. In this study, we extract the changes in the nucleation processes for crystal growth, the changes in percent crystallinity, and the equation of state for the material as a function of compression ratio. Those results, in preparation for publication, are tested against a new analytical prediction for the growth process and are greatly facilitated by the statistical learning tools developed in Section XII.B.1. The key findings of this study are: i) upon compression, a melt of the material is plunged below its equilibrium melting temperature and that melting temperature continues to rise with the pressure, thus increasing the effective quench depth even though the material is held at constant temperature; ii) the percent crystallinity grows as a function of compression in functional form similar to that expressed in simple experiments in which a melt is quenched below its melting point at standard pressure, but the role of time is replaced with that of the compression ratio; iii) the number of nuclei follow similar trends to those observed in the standard pressure experiment (again with compression ratio playing the role of time) until impingement between the nuclei occurs and consolidation diminishes their numbers; iv) the Tait equation of state appears to describe the data, even though the material moves through a phase transition; and v) a straightforward extension of the theory due to Kundagrami and Muthukumar [90] captures the crystal growth kinetics when active mass transport is introduced to their model.

In Section XII.B.3 we present a new theory for damage in polymeric materials, built from recent advances in network theory. Here, the microscopic details of chain connectivity are encoded in the principle eigenvector of the connectivity (adjacency) matrix. Drawing an analogy to canonical ensembles in statistical mechanics, we construct a model that uses eigenvector centrality as a metric of importance of each junction in the material. Appealing to a scaling ansatz, we then produce an estimate for the Young's tensile modulus based upon the centrality metric. We are still in the process of applying this new theory to PE, but have successfully demonstrated its capability to link the microscopic details to the macro-scale modulus by applying it to self-healing poly(dimethyl siloxane) (PDMS) data reported in the literature. Our results were reported in *Scientific Reports* in 2017.

XII.A.1 External Presentations

1) December 2015 TCG Meeting held at SNL.
2) December 2016 TCG Meeting held at LANL.
3) NSEC Summer School presentation.

XII.A.2 External Publications

1) P. M. Welch, Journal of Chemical Physics, **146**, 044901, (2017).
2) P. M. Welch and C. F. Welch, Scientific Reports, **7**, 1241, (2017).

XII.B Technical Summary

XII.B.1 Polymer Crystallization Dynamics and Statistical Learning

Introduction to the Challenges of Modeling Polymer Crystallization

The complexity and ubiquity of polymer crystallization has motivated many different theoretical treatments of the associated dynamics. Yet, a completely satisfactory picture of the many different physical processes active remains elusive. Conventionally, one divides these processes into a primary nucleation phase for pure melts or a secondary nucleation step for melts with contaminant inclusions, followed by a growth phase that results in a multi-scale mosaic of chain-folded, lamellar, and spherulitic structures [91]. The details of these processes are not universally agreed upon, however, and questions surrounding the formation of the earliest structures remain a vigorous topic for study. An overview of many of the relevant theories can be found in the review by Armitstead and Goldbeck-Wood [92], as well as the more recent set of *Lecture Notes in Physics* edited by Reiter and Strobl [93]. Broadly speaking, molecular theories of polymer crystallization either propose a nucleation and growth scheme for the early stages of structure formation or a spinodal-like density segregation with concurrent ordering. There appears to be a consensus, however, that some ordering in the non-crystalline domain must occur prior to the formation of full-fledged lamellae. The standard model due to Hoffman [94,95] and Lauritzen, for example, envisions the formation of straightened chain segments that attach to the growing crystal face. Studies by Muthukumar [96,97] and coworkers indicate that ordering occurs as a precursor to full nuclei formation and that an entropic barrier must be traversed by incoming chains at the growth front as they order. Olmsted [135] and coworkers proposed a coupling between density and chain order to describe a potential spinodal mode during the early stages of crystal formation. The model proposed by Strobl [98] postulates the formation of a mesomorphic phase characterized by a higher degree of chain ordering in the amorphous domain.

Computational studies [99–105] also demonstrate the significance of ordering in the amorphous phase. For example, Gee [103,104] and coworkers reported their results from large scale simulations of poly(vinylidene fluoride) and poly(ethylene) to propose that a period of coexistence of spinodal-like density separation and nucleation and growth exists before the onset of crystallization. Some authors [106,107] have also taken advantage of the accelerated onset of crystallization that accompanies pre-alignment of the chains. In addition to making simulation of crystallization from the homogeneous melt computationally tractable, preordering by mechanical deformation also establishes conditions that mimic the processing scenarios found in industrial applications [108–111]. This ordering plays a role in "shish kabob" formation from both melts [112,113] and solution [114], for example. This impact of starting conditions highlights not only the importance of ordering in the amorphous phase, but also the non-equilibrium nature of many of the key molecular processes.

As noted by Yamamoto, [111] the dominance of non-equilibrium mechanisms hinders the development of a completely successful analytical treatment. Similarly, reliably identifying those atoms participating in emerging crystalline domains presents a subtle challenge for computational studies aimed at revealing the molecular processes underlying the early stages of homogeneous crystallization. As Sommer and Luo [115] point out, the earliest ordered domains can be difficult to define since i) both straight and flexed chain segments are involved; ii) the chain conformations are fluctuating; and iii) the ordered domains can be very close to one another and difficult to enumerate. The most common approach to identifying crystalline domains, defining a threshold value for an orientational order parameter, can fail to reliably capture subtle processes. This leads those authors to define a more sophisticated measure that includes temporal persistence [116].

Here, we probe the out-of-equilibrium molecular ordering processes in the early stages of crystallization from the homogeneous melt using simulation and statistical learning [117] tools to identify those atoms that compose crystalline domains. Simulation has proven to be a powerful tool for teaching us about the molecular processes involved in polymer crystallization; [118] combining computer modeling with statistical learning methods can assist us in extracting yet more insight from numerical studies. We specifically focus on the relationship between the evolution of local ordering fluctuations in the amorphous domain and the rate of crystallization. This leads to a simple phenomenological kinetics expression, but one that draws from a different perspective than previously considered. Equation 12 below constitutes the proposed kinetics relationship. It is built upon three postulates: i) there exists a proportionality between the fluctuations in the rate of on-chain ordering and the fluctuations in the rate of increase in percent crystallinity; ii) a characteristic ordering rate dominates the well-known linear-in-time growth in percent crystallinity over a large timespan; and iii) the proportionality proposed above decays with time, since chain mobility within the material drops as a frozen network sets up due to the physical crosslinks imposed by the growing nuclei.

Proposed Kinetics Model

We hypothesize that the fluctuations in the rate of local on-chain ordering δR_s in the amorphous domain are proportional to the fluctuations in the rate of crystallinity growth δR_c during homogeneous crystallization from the melt. The focus here is on the entire sample, not a single crystalline domain. As time progresses, kinetic constraints on the molecular dynamics impact the ability of chains to add to growing crystal domains; segment mobility is frustrated as a network of chains connecting different crystal nuclei forms. Thus, one expects that the proposed proportionality decays with time. We assume a simple exponential decay dependence on the time elapsed since crystallization began, t. Thus, we expect $\exp[-t/\tau]\delta R_s \propto \delta R_c$. If such a relationship is valid, experimental evidence strongly indicates that over a substantial period of time during crystal growth R_s must be a fixed constant. One expects this since, in the linear growth regime, the increase in percent crystallinity χ is linear with time and R_c is fixed. We therefore consider variations about this steady-state rate of ordering, r_s, and define $\delta R_s \equiv \frac{ds}{dt} - r_s$ where $\frac{ds}{dt}$ is the instantaneous change in local, on-chain order. Note that $R_c \equiv \frac{d\chi}{dt}$. Introducing a proportionality constant α, we arrive at Eq. 12:

$$\exp(-t/\tau)\alpha\left(\frac{ds}{dt} - r_s\right) = \frac{d^2\chi}{dt^2} \tag{12}$$

Typically, the percent crystallinity χ of a quenched melt displays a sigmoidal dependence on time [91]. At early times, during the "induction period," χ changes very slowly, perhaps undetectably so. This is followed by a linear growth regime in which $\chi \propto t$. Finally, the percent crystallinity grows only very slowly at late times such that $\chi \propto log(t)$. One readily sees that Eq. 12 satisfies our assumption that $\frac{ds}{dt} = r_s$ in the linear growth regime. Whether it also satisfies the observed behaviors in the early and late time regimes depends upon how $\frac{ds}{dt}$ behaves in these time spans. To our knowledge, this behavior is not yet known from experiment. Below, we appeal to simulation to extract how $\frac{ds}{dt}$ varies in the earliest stages of homogeneous crystallization. We note that to match the typical sigmoidal shape, Eq. 12 appears to demand that $\frac{ds}{dt} \equiv r_s$ in this time regime, too. However, this typical behavior is not universally observed in simulations, as indicated above; χ may or may not display the weak dependence on time associated with the induction period. One expects that the observed behavior is impacted by the sensitivity of the experimental apparatus used to measure χ, as well as the initial conditions of the melt. We see below that, for the conditions simulated here, $\frac{ds}{dt} > r_s$ in the early stages of nucleation.

Simulation Model and Analysis Methods

We applied a slightly modified version of a previously reported [100] united atom model for the crystallization of polyethylene that originally derived from the work of Paul et al [120]; the on-chain

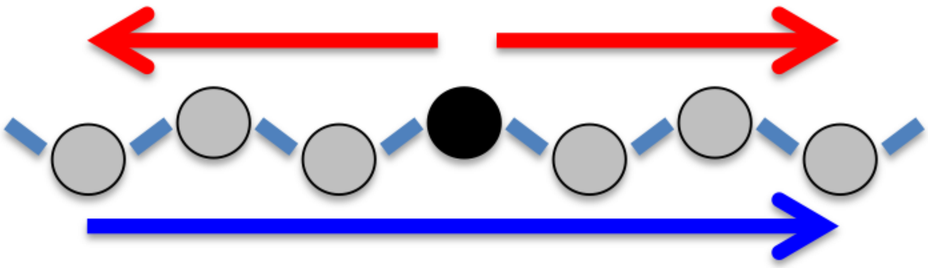

Figure 60: A sketch of the simulation model and the vectors employed in calculating the two order parameter measures constituting the feature space. The black bead in the center indicates a reference bead. The red arrows define the two vectors used for the on-chain order parameter, while the blue indicates the vector used for the inter-stem measure.

pairwise interactions are turned off for beads that are closer than or equal to three bonds apart. Figure 60 contains a cartoon representation of the model. A single bead represents each methyl unit, comprised of one carbon and two hydrogens. The terminal beads of each chain are modeled by the same united atom as those internal to the chain backbone; CH_3 groups are approximated as CH_2 units on the chain ends. In addition to pairwise and bonded interactions, the model includes both bond angle constraints and dihedral forces. The equilibrium bond length l_0 is set to unity in the simulation and defines the basic length scale for the model. The equilibrium well depth for the pairwise interactions ϵ is also set to one and defines the energy scale for the simulations. To facilitate rapid equilibration, the masses of all united atoms are set to unity. A modified version of the LAMMPS [121, 122] MD code is used. Modifications to allow for the slightly different pairwise and dihedral potentials were made in accord with the procedure outlined in the LAMMPS manual. The Langevin thermostat maintained the temperature with a damping coefficient set to one and an integration time step $dt = 0.004$. All time results are reported in arbitrary simulation units $t^* \equiv 250dt$. Further details about the simulation model and algorithm may be found in reference [123].

The ill-defined nature of coarse-grained polymer crystal models in the early stages of ordering hinders quantitative analysis of the simulations. While crystals of small molecules and metals typically provide sharp boundaries delimiting crystalline and amorphous domains, fold surfaces (where the chains make hairpin turns to re-enter the crystal) and crystal-amorphous transition regions characterize the boundaries in polymer samples. Defects in the crystalline domains further complicate the analysis. As in experimental evaluations of semi-crystalline polymers, this leads to some ambiguity in the assignment of crystalline or amorphous domains. Nevertheless, we require a systematic metric for the percent crystallinity of the samples, as well as a measure of the number of nuclei in the sample. Rather than rely on arbitrary fixed rules or impractical manual evaluation to classify the domains and to identify the crystal nuclei, we have applied statistical learning methods. Appealing to these tools eliminates the need to fine-tune some threshold until an arbitrary standard of acceptability is reached and safeguards against introducing bias into the analysis [117].

Support vector machines [124] (SVM), a supervised learning classification technique, provides us a means to label each atom in the sample as participating in either an amorphous or crystalline domain in accord with our manual interpretation. The key idea underlying SVM is that one draws a line (more precisely, a hyper-plane) separating two classes of objects in such a way that we maximize our margin of error, the gap between the line and the closest data points (the support vectors). Typically, the systems of interest are not linearly separable in the feature space naively chosen and we must appeal to the kernel trick [125]. That is, the basic feature space picked to capture the underlying pattern is mapped into some higher dimensional space. The trick lies in the realization that we only need inner products from that space during the constrained optimization selecting the weights for the model that corresponds to the learning step. The various kernel functions mimic those products and we never have to actually visit that space [124, 125].

We trained a soft-margin SVM with a radial basis function kernel to distinguish between crystalline and amorphous domains by preparing a set of 250 samples randomly chosen from a small single crystal, multi-chain, non-periodic simulation snapshot composed of 8000 united atoms. Here, "soft-margin" means that we allow some misclassification to occur, effectively applying a regularization scheme to prevent over-fitting. The selected atom and a small number of its neighbors were graphically rendered and manually labeled as either falling within an amorphous or crystalline domain. A two-dimensional feature space described each united atom with one dimension designed to capture on-chain order and one tailored to reflect inter-stem order. Specifically, the on-chain order parameter is defined as $S_c \equiv 2\cos^2\phi - 1$. Here, ϕ is the angle between two vectors whose origins fall on a tagged united atom and extend in opposite directions along the chain backbone for three bonds. The red arrows in Figure 60 illustrate these vectors. The exact feature along this dimension used for each bead, $\langle S_c \rangle$, is defined to be the local spatial average of S_c for all united atoms further than three bonds away along the chain backbone and at a spatial distance less than $5.15/l_0$; each bead is assigned a value along this direction that reflects its neighbors' on-chain order. This counterintuitive assignment was chosen to better separate configurations due to chain persistence from those due to local spatial ordering. The second dimension of the feature space captures the inter-stem order. This is simply defined as $S_N \equiv \cos\phi_c$. As illustrated in Figure 60 (blue arrow), a vector is drawn from the end points of the two vectors used in defining the on-chain order. The angle between this vector for the selected united atom and its closest neighbor that meets the connectivity and distance constraints listed above for the calculation of $\langle S_c \rangle$ defines ϕ_c. The exact feature used for this dimension, $\langle S_N \rangle$, is the average of S_N over the neighboring beads calculated according to the same rules applied in obtaining $\langle S_c \rangle$. The training and labeling was carried out with the R statistical analysis language and employed the e1071 [126] library. Specifically, we used the "svm" function with a cost parameter equal to 50.

Figure 61 presents a map of the SVM solution with the gray area representing regions of the feature space that are assigned a crystalline tag. The non-shaded area corresponds to the amorphous region of the space. The data points superimposed on this map indicate the 250 training set points and their manually selected labels. The crystalline domains are shown in red and the amorphous in black. Note the non-linear boundary in the feature space that separates the amorphous and crystalline territories. This demonstrates the risk of misclassification associated with simply choosing arbitrary thresholds for use in labeling the beads.

Application of the SVM solution to the training set revealed an approximately 10.8% disagreement with our manual assignment of the local morphology. The majority of the contrasting labels derive from those manually tagged as amorphous. Therefore, one should expect the SVM solution to err on the side of making erroneous crystal labeling of amorphous regions. However, the disagreement can arise largely from errors in the manual classification of the atoms. Figure 62 illustrates the high precision of the SVM solution. The figure contains an image of the small simulation crystal sampled for the training set. The blue beads are those that the SVM solution tagged as amorphous and the white are assessed to be in a crystalline domain. Clearly, this mapping closely matches intuition. The fold surface is tagged as amorphous, the stems running between the fold surfaces are labeled as crystalline, and the chain segments (near the image top) that have not incorporated in the crystal are marked as amorphous. We applied this SVM solution without further modification to all of the simulations discussed below.

An unsupervised learning scheme gives us the means to separate the individual crystal nuclei in the

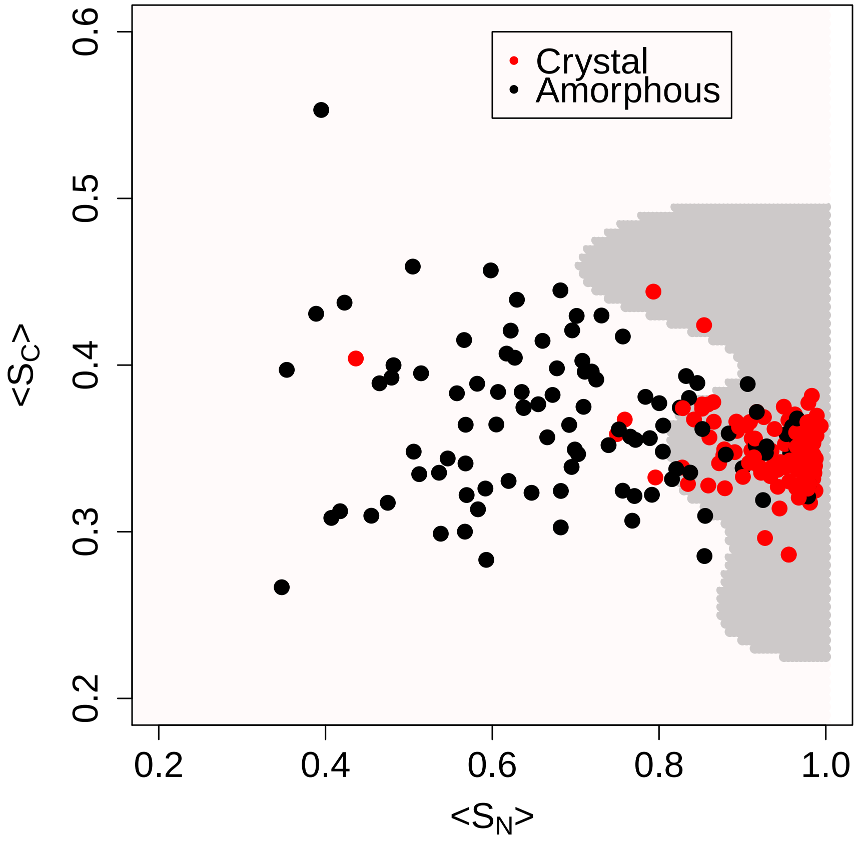

Figure 61: A map of the two-dimensional basic feature space for the training set used to parameterize the SVM employed herein to identify crystalline and amorphous domains. The black dots correspond to those points manually tagged as amorphous, while the red dots are those that were labeled as crystalline. The gray area denotes the crystalline domain according to the SVM solution.

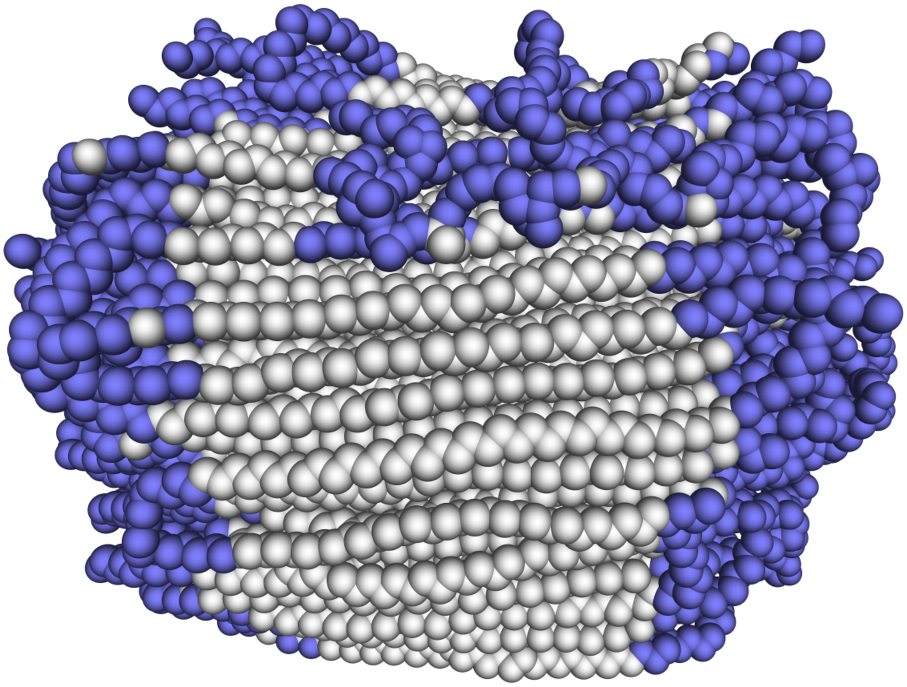

Figure 62: The snapshot of the multi-chain single crystal sampled for the training set. The blue united atoms are those that the trained SVM labeled as amorphous, while the white beads are those tagged as crystalline by the SVM.

sample. We used the DBSCAN [127] clustering algorithm as implemented in the fpc [128] R library to track the growth and size of the nuclei as crystallization progressed. We accomplish this by performing clustering on the coordinates of the atoms tagged as falling within crystalline domains. The essential concept underlying DBSCAN is that data points in a cluster must be "density reachable"; in some space they must be within a given cutoff distance of one another, and at least one of the points must have sufficient neighbors surrounding it to be labeled as falling within a cluster. We choose a search radius of $3/l_0$ and a minimum occupancy of 10. This allowed us to further filter the data such that only those united atoms that were both tagged by the SVM solution as crystalline and that fell in a cluster of at least 9 other similarly tagged atoms are counted among the crystalline domains in the analysis that follows below.

Results and Discussions

We applied the statistical learning tools to the simulations of the 1188 chain systems quenched from above the melting point to three different temperatures. As in the case of the training set, the first step to using these tools requires the calculation of the features for each united atom in the model. Application of the SVM solution obtained from the smaller crystal training set in combination with the DBSCAN clustering does yield effective discrimination of the amorphous and crystalline domains. Figure 63 presents a snapshot from a simulation with $kT/\epsilon = 9.0$ at $t/t^* = 200$. The top image contains all of the beads in the system except for a few that were filtered out by clustering from those initially tagged as crystalline. The blue beads are the amorphous set and the white belong to crystalline domains. The bottom picture more clearly illustrates the formation of crystal nuclei and the efficacy of the classification and clustering to isolate those united atoms occupying nuclei. There, only those beads tagged as crystalline and falling into clusters constrained as described above are drawn. Note that these "baby nuclei", a term coined by Muthukumar [96,97,100]for these early proto-nuclei, display a rough appearance, as suggested for a possible growth front in the pioneering work of Sadler and Gilmer [119]. We therefore proceed, assuming that this combination of classification and clustering provides a reasonable, systematic identification of the crystalline united atoms. Below, we use only those down-selected beads in the analysis of the crystalline domains that follows, rather than the complete set labeled as crystalline by the SVM solution alone. Only those tagged as amorphous by the SVM solution are included in analyzing the non-crystalline domains.

In order to evaluate the applicability of Eq. 12, we require a measure of the orientational ordering rate in the amorphous phase. The on-chain orientational order parameter S_c, as defined above, provides a useful measure for the amorphous order once averaged over all amorphous beads within the model at a given time. We therefore define $S_c^A \equiv \frac{1}{n}\Sigma_n S_c$, where n is the number of amorphous beads in the system. Estimating the instantaneous time derivative of this metric, $\frac{ds}{dt} \equiv d_t S_c^A$, demands care in treating the time-series data; the rapid fluctuations in the value of S_c^A means that a simple finite difference scheme to estimate the derivative will yield wildly fluctuating values. To circumvent this numerical issue, we used a kernel-smoothing scheme provided by the KernSmooth [134] R library to estimate the first time derivative of S_c^A. To avoid spurious results that occur near the boundaries of the time series, we dropped the first six and last six estimates for $d_t S_c^A$ from the plot and in the analysis that follows below. The rate of amorphous ordering rapidly drops and all three cases overlap. This rapid change can be attributed to a sudden re-arrangement of the rotational isomeric states for those united atoms faced with little network mobility constraints, followed by a progressive loss of mobility as competition between the beads for constraint release sets in. Following this rapid drop, $d_t S_c^A$ begins to asymptote to a smaller value for a large fraction of the simulated time. We associate this plateau value with r_s, the proposed characteristic ordering rate in the amorphous phase. Note that the profiles for all three quench depths overlap and that the specific trajectory values likely depend on the initial conditions chosen. All three simulations began from the same initial condition, permitting us to eliminate this dependency on starting condition in our analysis.

We estimated the second derivative in the percent crystallinity, $\frac{d\chi}{dt} \equiv d_t^2 \chi$ by again appealing to the KernSmooth library, as above, and dropping the first six and last six data points from the analysis.

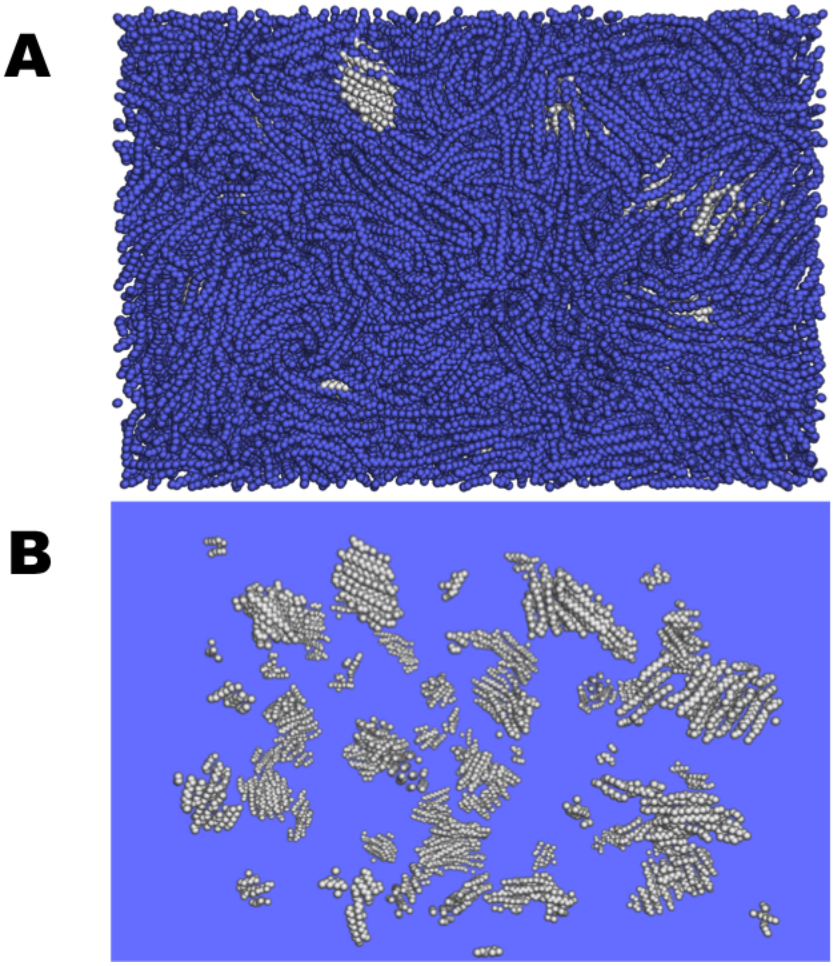

Figure 63: Snapshots from the simulation labeled by the SVM (A) and reduced with DBSCAN (B).

To test the proposed kinetics expression, Eq. 12, we plot in Figure 64 the average across all three quench depths of $d_t^2\chi$ as a function of the average of $d_t S_c^A$, multiplied by $\exp(-t/\tau)$. Though all three simulations individually displayed a similar trend as that shown, the need to specify a value for τ and r_s demanded better statistics than provided by single simulations. The overlap of the data in the early stages justifies this choice of averaging; we are interested in the rates of change of ordering and percent crystallinity, not their absolute values. We found $r_s t^* = 1.06 \times 10^{-4}$ and $\tau/t^* = 0.05$. The results clearly display the expected linear relationship over a broad range of the data, corresponding to the earliest time steps in the simulations. The noisy behavior near the origin reflects the linear growth regime where the second derivative in χ fluctuates about zero. Initially surprising, the slope, reflecting the value of α, presents a negative value. However, this must be expected since the ordering begins above r_s and decays, while the percent crystallinity initially jumps before rolling over into the linear regime. One may speculate that at longer times, when the percent crystallinity rolls over from the linear growth regime into a slower, logarithmic growth law, the slope must become positive as $d_t S_c^A$ drops below r_s.

XII.B.2 Polymer Crystallization Dynamics Under Compression

New Theory for Crystallization Dynamics Under Compression

Thus armed with a new method for analyzing the complicated morphology in simulations of semi-crystalline polymers, we may now proceed to examine the impact of mechanical insult on this class of material. Let us consider a simple mass-transport model, coupled to Kundagrami and Muthukumar's entropy barrier treatment [90] of crystal growth. Following those authors, we imagine a cylindrical crystal bundle. The top and bottom of the bundle are fold surfaces. The non-cap surface comprises the growth face. The face is surrounded by a transition region in which there is an entropic barrier to the chains attempting to attach to the growing crystal face. Placing the origin at the center of the cylinder, the lateral radius of the crystal is defined as $R(t)$ and the outer boundary of the transition region lies at $B(t)$. The concentration of monomers within the crystal is C_x and holds a value of C_m in the bulk (outside of the transition region). We will assume an isotropic velocity $\vec{V}$ moving toward the center of the cylinder. Given the cylindrical symmetry, we will employ cylindrical coordinates throughout.

The change in the local concentration as a function of time is given by the standard continuity expression: $\frac{\partial c}{\partial t} = \nabla \cdot J$. In general, $J_i = cV_i - D_{i,j}\partial_j c + c\beta D_{i,j} F_j$. Here, i and j are the coordinate indexes, β plays its usual role of the inverse thermal energy, and $D_{i,j}$ is the diffusivity tensor. The first term reflects driven mass movement. The second term captures diffusion. The third term reflects the resistance to mass transport due to an external force F_j. Deviating from the original treatment of Kundagrami and Muthukumar, we assume that the second, diffusive term is negligible over the time scales of interest here and focus on the impact of driven mass transport. The external force F_j derives from the entropic barrier, discussed below.

We will here assume that only the flux perpendicular to the growth face within the transition region plays a significant role in crystal growth. Thus, we have that:

$$\frac{\partial c}{\partial t} = \nabla \cdot J \approx \frac{1}{r}\frac{\partial}{\partial r}\left[r\left(cv_r + \beta c D F_r\right)\right] \tag{13}$$

An effective potential of mean force $\phi(r)$ determines the barrier force by $F_r = -\frac{\partial \phi}{\partial r}$. For simplicity, we assume:

$$\phi(r) = E - \frac{E}{\Delta^2}\left(r - \Delta\right)^2 \tag{14}$$

Here, $\Delta \equiv [R(t) - B(t)]/2$ and E is the barrier height. As discussed by Kundagrami and Muthukumar, E depends upon the quench depth ΔT below the melting temperature T_m. Since T_m depends heavily

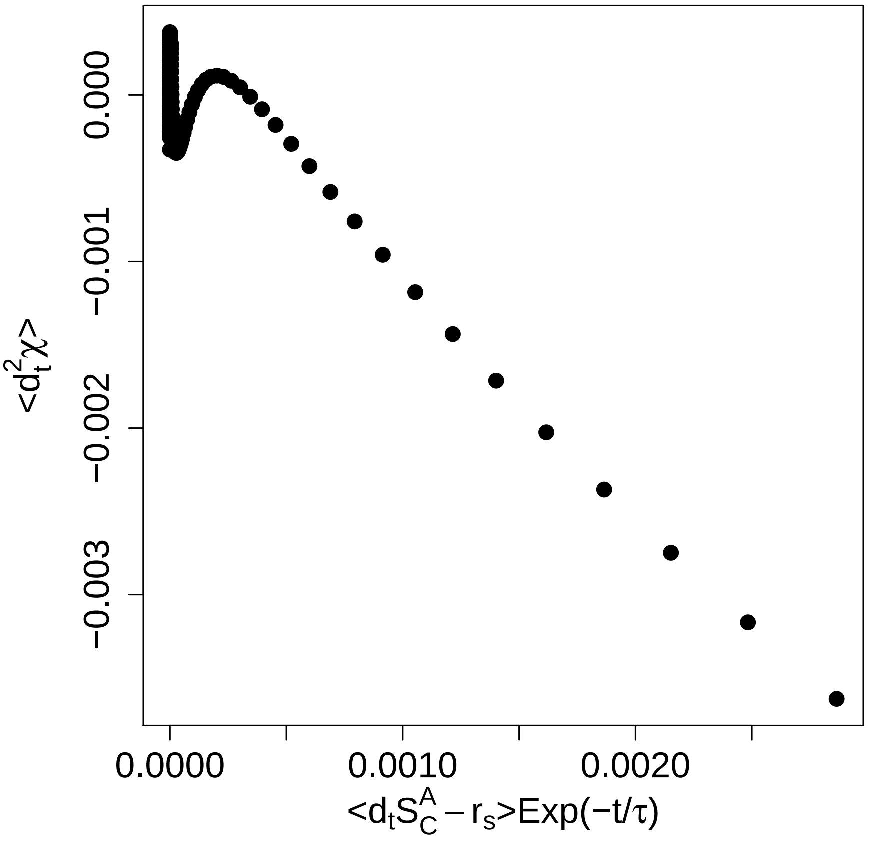

Figure 64: A plot of the average second derivative with respect to time of the percent crystallinity, $< d_t^2\chi >$, as a function of the average time derivative of the on-chain ordering rate in the amorphous fraction minus the characteristic rate from the linear growth regime, $< d_tS_C^A - r_s >$. Here, the averages are across all three temperatures simulated, and the independent variable is multiplied by an exponential decay function in accord with the proposed kinetics law given by Eq. 12. The linear dependence shown supports the validity of Eq. 12.

on the pressure which is increasing as compression progresses, E is also time-dependent. Defining $\Gamma(t) \equiv \beta D \frac{2E(t)}{\Delta(t)^2}$, we may therefore rewrite Eq. 13 above as:

$$\frac{\partial c}{\partial t} \approx \frac{1}{r}\frac{\partial}{\partial r}\left[r\left(cv_r + c\Gamma(t)r - c\Gamma(t)\Delta(t)\right)\right] \tag{15}$$

Now, assuming that the concentration within the barrier region remains fixed we may make the steady state approximation and write $\frac{\partial c}{\partial t} = 0$. Given that below we study samples being isotropically compressed, this approximation has limited applicability. However, in the early stages of compression C_x probably changes little and the concentration within the transition region must fall between C_x and C_m. Using these boundaries, applying the steady-state approximation and using the definition of Δ to eliminate $B(t)$ leads to:

$$\frac{C_x}{C_m} = \left(\frac{\Gamma(t)(R(t) - 2\Delta(t)) + v_r - \Gamma(t)\Delta(t)}{\Gamma(t)R(t) + v_r - \Gamma(t)\Delta(t)}\right) \tag{16}$$

$$\times \frac{R(t) - 2\Delta(t)}{R(t)}$$

We may now solve for how the radius of the crystallite $R(t)$ grows as a function of the time-dependent functions. We find it is given by the simple quadratic solution:

$$R(t) = \frac{-b \pm \sqrt{b^2 - 4ad}}{2a} \tag{17}$$

Here, we have defined:
$a \equiv \Gamma(t) - \frac{C_x}{C_m}\Gamma(t)$
$b \equiv 4\Delta(t)\Gamma(t) - \frac{C_x}{C_m}\Delta(t)\Gamma(t) - v_r + \frac{C_x}{C_m}v_r + \Gamma(t)v_r$
$d \equiv 4\Delta(t)^2\Gamma(t) - 2\Delta(t)v_r + 2\Delta(t)\Gamma(t)v_r$

Simulation Model and Approach

A variation of the model and analysis approach reported in Section XII.B.1 above was adopted to study isotropic compression in a model of PE. In particular, purely amorphous samples were prepared by filling a periodic box with 1188 chains with 200 united atoms each at a relatively low density. The chains were then relaxed at $kT/\epsilon = 15$ for 1,500,000 time steps. Next, the box was isotropically compressed to a density equal to that of amorphous polyethylene at ambient pressure with $\rho = 0.853 g/cm^3$ over an additional 1,500,000 time steps. The box volume was then held fixed and the chains allowed to relax an additional 500,000 time steps. Boxes with higher density were built iteratively on the resulting configuration from this simulation by further compressing the volume over 1,500,000 time steps and relaxing at fixed volume for 500,000 time steps (viz. the result of each compressed box equilibrated at $kT/\epsilon = 15$ served as the starting point for the next denser model). The same SVM trained for the non-compressed samples reported in Section XII.B.1 aided in the analysis that follows.

The snapshots in Figure 65 below represent typical compressed states at different densities. The volume changes from that corresponding to the ambient density for polyethylene, V_0, according to $V = V_0(0.91)^\gamma$. From top to bottom, $\gamma = 0, 1, 2, 3, 4$, and 5. The initially amorphous phase clearly undergoes substantial crystallization as the density increases, even though the temperature lies well above the melting point for the model at ambient pressure. Figure 66 illustrates the true utility of the statistical learning approach developed in Section XII.B.1, demonstrating the SVM's facile ability to extract crystalline domains from the highly heterogeneous compressed samples.

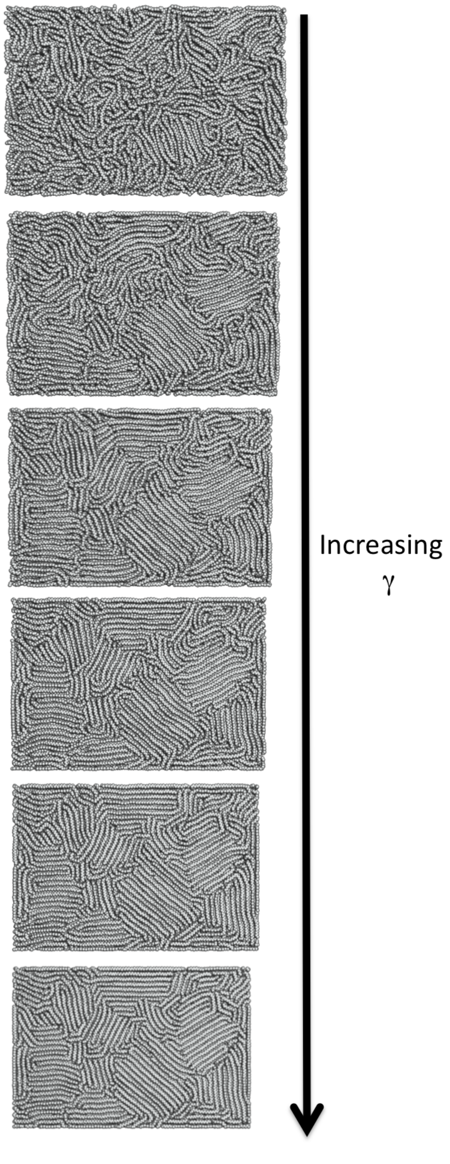

Figure 65: Compression sequence snapshots from the simulations.

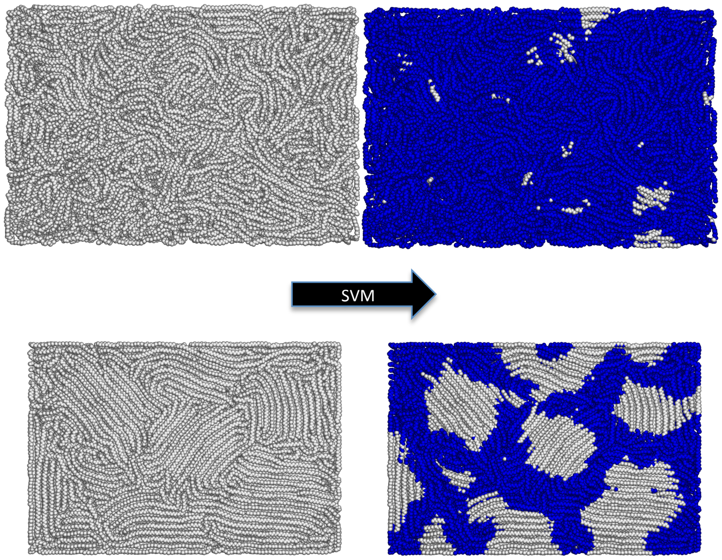

Figure 66: Simulation snapshots labeled with the SVM. Top, $\gamma = 0$. Bottom, $\gamma = 3$.

Results and Discussions

During the course of the simulations across all compressions, the pressure was monitored. Surprisingly, the simple Tait equation of state (EOS) expression proved to capture the pressure-volume relationship, even through the transition across the melt-line where the melting temperature drops below the simulation temperature between values of V_0/V of 1.0 and 1.1. Figure 67 illustrates the fidelity of this EOS to the data. Here, the simulation data was fit to the Tait expression $P = (exp(-(V/V_0 - 1.0)/0.0894) - 1) * 0.005$.

The number of distinct crystalline nuclei in the material provides the key to understanding the development of network-like structure during compression. Using the combination of the SVM and DBSCAN described above, we extracted this information, as presented in Figure 68. Surprisingly, during the initial stages of compression (at low V_0/V), the number of nuclei grows linearly. This is the analogous behavior one observes in simple quench experiments without compression; here, V_0/V appears to play the role of time. Unlike the quench experiments, however, the number of nuclei quickly reach a maximum and then begin to drop in number as the distinct crystalline regions begin to merge.

Changes in the percent crystallinity upon compression are reflected by variations in mechanical properties, as well as the materials' thermodynamic response as discussed elsewhere in this report. To track this morphological change and to test the theory, the statistical learning tools were used to quantify the total number of united atoms participating in crystalline domains. Figure 69 illustrates these findings. One notes that, again, V_0/V appears to play the analogous role of that time plays in the simple quench studies. At low compressions, an induction period during which the number of nuclei quickly rise is followed by a linear growth law for the percent crystallinity χ. At higher compressions, the rate of change in χ rolls over and drops to zero, suggesting that the material has become kinetically frustrated and that no further amorphous chain segments may travel to growing crystal faces.

To test the theory described above, χ was estimated by modeling the growth of each nuclei identified in Figure 68 and summing the total crystalline mass. This was done by fitting the expression for the growing crystal radii with eight parameters, five of which were required to model the change in the melting temperature with pressure. Though, in principle, one could obtain this latter relation-

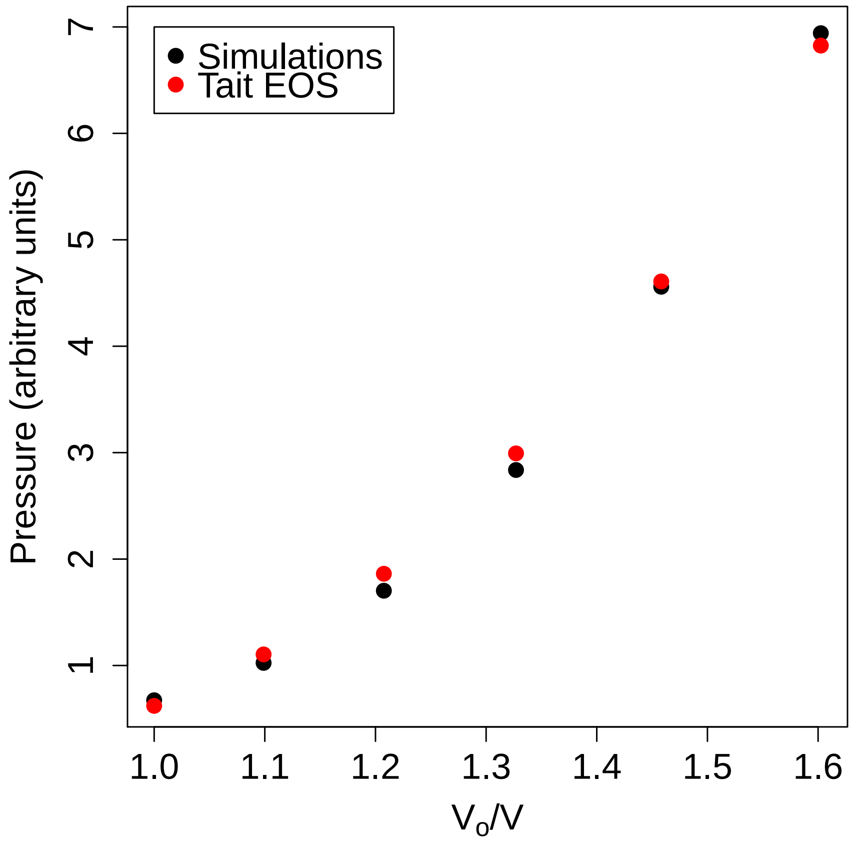

Figure 67: The pressure of the simulated material as a function of V_0/V. The black circles represent the simulation values. The red circles are those obtained by fitting the Tait expression.

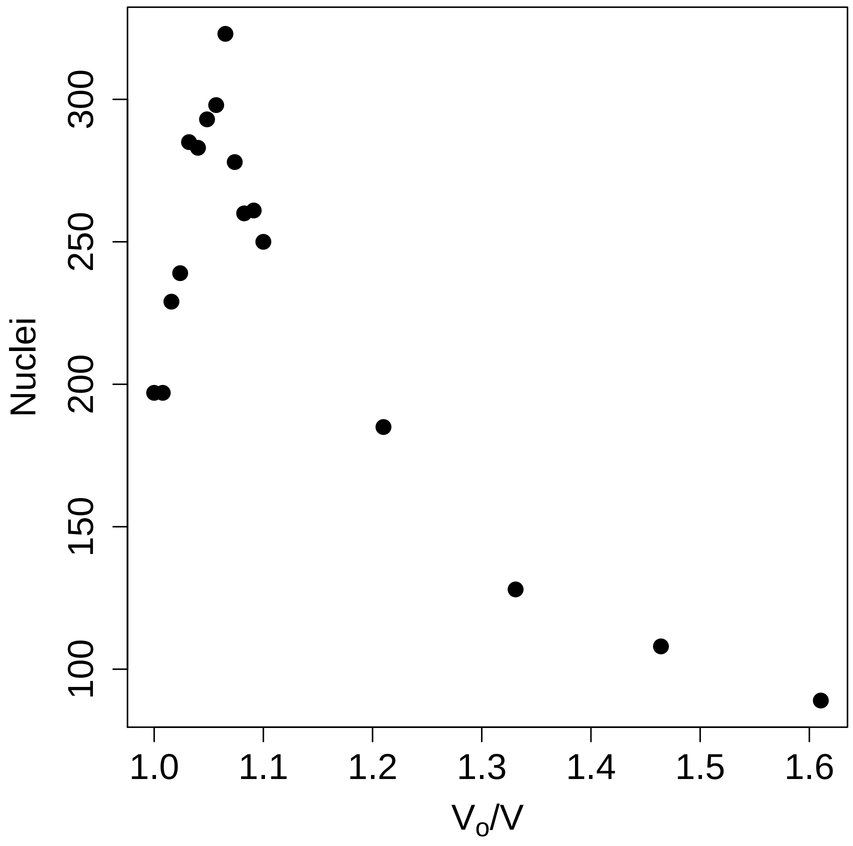

Figure 68: Number of nuclei in the material as a function of V_0/V.

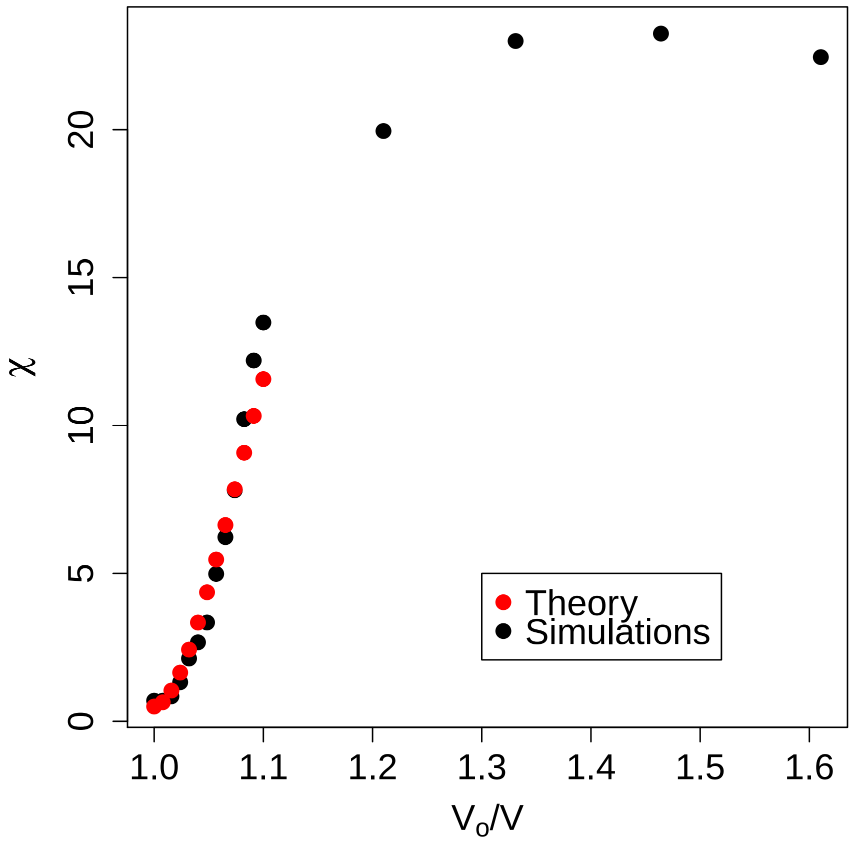

Figure 69: The percent crystallinity in the simulated material. The black circles represent the simulation results. The red circles represent the fit to theory.

ship computationally (or experimentally for real systems), the computational cost for this becomes prohibitive since a much smaller discretization in time is needed upon heating the compressed models for the simulations to remain stable. Nevertheless, the fit presented by the red circles show that the simple theory holds promise.

XII.B.3 Network Theory for Polymer Damage and Recovery

Introduction to the Challenges of Modeling Damage in Polymers

Though the theoretical and computational methods developed in the sections above provide new approaches for predicting morphological evolution in semi-crystalline polymers, new advances in linking that morphology to macroscopic properties are needed. Predicting the macroscopic mechanical response of polymeric solids based on the underlying material structure remains an elusive problem, even after many decades have passed since the development of the earliest molecularly-aware theories. Rather than applying a detailed evaluation of structure at either the micro- or meso-scopic length scales, in practice, one often resorts to using toy mechanical models that suffer from a proliferation of coefficients and are disconnected from the underlying molecular picture. Though much effort has been invested in capturing the rich phenomena at the molecular scale [136–138], including chain conformational statistics, chemical and physical cross-linking, and entanglements, we still lack a satisfactory means to pass that information up to the macroscopic length scales [139]. This problem becomes more challenging when damage occurs during the use of the material and is especially relevant to the emerging field of self-healing materials [140–142], in which the mechanical characteristics evolve with time as the result of molecular processes.

Here, we propose that developments in graph theory that are finding broad application in the arena of information science [143–145] may provide a systematic means to encode specific structural details and to do so in a manner cognizant of the relative importance of different portions of the material. This latter trait should prove especially useful in evaluating the robustness of a given material in a specific application. Moreover, these developments also provide a means to capture the network details in a reduced order model.

Eigenvector centrality [146] and its variants find use in such diverse information science applications as contemporary search engines [143] and community identification [144,145]. It is especially useful in ranking the importance of each node in a network based not only on its own functionality or degree, but also on the connectivity of its neighbors. To gather this information, one need only find the principle eigenvector of the adjacency matrix for the network. That is, one finds the eigenvector with the largest eigenvalue for the matrix that has non-zero element entries for pairs of nodes that are connected (when represented in the natural basis of node-identity). The relative value of the elements of the eigenvector indicates the relative importance that the corresponding node holds in the network. In the context of academic papers, this may highlight those articles that hold the most impact in a given scientific community. In the context of polymers, we postulate that network importance ranking can inform models of mechanical response. While the application of graph theory ideas to polymer mechanics has a long history [147], the application of centrality appears not to have been previously explored.

The adjacency matrix $\hat{A}$ provides a table denoting which nodes in the network are linked. For example, $\hat{A}$ for a linear chain whose nodes are numbered consecutively with node identification number n ranging from 1 to N is given by $A_{i,j} = \delta\left(j-(i+1)\right) + \delta\left(j-(i-1)\right)$ when using the node identification as the basis. The principle eigenvector $\vec{e_1}$ holds the importance ranking of each node within the network. It has unit magnitude, but its elements do not sum to one. The eigenvalue λ is the maximum of either the importance-weighted average degree of the network or the square root of the largest value of degree found within the network [154]. Thus, it is a measure of the functionality of the most important nodes and encodes the relative quantities of different kinds of bonds in the network.

New Theory for Damage in Polymers

We construct a simple statistical mechanics model to exploit these characteristics via the following *ansatz.* Let us define an importance operator $\hat{\imath}$ that is represented in the $\vec{n}$ basis as a diagonal matrix with elements that are simply those of $\vec{e_1}$. Since the elements of $\vec{e_1}$ provide the relative importance of each node in the network, we associate $\vec{e_1}$ with a distribution function that partitions importance within the graph. Note that importance means the relative contribution that a node makes to the network in the sense of its connectedness to other nodes; in short, high importance means a node is connected to many other nodes that are also highly connected. Thus, the trace of $\hat{\imath}$ may be associated with a partition sum $Z \equiv Tr\left[\hat{\imath}\right]$. We also identify an underlying Hamiltonian operator $\hat{H}$ such that $Z = Tr\left[\exp\left(-\Gamma \hat{H}\right)\right]$. Here, Γ is the inverse of the Lagrange multiplier that enforces average degree in the network and is the analog of the inverse thermal energy. We propose that this multiplier is proportional to the probability for any two nodes to form a link, P. Within this framework, we define a network free energy $F \equiv -P\log(Z)$.

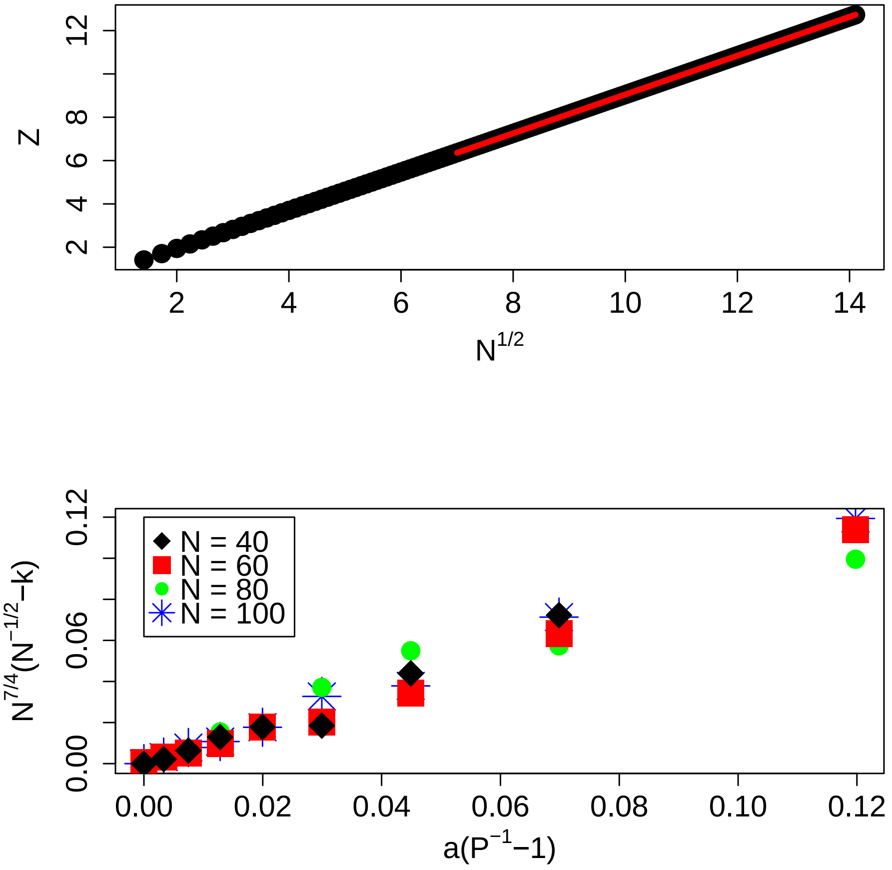

Figure 70: The top plot contains the partition function Z as a function of the square root of the number of nodes in a linear graph as calculated by direct evaluation of all of the eigenvectors and eigenvalues. The black circles represent the calculated values, while the red curve is a fit illustrating the proposed $N^{1/2}$ dependence. The bottom plot is the ensemble average value of the elements of the principle eigenvector for random networks as calculated with the power iteration method cast in a form of the proposed model that collapses the data, capturing variation in both P and N. The data derives from random networks with values of P spanning 0.2 to 1.0 and values of N ranging from 40 to 100.

Linear chains provide insight into how to link the Young's tensile modulus E to this free energy. Numerical interrogation of a number of linear graphs reveals that the partition sum is well approximated by $Z \approx \frac{2}{3}\xi\frac{N^2-1}{N}$. We also find that the value of the scale parameter may be approximated by $\xi \approx 1.48 \times 10^{-3} + 1.39N^{-1/2}$ over the range tested herein. If the exponent of $-1/2$ varies at higher values of N, the prefactor merely changes in the following analysis leading to Eq. 18. Recall that P is the ratio of the number of bonds formed in the network to the number possible. In the linear case, we have $P = 2(N-1)/(N^2-N)$. Thus, in the large N limit, $Z \propto N^{0.5}$, $P \propto 1/N$, and $F = -P\log(Z)$ decays as $\log(N)/N$. See Figure 70 (top), which contains a plot of Z versus $N^{1/2}$ for the linear chain case. Now, for linear chains the modulus E drops as $1/N$ [155]. We therefore predict that the modulus is related to the network free energy by Eq. 18, the guiding hypothesis for our analysis.

$$E \propto -F/\log(N) \tag{18}$$

Random networks (Erdös - Renyi graphs [156]) provide a more realistic model for real polymeric solids and have been applied in the past to describe both the onset of a percolated structure [157,158], as well as to capture the thermodynamics of elastomers [147]. Consider a set of N junctions that form links with any other junction with probability P. Here, one does not expect that the node identification number plays a role. Rather, $e_1(n) \equiv k$, a fixed constant with an average value that varies with P and N. From numerical interrogation of networks composed of $N = 40-100$ junctions and $P = 0.2-1.0$, we find that $k = -aN^{-7/4}\left(P^{-1}-1\right) + N^{-1/2}$. See Figure 70 (bottom), which contains a plot of $N^{7/4}\left(N^{-1/2}-k\right)$ versus $a\left(P^{-1}-1\right)$. Here, a is a numerical constant approximated by $a \approx 0.03$. The partition sum then becomes $Z = Nk = N^{1/2} - aN^{-3/4}\left(P^{-1}-1\right)$.

We assume that the junction density is fixed and that the volume of the solid grows as N. Applying the relationship between E and F above, Eq. 18, yields: $E \propto P\log(N^{1/2} - aN^{-3/4}\left(P^{-1}-1\right))/\log(N)$. Since $aN^{-3/4}\left(P^{-1}-1\right)$ is always small, one may further simplify the prediction for E by expanding the logarithm of Z to find that $E \propto P/2 - a\left(1-P\right)/\left(N^{5/4}\log(N)\right)$. Thus, the model predicts an N (or size) dependence for E only for very small networks, as expected.

The connection to classical rubber elasticity theory may be made clear by making explicit the connection to cross-linking density. In the classical theory, the modulus varies directly with the number of cross-links per unit volume, X. This may be approximated as $X \propto PN/V \propto PN/N$, where V is the sample volume. Thus, we find that $E \propto P \propto X$. That is, for a fixed network density, the application of eigenvector centrality and the hypothesis that Eq. 18 holds predicts that the modulus varies directly with cross-link density, in accord with classical models [138].

To illustrate how heterogeneity impacts the modulus and how to encode it in the proposed scheme, consider a modification to the random network constructed as above. Let there be a ninety percent chance that a given link is "weak" in the sense that it contributes less to the network structure, while the remaining ten percent are "strong." This may mimic, for example, a network composed of physical cross-links (weak) and covalent cross-links (strong). We encode this weakness in $\hat{A}$ by assigning a value of 0.1 rather than 1.0 to the entries for the weaker edges. Numerically estimating the modulus E confirms that this quantity is linear in P for both cases. However, both the homogeneous and heterogeneous networks produce trends that fall nearly upon one another; F only provides insight into the global organization of the network (i.e. random versus ordered), but does not probe details at the micro-structural level. The eigenvalue λ, presented in Figure 71 (top), does capture the variations due to heterogeneity; it captures microstructure. Now, λ is a measure of the importance-averaged degree in the network and is, thus, proportional to PN. Therefore, this formalism provides a direct means to pass specific mesoscale structure up to the macro-scale.

Materials often experience changes in their mechanical properties during their lifecycle [159,160]. Changes such as mechanical chain scission [141], chemical degradation [161,162], and morphological rearrangement [137] that result in the loss of macroscopic material properties are often grouped under the rubric of "damage." Quantifying and predicting these changes based on the micro- and mesoscopic pictures presents a serious challenge when modeling specific materials. Though an active area of research reported in the literature [163], we still lack a robust mathematical definition for damage that goes beyond noting changes at the macroscopic length scale. Here, we propose such a metric and illustrate its application.

Defining a new measure of damage follows from a straightforward extension of the two observations above: i) F captures information about how the network was prepared (random, ordered, etc.) and provides a link to E and ii) λ captures the micro-structural details and plays a role in the prefactor, discussed below. For a homogenous network, one may simply define a rate of damage as the change in F with change in P. This will be characteristic of the particular network type and will predict variations in E in the homogeneous case. This, however, fails to capture the micro-structural details that play a role in damage in real, heterogenous materials. Rather, we define two damage rates, one that captures network class and one that captures microstructure. Though F is insensitive to the particular details of how P is changed, λ does vary with P in a manner that depends upon the specific mode of link deletion employed. For example, consider a heterogeneous network like the one described above, beginning with $P = 0.5$. Figure 71 (bottom) presents two scenarios, the case in which the deletions are carried out randomly and the case in which deletions are performed only on the "strong" links. The latter scenario may correspond to, for example, the case of chemical degredation of the covalent bonds. Clearly, λ falls much more quickly as a function of P in the case where only the strongly contributing bonds are removed.

We therefore propose a new damage model. First, we introduce a function Ψ to complete the equality between E and F. It is dependent on $\lambda/(PN) - \Lambda$ in order to preserve the scaling relied upon to arrive at Eq. 18 and a numerical prefactor that absorbs the $log(N)$ term (discussed further below in the context of the model's application). We further assume that Ψ is a power law, giving Eq. 19 as our final model form.

$$E \equiv \Psi F = exp(b)\left(\frac{\lambda}{PN} - \Lambda\right)^{m} F \tag{19}$$

The new parameter Λ is the value of λ/PN upon the formation of a percolated network, while the prefactor $exp(b)$ and exponent m are free fitting parameters that capture the chemical details. Next, we define a global damage rate defined as $\delta F \equiv \frac{dF}{dP}$ and a microstructure damage rate $\delta\lambda \equiv \left.\frac{d\lambda}{dP}\right|_M$. Here, the suffix "M" implies that the links are deleted in a specific fashion or mode (e. g. randomly chosen, only those of a certain class, etc.). Combining these two terms yields a total damage rate measure suitable for predicting the trend in E under a given mode of link removal:

$$\delta E \equiv \left(F \left.\frac{d\Psi}{d\lambda}\right|_M \delta\lambda + \Psi \delta F \right) \tag{20}$$

Clearly, if Eq. 20 does not vary with λ under the mode of link deletion, then the variation in E resides entirely in the second term. One expects that this is true when bond deletion occurs randomly rather than targeting specific link categories. For example, the slope for the heterogenous case in Figure 71 (top) is identical to that for the random case in Figure 71 (bottom) in which all bonds are randomly deleted; one does not expect that the prefactor changes as a function of cross-linking if the relative proportion of the junctions, weak to strong, remains fixed. That is, there is a variation in Ψ only if the ratio of $\lambda/(PN)$ changes. The random deletion case, in which $\lambda/(PN)$ remains fixed is illustrated by the "Random" line for one specific ratio of "strong" to "weak" in Figure 71. The "Strong" line corresponds to how λ varies with P under a non-fixed ratio of linkage types. These slopes correspond to variations of two different functions; that found in the prefactor Ψ and that in $\delta\lambda$, respectively.

Application to Self-Healing Poly(dimethyl siloxane) Data from the Literature

The recent study by Bao and coworkers [164] provides an excellent test application for this model, since their polymer structure is well defined, the cross-linking density is controlled, damage is induced,

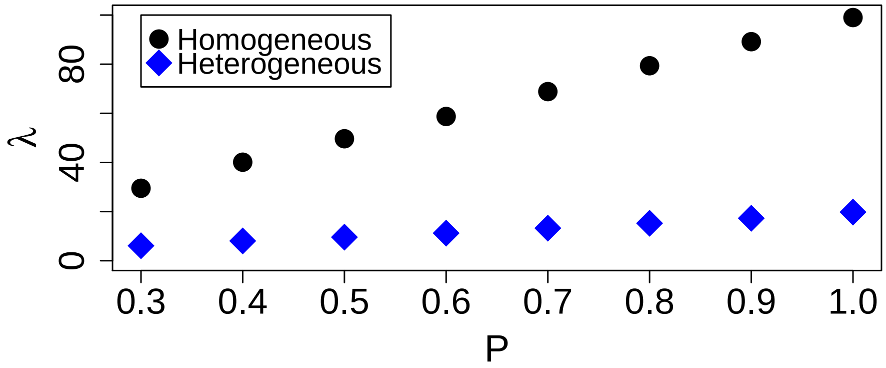

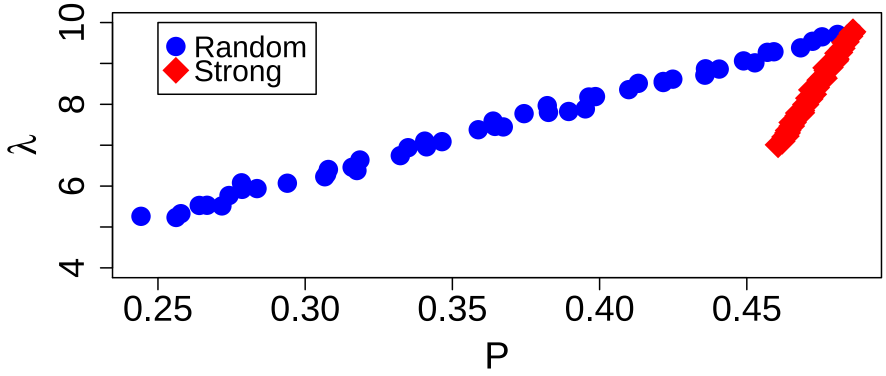

Figure 71: The top plot contains the principle eigenvalue λ as a function of bonding probability P for example homogeneous and heterogeneous networks. The bottom plot contains λ for a heterogenous network under two different modes of link deletion as a function of P. Initially, the network is composed of a ratio of 9-to-1 links with weights 0.1 and 1.0. At construction, $P = 0.5$. The mode labeled "Random" involves the random selection of links for deletion. The mode labeled "Strong" corresponds to deleting only links with weight equal to 1.0.

and the nature of the entanglements are well understood for their chemistry. Those investigators prepared a self-healing elastomer composed of chain-extended poly(dimethyl siloxane) (PDMS) linked by moieties (2,6-pyridinedicarboxamide, or H2pdca) that act as ligands in iron complexes. Each of their chain-extended threads had roughly nineteen iron binding sites and eighteen runs of 6,000 g/mol PDMS. To these threads, they added $FeCl_3$, which undergoes ligand exchange to form bonds with the polymer threads (via the H2pdca sites) to form a cross-linked network. They demonstrated that the elastomer thus prepared suffered damage upon elongation followed by subsequent healing, supporting the idea that the polymer-iron-polymer bonds were broken and re-formed. The cross-linking density was varied by changing the ratio of the iron-binding sites to the amount of $FeCl_3$ added to the material.

The essential step in applying the proposed model to this material lies in generating an ensemble of random adjacency matrices that conform to the known facts about the material. We build this ensemble based on a coarse-grained model of the polymer threads: each thread is composed of nineteen iron-binding sites and eighteen potential PDMS entanglement sites, with the two site types alternating along the chain backbone. If we assume a mono-disperse collection of threads, then we know that there are well-defined static covalent bonds in the system. We give those bonds a weighting of 1 in every realization of $\hat{A}$. We also know that there should be on average nine entanglement sites per thread, since the entanglement molecular weight of PDMS is roughly 12,000 g/mol [165] and the total molecular weight of the threads is about 108,000 g/mol. Thus, each entanglement site forms a bond with another such site with probability of a half. Those bonds are assigned a weight of 0.1 in $\hat{A}$, reflecting the physical intuition that entanglement plays a lesser role in determining the modulus of the system. More on this choice follows below. Finally, we also have some knowledge of the probability for forming a polymer-iron-polymer bond for a given stoichiometric ratio of ligand to iron. Roughly speaking, each thread must have about two polymer-iron-polymer bonding sites at the onset of a percolated network. This is rough since some chains may be part of the network but form dangling ends, while other chains that satisfy this criteria may be bound only intramolecularly. Given this, examining Bao's data, we estimate that the $FeCl_3$ is only 50% efficient in forming cross-links, since one would need $\frac{1}{2}\frac{2}{19} \approx 5\%$ $FeCl_3$ upon network formation, while extrapolating the data to zero modulus indicates that the threshold value is closer to 10%. The factor of a half reflects the fact that each polymer-iron-polymer bond has one iron per every two bound polymer sites. That the efficiency is less than one comports with the physical expectation that not every iron finds two polymer ligand sites due to kinetic frustration. Thus, each iron-binding site has a probability $P_f \approx 17\%$ of forming a polymer-iron-polymer bond for the scenario in which one $FeCl_3$ molecule is added for every six iron-binding sites (i.e., 1:6 Fe:Hpdca-PDMS), the lowest ratio reported by Bao. To those sites, we assigned a weight of 0.99 in $\hat{A}$. We choose a representative sample size of sixty chains to generate an ensemble of one thousand independent realizations of $\hat{A}$ within this picture, generating average values for F and $\lambda/(PN)$. This choice, as well as the choices for the weights, set the scale for the two fitting parameters reported below; nevertheless, once these choices are made, quantitative predictions regarding the changes in the numbers of bonds may be calculated. The assignment of the weights for more general problems merits further study. However, for the particular problem and material that we have studied herein, the weights can be arbitrarily set. This is true because we are breaking only one type of bond (polymer-iron-polymer), and those bonds also set the percolation threshold. A straightforward calculation provided in the Appendix of reference [166] demonstrates that changing the weights only impacts the magnitude of the prefactor fitting term in Ψ.

We note that we make no assumptions regarding affine deformation or spatial heterogeneity. Heterogeneity is captured with the numerical evaluation of the eigenvector and eigenvalues. That is, statistical variations across the network are accounted for if they are encoded within the adjacency matrix. To consider something that is strongly heterogeneous spatially, such as a gradient in cross-linking density across a sample, requires modification of the actual numerical simulations of the networks. This can be done by building correlations into the connectivity of the graph. The basic theoretical model, however, is capable of capturing strong heterogeneity.

The details of the algorithm employed herein to both fit the model and apply it to estimate the

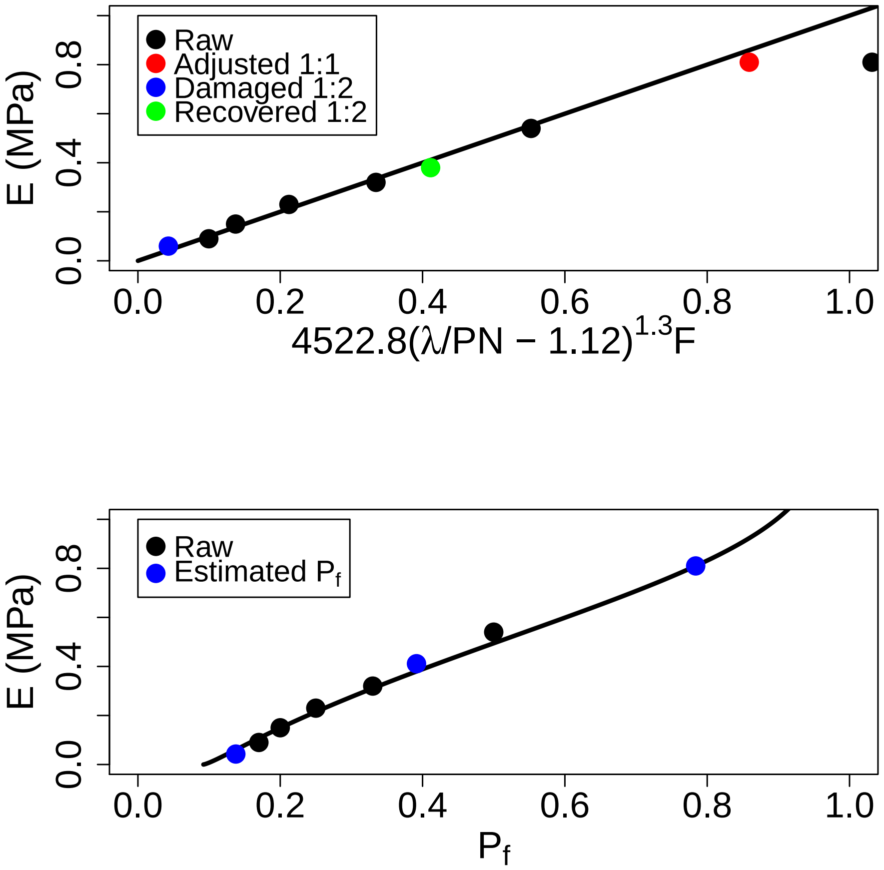

Figure 72: Data taken from Bao *et al.* The top plot contains the experimental modulus as a function of the two-parameter fit to the theory. The colored circles indicate where we invert the model to predict the value of the fraction of cross-linker bonds formed P_f. The red circle is the outlier point adjusted with a more realistic value of P_f. The blue is a damaged sample and the green is the same sample after one hour of recovery. The bottom plot shows the modulus as a function of P_f and the fitted theoretical curve.

unknown values of P_f for damaged samples are given below. Note that three functions are used to invert the model so that P_f may be found for a given value of the modulus and one function is used to extrapolate the value of Λ. These functional forms are motivated by examination of the data rather than any theoretical considerations. The former three are simple functions that fit the numerical data and whose estimates are ultimately checked for consistency in step 6. The latter function is a straightforward linear interpolation. The fit coefficients (a, b, c, and m) are given subscripts indicating in which step they are calculated. The algorithm follows.

1) Construct network models for the values of P_f of interest and perform the centrality calculation: a) Randomly assemble 1000 independent adjacency matrixes for a given value of P_f, b) use power iteration to estimate the principle eigenvalue λ and eigenvector for each realization, c) calculate the partition sum Z, and d) estimate $\langle Z\rangle$ and $\langle\lambda\rangle$ where the averages are across the 1000 samples.

2) Estimate the value of Λ, that is, $\lambda/(PN)$ at the percolation threshold of $P_f = 0.05$: construct a linear fit for $\lambda/(PN) = m_2P_f + b_2$ for the smallest four values of P_f considered and use the fit parameters m_2 and b_2 to calculate Λ.

3) Fit the experimental moduli values for all the non-strained samples (except that corresponding to the highest iron concentration) to the model using the values of $\langle Z\rangle$ and $\langle\lambda\rangle$ as the independent variable: construct a linear fit to $\log\left(E/\langle F\rangle\right) = b_3 + m_3 \log\left(\langle\lambda\rangle/(PN) - \Lambda\right)$, where $\langle F\rangle$ is calculated from $\langle Z\rangle$.

4) For a sample with unknown P_f, construct an estimate of the sample's PN/λ (note that this quantity rather than its inverse is modeled as a matter of numerical convenience): a) fit $PN/\lambda = a_4\left(b_4 + \exp(-c_4F)\right)$ for the full range of values calculated in step 1 and b) find the value of F (and, thus, PN/λ) that minimizes the squared difference between the target modulus E^* and the model, using the fit in step 4.a - that is, minimize $[E^* - F\exp(b_3)\left(\lambda/(PN) - \Lambda\right)^{m_3}]^2$ over F with $\lambda/(PN)$ dependent upon the value of F via the fit in step 4.a.

5) For a sample with unknown P_f, estimate this value using the resulting value of $\lambda/(PN)$ from step 4: Construct a linear fit across all values simulated in step 1 above for $\log(P_f) = m_5\log(\lambda/(PN)) + b_5$ and use it to estimate P_f for the unknown.

6) For a sample with unknown P_f, validate the estimate from step 5 by following the procedure in step 1 to more accurately estimate the values of $\langle Z\rangle$ and $\langle\lambda\rangle$ for the sample and to place it on the curve with the known samples.

Working within the model described above by Eq. 19 and the enumerated algorithm, we find that $E \approx 4522.8(\lambda/(PN) - \Lambda)^{1.3}F$ for this system when the five lowest concentrations of iron are considered. The value of $\Lambda \approx 1.12$ is found by estimating $\lambda/(PN)$ for the case of the probability of forming polymer-iron-polymer bonds $P_f = 0.05$. Figure 72 (top) plots Bao's data in units of MPa in black circles as a function of this fit. The line is the ideal relationship. Note that the value excluded from the fit, that is, the black circle data point with the highest modulus value, falls well off the trend line. This data point corresponds to Bao's 1:1 Fe:Hpdca-PDMS sample, a stoichiometry that should match one iron to two ligands (if the assumed efficiency described above is correct) and could, in principle, result in all ligands participating in polymer-iron-polymer bonds. Clearly, however, this is physically improbable, since kinetic effects will always prevent the complete formation of all of the possible bonds in the system. We may calculate the true fraction of bonds formed at this saturated concentration by inverting the relationship between the modulus and bonding probability P_f. This leads to an estimate of $P_f \approx 79\%$ for this iron concentration. Calculating an ensemble of adjacency matrices with that value produces the value along the horizontal axis for the red circle in Figure 72 (top). Following the same procedure, we estimate the values of P_f for the case of the second highest iron concentration considered, the 1:2 Fe:Hpdca-PDMS sample, after damage induced by elongation to 1500% strain. The stress-strain curves immediately following the strain and after a one-hour recovery period were presented by Bao. From those curves, we estimate the corresponding values of the modulus. Given that data, we estimate that $P_f \approx 14\%$ immediately after the 1500% strain and $P_f \approx 39\%$ after one hour of recovery. Remarkably, given an original $P_f = 50\%$, that translates into an 72% loss of iron cross-links after the damaging strain measurement with a subsequent recovery to a 22% loss after one hour. Experimental validation of our analysis and tracking of the recovered bond fractions as a function of time could provide interesting insight into the self-healing process. Figure 72 (bottom) presents all values of the modulus as a function of bonding probability, illustrating the overall dependence of the tensile properties on that parameter as captured by the model presented herein. Finally, we note that we employed an estimate of the efficiency of cross-linking by the $FeCl_3$ (50%) in the analysis above. Experimental determination of this efficiency would improve the fidelity of our predictions for P_f. We varied this value from 45% to 55% and found that both the exponent m and percolation threshold value Λ were insensitive to this choice. However, the prefactor $exp(b)$ obtained values of 3816.6, 4522.8, and 3675.5 for efficiencies of $45\%, 50\%$, and 55%, respectively. Similarly, P_f for the 1:1 Fe:Hpdca-PDMS sample varied as $74\%, 79\%$, and 91% for those efficiencies. The same quantity for the 1:2 Fe:Hpdca-PDMS sample immediately following damage presented values of $12\%, 14\%$, and 14%, while the recovered sample displayed values of P_f equal to $35\%, 39\%$, and 45%. The analogous plots to Figure 72 for those other cross-linking efficiencies are available in the Supplementary Information of reference [166].

XIII GAP Modeling (*Clements*)

XIII.A Introduction

This section is a review of the Glassy Amorphous Polymer (GAP) model, which is a critical part of this Level 2 (L2) Milestone on the modeling and characterization of HDPE and UHMWPE. GAP was developed [1] to address well-known failings of existing polymer models, the primary one being a lack of versatility across the wide range of conditions that a polymer might experience in DOE and DoD applications. In developing the model, the most surprising feature that arose was the necessity of a non-equilibrium component to the volumetric response in order to match both low-rate experimental data and high rate shock data. While viscoelasticity is highly anticipated in the deviatoric (shear) response, this was not the case for the volumetric part of the free energy. In this L2, both HDPE and UHMWPE are the focus materials. In the original work of Clements [1], only PMMA had sufficient data to near completely calibrate the model. Section XIII.B contains a brief discussion of the thermodynamic theory embodied by the GAP model. An important part of this L2 report is to convey to fellow theoreticians and experimentalists the required knowledge to parameterize the many parts of the GAP model. Thus, sufficient discussion will be devoted to model calibration. Discussion (not found in-depth in text books on polymers) on viscoelasticity and calibration is provided in Section XIII.C. The wide-ranging and accurate plasticity model developed for GAP is novel, and is described in Section XIII.D. Again, enough discussion is devoted to the (nontrivial) calibration of the plasticity model. Sections XIII.C and XIII.D rely heavily on the stress-strain measurements of Cady, *et al.* described in Section VI above. Section XIII.E provides a discussion of the EOS used by GAP. The theory is based on an empirical Gibbs free energy that uses heat capacity data of Welch, *et al.* outlined in see Section X above, phase information provided by Dattelbaum, *et al.* and dilatometry data of Zoller, *et al.* The shock experiments detailed in Section VII were critical to the calibration of the entire volumetric response (thus extending the theory to high rates of deformation) and this is described in Section XIII.F. Volumetric and shear damage incorporated in GAP is then highlighted in Section XIII.G. Damage calibration experiments used in this work were Taylor impact tests conducted by Cady and Clark, as well as Dynamic Tensile Extrusion performed earlier by J. Furmanski, *et al.* [14, 191]). Brief discussion of these experiments and simulations are also provided in Section XIII.G. Finally, an important point is that different calibration of GAP parameters can be found to give reasonable agreement with all the aforementioned experiments. Thus, Section XIII.H is devoted to illustrate this point. The implication is that more experiments are required to help refine parameterization. Brief conclusions are provided in Section XIII.I.

XIII.B Thermodynamic Theory

In this section information on essential GAP equations is provided [1]. The model is based on a non-equilibrium Helmholtz free energy, which obeys thermodynamic consistency up to several articulated caveats. Our ansatz for the specific Helmholtz free energy is a sum of equilibrium and non-equilibrium terms

$$\rho a(\epsilon_v^E, e_{ij}^E, T; \{\dot{\epsilon}_v^E, \dot{e}_{ij}^E, \dot{T}\}) = \rho a^{(0)}(v, e_{ij}^E, T) + \frac{1}{2}\left(\sum_{n=1}^{N} \frac{s_{ij}^{(n)} s_{ij}^{(n)}}{2g^{(n)}} + \sum_{m=1}^{M} \frac{p^{(m)} p^{(m)}}{B_T^{(m)}}\right) \tag{21}$$

where $a^{(0)}(v, e_{ij}^E, T)$ is the equilibrium specific Helmholtz free energy and the second term is our approximation for the non-equilibrium contributions to both deviatoric and volumetric components of the free energy. There are $n = 1, ..., N$ deviatoric and $m = 1, ..., M$ volumetric *elements* in the model, respectively. Here $v = 1/\rho$ is the specific volume and e_{ij}^E is the elastic part of the deviatoric strain. The dots indicate time derivatives. The curly brackets in Eq. (21) convey that the total specific Helmholtz free energy is a functional of the strain and temperature history. The proper independent variables for the Helmholtz free energy enter through a judicious choice of the non-equilibrium contributions to the pressure $p^{(m)}$ and deviatoric stress $s_{ij}^{(n)}$ as

$$p^{(m)}(t) = \int_0^t dt_1 e^{\bar{\phi}^{(m)}(t_1)-\bar{\phi}^{(m)}(t)} B_T^{(m)}(t_1)\dot{\epsilon}_v(t_1) + \int_0^t dt_1 e^{\bar{\phi}^{(m)}(t_1)-\bar{\phi}^{(m)}(t)} \beta^{(m)}(t_1) B_T^{(m)}(t_1)\dot{T}(t_1) \quad (22)$$

and

$$s_{ij}^{(n)}(t) = \int_0^t dt_1 e^{\phi^{(n)}(t_1)-\phi^{(n)}(t)} 2g^{(n)}(t_1)\dot{e}_{ij}^{\eta(n)}(t_1) \quad (23)$$

In Eq. (22), t is the time, $B_T^{(m)}$ are the elements of the isothermal bulk relaxation modulus, $\beta^{(m)}$, defined formally in Eq. (46) below, is the m^{th} element of nonequilibrium volumetric expansion coefficient (also sometimes called the volumetric expansivity), T is the temperature, $g^{(n)}$ is the n^{th} shear relaxation modulus, and $de_v = -d\ln v$ is the volumetric strain increment (chosen to be positive in compression). $\phi^{(n)}(t) = \phi^{(n)}\left(\tau^{(n)}(t)\right)$ and $\bar{\phi}^{(m)}(t) = \bar{\phi}^{(m)}\left(\bar{\tau}^{(m)}(t)\right)$, defined below, are functions of the shear and volumetric relaxation times, $\tau^{(n)}$ and $\bar{\tau}^{(m)}$, respectively. The strain rate $\dot{e}_{ij}^{\eta(n)} \equiv \dot{e}_{ij} - \dot{e}_{ij}^{P(n)} - \dot{e}_{ij}^{c(n)}$ differs from the total deviatoric strain rate by the inclusion of deviatoric plasticity, *i.e.*, $\dot{e}_{ij}^{P(n)}$, and the shear crack strain rate, $\dot{e}_{ij}^{c(n)}$. The moduli in Eq. (22) will be taken to be functions of the volumetric compression. The temperature dependence of the moduli enters through $\tau^{(n)}$ and $\bar{\tau}^{(m)}$. An important point is that because thermodynamic quantities (*i.e.*, quantities that are derivable from derivatives of the free energy) are already explicit in Eq. (22), these quantities must satisfy certain thermodynamic constraints.

The differential of Eq. (22) and (23) produces equations for each

$$dp^{(m)} = B_T^{(m)}(d\epsilon_v - d\epsilon_v^c) + \beta^{(m)} B_T^{(m)} dT - \frac{p^{(m)}}{\bar{\tau}^{(m)}} dt \quad (24)$$

and

$$ds_{ij}^{(n)} = 2g^{(n)} de_{ij}^{\eta(n)} - \frac{s_{ij}^{(n)}}{\tau^{(n)}} dt. \quad (25)$$

Equations (50) and (51) below are used to arrive at these expressions. Similar equilibrium expressions exist, but with the omission of the relaxation terms:

$$dp^{(0)} = B_T^{(0)}(d\epsilon_v - d\epsilon_v^c) + \beta^{(0)} B_T^{(0)} dT \quad (26)$$

and

$$ds_{ij}^{(0)} = 2g^{(0)} de_{ij}^{\eta(0)}. \quad (27)$$

The index 0 denotes the equilibrium values. Thus, for example, $B_T^{(0)}$ is to be determined by taking the volumetric derivatives of $a^{(0)}(v, e_{ij}^E, T)$ (see Eq. (43)) for the equivalent expression in terms of the Gibbs free energy). As such, it has a temperature and volume dependence derived from the equilibrium free energy. On the other hand, a simple parameterization is assigned to $B_T^{(m)}$ for $m \geq 1$, for which we use a polynomial approximation

$$B_T^{(m)}(t) = B_T^{(m)}\left(1 + \chi_1\epsilon_v(t) + \chi_2\epsilon_v^t(t)\right),\ m \geq 1, \quad (28)$$

where χ_1 and χ_2 are zero in expansion. Expressions for damage strains will be provided in Section XIII.G.

The differential of the Eq. (21) yields

$$\rho da = \rho da^{(0)} + \frac{1}{2}\left(\sum_{n=1}^{N} \frac{s_{ij}^{(n)}}{2g^{(n)}} ds_{ij}^{(n)} + \sum_{m=1}^{M} \frac{p^{(m)}}{B_T^{(m)}} dp^{(m)}\right), \quad (29)$$

where the approximation used to arrive at Eq. (29) was neglect of second-order terms in the volumetric and deviatoric strains. Inserting Eq. (24) and (25) into Eq. (29) results in

$$\begin{aligned}\rho da = \rho da^{(0)} + \sum_{m=1}^{M} \beta^{(m)} p^{(m)} dT - \sum_{m=1}^{M} \frac{p^{(m)}}{v} dv + \sum_{n=1}^{N} s_{ij}^{(n)} de_{ij}^{\eta(n)} \\ - \sum_{n=1}^{N} \frac{s_{ij}^{(n)} s_{ij}^{(n)}}{2g^{(n)}\tau^{(n)}} dt - \sum_{m=1}^{M} \frac{p^{(m)} p^{(m)}}{B_T^{(m)} \bar{\tau}^{(m)}} dt.\end{aligned} \tag{30}$$

The equilibrium contributions to the pressure, deviatoric stress, and specific entropy are

$$p^{(0)} = -\left(\frac{\partial a^{(0)}}{\partial v}\right)_{e_{ij}^{E(0)},T}, \tag{31}$$

$$s_{ij}^{(0)} = -\rho \left(\frac{\partial a^{(0)}}{\partial e_{ij}^{E(0)}}\right)_{v,T}, \tag{32}$$

and

$$s^{(0)} = -\left(\frac{\partial a^{(0)}}{\partial T}\right)_{e_{ij}^{E(0)},v}. \tag{33}$$

We now recall the well-known thermodynamic relation

$$Tds = -da - sdT + \rho^{-1} s_{ij} de_{ij} - pdv \geq 0. \tag{34}$$

Substituting (30) into (34), and equating the prefactors of dv, e_{ij}, and dT to zero (by the usual thermodynamic arguments), results in the pressure equation

$$p = p^{(0)} + \sum_{m=1}^{M} p^{(m)}, \tag{35}$$

the stress deviator equation

$$s_{ij} = s_{ij}^{(0)} + \sum_{n=1}^{N} s_{ij}^{(n)}, \tag{36}$$

and the specific entropy

$$s = s^{(0)} + \sum_{m=1}^{M} s^{(m)} = s^{(0)} - v \sum_{m=1}^{M} \beta^{(m)} p^{(m)}. \tag{37}$$

The remaining terms can be equated to the internal dissipation,

$$\rho T \gamma_D = \rho T \frac{ds}{dt} = \sum_{n=1}^{N} \frac{s_{ij}^{(n)} s_{ij}^{(n)}}{2g^{(n)}\tau^{(n)}} + \sum_{m=1}^{M} \frac{p^{(m)} p^{(m)}}{B_T^{(m)} \bar{\tau}^{(m)}} + \sum_{n=0}^{N} s_{ij}^{(n)} \dot{e}_{ij}^{P(n)}. \tag{38}$$

The last two terms in (38) are the deviatoric and volumetric viscoelastic dissipation while the third term arises from deviatoric plasticity. A crack contribution can be added.

All the standard thermodynamic definitions and relations apply to the equilibrium term:

$$c_v^{(0)} = T \left(\frac{\partial s^{(0)}}{\partial T}\right)_v, \tag{39}$$

$$c_p^{(0)} = T \left(\frac{\partial s^{(0)}}{\partial T}\right)_p, \tag{40}$$

$$\gamma^{(0)} c_v^{(0)} = v \left(\frac{\partial s^{(0)}}{\partial v} \right)_T , \tag{41}$$

$$\gamma^{(0)} T = -v \left(\frac{\partial T}{\partial v} \right)_s , \tag{42}$$

$$B_T^{(0)} = -v \left(\frac{\partial p^{(0)}}{\partial v} \right)_T , \tag{43}$$

$$\beta^{(0)} B_T^{(0)} = \left(\frac{\partial p^{(0)}}{\partial T} \right)_v , \tag{44}$$

and

$$\beta^{(0)} = \frac{1}{v} \left(\frac{\partial v}{\partial T} \right)_p . \tag{45}$$

The formal expression for $\beta^{(m)}$,

$$\beta^{(m)} = - \left(\frac{\partial \epsilon_v^{(m)}}{\partial T} \right)_{p^{(m)}, e_{ij}^{E(n)}} , \tag{46}$$

is analogous to (45). This quantity is totally unwieldy. In Ref. [1], a lengthy analysis and set of arguments leads to the approximation that

$$\beta^{(m)} \approx \beta^{(0)}. \tag{47}$$

It suffices to mention that the arguments leading to Eq. (47) do not rest so much on the validity of the approximation in Eq. (47) by itself, as much as the fact that $\beta^{(m)}$ occurs most often in the theory via the combination $\beta^{(m)} p^{(m)}$ and thus the approximation in Eq. (47) is essentially

$$\beta^{(m)} p^{(m)} \approx \beta^{(0)} p^{(m)}. \tag{48}$$

Finally, we introduce expressions for $\phi^{(n)}(t) = \phi^{(n)} \left(\tau^{(n)}(t) \right)$ and $\bar{\phi}^{(m)}(t) = \bar{\phi}^{(m)} \left(\bar{\tau}^{(m)}(t) \right)$ in Eq. (22). The deviatoric $\phi^{(n)}$ enters via an integral over time of the relation times $\tau^{(n)}$:

$$\phi^{(n)}(t) = \int_0^t \frac{dt'}{\tau^{(n)}(t')} \tag{49}$$

or equivalently

$$\dot{\phi}^{(n)}(t) = \frac{1}{\tau^{(n)}(t)}. \tag{50}$$

As will become clear in the next section, the temporal dependence of $\tau^{(n)}(t)$ arises from the temporal dependence of the temperature through a quantity called the shift function, $a_T(t)$.

As a final note, for polyethylene we do not have an adequate experimental measure for $a_T(t)$ for the volumetric viscoelastic contributions. Fortunately, the non-equilibrium bulk moduli tend to be insensitive to variations in temperature. Thus, we make the approximation

$$\bar{\phi}^{(m)}(t) = \int_0^t \frac{dt'}{\bar{\tau}^{(m)}(t')} \approx \frac{t}{\bar{\tau}^{(m)}} , \tag{51}$$

which is equivalent to assuming (room temperature) isothermal relaxation times.

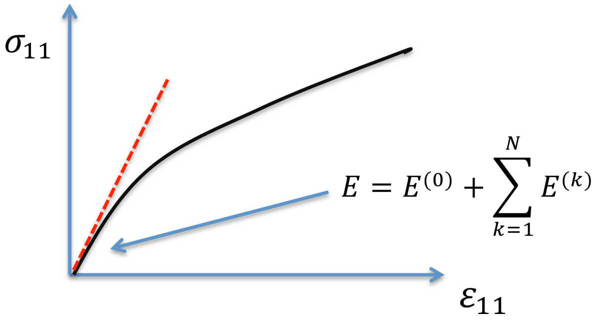

Figure 73: Independent of strain rate and temperature, the initial slope of a Generalized Maxwell Model is the sum of all the elemental Young's moduli.

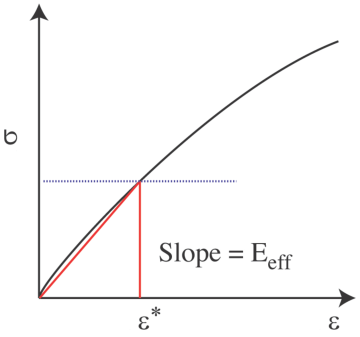

Figure 74: Stress and slope at $t = \Delta t$ for a uniaxial stress-strain curve.

XIII.C Viscoelasticity

In this section, we briefly describe the procedure for fitting the (shear) viscoelastic portion of the model. This is equivalent to answering the question: for a chosen set of relaxation times, $\{\tau^{(n)}\}$, what are the elements of the shear moduli $\{g^{(n)}\}$, that describe all the experimental stress-strain curves in the small-strain regime? The described method has a rigorous basis, but here plausibility arguments will suffice. The fitting procedure relies on having stress-strain data for a broad range of strain rates and temperatures. Because nonlinear effects appear at large values of strain, here we must focus on stress-strain behavior at small strains (strain below the occurrence of plastic flow discussed in the next section).

Figure 73 provides a depiction of a typical constant strain rate, isothermal stress-strain curve for a uniaxial compression experiment. The nature of our viscoelastic model, called a Generalized Maxwell Model, is such that, with sufficiently great resolution, we would observe that the slope of all stress-strain curves, in the limit of zero strain, approaches the sum of the entire set of moduli (the relevant moduli for uniaxial compression is Youngs moduli $E^{(k)}$). This is true, independent of the temperature and the strain rate.

For any finite value of strain, the stress has relaxed by an amount that is easily correlated to the temperature and strain rate. This is to say, the slope is no longer equal to the entire set of elements, but rather to a smaller subset, that depends on the temperature and strain rate. It will useful to single out a particular value of strain, and denote it by ϵ^*. As shown in Fig. 74, the slope corresponding to ϵ^* is now the secant modulus, and can be shown to be expressed well by

$$E_{eff} = E^{(0)} + \sum_{n=0}^{N} \beta^{(n)} E^{(n)}, \tag{52}$$

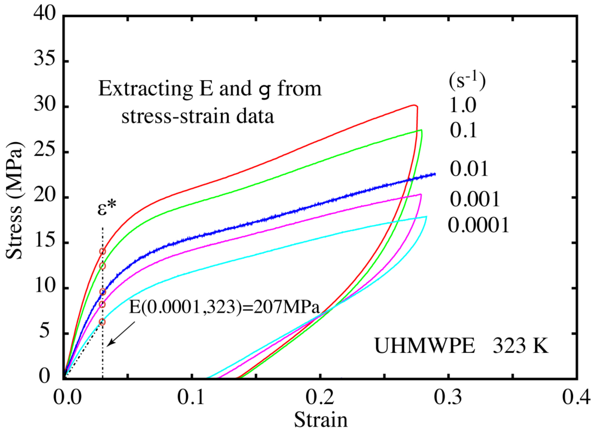

Figure 75: Characteristic effective moduli E extracted from UHMWPE data.

where

$$\beta^{(n)} = \frac{\left(1 - e^{\Delta t/\tau^{(n)}}\right)}{\Delta t/\tau^{(n)}}. \tag{53}$$

With the exception of a small transition zone, $\beta^{(n)}$ effectively assigns a weight equal to unity to the moduli satisfying $\epsilon^*/\dot{\epsilon} \leq \log \tau^{(n)}$ and zero to the moduli that have already fully relaxed. We will use this fact to determine values of the entire set of moduli $\{E^{(0)}, ..., E^{(N)}$.

The calibration proceeds as follows. For a given stress strain curve (thus, for a particular strain rate and temperature), what needs to be extracted from the stress-strain curves are the effective Young's moduli $E_{eff}(\epsilon^*)$, which are the sum of active moduli (non-relaxed) for the various modes, n, according to Eq. (52) and

$$\sigma_{11}(\Delta t) = E_{eff}\dot{\epsilon}_{11}\Delta t = E_{eff}\epsilon^* \tag{54}$$

We must choose the small strain, ϵ^*. Note that ϵ^* need not be the minimum strain determined by the resolution of the experiment. Indeed, that would not be a good value to use in actuality. Rather, because the goal is to obtain a reasonably good fit to the entire family of stress-strain curves, ϵ^* is chosen with that goal in mind. For both HDPE and UHMWPE, we take $\epsilon^* = 0.03$.

The details of the calibration technique are illustrated for UHMWPE, and only final results for HDPE are stated. The effective Young's moduli are determined for each strain rate and temperature by reading off the stress and dividing by 0.03 to get the secant moduli. For example, the effective Young's modulus for a strain rate of 0.0001 s^{-1} and temperature of 323K, at ϵ^*=0.03, is 207 MPa (*c.f.* Fig. 75). This procedure is then repeated for all stress-strain data measured for UHMWPE. While somewhat more difficult, this procedure includes the SPHB data. The results are summarized in Table 17.

Inspection of Table 17 shows that we have also completed a column of values for the effective shear moduli, g. In principle, it is not a simple task to extract the shear moduli from E for a viscoelastic material. Presently, this is accomplished by using an approximation based on linear elasticity theory: $E \approx 3g$, valid for $K \gg g$. In spite of its simplicity, this simple approximation always works well.

The next step is to construct the experimental master curve. The nine isotherms of the shear moduli, g, corresponding to the nine temperatures measured in this work, are plotted against the logarithm of the strain rate as in the Fig. 76. Dotted lines are used to connect the isotherms. To construct an experimental master curve, from which the moduli can be deduced, standard polymer techniques are used: the master curve is obtained by horizontally displacing isotherms to the left and right of a chosen reference isotherm. It is convenient to pick the reference isotherm to be room temperature where the largest amount of data is typically collected. For UHMWPE, the reference

Table 17: Effective moduli E and g extracted from UHMWPE stress-strain curve data.

T(K)	$\dot{\epsilon}(\mathrm{s}^{-1})$	σ(MPa)	$g = E_{eff}/(3\epsilon^{*})$(MPa)
198	0.01	37.3	419
223	1.0	36.4	404
223	0.01	31.3	348
248	0.01	24.5	272
253	0.1	25.5	283
253	0.001	22.4	249
275	1.0	2.1	246
275	0.1	21.9	243
275	0.01	17.8	198
275	0.001	17.8	198
297	1.0	18.6	207
297	0.1	16.8	187
297	0.01	15.1	168
297	0.001	13.4	149
297	0.0001	10.5	117
323	1.0	13.9	154
323	0.1	12.4	138
323	0.01	9.1	101
323	0.001	8.1	90
323	0.0001	6.2	69
348	1.0	9.1	101
348	0.1	7.9	88
348	0.01	5.2	58
348	0.001	5.2	58
373	1.0	5.6	62
373	0.1	4.2	47
373	0.01	2.9	32
373	0.001	2.6	29
198	2000	67.2	747
223	2050	53.8	598
248	2000	43.0	478
275	2000	35.7	397
293	2250	28.5	317
323	2000	21.1	234
348	2000	15.2	169
373	2000	10.6	118

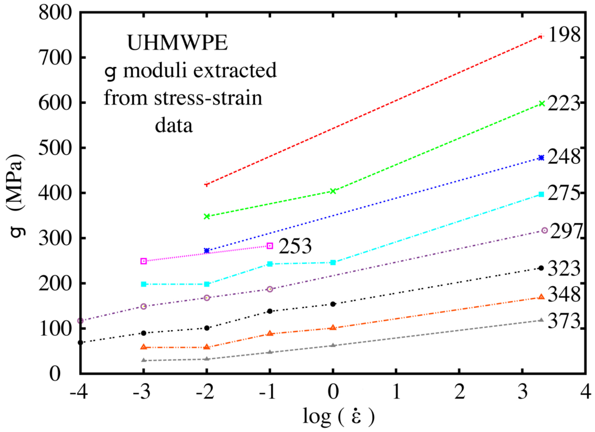

Figure 76: UHMWPE isotherms of g plotted as a function of strain rate.

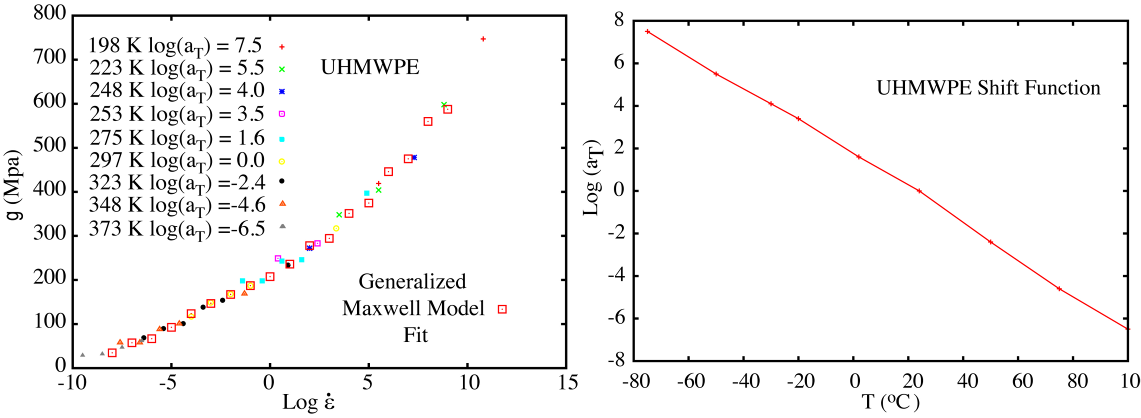

Figure 77: UHMWPE experimental master curve (left) and the associated shift function (right).

isotherm is taken to be 297K. Isotherms are then horizontally shifted left and right of the reference isotherm and a record is kept of the shift amount for each isotherm. The shift is by definition $\log_{10} a_T(T)$. The shifted isotherms and a plot of $\log_{10} a_T(T)$ are shown in Fig. 77. Upon completing the shift, and dropping the connecting dotted lines, a continuous locus of points emerges. Note that the range of strain rates has been greatly expanded to cover 10^{-10} to 10^{15} s^{-1}. This procedure is called Time-Temperature Superposition (TTS).

A model fit of the experimental master curve loci will provide the shear moduli needed in the viscoelastic model (this procedure will result with the red boxes drawn through the data in Fig. 77). To understand this, note that for a constant strain rate, isothermal (at T_{Ref}), uniaxial compression experiment, the slope E, is given by our model as the sum of the elemental values

$$E = E^{(0)} + \sum_{k=1}^{N} E^{(k)} e^{-\epsilon_{11}/(\dot{\epsilon}_{11}\tau^{(k)})}. \tag{55}$$

In the above discussion, we also argued that $E \approx 3g$. Making this substitution yields

$$g = g^{(0)} + \sum_{k=1}^{N} g^{(k)} e^{-\epsilon_{11}/(\dot{\epsilon}_{11}\tau^{(k)})}. \tag{56}$$

Table 18: Generalized Maxwell model parameters for UHMWPE and HDPE.

n	$\log_{10}(\tau^{(n)})$(s) (UHMWPE)	$g^{(n)}$(MPa) (UHMWPE)	$\log_{10}(\tau^{(n)})$(s) (HDPE)	$g^{(n)}$(MPa) (HDPE)
0		33		44
1	6	33	6	40
2	4	34	4	62
3	3	32	3	55
4	2	20	2	40
5	1	20	1	37
6	0	20	0	38
7	-1	20	-1	38
8	-2	30	-2	55
9	-3	50	-3	75
10	-5	80	-5	105
11	-7	100	-7	110
12	-9	119	-9	115

From our choice of $\epsilon_{11} = \epsilon^*$, Eq. (55) is nothing more than a function $g = g(\dot{\epsilon})$:

$$g(\dot{\epsilon}) = g^{(0)} + \sum_{k=1}^{N} g^{(k)} e^{-\epsilon^*/(\dot{\epsilon}_{11}\tau^{(k)})}, \tag{57}$$

where the relaxation times are evaluated at T_{Ref}, *i.e.*, they are the reference values. Thus, by choosing a set of relaxation times, we can fit Eq. (57) to the experimental master curve, and deduce the shear moduli, $\{g^{(k)}\}$. There is always some leeway in the choice of relaxation times. A *rule of thumb* is that for a given strain rate of interest, there should be a corresponding relaxation time such that $\tau^{(n)} \sim 1/\dot{\epsilon}$. We choose $N = 12$ relaxation times as this allows us to cover deformation rates between quasi-static (10^{-4} s^{-1}) and shocks (10^6 s^{-1}). Table 18 lists $\{\tau^{(n)}, g^{(n)}\}$ that fit the experimental master curve (both are shown in Fig. 77). The same procedure was applied to HDPE, the results are also tabulated in Table 18.

To complete the viscoelastic analysis, a brief discussion is required on the shift function $\log(a_T(t))$. A generic shift function is shown in Fig. 78. For a choice of reference temperature, T_{Ref} defined by $\log_{10} a_T(T_{Ref}) = 0$, most shift functions resemble that in Fig. 78. For temperatures above T_{Ref}, the logarithm of the shift function is negative, and below T_{Ref}, the logarithm of the shift function is positive. This has the effect of softening ($T > T_{Ref}$) and stiffening ($T < T_{Ref}$) the material by altering the exponential weight function of the instantaneous moduli for all finite values of strain. Omitting the details (that parrot those of UHMWPE), Fig. 79 shows the experimental master curve and shift function for HDPE.

The final step in the procedure it to see how well the chosen set of viscoelastic parameters fit the small strain regime of the experimental stress-strain curves. For brevity, it suffices to show comparisons of the model for one isotherm (323 K) of UHMWPE. As well, fits to the SHPB rates are illuminating. These are both shown in Fig. 80. The fit is deemed suitable if for all strain rates and temperatures the slope of the theoretical curves match well with the slopes of the measured stress-stress-strain curves. Note that the manner in which the theoretical curves are actually obtained was by solving the complete GAP model, but with the plastic flow disabled. It is seen from Fig. 80 that the fit is suitable, which justifies the choice of $\epsilon^* = 0.03$. Comment is necessary about the SHPB rates. As the strain evolves in a SHPB experiment, the material first undergoes a process called stress equilibration. During this process, the strain rate it not constant, and data obtained in this regime are ignored in most theoretical analyses. Thus, the fact that the theoretical curves do not fit particularly well in this regime, is anticipated and not considered to be of concern.

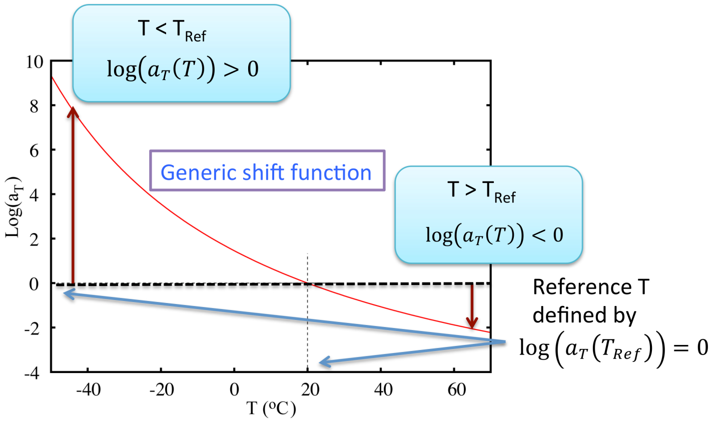

Figure 78: “Typical” temperature dependence of $\log_{10} a_T(T)$ with $T_{Ref} = 20°\mathrm{C}$.

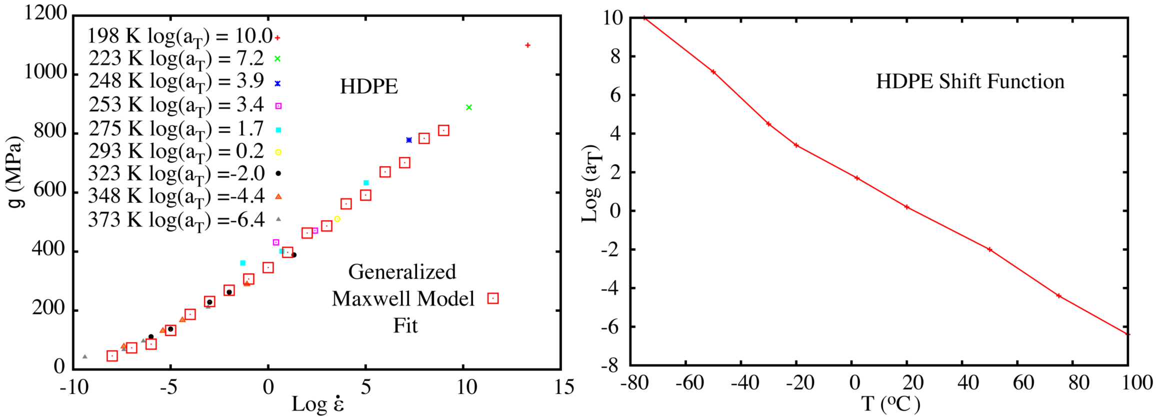

Figure 79: HDPE experimental master curve (left) and the associated shift function (right).

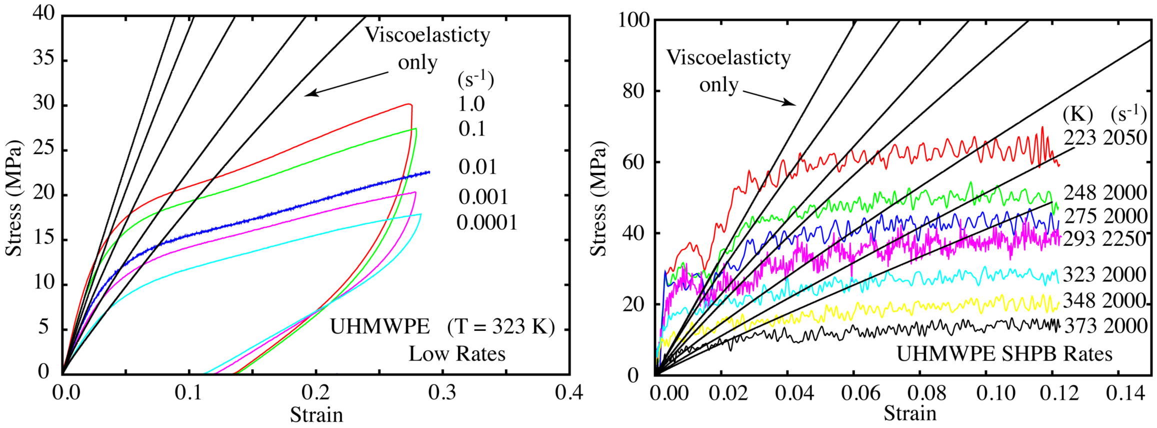

Figure 80: UHMWPE comparisons of experimental stress-strain measurements and the viscoelastic model at low (left) and SHPB rates (right).

XIII.D Plasticity

Only deviatoric plasticity is considered in this work. The plasticity model used in GAP is novel [1], as will become clear in the below discussion. Plastic flow is introduced through a modified Prandtl-Reuss (see for example Ref. [4]) viscoplastic flow law for the deviatoric plastic strain increment

$$de_{ij}^{P(n)} = \Lambda_P^{(n)} s_{ij}^{(n)} dt, \tag{58}$$

where the flow rule function $\Lambda_P^{(n)}$ has a form resembling that used by Bodner and Partom [5] and Frank and Brockman [6]

$$\Lambda_P^{(n)}(t) = \frac{D_0}{\sqrt{J_2^{(n)}(t)}} \left(\frac{\dot{\epsilon}_{eff}(t)}{\dot{\epsilon}_0}\right)^{n_z} \left(\frac{3J_2^{(n)}(t)}{[Z^{(n)}(t)]^2}\right)^{n_p}, \tag{59}$$

but with several modifications. Each Maxwell element n will flow plastically according to the deviator, $s_{ij}^{(n)}$, of that element. For an element deviator $s_{ij}^{(n)}$ to contribute significantly to the total deviator stress, s_{ij}, it must, as a rule, satisfy $\tau^{(n)}\dot{\epsilon} \gg 0$, where $\dot{\epsilon}$ is a measure of the applied strain rate. It is in the sense that the flow rule (Eq. (59)) depends on n, that the present model resembles that proposed by Frank and Brockman [6].

The material parameter D_0 is the limiting shear strain rate in Eq. (59). The factor, $2J_2^{(n)} = s_{ij}^{(n)} s_{ij}^{(n)}$, is the second invariant of the deviatoric stress for element n. The material parameters, n_z and n_p, are rate sensitivity parameters. The normalization strain rate $\dot{\epsilon}_0$ is a material constant and typically chosen to be the minimum strain rate in the problem (here it is taken as 10^{-4} s^{-1}). The effective strain rate in Eq. (59) is given by

$$\dot{\epsilon}_{eff} = \sqrt{\frac{2}{3}\dot{e}_{ij}\dot{e}_{ij}}. \tag{60}$$

Letting $\bar{W}_P^{(n)}$ denote the plastic work per unit volume for element n, the corresponding plastic work increment is given by

$$d\bar{W}_P^{(n)} = s_{ij}^{(n)} de_{ij}^{P(n)}. \tag{61}$$

The bar over the work, $\bar{W}_P^{(n)}$, distinguishes it from the work per unit mass used in the thermodynamic part of the theory.

$Z^{(n)}(t)$ is the sum of two terms: $Z_0^{(n)}(t)$ plus a work hardening contribution proportional $\bar{W}_P^{(n)}$

$$Z^{(n)}(t) = Z_0^{(n)}(t) + \alpha_W \bar{W}_P^{(n)}(t), \tag{62}$$

where α_W is a unitless material parameter. Equation (62) is similar to that used by Frank and Brockman [6]. In the present flow model, the accumulated plastic work is used as a scalar measure of the plastic strain achieved during deformation.

A critical difference between the present strength model and that of Bodner and Partom or Frank and Brockman is that the latter two include yielding and work hardening, whereas the present theory also has strain softening. To enable this modification, $Z_0^{(n)}(t)$ evolve under a load according to a hierarchical set of ordinary differential equations [1]

$$dZ_j^{(n)}(t) = m_j \left(1 - \frac{Z_j^{(n)}(t)}{Z_{j+1}^{(n)}(t)}\right) d\bar{W}_P^{(n)}(t),\ n = 0, ..., N;\ j = 0, ..., J \tag{63}$$

with initial conditions

$$Z_j^{(n)}(t=0) = Z_0 K_j \left(\frac{g^{(n)}}{\sum_{k=0}^{N} g^{(k)}}\right),\ n = 0, ..., N;\ j = 0, ..., J. \tag{64}$$

The n^{th} element, $Z_j^{(n)}(t=0)$ scales with a *distribution* of shear relaxation strengths, here approximated by the term in the parentheses of Eq. (64). This scaling is in accord with molecular cooperativity theory as discussed by Frank and Brockman [6]. Z_0 is a material constant and has dimensions of stress. Five values of j are found to suffice, and thus the hierarchical series of evolution equations is truncated at $J=4$, with $Z_5^{(n)}$ being specified as a material constant. K_j and m_j are regarded as material parameters.

We must discuss the $Z^{(n)}(t)$ behavior. Outwardly, this appears to be the most difficult dependence to quantify. As mentioned $Z^{(n)}(t)$ comprises two terms according to Eq. (62). The second term is a simple constant scaling proportional to the plastic work, *i.e.* work hardening. The first term, $Z_0^{(n)}(t)$, is the solution of a coupled set of differential equations (Eq. (63)) subject to initial conditions, Eq. (64), with the plastic work (the integration over time of Eq. (61)) providing the driving force. We can go a long way to understanding the behavior of these ODEs, because the ODEs follow a simple set of rules. Because each element n has its own set of ODEs, we focus on one generic n, i.e., consider n frozen for this discussion.

First, we label K_j as the j^{th} shape parameter. From the initial conditions, Eq. (64), the solution of each ODE (each j) initiates at $Z_j^{(n)}(t=0)=Z_0K_j(g^{(n)}/g_{tot})$, where Z_0 has units of stress, and adjusts the overall strength of the initial yield. Less obvious, for larger values of plastic work, $\bar{W}_P^{(n)}(t)$, *every* $Z_j^{(n)}$ of the hierarchy individually converges to the *single* value $Z_0K_5(g^{(n)}/g_{tot})$, and the rate of convergence to that value is controlled by m_j, which multiplies $\bar{W}_P^{(n)}(t)$ in Eq. (63). The intermediate K_j, *i.e.*, K_1-K_4, control the shape of $Z_j^{(n)}(t)$. By applying this theory to numerous materials, it has been determined that a single set of parameters m_j, independent of the material, works well. This is important as it eliminates having to go through the process of finding them by invoking some sort of trial and error procedure. The chosen set is $\{m_0,...,m_4\}=\{540.0,70.2,16.2,15.0,15.0\}$.

Figure 81 displays plots of the numerical solutions of $Z^{(n)}(t)=Z_0^{(n)}(t)$ (the work hardening parameter α_W is set to zero) for different choices of shape parameters, as a function of the plastic work. For each plot $Z_0^{(n)}(0)=Z_0K_0(g^{(n)}/g_{tot})$ was arbitrarily set equal to a value of 2, for demonstration. The plot shows the variety of behaviors that can be obtained for $Z^{(n)}(t)$ (and thus stress-strain curves) by using different K_j choices.

Given the functional dependence of shape parameters, the strategy is to take $\dot{\epsilon}_0=10^{-4}$ s^{-1}, $D_0=10^4\ s^{-1}$, $n_p=5$ (these parameters work well for many polymers and are used for both UHMWPE and HDPE in the present work) and to choose as initial estimates $\alpha_W\sim 0$, $n_z\sim 1$, and $K_0\sim 1$. Next choose the shape parameters $K_1,...,K_5$ to fit the functional shape of the stress-strain curves, with Z_0 adjusted to get the overall magnitude of the yield correct. Approximately, the first few shape parameters (K_1,K_2) are chosen to get the first stress-strain yield maxima, the next couple (K_3,K_4) to fit the minima, and the last (K_5,α_W) to get the large strain stress hardening. After obtaining a fit that may be described as generally good, the parameters can be altered by small amounts to converge to the experimental stress-strain curves. By the conclusion of these processes, the viscoelastic parameters (Table 18) and the plasticity model (Table 19) are calibrated. In principle, there is great flexibility in the stress-strain curves that can be fit by this procedure. Note for example that the shape functions are allowed to vary according to n, for which we chose only two regimes ($n=0$ and $1-12$, for UHMWPE). We could have used 3 regimes, and so on, to fit the stress-strain curves to get precision. Accounting for scatter in the experimental measured curves, this exercise is typically deemed unwarranted.

Having completed parameterizing the model to the experimental stress-strain curves, we now show all experiment-model comparisons. These are done in Figs. 82 and 83 for UHMWPE and 84 and 85 for HDPE. To help comprehend the full range of variability of these materials, it is useful to show plots (Fig. 82 and 84) where as much data is overlaid as possible (without over-confusing the plots). The fact that the model fits this extreme range in behavior is a testament to the adequacy of the model.

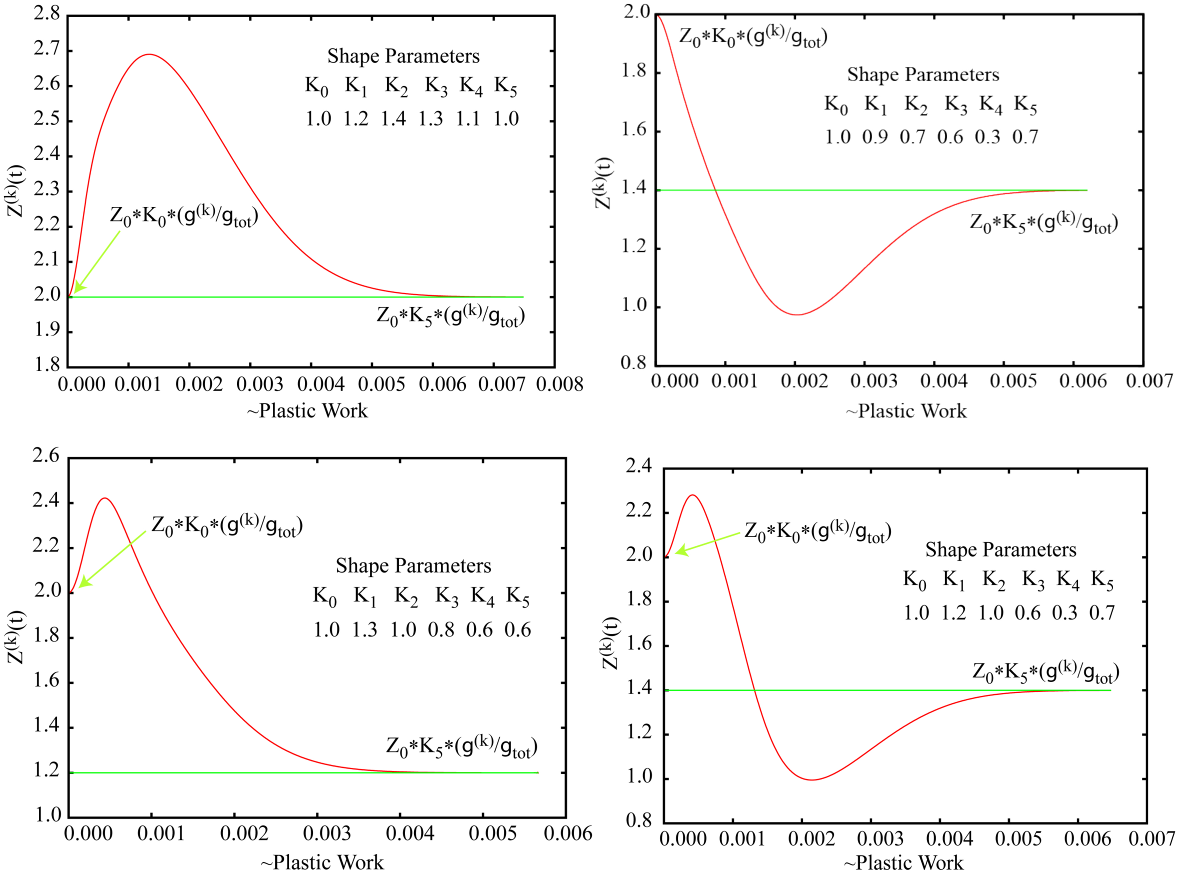

Figure 81: $Z^{(k)}(t)$ as a function of plastic work for different shape parameters.

Table 19: Plasticity model parameters for UHMWPE and HDPE.

	$n = 0$ (UHMWPE)	$n = 1 - 12$ (UHMWPE)	$n = 0, 1$ (HDPE)	$n = 2 - 12$ (HDPE)
Z_0 (MPa)	400	400	580	580
K_0	1.0	1.0	1.0	0.9
K_1	1.9	1.1	1.4	1.0
K_2	3.3	0.9	1.8	0.9
K_3	2.0	1.6	1.4	1.2
K_4	1.0	1.3	1.1	1.5
K_5	1.0	0.6	1.0	1.7
n_Z	1.1	1.1	1.1	1.1
α_W	12.0	12.0	4.0	4.0

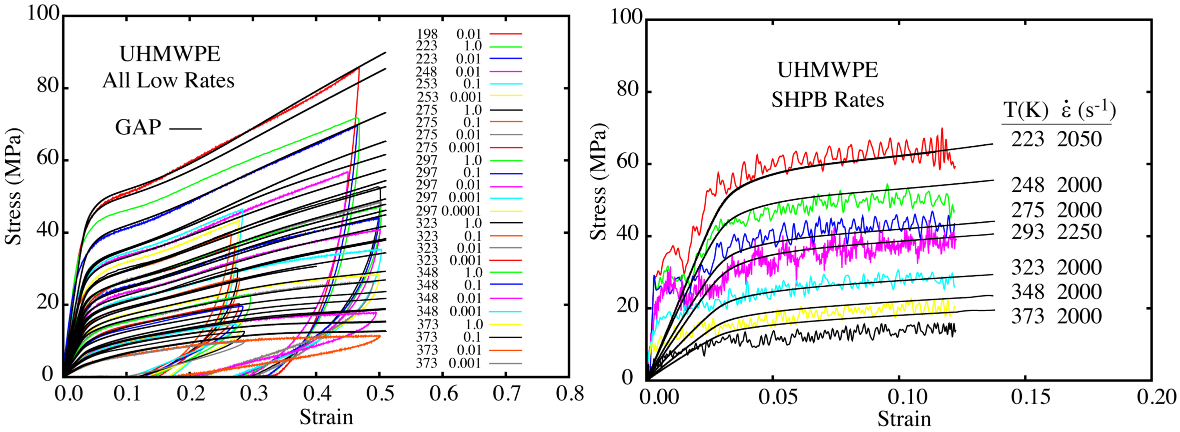

Figure 82: UHMWPE GAP model and experiment comparison for the totality of low strain rates (left) and SHPB rates (right).

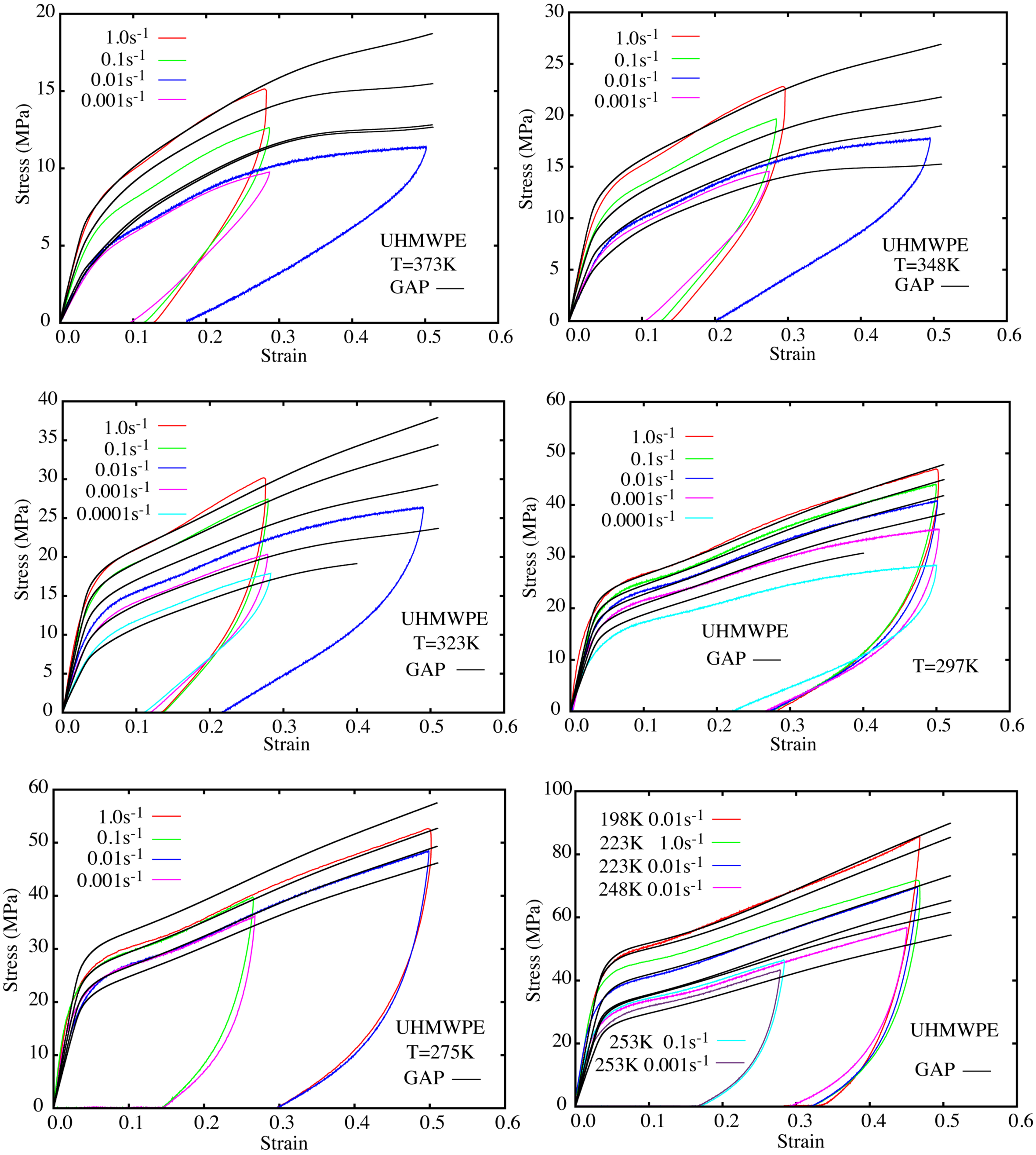

Figure 83: UHMWPE GAP model and experiment comparison for various temperatures for the low strain rates.

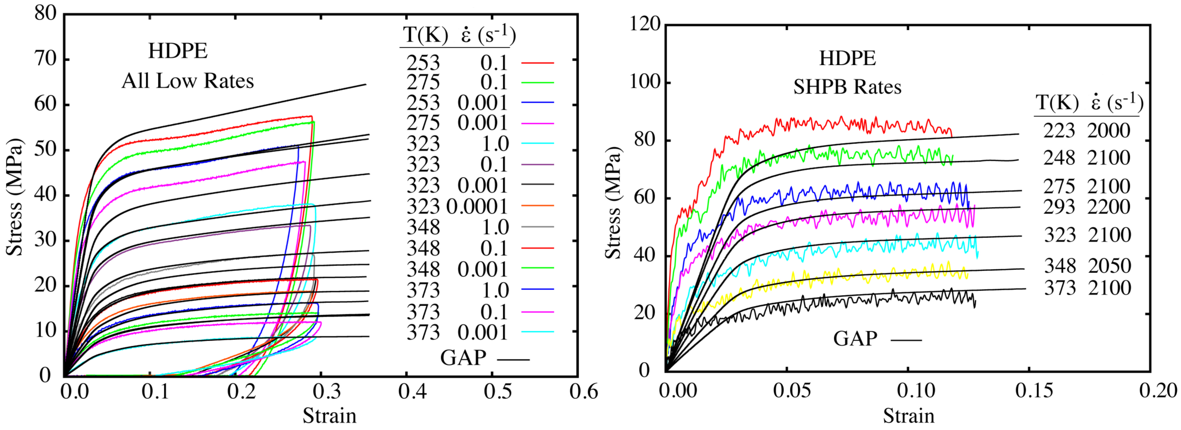

Figure 84: HDPE model and experiment comparison for the low (left) and SHPB rates (right).

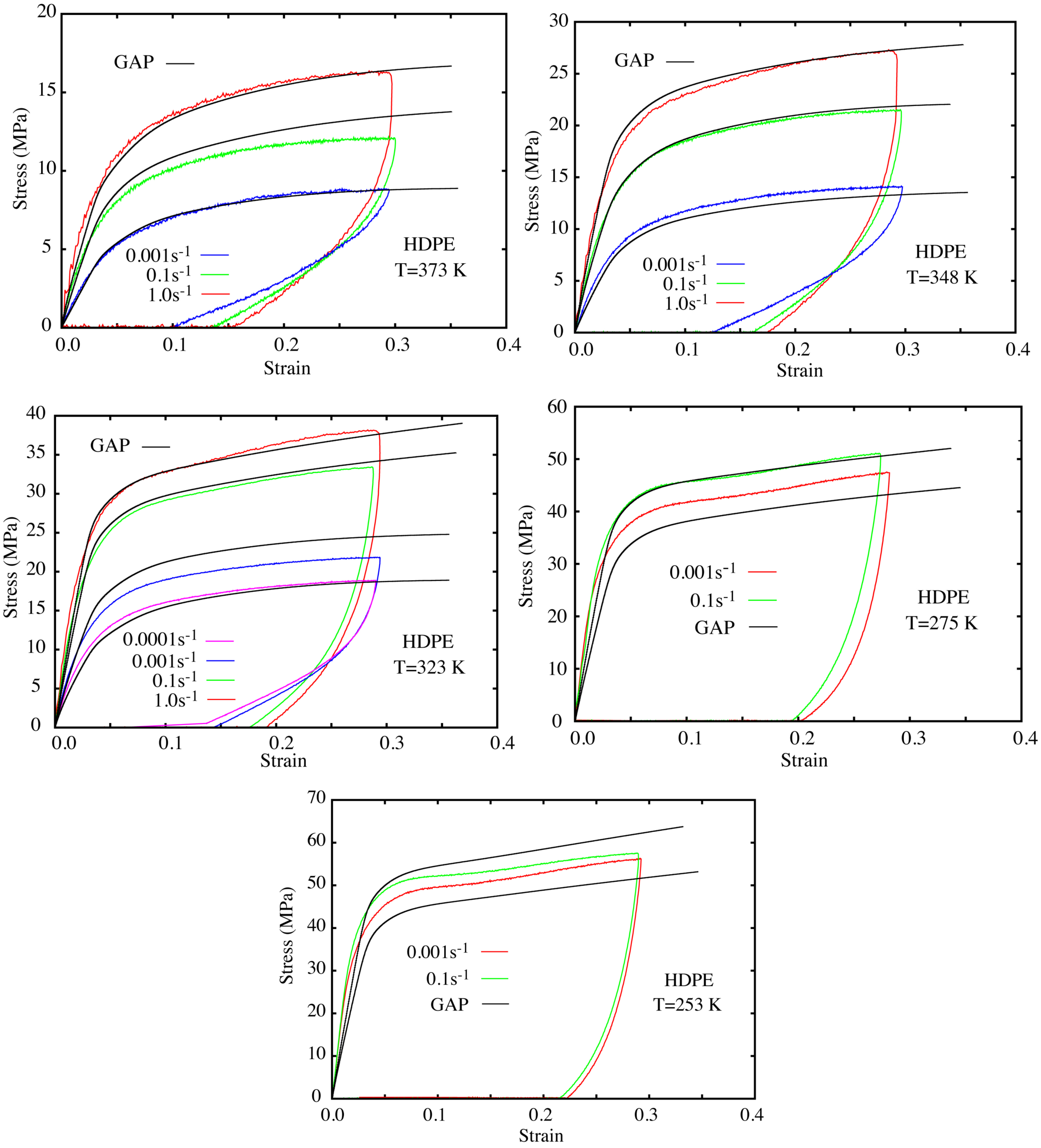

Figure 85: Similar to Fig. 83 but for HDPE.

XIII.E Equilibrium EOS

Equilibrium is an ambiguous concept for polymers, and this is certainly true for the volumetric behavior. Here we will define the equilibrium EOS as that which is obtained by using "slow" measurements, *i.e.*, those lasting minutes to hours. This time scale is very long compared to the deformation scenarios intended for the model. Measurements satisfying this criterion are for example the dilatometry-measured specific volume and the calorimetric-measured specific heat. For convenience, when it is clear, we suppress the superscript (0) on the below equations, with the understanding that all quantities in this section are the equilibrium expressions.

Equilibrium specific heat and dilatometry data were obtained for both HDPE and UHMWPE. To use the data, a simple semi-empirical expression for the specific Gibbs free energy, $g(p,T)$, is chosen:

$$g(p,T) = \sum_{k=0} c_m T^m + c_L T \ln T + v_0 \left[p - R \left\{ \left(B_T^{(0)} + p \right) \ln \left(1 + \frac{p}{B_T^{(0)}} \right) - p \right\} \right], \tag{65}$$

The dimensionless constant R in this equation is equal to 0.0894. The quantities $v_0(T)$ and $B_T^{(0)}$ are related to the zero-pressure specific volume and (equilibrium) isothermal bulk modulus. The coefficients c_m and c_L are determined from specific heat data at ambient pressure (assumed zero), and the remaining parameters are determined from dilatometry data. Equation (65) is consistent with the Tait specific volume [7]

$$v(p,T) = \left(\frac{\partial g}{\partial p} \right)_T = v_0(T) \left[1 - R \ln \left(1 + \frac{p}{B_T^{(0)}} \right) \right] \tag{66}$$

shown to adequately model $v(p,T)$ for many polymers. $v_0(T)$ and $B_T^{(0)}$ are assigned the simple parametric forms

$$B_T^{(0)} = B_0 e^{B_1 T + B_2 T^2}, \tag{67}$$

and

$$v_0(T) = a_0 + a_1 T. \tag{68}$$

Derivatives of $g(p,T)$ give equilibrium quantities required by the model:

$$c_p(p,T) = -T \left(\frac{\partial^2 g}{\partial T^2} \right)_p, \tag{69}$$

$$\frac{1}{B_T^{(0)}(p,T)} = -\frac{1}{v} \left(\frac{\partial p^2}{\partial^2 g} \right)_T, \tag{70}$$

$$\gamma(p,T) = \frac{v \beta B_T^{(0)}}{c_v}, \tag{71}$$

$$\beta(p,T) = \frac{1}{v} \frac{\partial^2 g}{\partial p \partial T}, \tag{72}$$

and

$$c_v = c_p - v\beta^2 B_T^{(0)} T. \tag{73}$$

$B_T^{(0)}$, β, γ, and c_v are the equilibrium isothermal bulk modulus, volumetric expansion coefficient, Grüneisen coefficient, and specific heat at constant volume, respectively. When the glass transition occurs in the regimes of interest, Eqs. (65) through (68) are fit to the separate regimes above and below the transition. Likewise, when a polymer undergoes a first-order phase transition in the crystalline domains of the polymer, a jump discontinuity occurs in the specific volume, and a latent heat spike

Table 20: Equilibrium EOS parameters for UHMWPE from fitting experimental c_p and v data.

	c_0(J/kg)	c_1[J/(kg×K)]	c_2[J/(kg×K^2)]	c_3[J/(kg×K^3)]	c_L[J/(kg×K)]
	0.0	1027	1.1	0.002867	-1027
	B_0(Pa)	B_1(1/°C)	B_2(1/°C^2)	a_0(m^3/kg)	a_1[m^3/(kg×°C)]
$T < T_m$	2.1276e8	-5.9e-3	1.0e-6	1.069e-3	0.80e-6
$T \geq T_m$	1.3793e8	-5.0e-3	0.0	1.165e-3	0.87e-6

Table 21: Equilibrium EOS parameters for HDPE from fitting experimental c_p and v data.

	c_0(J/kg)	c_1[J/(kg×K)]	c_2[J/(kg×K^2)]	c_3[J/(kg×K^3)]	c_L[J/(kg×K)]
	0.0	715.0	0.05	2.0e-3	-715
	B_0(Pa)	B_1(1/°C)	B_2(1/°C^2)	a_0(m^3/kg)	a_1[m^3/(kg×°C)]
$T < T_m$	3.600e8	-5.7e-3	2.0e-6	1.020e-3	5.6e-7
$T \geq T_m$	2.051e8	-5.0e-3	0.0	1.126e-3	1.03e-6

appears in the specific heat. Again, the approach is to separately fit the equilibrium equations to the different regimes.

In the experimental portion of this work, the specific heat and specific volume have been measured for both UHMWPE and HDPE. This information is sufficient to determine the equilibrium Gibbs free energy parameters in Eqs. (65)-(68) and these are listed in Tables 20 and 21 for the two polymers. In the experimental specific heat, there is an indication of a glass transition at about -35°C. Because the transition produces a jump discontinuity in the specific heat below the scatter in the data (as indicated by the error bars), it is ignored here. The melt transition temperature occurs at about $T_m \approx 420$ K for both polymers. We have no data for the specific heat above that temperature, thus the low temperature specific heat has been extrapolated to above T_m, with the understanding that we are most interested in temperatures below T_m. The data and the model fit to them are shown in Fig. 86 for UHMWPE and Fig. 87 for HDPE. The corresponding equilibrium specific Gibbs free energy is shown in Fig. 88. By taking the appropriate thermodynamic derivatives of the Gibbs free energy and use of thermodynamic relations, all other thermodynamic quantities can be determined. UHMWPE (HDPE) thermodynamic quantities are shown in Fig. 89 (Fig. 90). Each plot shows a family of isobars spanning 0 and 400 MPa.

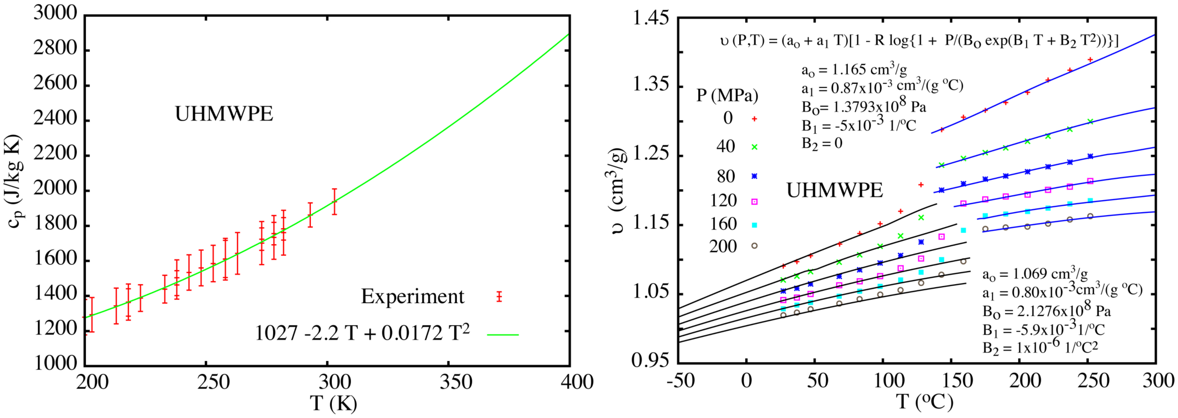

Figure 86: Specific heat and specific volume data, and model fits, for UHMWPE.

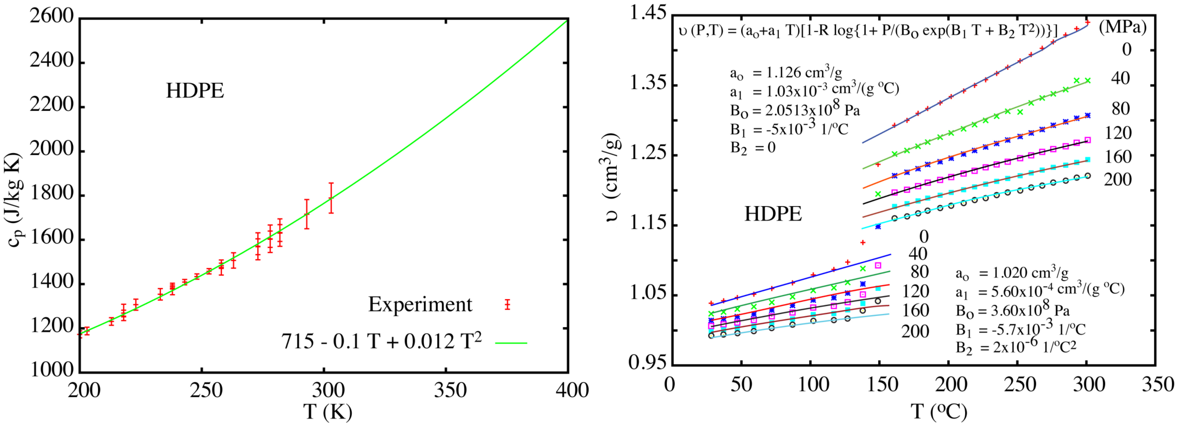

Figure 87: Specific heat and specific volume data, and model fits, for HDPE.

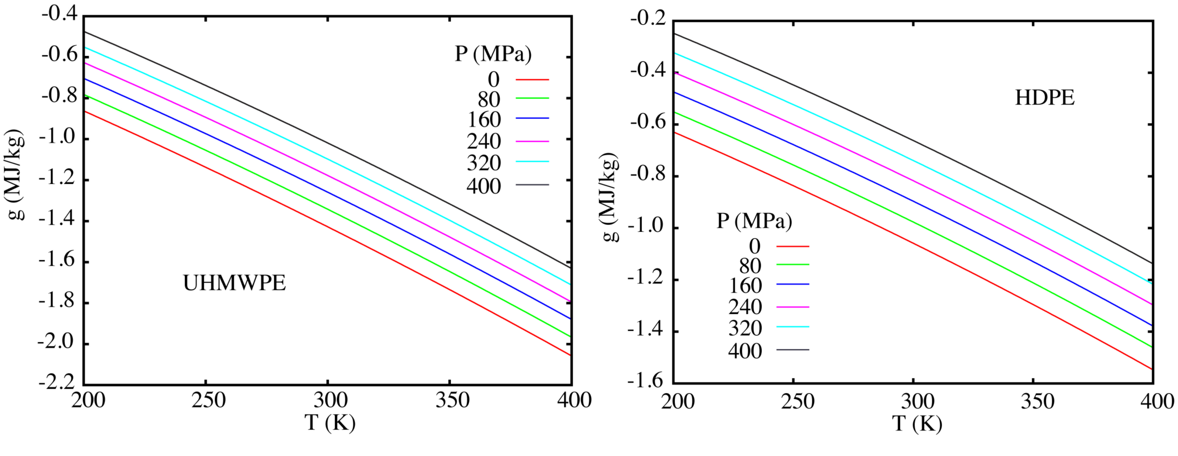

Figure 88: Isobars of the specific Gibbs free energy calculated from Eq. (5.1) for UHMWPE (left) and HDPE (right).

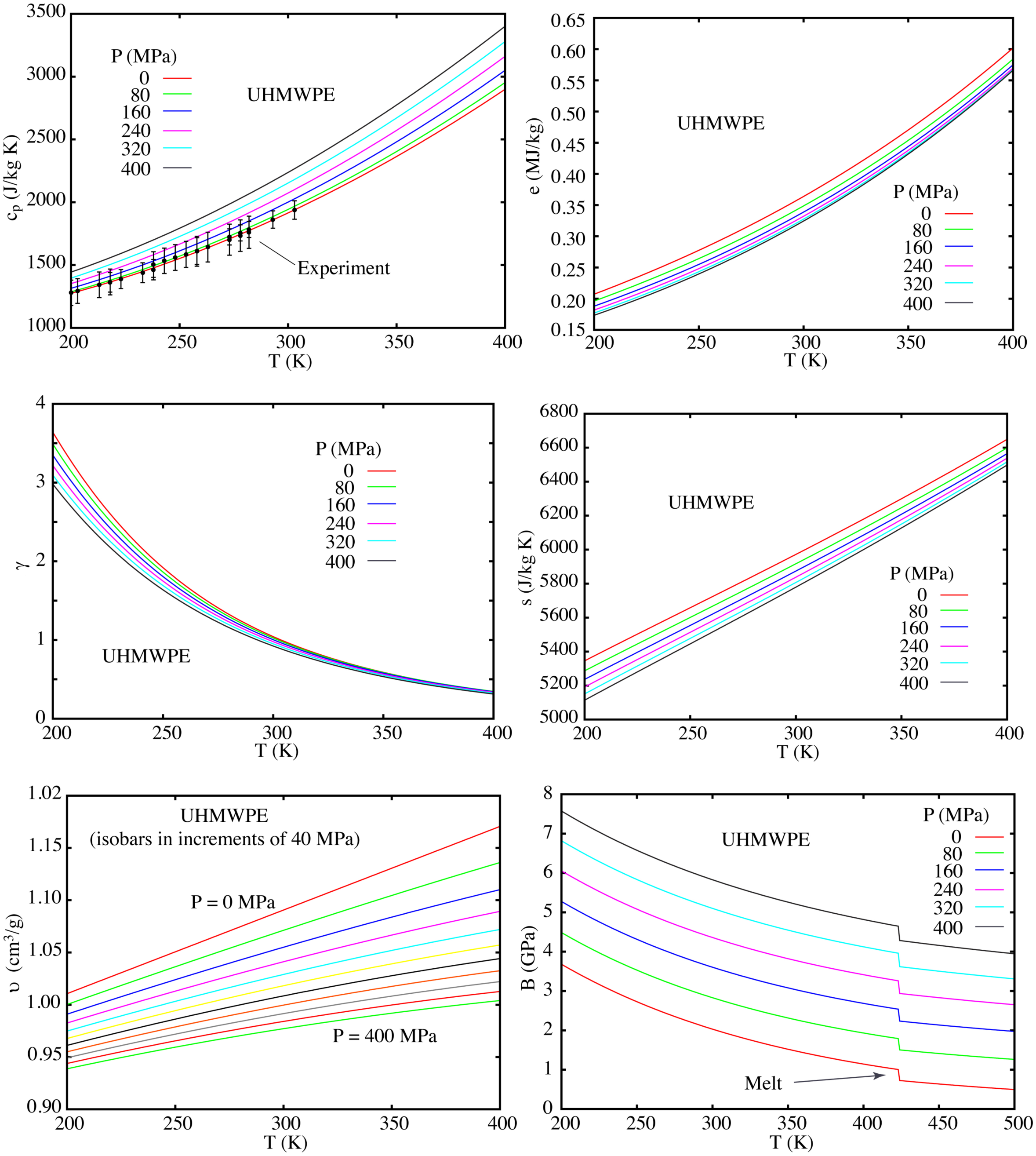

Figure 89: Isobars of equilibrium thermodynamic: specific volume v, isothermal bulk modulus $B \equiv B_T^{(0)}$, Grüneisen coefficient γ, specific entropy s, specific heat at constant pressure c_p, and specific internal energy e for UHMWPE.

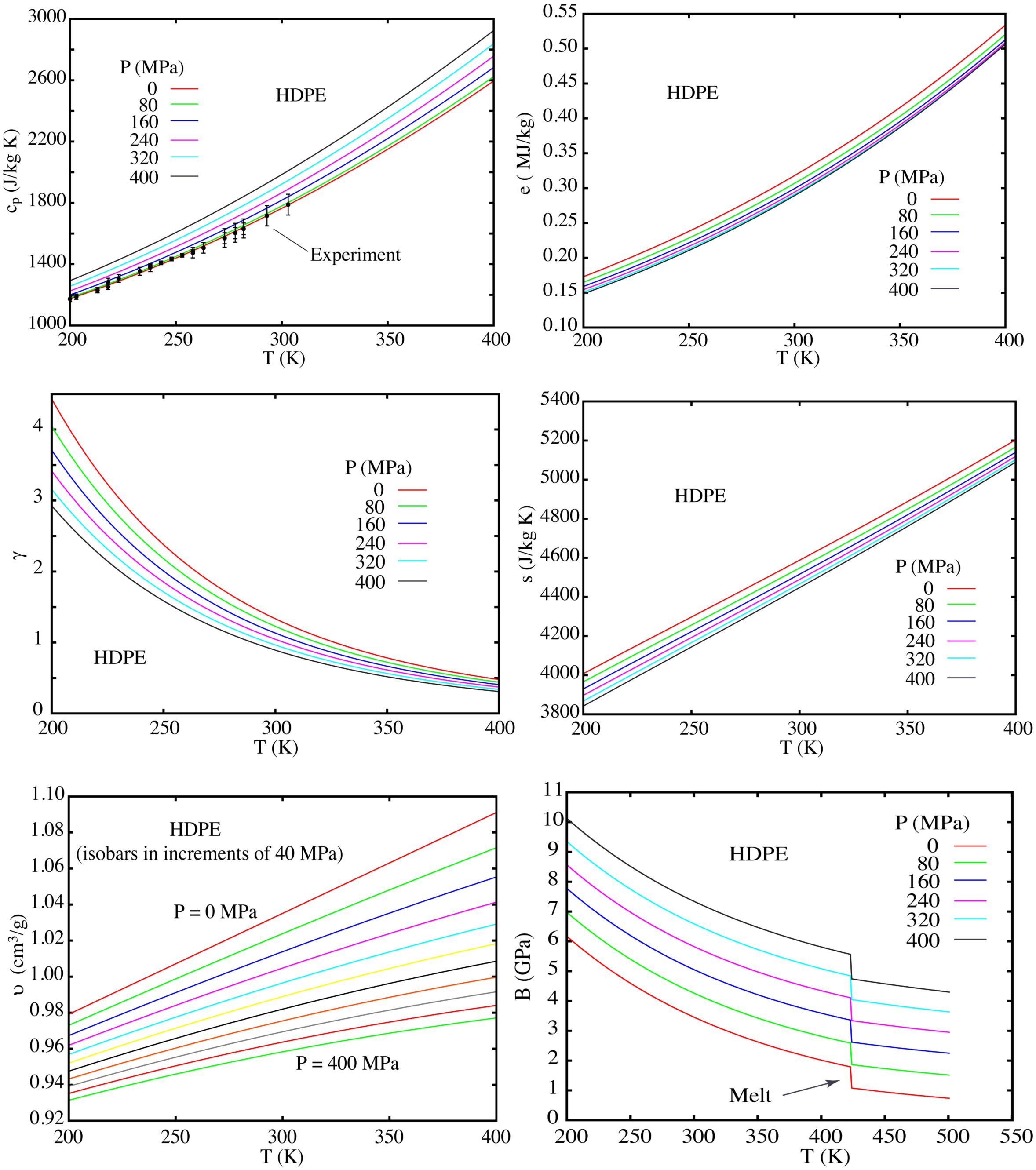

Figure 90: Isobars of equilibrium thermodynamic: specific volume v, isothermal bulk modulus $B \equiv B_T^{(0)}$, Grüneisen coefficient γ, specific entropy s, specific heat at constant pressure c_p, and specific internal energy e for HDPE.

XIII.F Volumetric Viscoelasticity (non-equilibrium volumetric dependence)

Given that the equilibrium EOS (Eq. (65)) is thermodynamically complete, we can calculate the corresponding Hugoniot. That is, from the quantities calculated in the previous section, we can calculate the internal energy, E, and then the locus of points in thermodynamic space satisfying the Rankine-Hugoniot jump conditions:

$$E_H = E_0 + \frac{1}{2}(P + P_0)(V_0 - V). \tag{74}$$

It is convenient to express the results in terms of the shock, U_S, and particle, u_p, velocities *via*

$$U_S = V_0\sqrt{\frac{P - P_0}{V_0 - V}} \tag{75}$$

and

$$u_p = \sqrt{(P - P_0)(V_0 - V)}. \tag{76}$$

This analyis has been completed and the results are shown in Fig. 91 for both UHMWPE and HDPE.

An issue arises when these theoretical equilibrium Hugoniots of Fig. 91 are contrasted to the experimentally measured data points shown in Fig. 92. Note, for this discussion only the instantaneous (*i.e.* non-relaxed, corresponding to the instantaneous moduli [1]) Hugoniots are shown for experiment (the theoretical dash-dotted lines will be discussed below). Because total relaxation of the polymers is not possible in the duration of a shock experiment, the instantaneous modulus (and the Hugoniot) is the only truly non-ambiguous quantity to discuss. That equilibrium (Fig. 91) and experimental shock values (Fig. 92) disagree was anticipated, and was the reason for incorporating non-equilibrium contributions to the pressure $p^{(m)}$ in Eq. (21).

To determine the isothermal moduli, $B_T^{(m)}$ in Eq. (21), and thus lead to a theory that agrees with the experimental shock Hugoniot, we will use measured shock velocity profiles from Dattelbaum, *et al.*, discussed in Section VII above. Experimental schematics of the setup are provided in experimental sections. To parameterize GAP using this data, that is, to determine $B_T^{(m)}$, we used shots #1578, 1579, 1580 and 1595 for UHMWPE. Similarly, for HDPE parameterization, we used shots #1550, 1591, and 1599, and spall configurations #1585, 1586, and 1602. This has been accomplished by the procedure now described.

The rounded profile observed at the shock front of each experimental velocity profile occurs because the stress relaxes from its instantaneous moduli value to a relaxed value. Calibration of GAP used this information. By fitting the profiles in this region, we determined (to an acceptable level) the moduli $B_T^{(m)}$. The resulting parameters for the bulk-viscoelastic model obtained using this procedure are listed in Table 22. Values for parameters χ_1 and χ_2 (Eq. (28)) for UHMWPE were adjusted to be 7 and 27, respectively. For HDPE, they were taken to be 7 and 24, respectively. These parameters are used to incorporate *shock-up* phenomena and to decrease the shock rise time in the theoretical profiles. Clearly

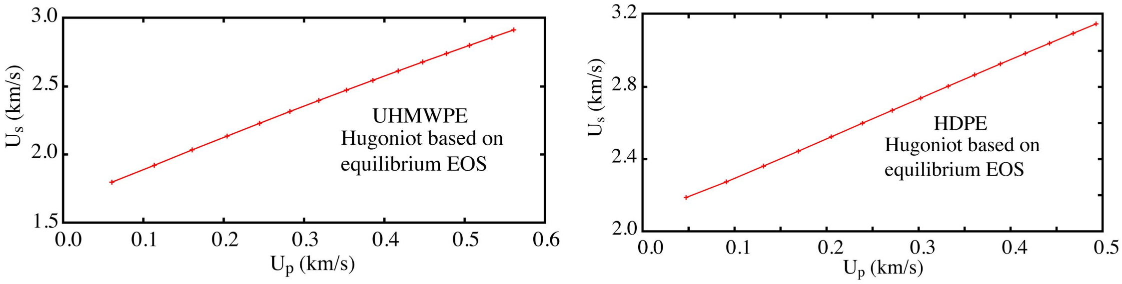

Figure 91: Hugoniot calculated from the equilibrium EOS: UWMWPE (left) and HDPE (right).

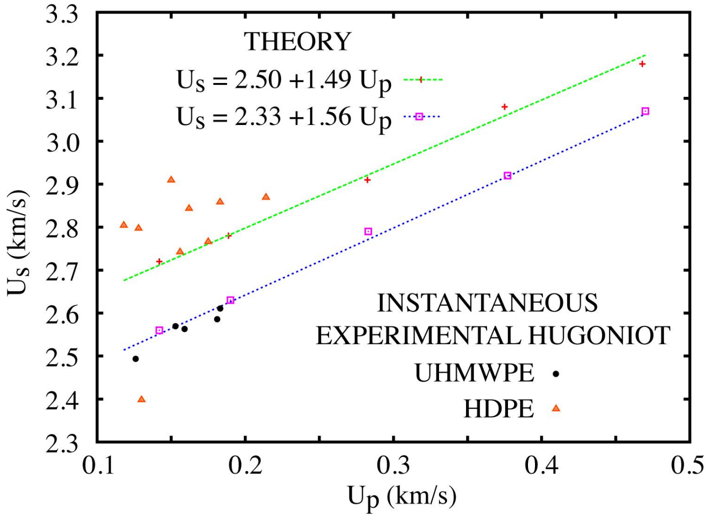

Figure 92: Experimental instantaneous Hugoniots measured by Dattelbaum, *et al.* for HDPE and UHMWPE. The experimental Hugoniots are clearly much larger in magnitude than the theoretical Hugoniots calculated from the equilibrium EOS, displayed in Fig. 91. They are corrected upon including non-equilibrium contribution to the pressure.

Table 22: Generalized Bulk-Maxwell model parameters for UHMWPE and HDPE.

m	$\log_{10}(\bar{\tau}^{(m)})(s)$ (HDPE)	$B_T^{(m)}$(GPa) (HDPE)	$\log_{10}(\bar{\tau}^{(m)})(s)$ (UHMWPE)	$B_T^{(m)}$(GPa) (UHMWPE)
1	-4	1.8	-4	1.1
2	-5	1.4	-5	1.0
3	-6	0.4	-6	0.9
4	-7	0.3	-7	0.3
5	-8	0.3	-8	0.3
6	-9	0.3	-9	0.3

the utilized procedure for determining the parameter set $\left\{B_T^{(m)}, \chi_1, \chi_2\right\}$ is not unique, and differing sets of parameters can likely be found that will fit the data as well (Sec. XIII.H). Experimental profiles, along with the parameterized GAP model predictions are shown in Figs. 93 and 94.

Several comments are necessary. First, Figs. 93 and 94 also show a theoretical velocity profile that emerges at zero time. These particle velocities are the instantaneous velocities for that shot, that is, they correspond to the velocity profiles positioned at the impact interface. Second, within each plot there are 9 experimental velocity profiles, taken from 9 embedded electromagnetic gauges, with 9 theoretical profiles. The gauge position of each gauge is known from the experimental setup, and is used in the simulations. Note that the agreement between theory and experimental particle velocities is very good, including the arrival times for all 9 gauges. As a caveat, this agreement is up to a net shift δt listed on each plot, corresponding to the fact that simulation did not include the effects, for example, of glue bond dimensions and so forth. Third, a single fixed sample and impactor dimension was used for all the shock experiments, because our concern was only for the Hugoniot information. The exception to this was in the spallation simulations, where exact dimensions of the impactor and sample were applied (Fig. 94). The consequence of using a single fixed dimension was that releases arriving from the back surface of the impactor did not correlate with the experiments.

Finally, Fig. 94 contains a spallation plot on HDPE, which refers to the dynamic damage process

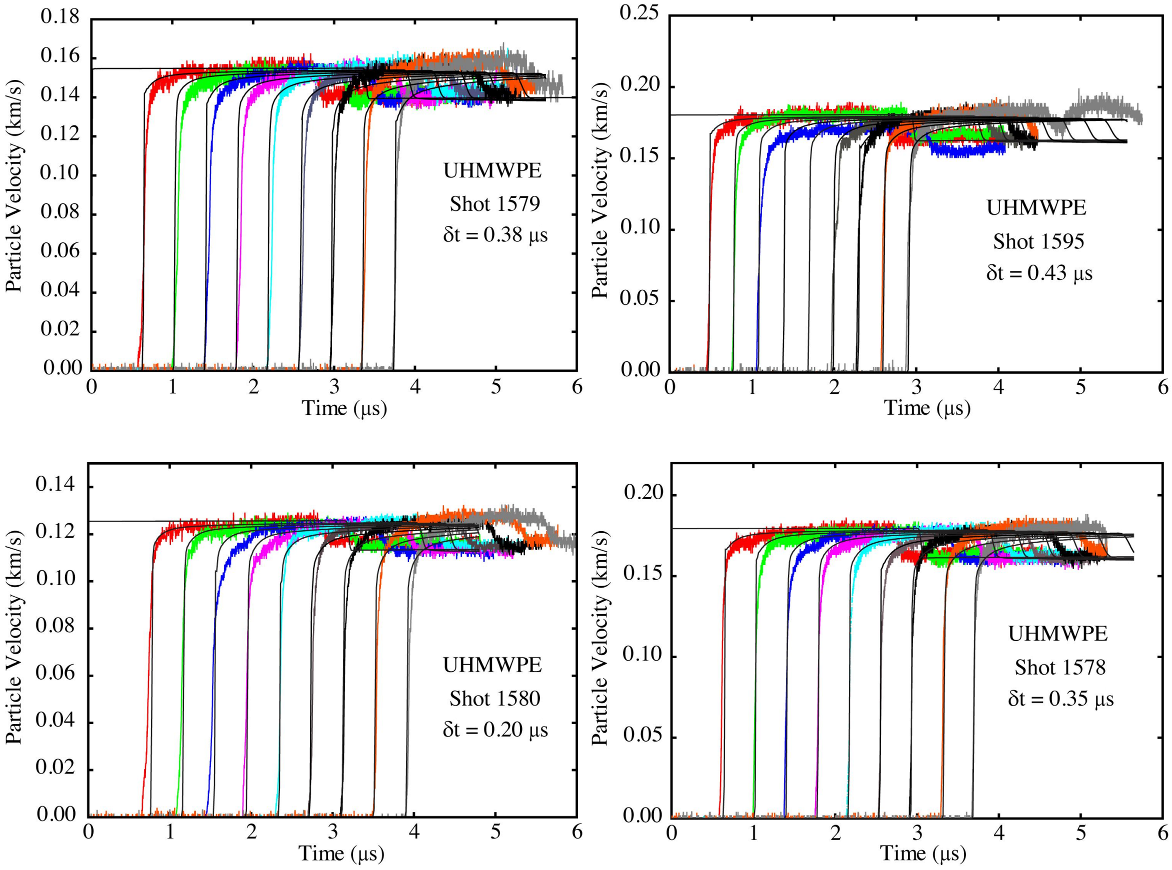

Figure 93: Experimental velocity profiles for UHMWPE (colored lines) and GAP model (black) lines.

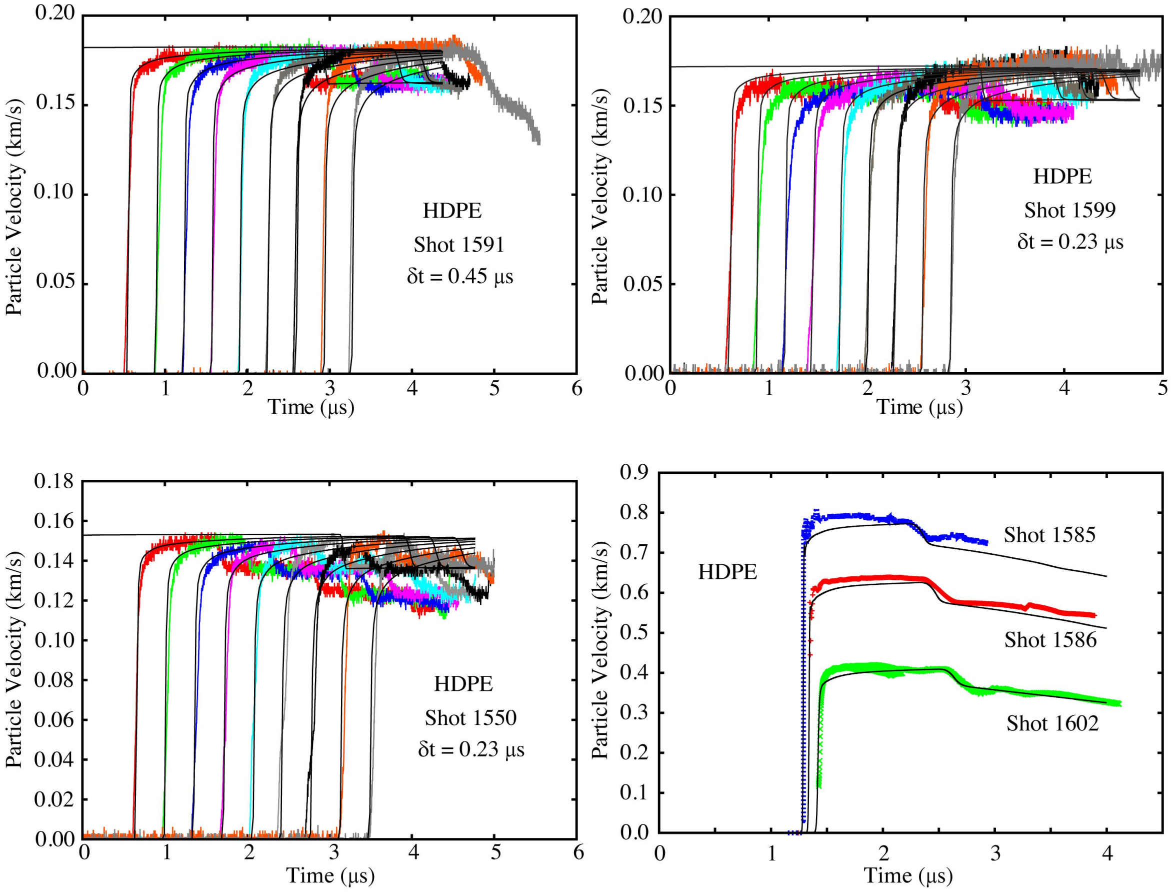

Figure 94: Experimental velocity profiles for HDPE (colored) and GAP model (black). Lower right plot shows the spallation profiles.

that occurs when sufficient tensile stresses arise to partially or completely “spall-off” a piece of an impacted sample. By design, propagating tensile waves can be made to constructively interfere in shock propagation experiments to produce tensile stresses sufficient to spall the sample. Spallation experiments thus elucidate dynamic failure strengths of a material. Further discussions of the GAP damage model and spallation will be provided in the next section.

XIII.G Damage in GAP

We will make the assumption that polyethylene damages by brittle-like crack growth mechanisms. While polyethylene is clearly not truly brittle, we find that this assumption can explain many of the observed experiments involving damage evolution reported earlier in this L2 report. We thus proceed with this as our hypothesis. Parenthetically, much of the work below is based on the work of J. Dienes [8].

Recall that in fracture mechanics, it is not the crack size, c, nor applied stress, σ, that is important, but rather a combination, called the stress intensity K, with units of $c^{1/2}\sigma$, which governs the crack growth in a brittle material. GAP considers micro-crack growth of both tensile cracks (mode I) and shear (mode II). The stress intensity for shear, is expressed in terms of the deviatoric stress, $s_{ij} = \sigma_{ij} - p\delta_{ij}$, where p is a third of the trace of the Cauchy stress tensor σ_{ij}:

$$K = \sqrt{\frac{3}{2}\pi c s_{ij} s_{ij}}. \tag{77}$$

In pure model I, the relevant stress intensity, $\bar{K}$, for a tensile crack $\bar{c}$ is taken to be

$$\bar{K} = \sqrt{\frac{9}{2}\pi \bar{c} p^2}. \tag{78}$$

In Eq. (77), the Einstein summation convention is implied and $s_{ij}s_{ij}$ is related to the second invariant of the deviatoric stress tensor.

In his modeling of the fracture process, Dienes used the experimental observation that the speed of a growing shear crack, $\dot{c}$, is divided into slow and rapid growth regimes, as a function of the stress intensity [8]. The value of the stress intensity at the transition point between the two regimes is a material property called the fracture toughness $K_{0\mu}$. In GAP, $K_{0\mu}$ is taken to be a function of the applied pressure, for a material in compression. It is also a function of strain rate and temperature. The label μ in $K_{0\mu}$ represents the coefficient of friction dependence of the fracture toughness. The concept is simple: under hydrostatic compression, shear crack growth is deterred by frictional forces acting between closed crack surfaces. A simple presentation of many of these concepts can be found in Ref. [9].

Similar ideas apply to the mode I tensile cracks. The speed of a growing mode I crack, $\dot{\bar{c}}$, is again divided into slow and rapid growth regimes, as a function of the stress intensity. The value of the stress intensity at the transition point between the two regimes is the fracture toughness, $\bar{K}_0$, which is only active when the material is in tension, thus the coefficient of friction plays no role.

Figure 95 shows the qualitative behavior of the shear crack speed - stress intensity relation. Up to a constant factor denoted f_1, the transition between slow and rapid growth is governed by $K_{0\mu}$. The other notable observation is that in the rapid growth regime, shear crack speeds (in homogeneous materials) will not exceed the shear wave speed of the material. Thus, an upper limit is given by $\nu_{max} = \nu\sqrt{g/\rho}$, where g is a measure of the shear modulus, ρ is the density, and $0 < \nu < 1$ is a scale factor for shear. This same condition is also applied to the mode I cracks, as well, but with parameter $\bar{\nu}$ replacing ν. In the slow growth regime, a simple power law, with a constant exponent m is used:

$$\dot{c} = \nu_{max}\frac{1}{f_2^m}\left(\frac{K}{K_{0\mu}}\right)^m, \ K < K_{0\mu} f_1, \tag{79}$$

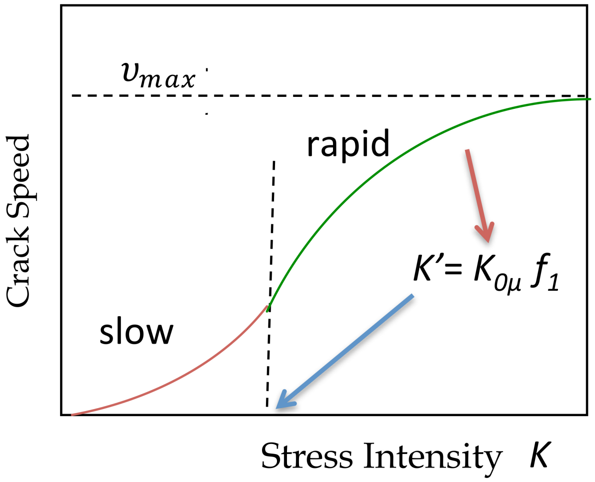

Figure 95: Shear crack growth is divided into slow and rapid crack growth regimes, separated by the fracture toughness.

where f_1 and f_2 are constants given by the expressions

$$f_1 = \sqrt{1 + \frac{2}{m}},\ f_2 = f_1 \left(1 + \frac{m}{2}\right)^{1/m}. \tag{80}$$

Throughout this report (and for all other materials investigated), for mode II damage a simple cubic with $m = 3$ is used, but note that other values are allowed.

In the rapid growth regime, another simple function of K is used:

$$\dot{c} = \nu_{max} \left[1 - \left(\frac{K_{0\mu}}{K}\right)^2\right],\ K > K_{0\mu} f_1. \tag{81}$$

It is easily seen that the functional expressions, Eqs. (79) and (81), and their first derivatives are continuous at $K = K_{0\mu} f_1$, and that Eq. (81) asymptotes to the correct limit of ν_{max}, for large K.

In GAP, the shear fraction toughness $K_{0\mu}$ is pressure, strain rate, and temperature dependent:

$$K_{0\mu} = K_0(\dot{\epsilon}, T) \left[1 + \frac{\pi \mu' \Theta(p) \sqrt{c}}{K_0(\dot{\epsilon}, T)} \left(1 + \frac{\mu' \Theta(p) \sqrt{c}}{K_0(\dot{\epsilon}, T)}\right)\right]^{1/2}, \tag{82}$$

where μ_s is the coefficient of friction, and

$$\mu' \equiv \mu_S \sqrt{\frac{45}{2(3 - 2\mu_S^2)}}. \tag{83}$$

In Eq. (82), $p = -p_m$ is the EOS pressure, and is defined to be positive in compression. The function $\Theta(p) = p$, when p is compressive, and zero otherwise. $K_0(\dot{\epsilon}, T)$ is

$$\log_{10} K_0(\dot{\epsilon}, T) = k_0 + k_T \log_{10} a_T(T) - k_E \log_{10} \left(\frac{\dot{\epsilon}_{eff}}{\dot{\epsilon}_0}\right), \tag{84}$$

where $\dot{\epsilon}_0$ is a material parameter, and

$$\dot{\epsilon}_{eff} = \sqrt{\frac{2}{3} \dot{\epsilon}_{ij} \dot{\epsilon}_{ij}}. \tag{85}$$

As seen from Eq. (84), the temperature dependence enters the fracture toughness through the temperature-dependent function $a_T(T)$, the shift function, which is a quantity fundamental to viscoelastic theory (reviewed in Sec. XIII.C).

Similar expressions apply to mode I. First, $\bar{\nu}_{max} = \bar{\nu}\sqrt{g/\rho}$. Second, slow growth is described by

$$\dot{\bar{c}} = \bar{\nu}_{max} \frac{1}{f_2^3} \left(\frac{\bar{K}}{\bar{K}_0}\right)^m, \; \bar{K} < \bar{K}_0 f_1. \tag{86}$$

where f_1 and f_2 are defined previously, but using $m = 1$. In the rapid growth regime, we use:

$$\dot{\bar{c}} = \bar{\nu}_{max} \left[1 - \left(\frac{\bar{K}_0}{\bar{K}}\right)^2\right], \; \bar{K} > \bar{K}_0 f_1 \tag{87}$$

where

$$\log_{10} \bar{K}_0 = k_4. \tag{88}$$

Next, several "lengths" that characterize the cracked configuration are introduced. The first, as we have already discussed, is the size of an average shear $c(t)$ and tensile $\bar{c}(t)$ crack. Before the polymer is deformed, it is assumed that there are a large number of initial cracks that act as nucleation sites for growth. This may be thought of as pre-load damage. The average initial size is then denoted by c_0 and $\bar{c}_0$. These are insufficient to characterize the initial state of shear and volume crack damage. According to Continuum Damage Mechanics (CDM), the number of cracks per unit volume (*i.e.*, the number density of cracks) is also required [8]. To this end, divide the total volume V_{tot} of the polymer into cells of volume a_0^3 and $\bar{a}_0^3$. There is one shear crack per each volume a_0^3 and one tensile crack per each volume $\bar{a}_0^3$. We will take a_0 and $\bar{a}_0$ to be fixed values (*i.e.*, unlike the c's, they do not evolve with the deformation).

To complete the analysis, we need explicit representations of the crack strains of Eqs. (24)-(27). These are given by

$$g_{eff} \dot{\epsilon}_{ij}^c = \frac{d}{dt}\left[\left(\frac{c}{a_0}\right)^3 \sum_{n=0}^{N} s_{ij}^{(n)}\right] \tag{89}$$

$$B_{eff} \dot{\epsilon}_{\nu}^c = -\frac{d}{dt}\left[\left(\frac{\bar{c}}{\bar{a}_0}\right)^3 \sum_{m=0}^{M} p^{(m)}\right], \tag{90}$$

where

$$g_{eff} = \sum_{n=0}^{N} g^{(n)} \left(\frac{1 - e^{-\Delta\phi^{(n)}}}{\Delta\phi^{(n)}}\right), \tag{91}$$

$$B_{eff} = \sum_{m=0}^{M} B_T^{(m)} \left(\frac{1 - e^{-\Delta\bar{\phi}^{(m)}}}{\Delta\bar{\phi}^{(m)}}\right), \tag{92}$$

$$\Delta\phi^{(n)}(t) = \int_{t-\Delta t}^{t} \frac{dt'}{\tau^{(n)}(t')}, \tag{93}$$

and

$$\Delta\bar{\phi}^{(m)}(t) = \int_{t-\Delta t}^{t} \frac{dt'}{\bar{\tau}^{(m)}(t')}. \tag{94}$$

To calibrate the model thusly described, *i.e.*, the damage portion of GAP, several experiments were used. First, mode I damage as described by Eqs. (78), (86), (87), (88) and (90) are necessary to match the spallation experiments of Dattelbaum, *et al.* mentioned in the previous Section. Table 23 lists the parameters for HDPE. As shown in Fig. 94, while damage accumulates in the HDPE sample, it never completely spalls. Rather the sample slowly elongates in tension and the tensile damage accumulates accordingly. As it does, the free surface of the sample decelerates.

Table 23: Volumetric damage model parameters for HDPE and UHMWPE.

$\bar{c}_0$(m)	$\bar{a}_0$(m)	k_4(log Pa $\sqrt{m}$)	$\bar{\nu}$
8.0e-07	1.0e-06	7.3	1.0

Table 24: Shear damage model parameters for UHMWPE and HDPE.

	c_0(m)	a_0(m)	k_0 (log Pa $\sqrt{m}$)	k_T	k_E	$\dot{\epsilon}_0$/s	ν	μ_S
HDPE	3.0e-06	3.4e-05	8.0	0.0	0.2	1.0	0.4	0.1
UHMWPE	1.0e-06	3.4e-05	8.0	0.0	0.2	1.0	0.4	0.1

Second, Taylor impact experiments of Cady and Clark aid in restricting shear crack model parameters. Parameters used in the simulations described below, are listed in Table 24 for both polymers. In the HDPE Taylor experiment, a 0.3” diameter, by 1.5” long HDPE cylinder was fired into a steel anvil at 264.5 m/s. High speed imaging was then used to observe the deformation. The same sample dimensions were used in the UHMPE experiment and simulation, but the impact speed reduced slightly to 240 m/s. Figure 96 shows snap shots of a 3-Dim. simulation at initial time and then again at the moment of maximum compression for the two polymers. Comparison with the experiments is done in Fig. 97 and 98, and show the polyethylene sample at its fully compressed state, and also its relaxed state (during rebound). In both cases the coefficient of friction between the polyethylene and the steel anvil was taken to be 0.1. For approximately the same impact speed, HDPE tends to undergo larger permanent deformation than does UHMWPE. While the overall comparison to experiment was gratifying, the simulation showed very little relaxation from its fully compressed state. This is in contrast to the experiment, where the polymer continued to relax in the longitudinal direction far more than the model indicated. In fact, because the fully relaxed UHMWPE model prediction differed so little from the fully compressed values, the relaxed state is not included in Fig. 98. In principle, there should be sufficient generality in the GAP model to capture more of the observed late time relaxation, and thus better agree with the experiment. This would require recalibrating the model, which at this point will not be attempted.

A third experiment, called Dynamic Tensile Extrusion (DTE) is a large deformation experiment, and provides a strong illustration of evolving tensile and shear damage in HDPE. We defer discussion of this experiment, and the corresponding GAP simulation, to the next Section.

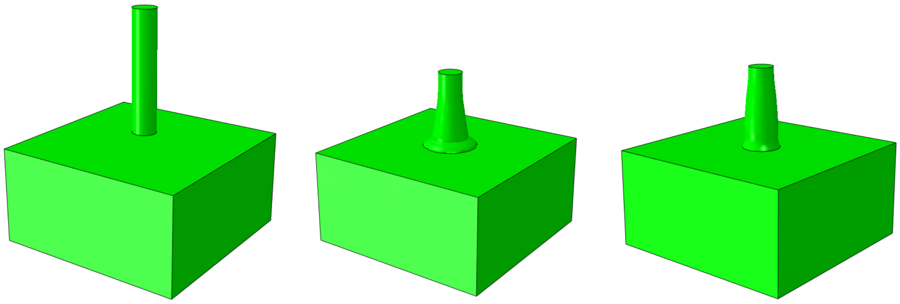

Figure 96: 3-Dim. Taylor impact simulations using the GAP model. Initial geometry (left), HDPE (center), UWMWPE (right) at their moment of maximum compression.

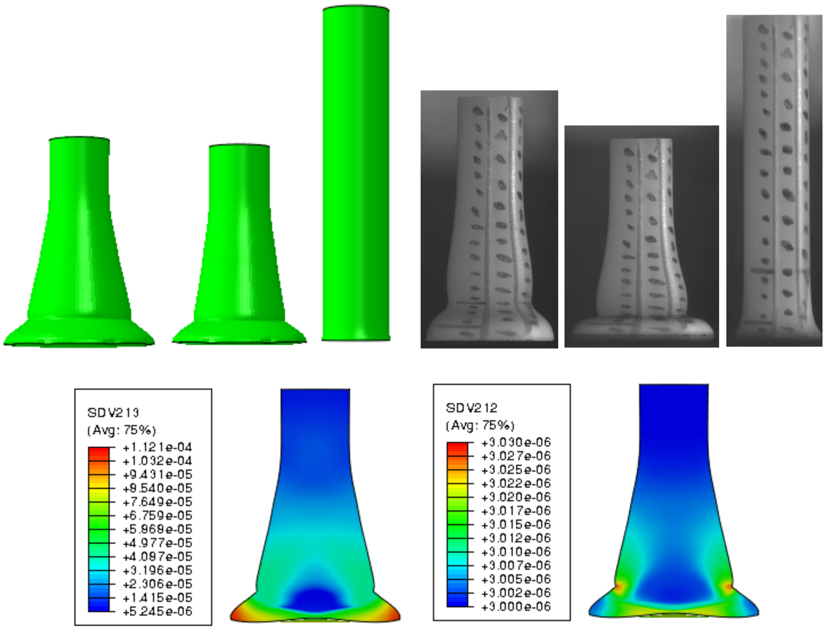

Figure 97: 3-Dim. HDPE Taylor impact simulations using the GAP model (three top left), with snap shots of the experiment (three top right). In each series of three images, the sample at impact (right), maximum compression (center), and relaxed after rebound (left) are shown. In the bottom two frames, the volumetric (left) and shear (right) crack size from evolving damage are shown. The color scheme indicates the current size of the mode I (SDV213) and II (SDV212) cracks.

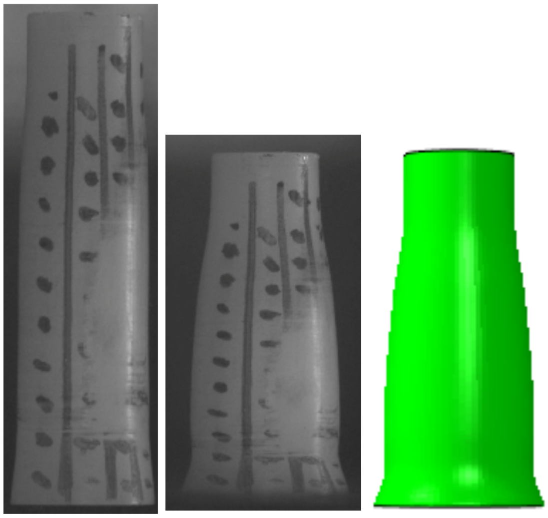

Figure 98: 3-Dim. UHMWPE Taylor impact simulation at maximum compression using the GAP model (right), with snap shots of the experiment at maximum compression (center). The fully relaxed experimental sample (after rebound) is also shown (left).

XIII.H Non-Uniqueness of Parameters

As was alluded to in Sec. XIII.F, the requirement for having a single model, namely GAP, general enough to fit many applications requires a model with many parameters. GAP is after all, a rate, pressure, and temperature-dependent viscoelastic, plastic, shear damage, volumetric damage, and EOS model, where the EOS model has equilibrium and non-equilibrium contributions. While the number of calibration experiments done for this L2 work was large, they remain insufficient to uniquely determine all the GAP parameters. To illustrate this, we change the initial pre-damage mode I crack size from 8.0e-07 m (Table 23) to 3.0e-07 m (Table 25). To fit the HDPE spall experiments of Dattelbaum, *et al.*, we must accordingly decrease k_4 from 7.3 to 6.9 log Pa $\sqrt{m}$. Moreover, the $B_T^{(m)}$ (Table 26) need to be altered as well. The result of this re-calibration, as shown in Fig. 99, is an equally good fit to the velocity profile data as obtained from the original fit (Fig. 94). It must be expected however, that there are experiments that would favor one calibration over the other.

Along these same lines, we can alter the shear damage parameters slightly. Table 27 has an altered parameter set, contrasted to Table 24. The overall shapes of the deformed Taylor sample (the experimental observable) vary a small amount, and the internal shear damage becomes more intense. These differences can be seen by contrasting Fig. 100 simulation results with Fig. 97. Clearly, while gross change in shape is visible to the eye, the magnitude of the shear damage changes more substantially.

We conclude this section with a discussion of DTE experiments and GAP simulations. Prior DTE experiments were conducted by J. Furmanski, *et al.* [14, 191]. Important features of Furmanskis work are captured in Fig. 101. First, at three velocities investigated (450, 486, and 550 m/s), the spherical HDPE ball is permanently deformed in the extrusion process. At 486 m/s and above, the HDPE completely fractures (and even fragments). Post-mortem examination of the polymer texture reveals large tensile and shear strains prior to the sample failing. The v-shaped chevron at the failure surface (bottom image of Fig. 101) indicates that shear, along with tension, plays a role in the dynamic failure of the HDPE.

Naturally, this begs the question if the GAP model can capture any of these experimental observations. To avoid ambiguity, we note that we used the original GAP parameterization, including the EOS (Table 22) and volumetric damage parameter set (Table 23), although the simulation below corresponds to the shear parameter set from Table 27. We carried out a DTE simulation corresponding to a HDPE ball extruded through the conical orifice with an initial velocity of 500 m/s. The model predictions are shown in Fig. 102. As indicated above, the HDPE ball undergoes very large tensile deformation. Once again, it is gratifying to observe that the GAP model produces simulation results that agree with many of the details of the DTE experiments of Furmanski, *et al.* [14, 191]. These comparisons include the overall shape, the extensive tensile damage spanning the deformed sample, and the v-shaped chevron shear structure. Unfortunately, we were unable to fail (or fragment) the sample, using the known FEM technique of element deletion, as this resulted in the simulation crashing, immediately following the deletion. Nevertheless, the localized shear, atop the tensile damage, looks to be in agreement with one's intuition of what occurs in the experiment.

Table 25: New volumetric damage model parameters for HDPE.

$\bar{c}_0$(m)	$\bar{a}_0$(m)	k_4(log Pa $\sqrt{m}$)	$\bar{\nu}$
3.0e-07	1.0e-06	6.9	1.0

Table 26: Original and new Bulk-Maxwell model parameters for HDPE.

m	$\log_{10}(\bar{\tau}^{(m)})(s)$ (old)	$B_T^{(m)}$(GPa) (old)	$B_T^{(m)}$(GPa) (new)
1	-4	1.1	0.4
2	-5	1.0	0.3
3	-6	0.9	0.2
4	-7	0.3	0.2
5	-8	0.3	0.2
6	-9	0.3	0.2

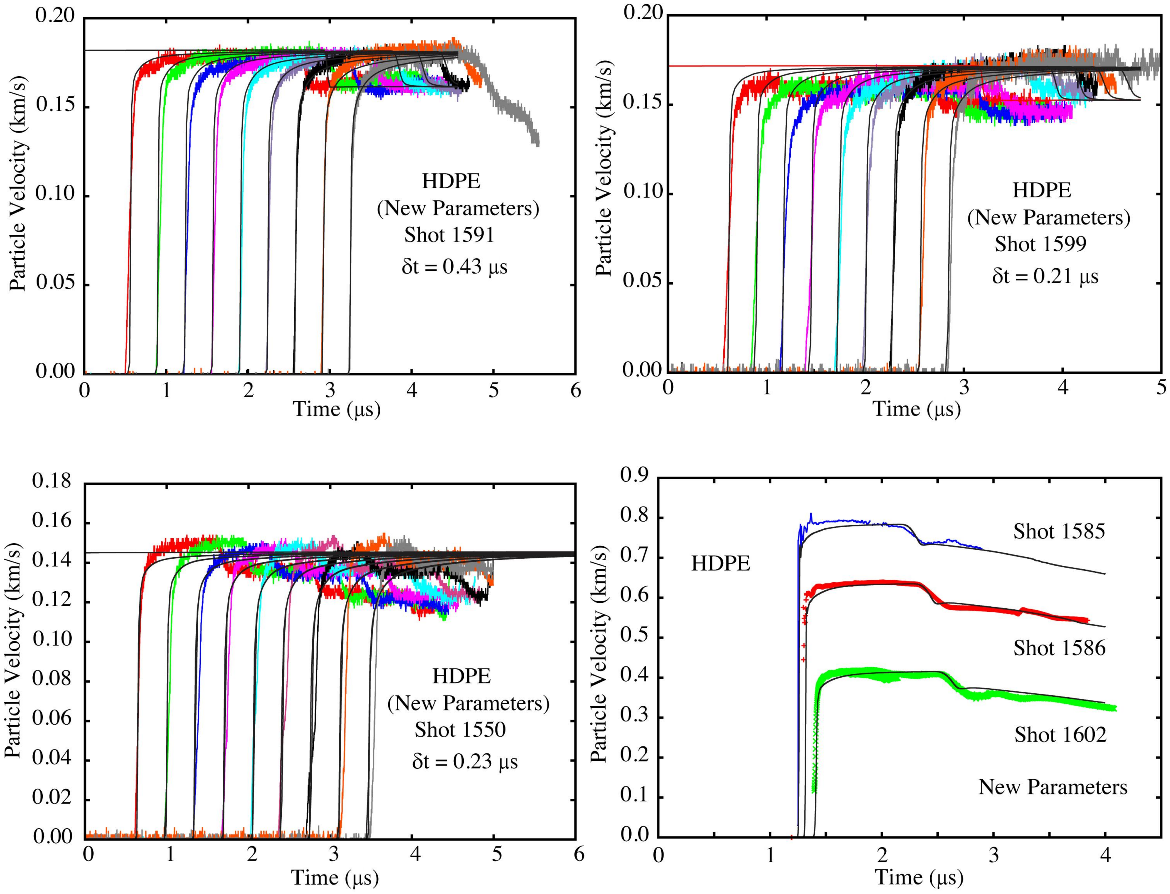

Figure 99: Experimental velocity profiles for HDPE (colored) and GAP model (black) using a recalibrated parameter set. Lower-right plot shows the spallation profiles.

Table 27: Re-calibrated shear damage model parameters for HDPE.

	c_0(m)	a_0(m)	k_0 (log Pa $\sqrt{m}$)	k_T	k_E	$\dot{\epsilon}_0$/s	ν	μ_S
HDPE	3.0e-06	3.4e-05	7.4	0.0	0.2	1.0	0.4	0.1

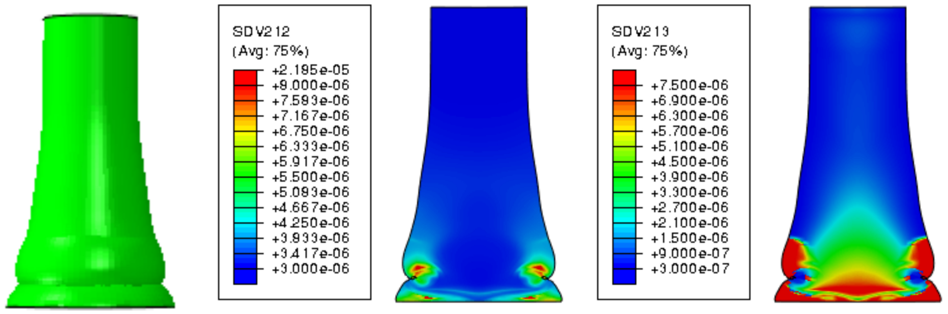

Figure 100: 3-Dim. HDPE Taylor impact simulations using the GAP with the modified shear damage parameters of Table 27. In the bottom two frames, the volumetric (left) and shear (right) crack size from evolving damage are shown. The color scheme indicates the current size of the mode I (SDV213) and II (SDV212) cracks.

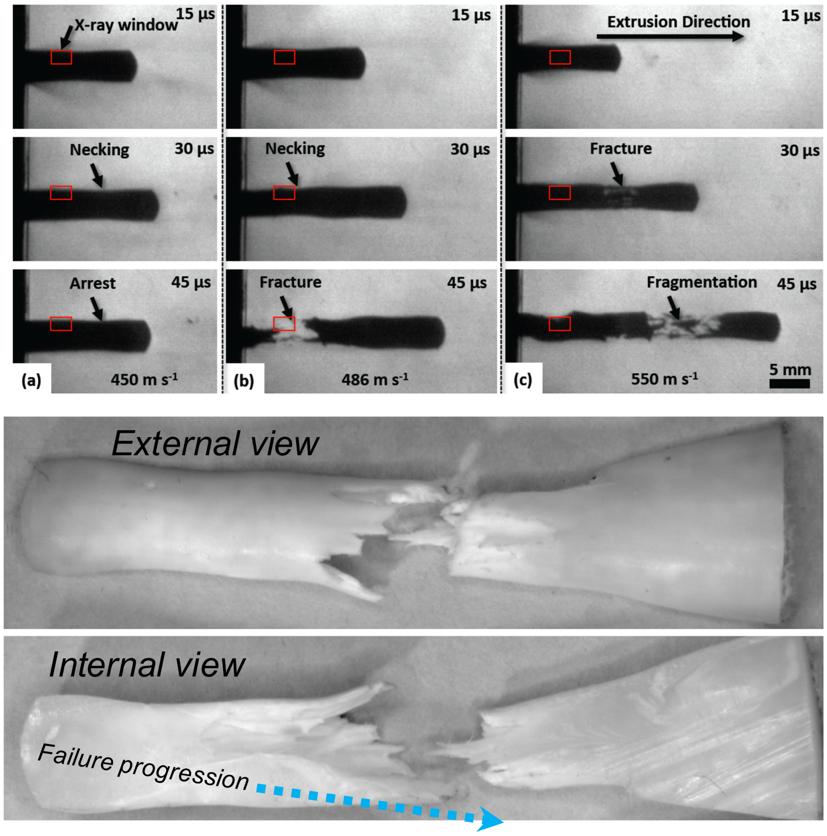

Figure 101: High speed images of HDPE undergoing large deformation after it extrudes through the DTE die at 450-550 m/s (top set). The bottom pair of images show the post-fired samples that have undergone complete failure. The bottom image shows the sample that has been cleaved in half.

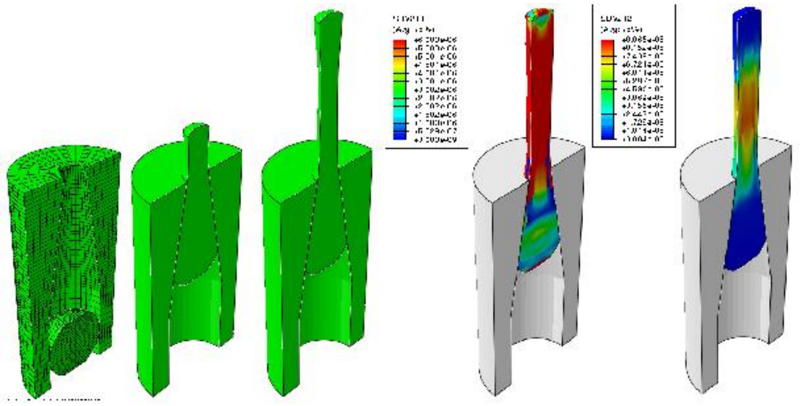

Figure 102: 3-Dim. HDPE DTE simulation using GAP. The initial speed of the ball is 500 m/s. The left-most figure is the meshed initial geometry. Proceeding from left to right, the next two images are later time snapshots, followed by the accumulated volumetric and shear damage. As before, the color scheme indicates the current size of the mode I (SDV213) and II (SDV212) cracks.

XIII.I Conclusions of the GAP Model Applied to HDPE and UHMWPE.

The Glassy Amorphous Polymer (GAP) model is based on the *ansatz* that both the deviatoric and the volumetric contributions to the thermodynamic free energy are functions of the rate of deformation. GAP is a rate, pressure, and temperature-dependent viscoelastic, plastic, shear damage, volumetric damage, and EOS model. The resulting model has been shown to accurately capture the thermomechanical polymer behavior ranging from equilibrium properties all the way to that observed in high-rate shock experiments. Our L2 investigation focused on polyethylene of two types: HDPE and UHMWPE. Besides PMMA, owing to the extensive experimental program completed as part of this L2, only HDPE and UHMWPE have sufficient experiments completed to determine well (*i.e.*, calibrate) the many parameters required by the GAP model. Included in this L2 investigation were several experiments where polymer damage played a critical role. These were Taylor impact, plate impact spallation, and Dynamic Tensile Extrusion (DTE) tests. Of the three, the Taylor tests probably coupled least to damage. Based on the hypothesis that both types of polyethylene damage via brittle-like crack growth mechanisms, we found that we could explain many of the features observed in these three experiments. Finally, we mention that all of our simulations used GAP implemented in the commercial Lagrangian finite element code Abaqus [10]. Future work will include implementing GAP in other codes of interest to the NNSA.

XIV Acknowledgements

This work was conducted at Los Alamos National Laboratory, which is operated by Los Alamos National Security, LLC, for the National Nuclear Security Administration of the U.S. Department of Energy under contract DE-AC52-06NA25396.

Section VII - The authors are grateful for target assembly and firing support from Lee Gibson, Brian Bartram, Austin Goodbody, and Justin Jones.

Section VIII - The IMPULSE team, Sector 32, and the Dynamic Compression Sector are gratefully acknowledged. This research used resources of the Advanced Photon Source, a U.S. Department of Energy (DOE) Office of Science User Facility operated for the DOE Office of Science by Argonne National Laboratory under Contract No. DE-AC02-06CH11357.

Section IX - We are grateful to Brian Bartram and Lee Gibson for assembling and performing measurements on the experimental assemblies, and to John Wright and Tim Tucker for performing shot operations on the gas gun.

Section X - We are grateful to Joseph Torres, Robert Gianan, Jillian Adams, Caleb Van Buskirk, and Olivia Trautschold for performing DSC, MDSC, CTE, and torsional DMA measurements.

Bibliography

[1] B. E. Clements, J. Appl. Phys. **112**, 083511 (2012); ibid., in Shock Compression of Condensed Matter-2009, edited by M. L. Elert, W. T. Butler, M. D. Furnish, W. W. Anderson and W. G. Proud, 2009 AIP, 1223-1228 (2009); B. E. Clements in http://arxiv.org/abs/1207.2723

[2] http://polymerindustries.com/wp/densetec-hdpe. Retrieved 10-16-2019.

[3] http://polymerindustries.com/wp/polyslick-uhmw-sheet. Retrieved 10-16-2019.

[4] R. Hill, *The Mathematical Theory of Plasticity*, Oxford Engineering Science Series 11, (Oxford University Press, New York) 1950.

[5] S. R. Bodner and Y. Partom, J. Appl. Mech. **42**, 385-389, (1975).

[6] G. J. Frank and R. A. Brockman, Int. J. Solids Struct. **38**, 51495164 (2001).

[7] P. G. Tait, Physics and Chemistry of the Voyage of H.M.S. Challenger, Vol. 2, Part IV. H.M.S.O. (1888).

[8] J. Dienes has published numerous articles on statistical crack mechanics. See for example, J. Dienes and J. D. Kershner, Multiple shock initiation via statistical crack mechanics, CONF-980803, (**LA-UR-98 3046**), The 11th International Detonation Symposium, Snowmass, Colorado, August 31 -September 4, (1998); J. Dienes, Statistical Crack Mechanics, Report **LA-UR-831705**, Los Alamos National Laboratory, Los Alamos, NM; J. Dienes, K. Zuo, and J. D. Kershner, Impact initiation of explosives and propellants via statistical crack mechanics, J. Mech. Phys. Solids, 54, 1237-1275 (2006); J. Dienes, J. Geophys Res., 88, No. B2, 1173-1179, (1983).

[9] J. G. Bennett, K. S. Haberman, J. N. Johnson, B. W. Asay, and B. F. Henson, J. Mech. Phys. Solids, **46**, No. 12, 2303-2322, (1998).

[10] `Abaqus`, 2009. The Abaqus Software is a product of Dassault Systmes Simulia Corp., Providence, RI, USA.©Dassault Systmes.

[11] E. N. Brown, C. P. Trujillo, and G. T. Gray III, *Shock Compression of Condensed Matter - 2007*, AIP Conf. Proc. **955**, 691 (2008).

[12] F. Cao, E. K. Cerreta, C. P. Trujillo, and G. T. Gray III, Acta Materialia **56**, 5804 (2008).

[13] G. T. Gray III, E. Cerreta, C. A. Yablinsky, L. B. Addessio, B. L. Henrie, B. H. Sencer, M. Burkett, P. J. Maudlin, S. A. Maloy, C. P. Trujillo, and M. F. Lopez, *Shock Compression of Condensed Matter - 2005*, AIP Conf. Proc. **845**, 725 (2006)

[14] J. Furmanski, E. N. Brown, B. Clements, C. M. Cady and G. T. Gray III, *EPJ Web Conferences* **26**, 01057 (2012).

[15] T. Y. Cho, B. Heck, and G. Strobl, Colloid Polym. Sci. **282**, 825 (2004).

[16] B. Crist, J. Polym. Sci. B: Polym. Phys. **45**, 3231 (2007).

[17] J. D. Hoffman, R. L. Miller, H. Marand, and D. B. Roitman, Macromolecules **25**, 2221 (1992).

[18] M. F. Butler, A. M. Donald, A. J. Ryan, Polymer **38**, 5521 (1997).

[19] H. Zhou and G. L. Wilkes, Polymer **38**, 5735 (1997).

[20] A. Pawlak and A. Galeski, Macromolecules **38**, 9688 (2005).

[21] A. Pawlak, Polymer **48**, 1397 (2007).

[22] D. M. Dattelbaum and J. D. Coe, "The dynamic loading response of carbon-fiber-filled polymer composites", in *Dynamic Deformation, Damage and Fracture in Composite Materials and Structures*, Elsevier Ltd. (2016)

[23] G. E. Hauver, *Proceedings of the Fifth Symposium (International) on Detonation*, 387 (1970).

[24] E. Z. Novitskii, A. G. Ivanov, and N. P. Khokhlov in "Combustion and Explosion, Proceedings Third All-Union Symposium on Combustion and Explosion", Nauka, Moscow, 1971, p 579, in Russian.

[25] R. A. Graham, J. Phys. Chem. **83**, 3048 (1979).

[26] A. R. Champion, J. Appl. Phys. **43**, 2216 (1972).

[27] Y. Mori, T. Tamura, and K. Nagayama, Rev. Sci. Instrum. **69**(4), 1730 (1998).

[28] K. Nagayama, Y. Mori, K. Hidaka, J. Mater. Processing Tech., **85**, 20 (1999).

[29] C. E. Morris, J. N. Fritz, and R. G. McQueen, J. Chem. Phys. **80**, 5203 (1984).

[30] C. E. Morris, E. D. Loughran, G. F. Mortensen, G. T. Gray, and M. S. Shaw, *Shock Compression of Condensed Matter-1989*, 687 (1990).

[31] F. Dowell, "A simple EOS for 'Linear' (High Density) Polyethylene (Marlex)," **LA-9564-MS**, Los Alamos National Laboratory report (1982).

[32] W. J. Nellis, F. H. Ree, R. J. Trainor, A. C. Mitchell, and M. B. Boslough, J. Chem. Phys. **80**, 2789 (1984).

[33] See [66], pages 121-131.

[34] See [66], pages 777-800.

[35] J. C. F. Millett, N. K. Bourne, E. N. Brown, and G. T. Gray III, *Shock Compression of Condensed Matter-2007*, Vol. 2, 719 (2008).

[36] D. M. Dattelbaum, B. F. Schilling, B. E. Clements, J. Jordan, C. F. Welch, and J. A. Stull, Proceedia Eng., in press, 2017.

[37] D. A. Fredenburg, J. M. Lang, D. M. Dattelbaum, and L. S. Bennett, "Design considerations for obtaining deep release in reacted Epon 828," **LA-UR-16-21748**, Los Alamos National Laboratory, (2016).

[38] P. A. Rigg, R. J. Scharff, and R. S. Hixson, Journal of Physics: Conference Series **500**, 032018 (2014).

[39] J. M. Lang, D. A. Fredenburg, J. D. Coe, and D. M. Dattelbaum, *Shock Compression of Condensed Matter-2017*, in press (2017).

[40] P. A. Rigg, M. D. Knudsen, R. J. Scharff, and R. S. Hixson, J. Appl. Phys. **116**, 033515 (2014).

[41] L. Fontana, D. Q. Vinh, M. Santoro, S. Scandolo, F. A. Gorelli, R. Bini, M. Hanfland, Phys. Rev. B. **75**, 174112 (2007).

[42] L. Fontana, M. Santoro, R. Bini, D. Q. Vinh, S. Scandolo, J. Chem. Phys. **133**, 204502 (2010).

[43] O. T. Strand, D. R. Goosman, C. Martinez, T. L. Whitworth and W. W. Kuhlow, Rev. Sci. Inst. **77**, 083108 (2006).

[44] L. M. Barker and R. E. Hollenbach, J. Appl. Phys. **43**, 4669 (1972).

[45] S. P. Marsh, ed., *LASL Shock Hugoniot Data*, University of California Press, Berkeley, 1980.

[46] D. A. Fredenburg, (U) "Epon 828 Polymer Modeling", **LA-CP 16-00822**, Los Alamos National Laboratory (2016)

[47] E. Chisolm, C. Greeff, and D. George, "Constructing Explicit Multiphase Equations of State with OpenSesame", **LA-UR-05-9413**, Los Alamos National Laboratory (2005)

[48] R. Vignjevic,J. C. F. Millet, N. K. Bourne, Y. Meziere, and A. Lukyanov, Shock compression of condensed matter - 2005, American Institute of Physics, 825 (2006).

[49] W. J. Carter and S. P. Marsh, "Hugoniot Equation of State for Polymers", **LA-13006-MS**, Los Alamos National Laboratory, (1995).

[50] Hexcel HexTow carbon fiber datasheet. `http://www.hexcel.com`.

[51] S. Alexander, C. T. Key, and S. C. Schumaker, *J. Appl. Phys.* **114**, 223515 (2013).

[52] R. G. Parr and W. Yang, *Density-Functional Theory of Atoms and Molecules*, Oxford University Press (New York, NY), 1989.

[53] P. J. Rae and E. N. Brown, Exp. Techniques **40**, 1085 (2016).

[54] E. N. Brown, R. B. Willms, G. T. Gray III, P. J. Rae, C. M. Cady, K. S. Vecchio, J. Flowers, and M. Y. Martinez, Exp. Mech. **47**, 381 (2007).

[55] R. S. Hixson, private communication.

[56] T. Antoun, L. Seaman, D. R. Curran, G. I. Kanel, S. V. Razorenov, and A. V. Utkin, *Spall Fracture*, New York: Springer (2003).

[57] O. T. Strand , D. R. Goosman, C. Martinez, T. L. Whitworth, and W. W. Kuhlow W W, *Rev. Sci. Instr.* **77** 083108 (2006).

[58] A. Sollier, V. Bouyer, L. P. Terzulli, M. Doucet, L. Decaris, and P. Hebert, *PDV characterization of the expanding detonation products of a TATB based high explosive* presented at the 6^{th} Annual PDV Workshop, Nov. 3-4, 2011, Livermore, CA. `http://kb.osu.edu/dspace/handle/1811/52739`

[59] D. C. Smith, Ind. Eng. Chem. **48**, 1161 (1956).

[60] T. D. Aslam, R. L. Gustavsen and B. D. Bartram, J. Phys. Conf. Series, **500**, 032001(2014) `http://dx.doi.org/10.1088/1742-6596/500/3/032001`

[61] R. F. Boyer, J. Macromol. Sci. B **8**, 503 (1973).

[62] *Standard Test Method for Determining Specific Heat Capacity by Sinusoidal Modulated Temperature Differential Scanning Calorimetry*, ASTM E2716-09 (2009; Reapproved 2014).

[63] L. C. Thomas, Modulated DSC Paper #2, “Modulated DSC® Basics: Calculation and Calibration of MDSC Signals”, TA Instruments Technical Paper TP007.

[64] L. C. Thomas, Modulated DSC Paper #3, “Modulated DSC® Basics: Optimization of MDSC® Experimental Conditions”, TA Instruments Technical Paper TP008.

[65] D. A. Ditmars, S. Ishihara, S. S. Chang, and G. Bernstein, J. Res. Nat. Bur. Stand. 87, 159-163 (1982).

[66] B. Wunderlich, *Thermal Analysis of Polymeric Materials* (Springer, The Netherlands, 2005).

[67] AThAS Database, SpringerMaterials Release 2014, Version 2014.06. Marek Pyda, ed. `http://materials.springer.com/polymerthermodynamics`

[68] J. J. Aklonis and W. J. MacKnight, *Introduction to Polymer Viscoelasticity, 2nd edition* (John Wiley & Sons, New York, 1983), pp. 36-56.

[69] P. Wood-Adams and S. Costeux, Macromolecules **34**, 6281 (2001).

[70] J. A. Resch, U. Kessner, and F. J. Stadler, Rheol. Acta **50**, 559 (2011).

[71] A. H. Pacheco, R. L. Gustavsen, T. D. Aslam, and B. D. Bartram, “Hugoniot based equation of state for solid polyurea and polyurea aerogels”, to be published.

[72] D. M. Dattelbaum, J. D. Coe, C. B. Kiyanda, R. L. Gustavsen and B. M. Patterson, J. Appl. Phys., **115**, 174908 (2014)

[73] R. G. McQueen, S. P. Marsh, J. W. Taylor, J. N. Fritz and W. J. Carter, *High-Velocity Impact Phenomena*, ed. R. Kinslow (New York, NY: Academic Press) pg. 293 (1970)

[74] P. A. Rigg, R. J. Scharff, R. S. Hixson and M. D. Knudson, J. Appl. Phys., **116**, 033515 (2014)

[75] R. V. Jones and P. J. Boeke, Ind. Eng. Chem. **48**, 1155 (1956).

[76] M. Mock, S. Bartyczak, G. Lee, J. Fedderly and K. Jordan, AIP Conf. Proc. **1195**, 1241 (2009)

[77] F. R. Svingala, M. J. Hargather and G. S. Settles, Int. J. Impact. Eng. **50**, 76 (2012)

[78] T. Jiao and R. J. Clifton, J. Phys. Conf. Series, **500**, 112036(2014) `http://dx.doi.org/10.1088/1742-6596/500/11/112036`

[79] Lee J K, Gould G L and Rhine W 2009 *J. Sol.-Gel. Sci. Techn.* **49** pp 209-220

[80] Leventis N, Sotiriou-Leventis C, Chandrasekaran N, Mulik S, Larimore Z J, Lu H, Churu G and Mang J T 2010 *Chem. Mater.* **22** pp 6692-6710

[81] http://www.buyaerogel.com/product/airloy-x103/

[82] Murnaghan F D 1944 *P. Nat. Acad. Sci. USA* **30** pp 244-247

[83] Herrmann W 1969 *J. Appl. Phys.* **40** pp 2490-2499

[84] Carroll M M and Holt A C 1972 *J. Appl. Phys.* **43** pp 1626-1636

[85] Bdzil J B, Menikoff R, Son S F, Kapila A K and Stewart D S 1999 *Phys. Fluids* **11** pp 378-402

[86] Aslam T D, Gustavsen R L, Sanchez N J and Bartram B D 2011 *AIP Conf. Proc.* **1426** pp 767-770

[87] Whitham G B 1974 *Linear and Nonlinear Waves* (New York: Wiley)

[88] Toro E F 1997 *Riemann Solvers and Numerical Methods for Fluid Dynamics* (Berlin: Springer)

[89] LeVeque R J 1992 *Numerical Methods for Conservation Laws* (Basel: Birkhauser)

[90] A. Kundagrami and M. Muthukumar, J. Chem. Phys. **126**, 144901 (2007).

[91] G. Strobl, *The Physics of Polymers* (Springer, New York, 1996).

[92] K. Armitstead and G. Goldbeck-Wood, Advances in Polymer Science **100**, 219 (1992).

[93] G. Reiter, G. R. Strobl, eds., *Progress in Understanding of Polymer Crystallization, Lecture Notes in Physics* **714** (Springer, Heidelberg, 2007).

[94] J. D. Hoffman, G. T. Davies, and J. L. Lauritzen, *Treatise on Solid-State Chemistry* **3** (Plenum Press, New York, 1976).

[95] J. D. Hoffman and R. L Miller, Polymer **38**, 3151 (1997)

[96] M. Muthukumar, Philosophical Transactions of the Royal Society of London A **361**, 539 (2003).

[97] M. Muthukumar, Advances in Polymer Science **191**, 241 (2005).

[98] G. Strobl, The European Physical Journal E **3**, 165 (2000).

[99] T. Yamamoto, Journal of Chemical Physics **107**, 2653 (1997).

[100] M. Muthukumar and P. Welch, Polymer **41**, 8833 (2000).

[101] T. Miura, R. Kishi, M. Mikami, and Y. Tanabe, Physical Review E **63**, 061807 (2001).

[102] A. Koyama, T. Yamamoto, K. Fukao, and Y. Miyamoto, Physical Review E **65**, 050801 (2002).

[103] R. H. Gee, N. Lacevic, and L. E. Fried, Nature Materials **5**, 39 (2006).

[104] N. Lacevic, L. E. Fried, and R. H. Gee, Journal of Chemical Physics **128**, 014903 (2008).

[105] M. Anwar, J. T. Berryman, T. Schilling, Journal of Chemical Physics **141**, 124910 (2014).

[106] M. J. Ko, N. Waheed, M. S. Lavine, and G. C. Rutledge, Journal of Chemical Physics **121**, 2823 (2004).

[107] T. Yamamoto, Macromolecules **47**, 3192 (2014).

[108] R. S. Graham and P. D. Olmsted, Physical Review Letters **103**, 115702 (2009).

[109] Y. Nie, H. Gao, M. Yu, Z. Hu, G. Reiter, and W. Hu, Polymer **54**, 3402 (2013).

[110] Y. Nie, H. Gao, M. Yu, and W. Hu, Polymer **55**, 1267 (2014).

[111] T. Yamamoto, Journal of Chemical Physics **139**, 054903 (2013).

[112] M. Wang, Journal of Physical Chemistry B **114**, 3488 (2010).

[113] O. O. Mykhaylyk, P. Chambon, R. S. Graham, J. P. A. Fairclough, P. D. Olmsted, and A. J. Ryan, Macromolecules **41**, 1901 (2008).

[114] I. Dukovski and M. Muthukumar, Journal of Chemical Physics **118**, 6648 (2003).

[115] J.-U. Sommer and C. Luo, Journal of Polymer Science: Part B: Polymer Physics **48**, 2222 (2010).

[116] C. Luo and J.-U. Sommer, Macromolecules **44**, 1523 (2011).

[117] Y. S. Abu-Mostafa, M. Magdon-Ismail, and H.-T. Lin, *Learning from Data: A Short Course* (AML, USA, 2012).

[118] T. Yamamoto, Polymer **50**, 1975 (2009).

[119] D. M. Sadler and G. H. Gilmer, Physical Review Letters **56**, 2708 (1986).

[120] W. Paul, D. Y. Yoon, and G. D. Smith, Journal of Chemical Physics **103**, 1702 (1995).

[121] S. Plimpton, Journal of Computational Physics **117**, 1 (1995)

[122] *http://lammps.sandia.gov*

[123] P. M. Welch, The Journal of Chemical Physics **146**, 044901, (2017).

[124] E. Alpaydin, *Introduction to Machine Learning* (MIT Press, Cambridge, 2004).

[125] C. M. Bishop, *Pattern Recognition and Machine Learning* (Springer, New York, 2006).

[126] D. Meyer et al., *http://cran.r-project.org/web/packages/e1071/index.html*, version 1.6-3.

[127] M. Ester, H.-P. Kriegel, J. Sander, and X. Xu, in *Proceedings of the Second International Conference on Knowledge Discovery and Data Mining*, 226 (1996).

[128] C. Hennig, *http://cran.r-project.org/web/packages/fpc/index.html*, version 2.1-4.

[129] C. Luo and J.-U. Sommer, Physical Review Letters **112**, 195702 (2014).

[130] M. Muthukumar, The Journal of Chemical Physics **145**, 031105 (2016).

[131] P. Yi, R. Locker, and G. C. Rutledge, Macromolecules **46**, 4723 (2013).

[132] T. A. Ezquerra, E. Lopez-Cabarcos, B. S. Hsiao, and F. J. Balta-Calleja, Physical Review E **54**, 989 (1996).

[133] M. Muthukumar, European Physical Journal E **3**, 199 (2000).

[134] M. Wand and B. Ripley, *http://cran.r-project.org/web/packages/KernSmooth/index.html*, version 2.23-8.

[135] P. D. Olmsted, W. C. K. Poon, T. C. B. McLeish, N. J. Terrill, and A. J. Ryan, Physical Review Letters **81**, 373, (1998).

[136] S. F. Edwards and Th. Vilgis, Polymer **27**, 483 (1986).

[137] S. Seiffert and J. Sprakel, Chem. Soc. Rev. **41**, 909 (2012).

[138] G. Heinrich, E. Straube, and G. Helmis, Adv. Polym. Sci. **85**, 33 (1988).

[139] H. E. H. Meijer and L. E. Govaert, Prog. Polym. Sci. **30**, 915 (2005).

[140] A. Lendlein and S. Kelch, Angew. Chem. Int. Ed. **41**, 2034 (2002).

[141] M. M. Caruso, D. A. Davis, Q. Shen, S. A. Odom, N. R. Sottos, S. R. White, and J. S. Moore, Chem. Rev. **109**, 5755 (2009).

[142] H. Meng and G. Li, Polymer **54**, 2199 (2013).

[143] S. Brin and L. Page, Computer Networks **56**, 3825 (2012).

[144] M. E. J. Newman, Phys. Rev. E **74**, 036104 (2006).

[145] M. Rosvall and C. T. Bergstrom, Proc. Natl. Acad. Sci. U.S.A. **105**, 1118 (2008).

[146] M. E. J. Newman, *Networks: An Introduction* (Oxford University Press: Oxford, UK, 2010).

[147] P. J. Flory, Proc. R. Soc. Lond. A **351**, 351 (1976).

[148] P. J. Flory and D. Y. Yoon, Nature **272**, 226 (1978).

[149] W. Wu, G. D. Wignall, and L. Mandelkern, Polymer **33**, 4137 (1992).

[150] L.-Z. Liu, B. S. Hsiao, B. X. Fu, S. Ran, S. Toki, B. Chu, A. H. Tsou, and P. K. Agarwal, Macromolecules **36**, 1920 (2003).

[151] Z. Jiang, Y. Tang, Y. Men, H.-F. Enderle, D. Lilge, S. V. Roth, R. Gehrke, and J. Rieger, Macromolecules **40**, 7263 (2007).

[152] B. Crist, C. J. Fisher, and P. R. Howard, Macromolecules **22**, 1709 (1989).

[153] M. A. Kennedy, A. J. Peacock, and L. Mandelkern, Macromolecules **27**, 5297 (1994).

[154] F. Chung, L. Lu, and V. Vu, Proc. Natl. Acad. Sci. U.S.A. **100**, 6313 (2003).

[155] P. G. de Gennes, *Scaling Concepts in Polymer Physics* (Cornell University Press: Ithaca, NY, 1979).

[156] P. Erdös and A. Rényi, Publicationes Mathematicae **6**, 290 (1959).

[157] A. Zippelius, P. M. Goldbart, and N. Goldenfeld, Europhys. Lett. **23**, 451 (1993).

[158] P. M. Goldbart, H. E. Castillo, and A. Zippelius, Adv. Phys. **45**, 393 (1996).

[159] H.-H. Kausch and G. H. Michler, Adv. Polym. Sci. **187**, 1 (2005).

[160] J. M. Hutchinson, Prog. Polym. Sci. **20**, 703 (1995).

[161] J. R. White, and A. J. Turnbull, Mater. Sci. **29**, 584 (1994).

[162] M. Celina, Polym. Degrad. Stab. **98**, 2419 (2013).

[163] See, for example: F. Meng, R. H. Pritchard, and E. M. Terentjev, Macromolecules **49**, 2843 (2016).

[164] C.-H. Li, C. Wang, C. Keplinger, J.-L. Zuo, L. Jin, Y. Sun, P. Zheng, Y. Cao, F. Lissel, C. Linder, X.-Z. You, and Z. Bao, Nature Chem. **8**, 618 (2016).

[165] L. J. Fetters, D. J. Lohse, and R. H. Colby, R.H., *Physical Properties of Polymers Handbook, 2nd ed.*, Ed. J.E. Mark (Springer: New York, 2007).

[166] P. M. Welch and C. F. Welch, Scientific Reports, 7, 1241 (2017).

[167] J. L. Jordan, D. T. Casem, J. M. Bradley, A. K. Dwivedi, E. N. Brown and C. W. Jordan, Journal of Dynamic Behavior of Materials **2** (4), 411-420 (2016).

[168] E. N. Brown, J. C. F. Millett, N. K. Bourne and G. T. Gray III, 2007 (unpublished).

[169] C. Vasile and M. Pascu, *Practical Guide to Polyethylene* (Rapra Technologies, LTD, 2005).

[170] N. K. Bourne, J. C. F. Millett and S. G. Goveas, Journal of Physics D: Applied Physics **40** (18), 5714 (2007).

[171] Y. Mori and K. Nagayama, *The Review of High Pressure Science and Technology* **7**, 841-843 (1998).

[172] Y. Mori and K. Nagayama, AIP Conference Proceedings **505**, 69-72 (2000).

[173] Y. Mori and K. Nagayama, AIP Conference Proceedings **505**, 149-152 (2000).

[174] Y. Mori and K. Nagayama, AIP Conference Proceedings **706**, 103 (2004).

[175] Y. Mori, K. Nagayama, M. D. Furnish, Y. M. Gupta and J. W. Forbes, presented at the AIP Conference Proceedings, 2004 (unpublished).

[176] C. R. Siviour and J. L. Jordan, Journal of Dynamic Behavior of Materials **2** (1), 15-32 (2016).

[177] K. Takahashi, Journal of Macromolecular Science, Part B: Physics **8** (3-4), 673-689 (1973).

[178] D. Curran, D. Shockey and L. Seaman, Journal of Applied Physics **44** (9), 4025-4038 (1973).

[179] Y. B. Kalmykov, G. I. Kanel', I. P. Parkhomenko, A. V. Utkin and V. E. Fortov, Journal of Applied Mechanics and Technical Physics **31** (1), 116-120 (1990).

[180] V. Golubev, S. Novikov and Y. S. Sobolev, Strength of Materials **14** (2), 234-237 (1982).

[181] V. Golubev, S. Novikov and Y. S. Sobolev, Journal of Applied Mechanics and Technical Physics **23** (1), 134-141 (1982).

[182] N. Bourne and G. T. Gray III, J. Appl. Phys. **98** (12), 123503 (2005).

[183] X. Wu and H. Liu, Med. Phys **30**, 2169-2179 (2003).

[184] S. W. Wilkins, T. E. Gureyev, D. Gao, A. Pogany and A. W. Stevenson, Nature **384** (6607), 335-338 (1996).

[185] J. D. Yeager, S. N. Luo, B. J. Jensen, K. Fezzaa, D. S. Montgomery and D. E. Hooks, Composites Part A: Applied Science and Manufacturing **43** (6), 885-892 (2012).

[186] K. J. Ramos, B. J. Jensen, J. D. Yeager, C. A. Bolme, A. J. Iverson, C. A. Carlson and K. Fezzaa, presented at *Dynamic Behavior of Materials, Volume 1: Proceedings of the 2013 Annual Conference on Experimental and Applied Mechanics*, DOI 10.1007/978-3-319-00771-7$_5$0, 2013 (unpublished).

[187] J. N. Johnson and J. J. Dick, AIP Conference Proceedings 505 (2000).

[188] J. Furmanski, C. M. Cady and E. N. Brown, Polymer **54** (1), 381390 (2013).

[189] J. C. F. Millett, E. N. Brown, G. T. Gray, N. K. Bourne, D. C. Wood and G. Appleby-Thomas, J Dynam Behav Mater **2** (3), 326336 (2016).

[190] J. Furmanski, C. P. Trujillo, D. T. Martinez, G. T. Gray and E. N. Brown, Polym Test **31** (8), 10311037 (2012).

[191] E. N. Brown, J. Furmanski, K. Ramos, D. M. Dattelbaum, B. J. Jensen, A. Iverson, C. Carlson, K. Fezzaa, G. T. Gray III and B. M. Patterson, C. P. Trujillo, D. T. Martinez and T. H. Pierce, J Phys: Conf. Ser. **500**, 112011 (2014).

[192] N. Bourne, J. Millett, E. N. Brown and G. T. Gray III, J. Appl. Phys. **102** (6) (2007).

[193] M. F. Omar, H. M. Akil and Z. A. Ahmad, Mater Sci Eng A **538**, 125134 (2012).

[194] J. Zhang, *Experimental Study of Stress Cracking in High Density Polyethylene Pipes*, Ph.D. Thesis, Drexel University (2005).

[195] X. Lu and N. Brown, Journal of Materials Science **25**, 29-34 (1990).

[196] N. Brown, X. Lu, Y.-L. Huang and R. Qian, Makromol. Chem., Macromol Symp. **41**, 55-67 (1991).

[197] N. Brown, J. Donofrio and X. Lu, Polymer **28** (July), 1326-1330 (1987).

[198] M. Cassady, G. Derringer, J. Hassell, L. Hulbert, A. Lustiger, K. Prabhat and F. Uralil, Project Number N-4559: *Development of Improved Plastic Piping Materials and Systems for Fuel Gas Distribution* (1984).

[199] D. M. Duan and J. G. Williams, Journal of Materials Science **33**, 625-638 (1998).

[200] A. Lustiger and R. D. Corneliussen, Journal of Materials Science **22**, 2470-2476 (1987).

[201] K. J. Ramos, B. J. Jensen, A. J. Iverson, J. D. Yeager, C. A. Carlson, D. S. Montgomery, D. G. Thompson, K. Fezzaa and D. E. Hooks, in 18th APS-SCCM and 24th AIRAPT, Pts 1-19, edited by W. Buttler, M. Furlanetto and W. Evans (2014), Vol. 500.

[202] Sajaev, V.V. (2013) Storage ring operation modes. http://aps.anl.gov/Facility/Storage_Ring_Parameters_Parameters Accessed 20 March 2013.

[203] Q. Shen, W.-K. Lee, K. Fezzaa, Y. S. Chu, F. De Carlo, P. Jemian, J. Ilavsky, M. Erdmann and G. G. Long, Nucl. Instrum. Methods Phys. Res. Sect. A: Accelerators, Spectrometers, Detectors and Associated Equipment **582** (1), 77-79 (2007).

[204] B. J. Jensen, C. T. Owens, K. J. Ramos, J. D. Yeager, R. A. Saavedra, A. J. Iverson, S. N. Luo, K. Fezzaa and D. E. Hooks, Rev. Sci. Instrum. **84** (1), 013904-013905 (2013).

[205] S. N. Luo, B. J. Jensen, D. E. Hooks, K. Fezzaa, K. J. Ramos, J. D. Yeager, K. Kwiatkowski and T. Shimada, Review of Scientific Instruments **83**, 073903 (2012).

[206] G. I. Kanel, S. V. Razorenov and V. E. Fortov, *Shock-Wave Phenomena and the Properties of Condensed Matter* (Springer-Verlag, New York, 2004).

[207] R. A. Graham and W. P. Brooks, J. Phys. Chem. Solids **32**, 2311-2330 (1971).

[208] J. Wackerle, J. Appl. Phys. **33** (3), 922-937 (1962).

[209] R. Fowles, Journal of Geophysical Research **72** (22), 5729-5742 (1967).

[210] B. Dodd and Y. Bai, ed. *Adiabatic Shear Localization*, Second Edition ed. (Elsevier, 2012).

[211] M. Langer, P. Cloetens, B. Hesse, H. Suhonen, A. Pacureanu, K. Raum and F. Peyrin, Phil. Trans. R. Soc. A **372**:20130129 (2014).

[212] R. P. Carnibella, M. J. Kitchen and A. Fouras, Optics Express **20** (14), 15962-15968 (2012).

[213] M. J. Kitchen, D. Paganin, R. A. Lewis, N. Yagi and Y. K. Uesugi, Nuclear Instruments and Methods in Physics Research A **548**, 240-246 (2005).

[214] J. L. Barber, “Background Analysis in Phase Contrast Imaging”, to be submitted (2016).

[215] L. M. Barker and R. E. Hollenbach, J. Appl. Phys. **41** (10), 4208-4226 (1970).